JOURNAL OF THE

Electrochemical Society

Vol. 115, No. 1 January 1968

IN THE LONG RUN...

You'll be ahead with GLC Anodes for chlor-alkali production.

PRODUCTS GLC YOU CAN TRUST ®

GRAPHITE PRODUCTS DIVISION
GREAT LAKES CARBON CORPORATION
299 Park Avenue • New York, N.Y. 10017
OFFICES AND AGENTS FROM COAST-TO-COAST AND AROUND THE WORLD

Great Lakes Carbon Corporation is one of the world's largest manufacturers of graphite for electrochemical and electrothermic processes—and for aerospace, nuclear, metallurgical and other industrial uses.

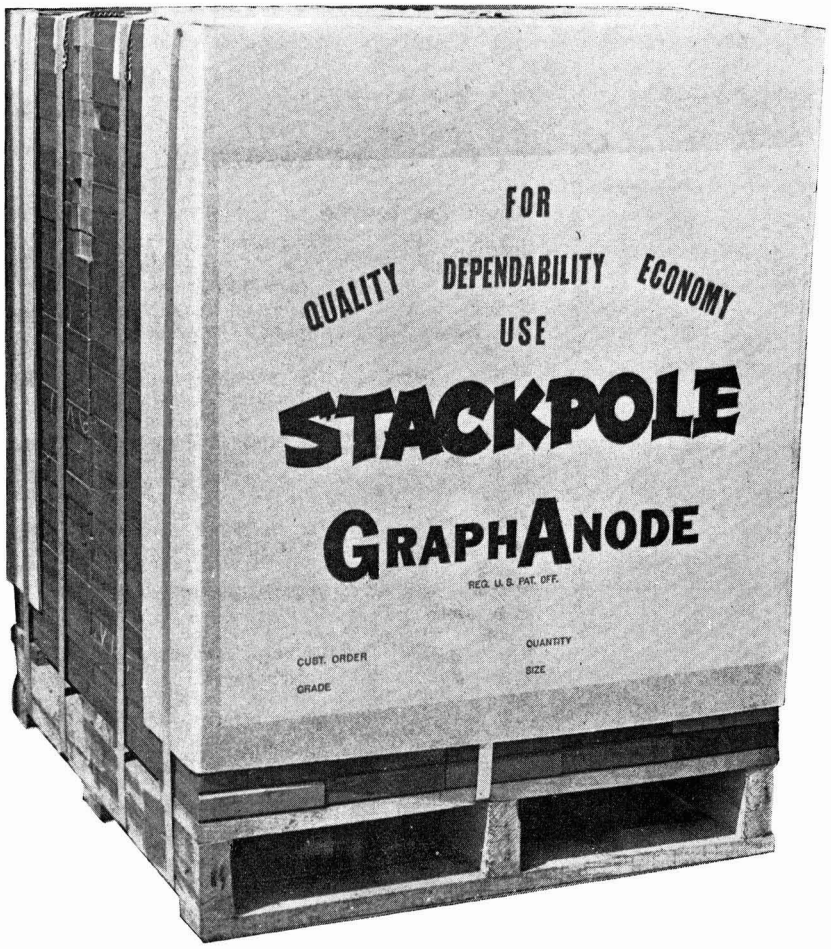

GET A LOAD OF THIS

If you're looking for improved performance, greater productivity, and reduced operating costs, investigate the savings of Stackpole GraphAnodes®. Rigid manufacturing controls assure material uniformity and permit proper cell alignment that makes for even wear and longer life. Whatever your anode needs, Stackpole GraphAnodes® can help you cut costs. Try a load. Write or call: Stackpole Carbon Company, Carbon Division, St. Marys, Pennsylvania 15857. Phone: 814-781-8463. TWX: 510-693-4511.

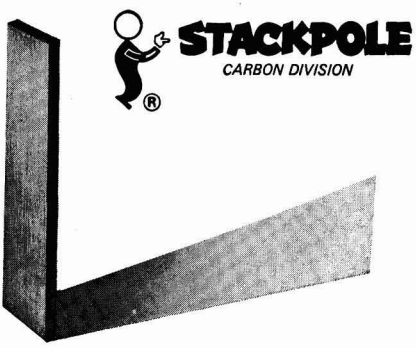

JOURNAL OF THE

C. L. Faust, Chairman, Publication Committee

Charles B. Moore, Director of Publications

EDITORIAL STAFF

Cecil V. King, Editor

Norman Hackerman, Technical Editor

Ruth G. Sterns, Managing Editor

Julius Kleror, Book Review Editor

Daniel J. Immediato, Assistant Editor

ADVERTISING OFFICE

Daniel J. Immediato, Assistant Editor

SOCIETY OFFICERS

Harry C. Gatos, President
Depts. of Met. & Electrical Eng.
Massachusetts Institute of Technology
Cambridge, Mass. 02139

Ivor E. Campbell, Vice-President
220 Gentry Road
Coraopolis, Pa. 15108

N. Corey Cahoon, Vice-President
Consumer Products Division
Union Carbide Corp.
Cleveland, Ohio 44101

Charles W. Tobias, Vice-President
Dept. of Chemistry and Chemical Engineering
University of California
Berkeley, Calif. 94720

R. Homer Cherry, Treasurer
Research and Developmept Center
Leeds & Northrup Co.
Dickerson Road
North Wales, Pa. 19454

Richard F. Bechtold, Secretary
Dow Chemical Europe A.G.,
Alfred Escher Strasse 39,
8027 Zurich, Switzerland

Ernest G. Enck, Executive Secretary
Society National Headquarters
30 East 42 St., New York, N. Y. 10017

JANUARY 1968

ELECTROCHEMICAL SCIENCE

TECHNICAL PAPERS

TECHNICAL NOTE

SOLID STATE SCIENCE

TECHNICAL PAPERS

ELECTROCHEMICAL SOCIETY

Vol. 115 • No. 1

TECHNICAL NOTES

BRIEF COMMUNICATIONS

ELECTROCHEMICAL SOCIETY NEWS AND REVIEWS

Manuscripts submitted to the Journal should be sent, in triplicate, to the Editorial Office at 30 East 42 St., New York, N. Y., 10017. They should conform to the revised Instructions to Authors available from Society Headquarters. Manuscripts so submitted, as well as papers presented before a National technical meeting, become the property of the Society and may not be published elsewhere in whole or in part without written permission of the Society. Address such requests to the Society Director of Publications.

The Electrochemical Society does not maintain a supply of reprints of papers appearing in its Journal. A photoprint copy of any particular paper, however, may be obtained by corresponding direct with the Engineering Societies Library, 345 E. 47 St., New York, N. Y., 10017.

Inquiries re positive microfilm copies of volumes should be addressed to University Microfilms, Inc., 300 N. Zeeb St., Ann Arbor, Mich.

Walter J. Johnson, Inc., 111 Fifth Ave., New York, N. Y., 10003, have reprint rights to out-of-print volumes of the Journal, and also have available for sale back volumes and single issues, with the exception of the current calendar year. Anyone interested in securing back copies should correspond direct with them.

Published monthly by The Electrochemical Society, Inc., at 215 Canal St., Manchester, N. H.; **Executive Offices, Editorial Office and Circulation Dept.**, and **Advertising Office** at 30 East 42 St., New York, N. Y., 10017, combining the JOURNAL and TRANSACTIONS OF THE ELECTROCHEMICAL SOCIETY. Statements and opinions given in articles and papers in the JOURNAL OF THE ELECTROCHEMICAL SOCIETY are those of the contributors, and The Electrochemical Society assumes no responsibility for them.

Claims for missing numbers will not be allowed if received more than 60 days from date of mailing plus time normally required for postal delivery of JOURNAL and claim. No claims allowed because of failure to notify the Circulation Dept., The Electrochemical Society, 30 East 42 St., New York, N. Y., 10017, of a change of address, or because copy is "missing from files." Subscription to members as part of membership service; subscription to nonmembers $24.00 plus $1.50 for postage outside U.S. and Canada. Single copies $1.70 to members, $2.25 to nonmembers.

Entered as second-class matter at the Post Office at Manchester N. H., under the act of August 24, 1912. Postage paid at Manchester, N. H.

Available 1968

ELECTRETS

and Related Electrostatic Charge Storage Phenomena

A Symposium
published by
The Electrochemical Society

This first volume in English collects 23 original papers on electret theory, experimental, and practical applications, which are of interest to scientists and engineers in such areas as:

- microphones
- air pollution control
- electrostatic printing
- computer memory storage
- high voltage generators
- prosthetic materials and blood coagulation
- telemetry instrumentation
- video and audio recording

Topics include:

- macroscopic and microscopic theories of electrets behavior
- production of electrets and charge decay
- effect of ionic additives
- ionic thermal currents
- electric conduction in films
- ice, wax, organic semiconductor, and ionic membrane electrets
- measurement of surface change

Edited from invited papers presented before the Dielectrics and Insulation Division of the Society at the 132nd National Meeting Fall, 1967 (Chicago).

---

please clip and return with remittance to

The Electrochemical Society, Inc.
30 East 42nd Street
New York, N. Y. 10017

Please enter my order for ..... copies of **Electrets**, available in the Fall at $11.00 each. My check or money order is enclosed for $ ..... (Payment must accompany order. No cash please. No discounts allowed.)

name

affiliation

mailing address

city

state zip code

Note: Remittances from outside the Continental United States must be by International Money Order or by bank draft on a New York bank.

The Electrochemical Society Offers–

• **Journal of The Electrochemical Society** is the fundamental research journal serving the interdisciplinary interests of chemistry, physics, electronics, biology, medicine, and engineering as they pertain to electrochemistry and to electrochemical phenomena. Written for the research scientist in industry, government, the independent laboratory, and the university, it publishes contributed Technical Papers, Technical Notes, and Brief Communications describing current basic research of original character, and is edited in two sections: (1) **Electrochemical Science** including such areas as batteries, fuel cells, corrosion and corrosion mechanisms, electrothermics and metallurgy, electrodeposition, electro-organic reactions and phenomena, and allied work of theoretical electrochemical nature. (2) **Solid State Science** including such areas as dielectrics and insulation, electrothermics and metallurgy, semiconductors, luminescence, and related solid state investigations. Also included is the Electrochemical Society News and Reviews section, keeping readers up to date on Society activities, news of its nineteen Sections and nine Divisions, book reviews, symposia plans, personals, etc.

• **Electrochemical Technology** is the journal of applied electrochemistry which serves the scientific and engineering interests of those responsible for research in development of electrochemical procedures, design and production of products and systems which rely on electrochemical phenomena for their function. It is written for the chemist, physicist, chemical engineer, electrical engineer, and metallurgist concerned with such products and processes as: batteries and fuel cells, corrosion and its mechanisms, dielectrics and insulation, electrodeposition and plating, electrothermics and metallurgy, electro-organic reactions, industrial electrolysis, and the electrochemical aspects of solid state technology, including luminescence and semiconductors. It publishes technical reports and original contributed papers of current progress in the application of electrochemistry and electrochemical phenomena to manufactured products and to the solution of manufacturing and processing problems. It publishes original contributed Technical Papers, Technical Papers, Technical Notes, and Brief Communications describing current application of electrochemistry and electrochemical phenomena to products and systems. Its Feature Section also publishes original contributed reviews pertinent to electrochemical interests.

• **Extended Abstracts** of some 400 papers presented at week-long Spring and Fall meetings include general papers as well as some 20 special topic symposia delivered at concurrent sessions during the meetings. A softbound Extended Abstracts volume is made available at low cost before and during each meeting and contains contributed as well as invited papers from distinguished scientists throughout the world.

Fill out and send to
The Electrochemical Society Inc., 30 East 42 St., New York N. Y. 10017

☐ Please send me information on the Society, including membership requirements ($20.00 annual dues includes the Journal).

☐ Electrochemical Technology to Members only 6.00

Herewith is my nonmember subscription, for the current calendar year, for which I enclose my remittance.

☐ Journal of The Electrochemical Society (monthly) $24.00
Overseas postage* 1.50

☐ Electrochemical Technology (bimonthly) 15.00
Overseas postage* 1.00

* This amount should be added to the subscription price for individuals located outside the Continental United States and must be remitted by New York bank draft.

Name **Title**

Business affiliation

Address

City **State**

Zip Code **Country**

JOURNAL OF THE ELECTROCHEMICAL SOCIETY

ELECTROCHEMICAL SCIENCE

JANUARY
1968

Journal of The Electrochemical Society is the fundamental research journal serving the interdisciplinary interests of chemistry, physics, electronics, biology, medicine, and engineering as they pertain to electrochemistry and to electrochemical phenomena. Written for the research scientist in industry, government, the independent laboratory and the university, it publishes contributed Technical Papers, Technical Notes and Brief Communications describing current basic research of original character, and is edited in two sections: 1) ***Electrochemical Science*** including such areas as batteries, fuel cells, corrosion and corrosion mechanisms, electrothermics and metallurgy, electrodeposition, electroorganic reactions and phenomena, and allied work of theoretical electrochemical nature. 2) ***Solid State Science*** including such areas as dielectrics and insulation, electrothermics and metallurgy, semiconductors, luminescence and related solid state investigations.

The Effect of Preoxidation and Meniscus Shape on the Hydrogen-Platinum Anode of a Molten-Carbonate Fuel Cell

James T. Cobb, Jr.[1] and Lyle F. Albright

School of Chemical Engineering, Purdue University, Lafayette, Indiana

ABSTRACT

Electrochemical phenomena in a hydrogen-oxygen fuel cell were studied at 723°K for the three-phase region on smooth platinum anode sheets, partially immersed in a eutectic mixture of lithium, sodium, and potassium carbonates. The meniscus shape varied with the composition of the gas phase and the potential of the anode. A platinum oxide surface was formed on the anode either by a preoxidation technique or by contacting the platinum with gaseous oxygen. A platinized surface, obtained by reduction with hydrogen of this surface, resulted in immediate large increases in current (activation), but the current slowly decreased with time (deactivation). Temporary increases in current were observed as the contact angle suddenly increased as the electrolyte film drained from the anode. The molten-carbonate film, obtained during raising the anode, was apparently relatively impermeable to hydrogen.

The current density at a selected polarization or voltage can be substantially increased through a smooth platinum anode completely submerged in an aqueous electrolyte by preoxidizing the anode surface (1, 2). The platinized surface, produced by the reduction of the oxide layer, slowly "recrystallizes," and the current density decreases toward its value before preoxidation. A similar effect is found on a smooth hydrogen-platinum anode partially immersed in an aqueous electrolyte (3).

On a smooth, partially immersed hydrogen-platinum anode, only well-developed menisci (formed by good wetting of the anode by the electrolyte) have been reported. However, evidence exists of variations in the contact angle on several other metal surfaces, partially immersed in aqueous solutions and exposed to various atmospheres and potentials (4-6). Changes in the contact angle have also been observed when the atmosphere was changed around sessile drops of molten sodium disilicate and molten lithium metaborate on smooth platinum surfaces at 1273°K (7, 8).

When a well-developed meniscus is present on an electrode partially immersed in an aqueous electrolyte, a film extends above the meniscus and over 75% of the current results from the transfer of the hydrogen through it (9-11). Migration of hydrogen along the surface of the anode has been shown to be insignificant under these conditions (9, 11). However, the possibility of significant bulk diffusion through the anode material of a high-temperature (723°-973°K) fuel cell has been postulated (12).

The present investigation concerned itself with these phenomena on a platinum anode partially immersed in a eutectic mixture of lithium, sodium, and potassium carbonates at 723°K. The effects of (*a*) preoxidation, (*b*) changes in composition of the gas phase, and (*c*) resistances to hydrogen transfer through an electrolyte film were investigated in regard to the current density through the anode and on the contact angle made by the molten salt with the anode.

Equipment.—The fuel cell used is shown schematically in Fig. 1. A 1:1:1 by weight mixture of lithium, sodium, and potassium carbonates (item 1) filled a 2500 ml Vycor beaker (item 2) to a depth of 12.5 cm. The salt was prepurified by melting and skimming the salt, then reducing metallic ions with a magnesium metal strip. An inverted 800 ml glass beaker (item 3) was immersed approximately 2.5 cm in the salt and served as the fuel chamber. It was supported by three 6 mm glass tubes. Two of these tubes (items 4 and 5) extended to within 2.5 cm of the top of the fuel chamber. One was the gas inlet and the other the gas outlet. A fourth tube, fused shut on the end, contained a chromel-alumel thermocouple, which was placed at the salt surface either just outside the fuel chamber or inside the chamber about 2.5 cm from the anode (item 7).

The glass tube (item 6), which supported the anode, contained a No. 16 B&W gauge Nichrome wire, spot welded to a 12.5 cm length of No. 20 B&W gauge platinum wire, which in turn was spot welded to the anode. The anodes were 4 x 4 cm squares of 0.0125 cm thick platinum sheets. Before use, they were cleaned for a few minutes in cold, concentrated HF. The position of the anode could be altered using a finely adjustable screw support device. Glass tubes and wire connections similar to those of the anode were provided for two platinum-air electrodes (one, the cathode; the other, the reference electrode) (items 8, 9, 10, and 11).

This cell assembly was positioned inside an electric oven (item 12), which had two 6.25 cm square windows, one in the front wall and the other in the back wall. A focused beam of light was directed through the back window. Visual reading of the contact angle allowed only approximate values (0°, 15°, 30°, 60°, and 90°) to be reported. The electric oven was covered with insulation which is not shown in Fig. 1.

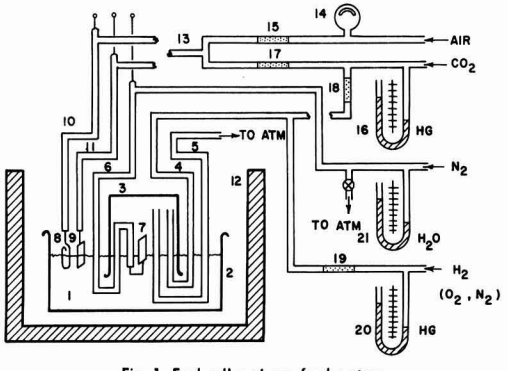

Fig. 1. Fuel cell and gas feed system

[1] Present address: U. S. Naval Weapons Center, China Lake, California.

A dry, metered mixture of about 6% CO_2 and 94% air was fed to the cathode and reference electrode through their support tubes (items 10, 11, 13, 14, 15, 16, and 17). Hydrogen, oxygen, nitrogen, carbon dioxide, and mixtures of these gases could be fed to the fuel chamber (items 4, 5, 16, 18, 19, 20, and 21). As a rule, the gas chamber contained about 10% carbon dioxide and 90% hydrogen.

A variable potential was applied to the anode by means of a set of wet cells connected across a voltage divider. The anode potential, with respect to the reference electrode, was measured using a combination of an L&N Type K potentiometer, a Rubicon galvanometer, and an Eppley standard cell. The current passing through the anode was measured using a Triplet Model 630 VOM meter.

Contact angles and menisci.—Advancing and receding contact angles are most commonly defined in a system where the entire mass of the liquid is in motion relative to the solid, *i.e.*, a drop of water running down a window pane or an electrode being raised from or lowered into an electrolyte. In the case of the experiments involving a stationary sessile drop or a meniscus on a stationary vertical plate, there was no movement of the bulk liquid with respect to the solid and so there was no classical advancing or receding contact angle. Only increasing or decreasing contact angles (which may have been related to receding and advancing contact angles, respectively) could be observed.

A meniscus whose contact angle is 0° has a film extending above it up the surface of the solid. No three-phase line was present, only a three-phase region at the top of the film. Once a finite contact angle appeared, then a three-phase line became well-defined at the top of the meniscus.

Effect of atmosphere on contact angle.—With hydrogen gas above the electrolyte in the beaker (item 3), the contact angle between a partially immersed platinum anode and the electrolyte was approximately 90° at open circuit conditions. The potential was —0.94v. As the hydrogen was replaced with nitrogen, the potential slowly rose, but the contact angle remained constant. After 5 hr the nitrogen was replaced by oxygen. Within several minutes, the potential had risen to a constant value of 0.08v and the contact angle had decreased to about 15°.

Preoxidation of anode.—A preoxidation procedure was used in which the anode was maintained briefly at a high potential (0.0-0.3v), and then returned to a lower one (usually —0.5v). Higher currents and changes of the contact angle were observed after preoxidation. Potentiostatic current-voltage curves had characteristics different from those found by Will (13), who did not mention any preoxidation effects. For example, a slightly roughened platinum anode partially immersed in the electrolyte at open circuit had a reference potential of —0.93v and an initial contact angle of about 90°. The potential was then adjusted in steps to —0.8, —0.6, —0.4, —0.2, and 0.0v in two sequences as shown in Fig. 2. The current tended to drop slightly with time after the potential was adjusted upward and to rise slightly with time after the potential was adjusted downward. In each case, the potential was maintained constant for 10 min, and the current was recorded at the end of this time.

When a potential of —0.20v was impressed, the contact angle of the meniscus changed to around 60°; at 0.00v, the angle became 0°. The meniscus height, measured with a cathetometer, was 0.40 cm. As the potential was lowered back to its open-circuit value, the contact angle slowly increased to 60°. After several hours at open circuit, the contact angle had increased to just under 90°. The current was significantly increased after preoxidation at 0.00v, as is seen in the second half of curve 2 of Fig. 2. Such an increase in current was also observed in several other current-voltage curves, obtained in a similar manner.

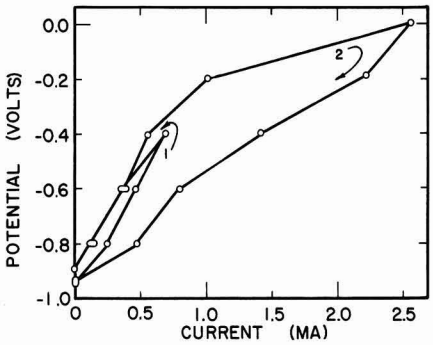

Fig. 2. Polarization of a platinum anode showing the effect of preoxidation.

The relationship between the conditions of preoxidation and the increase in activity of the anode following preoxidation was studied. Two series of runs were made with partially immersed anodes, in which the voltage was switched back and forth between —0.50v and 0.10v holding the potential steady at each value for 2 min. This operation was repeated several times and the current at the end of each 2-min interval was recorded, as shown in Fig. 3. Curves 1a and 1b are for a slightly roughened anode; curves 2a and 2b for a smooth one. The (a) portion of each curve indicates the values obtained at —0.50v; the (b) portion shows the data at 0.10v. The contact angle for the first point on the (a) portions was about 90°. For all the other points of the four curves, it was 0°. The current at —0.50v through both anodes increased by a factor of 1.8 in the interval of 2-6 min. This current was somewhat lower at 10 min, then gradually increased for the remainder of the 30-min experiment. At 0.10v, a sharp drop in current through both anodes (curves 1b and 2b) by a factor of about 0.7 was observed between the data points at 4 min and at 8 min. This drop in current was followed by a gradual increase until the very end of the experiment when a second drop in current seemed to be starting.

The rate at which the larger currents, following preoxidation, decreased was found to depend on the conditions of preoxidation. The data for curve 1 of Fig. 4 were obtained at an emergence height of 2.65 cm (*i.e.*, height that the top edge of the anode was above the undisturbed electrolyte surface), beginning with a relatively inactive surface (contact angle about 90°, current 0.71 ma, volts —0.5). Preoxidation was obtained using a potential of 0.10v for 1 min, from —1 to

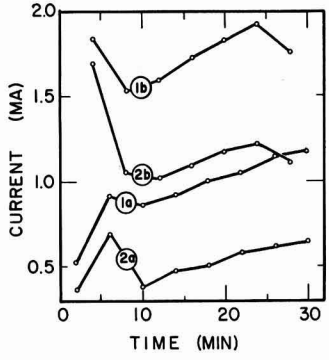

Fig. 3. Increase in current with time of preoxidation on a platinum anode.

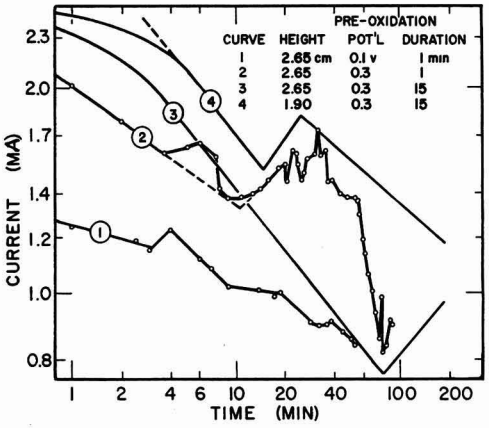

Fig. 4. Deactivation of a platinum anode following preoxidation

0 min on the abscissa (not shown). During this period, the contact angle changed to about 60°. At the end of this 1-min period, the external driving potential was removed temporarily to allow the cell potential to drop to —0.50v. The external driving potential was then reapplied, and the —0.50v cell potential was maintained for the next 55 min. The current decreased in general rather steadily during this period from about 1.25 to 0.82 ma. The contact angle remained at 60° during this entire period.

Curve 2 of Fig. 4 describes the behavior of an anode, also at 2.65 cm, which was preoxidized using a higher potential (0.3v for 1 min) then returned to —0.50v. A minute after preoxidation, the current was 2.0 ma. It decreased rapidly for 5 min, after which it rose slightly for 2 min, then fell rapidly to 1.38 ma at about 10 min after preoxidation. During the first 2 min of this initial 10-min period, the contact angle remained at 0°. For the last 8 min, ripples began to appear at the top of the meniscus. These ripples apparently were caused by the presence along the meniscus top of a number of small regions in which the meniscus was receding. The apparent contact angle increased to perhaps 10° or 20°, and thus a well-defined three-phase line was visible. The ripples were still apparent until 20 min, when the contact angle was around 30°. For the next 10 min, the contact angle continued to increase sporadically along the top of the meniscus. At 30 min, it averaged at about 60°. During this entire 20-min period, the current was generally increasing, although its value fluctuated significantly over short periods of time, as indicated by the data points shown on Fig. 4. Once the contact angle reached 60°, it remained there for the next 60 min. During this period, the current fell with some fluctuations from 1.74 to 0.82 ma.

The general increase in current by a factor of between 1.2 and 1.7 from curve 1 to curve 2 of Fig. 4 is attributed to the increase in the potential of the preoxidation process. Apparently the degree of oxidation and possibly the type of oxide on the platinum was different in each case.

Curves 3 and 4 of Fig. 4 and curve 1 of Fig. 5 were obtained on anodes at different emergence heights, which were preoxidized for even longer periods of time (15 min) at 0.30v and then returned to —0.50v. The generally higher current of curve 4 of Fig. 4 and lower current of curve 1 of Fig. 5 were apparently caused by the difference in the past history of the various portions of the anode surface at the three-phase region in each case. All three curves exhibited a temporary increase in current as rippling became noticeable (see Table I). The data points are not shown in these curves in order to maintain clarity. In general, there were fewer short-term current fluctuations than observed in curve 2 of Fig. 4. Curves 2 and 4 of Fig. 4 indicate that the rate of deactivation in the time period before ripples appear is a function of the length and potential of preoxidation.

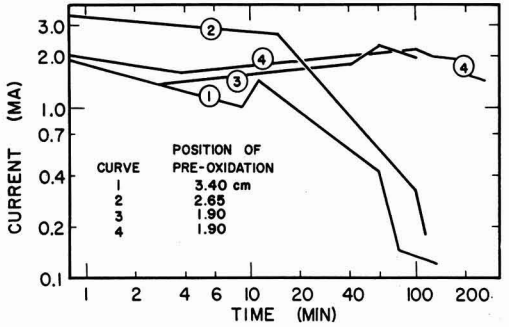

Fig. 5. Deactivation of a platinum anode following preoxidation

Raising the anode from one partially immersed position to another immediately after preoxidation tended to give immediately higher currents and/or increased currents over relatively long periods of time. The effect of this raising is shown in curves 2, 3, and 4 of Fig. 5. In each case, the anode was raised to an emergence height of 3.4 cm (*i.e.*, to a position where 3.4 cm of the anode was above the undisturbed electrolyte surface) immediately following preoxidation for 15 min at 0.30v. The position of preoxidation is indicated in the legend. After raising, the potential was maintained at —0.50v, and the current was observed for several hours.

The current increases depended on the distance that the anode was raised (as comparisons of curve 1 of Fig. 5 with curves 2, 3, and 4 indicate). The currents were higher when the anode was raised 0.75 cm as compared to those currents through the stationary anode. For the anodes raised 1.5 cm (curves 3 and 4), the higher currents remained for significantly longer periods of time than those through the stationary anode or through the anode raised 0.75 cm, although during the initial 20 min curves 3 and 4 were below curve 2. The contact angle behavior during the periods covered by each of the curves of Fig. 5 is also shown in Table I. In general, raising the anode after preoxidation lengthened the duration of both the lower contact angles and higher currents.

Current Distribution Profile

The current obtained as a function of the emergence height was investigated using an anode which had been preoxidized for 10 min (while completely submerged). Curve 1 of Fig. 6 records the current which was obtained when the anode was raised 0.05 cm every 2 min to an emergence height of 1.15 cm. The top of this anode was not quite horizontal so that its top edge did not rise completely above the level of the undisturbed salt surface until 0.4 cm. The current, which was 0.32 ma at complete submergence, increased very slowly during the initial 0.4 cm to a value of 0.40 ma. The current then increased rapidly for the next 0.6 cm with several small halts before reaching 1.00

Table I. Contact angles during time periods (in minutes) described by various curves of Fig. 4 and 5

Figure	Curve	0°	Ripples	30°	60°	90°
4	1				1-55	
4	2	1-2	2-20	20-30	30-90	
4	3	1-45	45-130	130-165		
4	4	1-2	2-11	11-20	20-195	
5	1	1-4	5-14	15-23	24-135	
5	2	1-7	8-13	14-24	24-76	80-128
5	3	1-64	70-109			
5	4	1-64	70-174	220-255	267-1485	

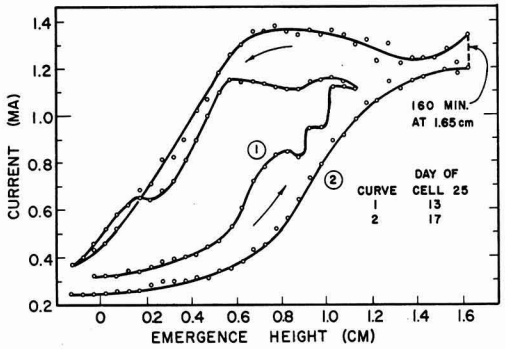

Fig. 6. Change in current through a platinum anode being raised and lowered.

cm emergence. Here the current leveled out at about 1.12 ma. The contact angle was 0° during the entire period of raising.

After 4 min at an emergence height of 1.15 cm the anode was slowly lowered to complete submergence, again at 0.05 cm intervals every 2 min. The contact angles at various heights were as follows

1.15 to 1.10 cm— 0°
1.05 to 1.00 cm—30°
0.95 to 0.75 cm—60°
0.70 to 0.10 cm—90°

At 0.10 cm the lowest part of the top edge of the anode became completely covered with electrolyte. The upper edge was not completely submerged until —0.15 cm had been reached. The current remained fairly constant at about 1.13 ma during lowering down to 0.50 cm. Only then did the current begin to decrease as lowering continued. The current reached a value of 0.37 ma at —0.15 cm.

A similar procedure was followed using an anode which had been preoxidized, raised, and lowered several times before the data, shown in curve 2 of Fig. 6, were taken. In this case the anode was raised to 1.65 cm and held there for 160 min before lowering was begun. The current during raising was 0.1-0.3 ma smaller than corresponding points on curve 1. The contact angle of the meniscus remained at 0°. During lowering, the current rose slightly and plateaued at about 1.35 ma until a height of 0.65 cm was reached. There the current began to drop. Its values were about 0.10 ma above the corresponding values of curve 1 at positions down to 0.20 cm and then about the same below that point. The contact angle did not rise above 30° during lowering until a height of 0.65 cm was reached. Below 0.65 cm on the lowering portion of the curve, the contact angle rose to around 60°.

Discussion of Results

The Platinum Surface

The results of this investigation imply that three basic surface structures were present at various times and positions on the platinum anodes described above. The first of these was smooth platinum covered with sorbed hydrogen (denoted Pt-H) in the potential range —1.0v to approximately —0.30v. The second was smooth platinum covered with sorbed oxygen (denoted Pt-O) in the potential range —0.20 to 0.30v. Finally, there was essentially smooth platinum covered by a thin platinized layer (denoted Pt*) also in the potential range —1.0 to —0.30v. Such surfaces have been postulated as occurring on platinum surfaces by previous investigators (1, 8, 2). These three surfaces help explain many of the results presented above.

The 90° contact angle on a stationary anode in a hydrogen atmosphere is attributed to the presence of the Pt-H surface at the three-phase boundary. The 0° contact angle is attributed to the Pt-O surface obtained from a Pt-H surface either by increasing the anode potential or changing the atmosphere to oxygen. The second of these methods shows that the change in contact angle from 90° to 0° is caused by a change in the chemical and physical, but not necessarily electrical, structure of the surface. Chemical changes of the surface affect the roughness (14) and surface tension (15, 8) of the surface. Pask (8) has discussed his results in light of these effects.

When hydrogen replaced oxygen in the atmosphere above the anode, or the potential was reduced below —0.20v (depending on which method was used to produce the Pt-O surface), the platinum oxide was reduced either directly, by diffusion of hydrogen along the surface or through the anode material, or by a small electrochemical "corrosion-type" cell on the anode surface. The rapid return of the potential to —0.50v, as noted in Fig. 4 and 5, indicates that the entire Pt-O surface is rapidly reduced. The slow return of the contact angle to high values, in spite of this rapid potential change, supports the hypothesis of the platinized surface (Pt*). The high degree of roughness, supposedly possessed by such a surface, should be sufficient, according to Johnson and Dettre (14), to maintain a low contact angle.

The activation by preoxidation techniques of a platinum anode for low-temperature cells has previously been reported to be caused by the thin platinum layer of the Pt* surface (1). However, no mention was made of changes in the meniscus shape as were noted in the present study. Platinized surfaces, however, presumably contain considerably more active catalytic sites than an atomically smooth surface; each site may also be more "active". The slow increase in contact angle, plus the decrease in current following preoxidation, strongly indicate that recrystallization of the platinized surfaces occurs slowly with time to form smooth surfaces again. The observed contact angle on a surface should increase as the surface roughness decreases (15, 14). However, the increase in contact angle will be slower than the roughness decrease, since the electrolyte is receding from the platinum surface (14). Thus, lower currents may be observed at the same contact angle with receding than with advancing menisci.

The Electrolyte Film

The results of this investigation also imply that any film of molten salt electrolyte above the meniscus region on the electrode is less pervious to transfer of reactants or of products to or from the anode surface than aqueous electrolyte films in low-temperature cells (13). In the present cell, hydrogen as fuel was transferred from the gas phase to the anode; the products, steam and carbon dioxide, were transferred from the anode to the gas phase. Based on molecular size considerations, transfer of the products might be more controlling than the transfer of the small hydrogen molecules.

When an activated anode was raised even relatively slowly, a film of electrolyte was pulled up on the previously submerged portions of the anode. The results of Fig. 6, especially curve 2, show that the presence of this film during raising may cause a current decrease of up to 1 ma from the value observed after the film has drained away. When a film is present, the three-phase region is at the top of this film. The ohmic resistance of the film increases the over-all ohmic resistance of the cell (11), thus lowering the current. There is insufficient transport of reactants or products across the film to counter the removal of the reaction sites to the top of the film.

When a film is present, as is always true to some extent, the resistance to ion transport in this film causes lower potentials toward the top of the film during preoxidation. Thus the upper portions of the anode

should not be as heavily oxidized, and thereafter platinized.

The sudden increase in current on stationary anodes, recorded in curves 2, 3, and 4 of Fig. 4 and in curve 1 of Fig. 5 is attributed to the drop of the three-phase region into the more heavily platinized regions below the top of the original well-developed meniscus. In addition, there was a simultaneous increase in the length of the three-phase region (when rippling appeared.)

Further indication of the nature of the electrolyte film is seen in curves 2, 3, and 4 of Fig. 5. When the anode was raised immediately after preoxidation, the reaction region again remained at a relatively well-defined three-phase region at the top of the film. Very soon (probably fractions of a minute) after preoxidation, this reaction region began to move down, because of film drainage, into a highly-oxidized region on the anode, thus explaining the lack of a sharp, upward increase in the current in these three cases. The fact that a higher initial current was obtained from the anode, which was raised only 0.75 cm, indicated that the film in this case was thick enough to support good currents at a reaction site about 0.35 cm above the top of the meniscus. Only when the anode was raised 1.60 cm after preoxidation did the ionic resistance in the film (mentioned before) lower the initial current. In this case, as the film thinned and drained away, the current slowly increased until the three-phase region reached the top of the meniscus about an hour following preoxidation. The contact angle was also increasing during this time.

When the anode was slowly lowered into the electrolyte and the contact angle of the advancing electrolyte increased up to 30°, the current, as observed in both curves 1 and 2 of Fig. 6, remained constant at its maximum value, or even rose slightly, until an emergence height of 0.50 cm. From this observation, it seems clear that diffusion of hydrogen along the electrolyte/solid interface or through the anode material itself from the Pt-H surface just above the three-phase region is the chief avenue of hydrogen to the reaction site.

Although platinum was the only material used for the anode, it is probable that results similar to those obtained in this investigation might be found with other types of anodes, such as nickel or palladium.

Conclusions

1. Platinum anodes immersed in a molten carbonate eutectic mixture at 723°K are activated by a preoxidation technique; the platinum surface is first oxidized and then reduced by hydrogen to platinized surfaces. Higher currents are obtained with platinized surfaces.

2. The contact angle between the 723°K molten carbonate eutectic mixture and a stationary, inactive platinum anode is around 90°. During preoxidation it decreases to 0°. The contact angle slowly changes to 90° during deactivation. If the hydrogen atmosphere above a stationary inactive anode is replaced by oxygen, the contact angle again becomes 0° and the height of the meniscus 0.40 cm.

3. At 723°K hydrogen diffuses mainly to the reaction site by a combination of diffusion along the interface of platinum and molten carbonates and/or diffusion through the bulk platinum.

4. Hydrogen apparently does not diffuse in appreciable amounts through the 723°K molten-carbonate film which may be present above the meniscus.

Acknowledgment

This work was supported by the Indiana Gas Association.

Manuscript received Aug. 29, 1966; revised manuscript received Sept. 7, 1967.

Any discussion of this paper will appear in a Discussion Section to be published in the December 1968 JOURNAL.

REFERENCES

1. W. C. French and T. Kuwana, *J. Phys. Chem.*, **68**, 1279 (1964).
2. S. Shibata, *Bull. Chem. Soc. Japan*, **36**, 525 (1963).
3. H. J. Davitt, Personal communication (1965).
4. M. Bonnemay, G. Bronoel, and E. Levart, *Compt. rend.*, **257**, 3394 (1963).
5. M. J. Sparnaay, *Surface Sci.*, **1**, 213 (1964).
6. H. C. Weber, H. P. Meissner, and D. A. Sama, *This Journal*, **109**, 994 (1962).
7. B. S. Ellefson and N. W. Taylor, *J. Am. Ceram. Soc.*, **21**, 205 (1938).
8. J. A. Pask and R. M. Fulrath, *ibid.*, **45**, 592 (1962).
9. R. P. Iczkowski, *This Journal*, **111**,1078 (1964).
10. T. Katan, E. A. Grens II, and R. M. Turner, *Preprints of Papers, Symposium on Fuel Cell Systems*, 31 (1963).
11. F. G. Will, *This Journal*, **110**, 152 (1963).
12. E. Gorin and H. L. Recht, *Fuel Cells*, **1**, 109 (1960).
13. F. G. Will, *This Journal*, **110**, 145 (1963).
14. R. E. Johnson, Jr., and R. H. Dettre, *Adv. Chem. Series*, **43**, 112 (1964).
15. A. W. Adamson and I. Ling, *Ibid.*, **43**, 57 (1964).

The Anodic Oxidation of Manganese Oxides in Alkaline Electrolytes

Hong Y. Kang and Charles C. Liang*

P. R. Mallory & Co., Inc., Laboratory for Physical Science, Burlington, Massachusetts

ABSTRACT

Manganese dioxide electrodes are discharged in electrolytes of 1M to 10M KOH and immediately reoxidized anodically. The efficiency of the oxidation, determined by chemical analysis as well as subsequent cathodic reduction, is a function of the concentration of KOH and decreases as the KOH concentration increases from 1M to 10M KOH. In 1M KOH, MnO_2 is reduced to a species tentatively identified as an active form of manganese (III) oxide, which can be efficiently reoxidized to MnO_2. In 10M KOH, however, MnO_2 is reduced first to manganese (III) oxide and subsequently to manganese (II) oxide. This manganese (II) oxide can be recharged only to an inactive form of manganese (III) oxide which is not reoxidized efficiently to MnO_2.

The cathodic reduction of manganese dioxide in alkaline electrolytes has been investigated by a number of authors (1-5). Kozawa and co-workers (1, 2) studied the discharge process of electrodeposited manganese dioxide on spectroscopic grade graphite rods in pure KOH solutions in the absence of the zinc electrode. Boden *et al.* (3), Cahoon and Kover (4), and

* Electrochemical Society Active Member.

Bell and Huber (5) investigated the same process for the pressed MnO_2-graphite electrode with and without zinc electrodes present. Kozawa *et al.* (1, 2) observed a two step reduction while other authors (3, 5) observed a three stage reduction in their systems.

The manganese dioxide electrode of rechargeable batteries (6-11) has also received some attention. Koval and Vorobeva (11) studied the anodic oxidation of a mixture of manganese oxide and nickel or iron hydroxide in alkaline electrolytes. They found that the efficiency of the oxidation of the electrode ranged from 6 to 20% and was dependent on the nature of the anion in the manganese salt used for the preparation of the electrode. However, no attempt was made by these authors to analyze and identify the products of the oxidation.

In view of the growing interest in the manganese dioxide-alkaline system in the secondary battery field, it was desirable to investigate the electrochemical behavior of the discharged manganese dioxide electrode. In the present work, electrodeposited manganese dioxide on graphite was first cathodically reduced in pure KOH solutions, then the anodic oxidation of the reduced electrode was studied under various conditions. The presence of a Zn electrode or ZnO in the KOH solution was avoided to eliminate any additional complications in interpreting the data.

Experimental

Preparation of the MnO_2 electrode.—Manganese dioxide was electrodeposited on 3.2 mm diameter spectroscopic graphite rods (AGKSP). The electrodeposition conditions were similar to those used by Nichols (12). Electrodes were plated at an apparent current density of 2 ma/cm² for 1500 sec from a solution containing 50g of $MnSO_4 \cdot H_2O$ and 65g of H_2SO_4 per liter at 80° ± 1°C. The electrodeposited manganese dioxide electrodes were washed thoroughly with distilled water and were kept in distilled water for at least 48 hr before use. From the chemical analysis by the method described below, 6.0 ± 0.3 mg of MnO_2 per electrode were obtained giving 1.97 ± 0.02 for the x value in MnO_x.

Constant current experiments.—The manganese dioxide electrodes were discharged and charged in KOH solutions. A platinum wire was used as the counter electrode in an H-cell with a sintered glass frit separating the two compartments. The discharge and charge processes were carried out at room temperature (25° ± 1°C) at constant current densities supplied by an E/M Model C614 constant current power supply. The working electrode potential during the electrolysis was measured against a Hg/HgO electrode in the same solution as the electrolyte by means of an E-H Model 250 electrometer. The potential-time curves were recorded by a Varian G-14 recorder. All the potentials reported in this paper are referred to the Hg/HgO electrode immersed in KOH of the same concentration as the electrolyte.

Chemical analyses of the electrodes.—The oxidation state of manganese on the electrode was determined from the chemical analysis as follows: The sample electrode was put in 50 ml of 6*N* HCl containing approximately 1g of KI. The HCl solution was well deaerated in advance by bubbling argon through it. The bubbling was continued until the manganese oxides on the electrode were completely dissolved. The oxidation power of the sample, *i.e.*, the amount of manganese oxides that oxidized iodide was then measured by a titration of the liberated I_2 with a standard 0.10*N* $Na_2S_2O_3$ solution using a microburet. After the titration, the total content of manganese in the solution was determined by the colorimetric analysis of the permanganate produced from the oxidation of Mn^{++} by KIO_4 (13). The x value in MnO_x was calculated from the total manganese content and the oxidizing power.

X-ray diffraction.—The manganese dioxide electrodes which had been subjected to discharge and recharge under various conditions were washed with distilled water until free from hydroxide ion. The electrodes were then dried in a vacuum oven at 60°-70°C for about 18 hr prior to the x-ray analyses. Debye-Scherrer x-ray powder photographs of the samples were made using standard techniques (Fe Kα radiation).

Results and Discussion

Manganese dioxide electrodes were discharged in various KOH solutions at a constant current density to a potential of —1.0v, whereupon the current was immediately reversed and the electrodes were charged anodically to various potentials. The current density used in these experiments were ranged from 0.2 to 2 ma/cm² of apparent surface area. The electrodes were then removed from the solution, and the oxidation state of manganese on each electrode was determined. The oxidation states of manganese thus determined were compared with those based on the total charge involved in the electrochemical process. Results of these comparisons are shown in Tables I and II. The recharge efficiency, expressed as the fraction of oxidized manganese to the total amount of oxidizable manganese, is also shown in the tables. These results indicate clearly that the rechargeability of the electrode was affected by the concentration of the KOH solution. The higher the concentration of the electrolyte the more difficult it was to reoxidize the electrode to manganese (IV) oxide. It also can be seen from Table II, in the range of current density studied, the general pattern of the electrochemical behavior was not affected by the current density.

It is also noted in Table I that when the manganese dioxide electrode was cathodized to the potential of —1.0v the oxidation state of manganese on the electrode or the depth of discharge differed in different KOH solutions. This is in agreement with the observations made by Kozawa and Yeager (1). The reduction of manganese (IV) stopped at manganese (III) when

Table I. Effect of KOH concentration on the recharge efficiency of the discharged manganese dioxide electrode at an apparent current density of 1 ma/cm²

KOH concentration, M	Anodization time at 1 ma/cm² sec	Potential at the end of charge volt (*vs.* Hg/HgO)	*X* in MnO_2 in electrode		Per cent[2] MnO_2 recovery efficiency	Per cent[3] Mn in electrolyte
			Analytical	Calculated[1]		
1	0	Initial[4]	1.51	1.52	—	0
	850	0.2	1.74	1.78	50.0	0
	1100	0.4	1.85	1.89	73.9	0
	1300	0.6	1.93	1.96	91.3	0
2	0	Initial	1.45	1.43	—	0
	900	0.2	1.70	1.73	48.1	0
	1300	0.4	1.81	1.88	69.2	0
	1500	0.6	1.89	1.95	84.6	0
4	0	Initial	1.35	1.32	—	0
	1100	0.2	1.64	1.75	46.8	0
	1500	0.4	1.76	1.84	66.1	0
	1800	0.6	1.78	1.91	69.4	5
6	0	Initial	1.24	1.26	—	0
	1300	0.2	1.56	1.70	42.1	0
	1700	0.4	1.71	1.79	61.8	0
	1900	0.6	1.72	1.94	63.2	5
10	0	Initial	1.14	1.15	—	4
	650	—0.3	1.24	1.24	12.0	4
	1300	0.2	1.52	1.59	41.9	5
	1600	0.2	1.62	1.69	57.8	10
	1800	0.4	1.68	1.79	65.1	17
	1900	0.55	1.65	1.87	61.4	20

[1] Calculated on the basis of the total charge (current × time) involved in discharge and recharge, and the total amount of Mn in the electrode

[2] Fraction of oxidized manganese to the total amount of manganese oxidizable to MnO_2.

[3] Fraction of manganese in the electrolyte at the end of each electrolysis to the total amount of manganese initially present.

[4] Initial state of the electrode is that obtained by cathodically discharging the original MnO_2 electrode to -1.0v (*vs.* Hg/HgO) in each KOH solution.

Table II. Recharge efficiency of the discharged manganese dioxide electrode at different current densities

Apparent current density ma/cm²	KOH Concentration, M	Anodization time, sec	Cut-off potential volt (*vs.* Hg/HgO)	X in MnO_x Analytical	X in MnO_x Calculated[1]	Per cent[2] MnO_2 recovery efficiency
0.2	1	0	Initial[3]	1.51	1.52	—
		4500	0.2	1.77	1.79	56.5
		5600	0.4	1.85	1.90	73.9
		6600	0.6	1.95	1.98	95.6
	10	0	Initial	1.14	1.15	—
		6700	0.2	1.52	1.60	45.8
		9000	0.4	1.65	1.79	61.5
		10500	0.6	1.65	1.93	61.5
2.0	1	0	Initial	1.51	1.52	—
		410	0.2	1.70	1.77	41.3
		540	0.4	1.82	1.88	67.4
		600	0.6	1.89	1.93	82.6
	10	0	Initial	1.14	1.15	—
		590	0.2	1.45	1.55	37.4
		850	0.4	1.63	1.71	59.1
		900	0.6	1.60	1.83	55.4

[1] Calculated on the basis of the total charge involved in discharge and recharge, and the total amount of Mn in the electrode.
[2] Fraction of oxidized manganese to the total amount of oxidizable manganese.
[3] The initial state of the electrode is that obtained by cathodically discharging the original MnO_2 electrode to -1.0v (*vs.* Hg/HgO) at 1 ma/cm² in each KOH solution.

the manganese dioxide electrode was discharged to —1.0v in 1M KOH or to —0.4v in 10M KOH. Further reduction from manganese (III) to manganese (II) occurred when the discharge was carried out in 10M KOH to the potential of —1.0v. It was concluded by these authors (1) that the second step discharge from manganese (III) to manganese (II) occurred through the dissolution of manganese (III) oxide in 10M KOH followed by reduction of Mn(III) in solution to Mn(II) and reprecipitation of manganese (II) in solution to solid manganese (II) oxide. The absence of the second step reduction in dilute KOH solutions was explained as the result of insolubility of manganese (III) oxide in dilute solutions (14).

In addition, the different KOH concentrations resulted in distinctive potential-time curves. This is well illustrated by Fig. 1 where two typical curves, *viz.*, one for 10M and another for 1M KOH, are shown. The dotted lines show the second discharge curves following the anodic oxidation. It is seen that in 10M KOH the recharge curve showed two plateaus whereas in 1M KOH no distinct plateau appeared in the recharge curve. Distinctive characteristics in different KOH solutions can be observed for the second discharge curves also. In 10M KOH the second discharge curve differed pronouncedly from the first discharge curve, indicating that the preceding recharge to the original manganese (IV) state was not efficient. On the other hand, in 1M KOH the second discharge curve was similar to the first one, indicating that the preceding recharge was efficient.

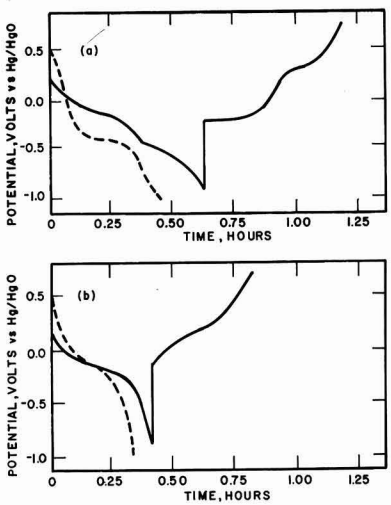

Fig. 1. Potential-time curves of the manganese dioxide electrode at a constant current density of 1 ma/cm²; (a) in 10M KOH; (b) in 1M KOH. ——— First discharge and charge; - - - - - second discharge.

The different behavior patterns of manganese oxides during their anodic oxidation in different KOH solutions may be attributed either to the effect of KOH concentration on the oxidation or to the depth of discharge at the initial point of the anodization. The observations shown in Fig. 2 seem to support the latter case. Figure 2a and 2b show the cases where the reoxidation of the discharged manganese dioxide electrode was started from the manganese (III) state. Figure 2c shows the recharge curve in 1M KOH when the initial oxidation state of manganese was the manganese (II) state. These time-potential curves clearly indicate that when the recharge following the discharge was carried out in the same solution the KOH concentration affected the anodic oxidation of the discharged manganese dioxide electrode only in that it brought about different depths of discharge. The depth of discharge at the initial point of the anodic oxidation determined the characteristics of the charge process. The chemical analyses of the oxidation states of manganese in these cases (Fig. 2) also supported the conclusion that the depth of discharge was responsible for the different behavior patterns during the anodic oxidation. For instance, when the recharge was started from manganese (II) state, even if it was carried out in 1M KOH (Fig. 2c), the oxidation state of manganese at the end of anodization was about the same as that for the case of 10M KOH.

A necessary consequence of the above conclusion is that the manganese (III) oxide produced from the cathodic reduction of manganese dioxide was more

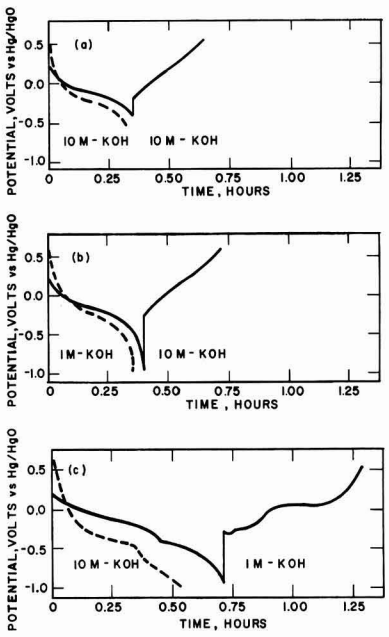

Fig. 2. Potential-time curves of the MnO_2 electrode at 1 ma/cm²; (a) Both discharge and charge in 10M KOH. (b) Discharge in 1M KOH, recharge in 10M KOH. (c) Discharge in 10M KOH, recharge in 1M KOH. ——— First discharge and charge; - - - - - second discharge.

active to the anodic reoxidation than the manganese (III) oxide formed by the anodic oxidation of manganese (II) oxide. Indeed either in 10M KOH or in 1M KOH the anodic oxidation beyond manganese (III) oxide was inefficient when the initial material of the oxidation was manganese (II) oxide. While manganese (III) oxide from the cathodic reduction of manganese dioxide was efficiently reoxidized to manganese dioxide in either 10M KOH or 1M KOH.[1]

Attempts to distinguish the two forms of electrochemically different manganese (III) oxide employing the x-ray diffraction technique were not successful because both the samples showed similar x-ray patterns corresponding to γ-Mn_2O_3. However, it was also found that both forms of manganese (III) oxide including the originally active one were inactive to the anodic oxidation to manganese dioxide after they were subjected to the washing and drying processes of the sample preparation for the x-ray analysis. Evidently, one or both of the manganese (III) oxides changed in crystal structure during the sample preparation, with a corresponding change in electrochemical behavior. Hence, in the present paper, the differentiation between the two forms of manganese (III) oxide is made primarily on the basis of electrochemical data.

It was proposed by Kozawa *et al.* (1, 2) that the mechanism of the first step discharge of $MnO_{2.0}$ to $MnO_{1.5}$ is a homogeneous phase reduction and that the product of this step is α-MnOOH. In the present work it was found that the anodic oxidation was always efficient whenever the preceding discharge of the manganese dioxide electrode was stopped at the point where one could expect α-MnOOH to be produced. Therefore, it seems logical to conclude that the active manganese (III) oxide which can be efficiently reoxidized to manganese dioxide was α-MnOOH. Both γ-MnO_2 and α-MnOOH have the same rhombic crystal structure. And since the mechanism of the cathodic reduction of γ-MnO_2 to α-MnOOH is a homogeneous phase reaction, it is probable that the anodic oxidation of α-MnOOH to γ-MnO_2 was a homogeneous phase process also.

The two forms of manganese (III) oxide may differ only in physical properties which lead, *e.g.*, to differences in the contact areas between the depolarizer and the conductor, or in chemical reactivity and identity with its consequences. Differences probably exist between the physical properties of the two forms of the oxide in view of the different paths leading to the two oxides. The active form was produced from γ-MnO_2 through a homogeneous phase reduction, and the inactive form was produced from γ-MnO_2 after it had undergone such processes as (*a*) a first step reduction, (*b*) a second step reduction which included (*i*) dissolution of manganese (III) oxide, (*ii*) solution reduction, and (*iii*) reprecipitation of manganese (II), and (*c*) reoxidation of manganese (II) oxide which may include again dissolution and reprecipitation. These processes most likely resulted in changes in the contact areas between the oxide and the substrate, in the particle size of the oxide, and in the site of deposition of the oxide. However, the electrochemical similarities between the electrodeposited manganese dioxide electrodes and the pressed manganese dioxide-graphite pellet electrodes suggested that these physical conditions alone could not be the decisive cause for the distinctive electrochemical behavior patterns of two forms of manganese (III) oxide.

This leaves the possibility that the two forms of the oxide differed in chemical identity. If this were the case, a possible chemical identity of the inactive form, among others, is γ-Mn_2O_3 according to the x-ray diffraction patterns discussed in the previous section. The data in Fig. 3 support this conclusion. In this series of experiments, the electrochemical behaviors of the γ-Mn_2O_3 electrode and that of the inactive Mn(III) oxide electrode were compared. The γ-Mn_2O_3 electrode could be prepared according to either of the following procedures.

[1] We shall refer the manganese (III) oxide which can be efficiently reoxidized to manganese dioxide as active form and the one which cannot be efficiently reoxidized to manganese dioxide as inactive form. Notice that both of these manganese (III) oxides are active to the cathodic reduction to manganese (II) oxide.

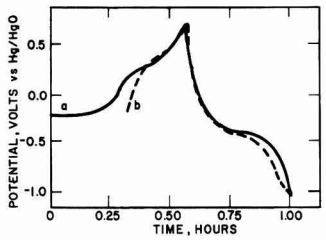

Fig. 3. Potential-time curves (charge and discharge) at 1 ma/cm² in 10M KOH. (a) —— Electrodeposited MnO_2 electrode discharged to —1.0v (vs. Hg/HgO); (b) - - - - - γ-Mn_2O_3 electrode made from the electrodeposited MnO_2 electrode by discharging it to manganese (II) oxide, then charging it to manganese (III) oxide, and washing and drying; it was identified by x-ray analysis.

1. An electrodeposited MnO_2 electrode was cathodized to —1.0v then anodized to 0.2v in 10M KOH. After the electrochemical treatment, the electrode was washed thoroughly and dried at about 60°C.

2. An electrodeposited MnO_2 electrode was cathodized to —1.0v in 10M KOH. The reduced electrode was then taken out of the solution and subjected to air oxidation for at least 8 hr.

Chemical analyses showed that the empirical formula of the manganese oxide in these electrodes was $MnO_{1.5\pm0.02}$ and the x-ray diffraction patterns proved that these were indeed γ-Mn_2O_3 electrodes. The potential-time curves for the anodic oxidation and the subsequent cathodic reduction of the γ-Mn_2O_3 are shown by the dotted curves in Fig. 3. When the electrode was anodized to +0.6v where the evolution of O_2 began to be visible, the oxidation state of manganese was analytically determined as 3.2 ± 0.04. These results clearly indicated that γ-Mn_2O_3 could not be efficiently oxidized to MnO_2 under the experimental conditions. This fact was also shown by the subsequent discharge curve. Most of the discharge process occurred at the potential near —0.4v where $MnO_{1.5}$ to MnO took place. When the potential-time curves for the anodization and subsequent cathodization of the Mn(II) oxide electrode (solid line in Fig. 3) were compared with those of the γ-Mn_2O_3 electrode, it revealed that they were superimposable after the Mn(II) oxide electrode reached —0.2v where the manganese oxide became Mn(III) oxide. Based on the similarity of the electrochemical behaviors of these Mn(III) oxides, it is suggested that the manganese (III) oxide produced during the anodic oxidation of manganese (II) oxide in 10M KOH was most likely γ-Mn_2O_3. In view of the fact that γ-Mn_2O_3 and $Mn(OH)_2$ have different crystal structure and that both $Mn(OH)_2$ and Mn_2O_3 dissolve in 10M KOH, the anodic oxidation of the manganese (II) oxide to the manganese (III) oxide probably involved dissolution, solution oxidation, and reprecipitation.

In summary, the electrochemical cycle of reduction-oxidation of the manganese dioxide in 10M KOH is postulated to comprise:

$$\begin{array}{l} \gamma\text{-}MnO_2 \\ \quad \Downarrow \\ \alpha\text{-}MnOOH \rightarrow Mn(III)\ (\text{in solution}) \rightleftharpoons \gamma\text{-}Mn_2O_3 \\ \qquad\qquad \Downarrow \\ \qquad\qquad Mn(II)\ (\text{in solution}) \rightleftharpoons Mn(OH)_2 \end{array}$$

The first step oxidation of $Mn(OH)_2$ to manganese (III) oxide may involve the dissolution of manganese (II), its solution oxidation to manganese (III) followed by the precipitation of manganese (III). The precipitated form of manganese (III) is thought to be γ-Mn_2O_3 which is inactive to further oxidation. When the discharge process of γ-MnO_2 is stopped at the end of the first step the reoxidation of the product manganese (III) oxide which is α-MnOOH is efficient. Also, once manganese (III) dissolves in KOH solution, reprecipitation to α-MnOOH seems to be inhibited.

Acknowledgment

The authors wish to express their thanks to Dr. P. Bro and Dr. R. G. Selim for their helpful discussions, to Mr. L. B. Griffiths for the x-ray diffraction measurements, and to Mr. G. H. Boyle for his help in preparing the graphs.

Manuscript received July 19, 1967; revised manuscript received Sept. 5, 1967. This paper was presented at the Chicago Meeting, Oct. 15-19, 1967 as Abstract No. 40.

Any discussion of this paper will appear in a Discussion Section to be published in the December 1968 JOURNAL.

REFERENCES

1. A. Kozawa and J. F. Yeager, *This Journal*, **112**, 959 (1965).
2. A. Kozawa and P. W. Powers, *ibid.*, **113**, 870 (1966).
3. D. Boden, C. J. Venuto, D. Wisler, and R. B. Wylie, *ibid.*, **114**, 415 (1967).
4. N. C. Cahoon and M. P. Kover, *ibid.*, **106**, 745 (1959).
5. G. S. Bell and R. Huber, *ibid.*, **111**, 1 (1964).
6. L. F. Urry, U. S. Pat., 3, 024,297 (1962).
7. L. F. Urry, U. S. Pat. 3,053,701 (1962).
8. K. V. Kordesch, U. S. Pat. 3,113,050 (1963).
9. G. R. Drengler, U. S. Pat. 3,226,260 (1965).
10. A. F. Daniel, J. J. Murphy, and J. M. Hovendon, "Batteries," Vol. 1, p. 169, D. H. Collins, Editor, McMillan Co., New York, (1963).
11. I. I. Koval and V. N. Vorobeva, Vestnik Elektropromyshlennoti, **4**, 47 (1958) (AD No. 243823, translated by G. Kinner).
12. G. W. Nichols, *Trans. Electrochem. Soc.*, **62**, 392 (1932).
13. L. F. Hamilton and S. G. Simpson, "Quantitative Chemical Analysis," p. 477, McMillan Co., New York (1964).
14. A. Kozawa, T. Kalnoki-Kiss, and J. F. Yeager, *This Journal*, **113**, 405 (1966).

The Chemistry and Crystallography of Basic Antimony Sulfates

H. E. Hintermann*[1] and C. J. Venuto*

ESB Incorporated, The Carl F. Norberg Research Center, Yardley, Pennsylvania

ABSTRACT

The system Sb_2O_3-SO_3-H_2O has been investigated in the H_2SO_4-molarity range $0 < M < 12.7$. Five distinct basic antimony sulfates, previously unreported, have been identified. The chemistry and crystallography of these salts have been established and their ranges of stability in H_2SO_4 determined at room temperature and at the boiling point of the acid. Earlier experimental findings suggesting large amounts of bound crystallization water in these compounds have been disproved.

The ternary system Sb_2O_3-SO_3-H_2O has not been studied extensively. The few reports providing substantial data are those published by Adie (1) in 1890 and more recently by the Russian workers Tananaev and Mizetskaya (2) and Veller and Sobol (3). The results reported on the chemical composition of the basic antimony sulfates are inconsistent and contradictory. The system is of theoretical and practical interest, however, since solutions of antimony or antimony trioxide in sulfuric acid are widely used in analytical procedures and in industry for producing a variety of antimony compounds and more recently in the development of a new battery system (4). This latter application has stimulated a more thorough study of the Sb_2O_3-SO_3-H_2O system at medium and low sulfuric acid concentrations.

The chemical compositions and crystal structures are well established for the two modifications of Sb_2O_3, *i.e.*, Valentinite (orthorhombic) and Senarmontite (cubic) and for the normal sulfate $Sb_2(SO_4)_3$ (5, 6). The composition of the basic sulfates, derived from $Sb_2(SO_4)_3$ as a hydrolysis product or produced by reacting Sb_2O_3 with polyhydrated sulfuric acid, $H_2SO_4 \times H_2O$, are uncertain. According to a comprehensive treatise on this subject (7), the normal sulfate $Sb_2(SO_4)_3$ is obtained in $H_2SO_4 \cdot 1\ H_2O$. By hydrolyzing this salt in cold water $2Sb_2O_3 \cdot SO_3$ is formed, by hydrolyzing it in hot water $7Sb_2O \cdot 2SO_3$. In the acid range $H_2SO_4 \cdot 2H_2O$ (12.3M) to $H_2SO_4 \cdot 4H_2O$ (8.7M) $Sb_2O_3 \cdot H_2O$ is said to be formed at room temperature while Sb_2O_3 is formed on heating. Further dilution leads to the precipitation of hydrated antimony trioxide $Sb_2O_3 \cdot 3H_2O$.

The Russian investigators (2, 3) obtained an even larger number of basic antimony sulfates by hydrolysis of the $Sb_2(SO_4)_3$. At concentrations lower than 8.6-10.7M H_2SO_4, compounds like $Sb_2(SO_4)_3 \cdot y\ H_2O$ are formed at room temperature with y being 5 or 10, and compounds like $Sb_2O_3 \cdot x\ SO_3 \cdot y\ H_2O$ at 100° and 155°C with x/y ratios of 2.5/24, 6/23, 20/100, 28/93, and 31/13, respectively.

The primary purpose of the Russian work was the determination of the solubility limits of trivalent antimony in aqueous sulfuric acid of various concentrations, rather than to investigate the composition of the solid phases formed during the reaction. The authors themselves regard the results of the proposed stoichiometry of the reported basic antimony sulfates as only an approximation. Hence not much accurate information exists on the chemical composition of basic antimony sulfates and none on their crystallography.

Experimental

The Sb_2O_3-SO_3-H_2O system requires a long time to reach equilibrium condition, *i.e.*, several months at

[1] Present address: Laboratoire Suisse de Recherches Horlogères, Neuchâtel, Suisse.
* Electrochemical Society Active Member.

room temperature and several days at boiling temperature of the solution. If equilibrium conditions are not attained, mixtures of basic sulfates will result and will make subsequent chemical analyses inaccurate. This is one possible source of error to explain the lack of consistency in the results of previous workers. In addition, once formed, the solid equilibrium reaction product is difficult to isolate from the mother solution in a pure state without further hydrolyzing it or otherwise changing it in the course of the washing procedure. Some workers (1, 3) omit washing the crystalline solid phase with any solvent at all. They attempt to remove the adherent film of mother liquid on the crystal faces by sedimentation, centrifugation, or drying between porous plates. None of these methods is effective enough, and it is obvious that the chemical analyses obtained with these procedures are inaccurate and unreliable.

We found that the high basic sulfates, produced at very low H_2SO_4 concentrations, could be washed effectively with cold water and the medium and lower basic sulfates with absolute methanol, without changing the structural features of these salts. X-ray powder diffraction patterns obtained on the reaction product before and after the washing procedure proved to be a sensitive means of detecting any change in the structure, and thus the chemical composition of the original salt, due to hydrolysis or solvolysis.

The experiments were carried out with reaction mixtures of 10g Sb_2O_3 in 1 liter H_2SO_4 of different concentrations in the molarity range $O < M < 12.7$. To obtain equilibrium conditions, the mixtures were either stored in glass stoppered Pyrex glass bottles at room temperature for 3 to 6 months or heated to the boiling point in Pyrex reaction kettles with reflux condensers for 15 to 25 days. Fisher Certified Analytical Chemicals were used. Prior to use the Sb_2O_3 was dried at 110°C in air for 5 hr. Its x-ray diffraction pattern agreed with that published by ASTM for Senarmontite.

The equilibrium reaction products were filtered through a Gooch crucible of 8-10μ pore size. A sample was taken from the still wet residue for x-ray powder diffraction, and some crystals were selected for single crystal analysis for use with a Weissenberg camera. They had a prismatic shape with dimensions of about 0.4 mm in one direction and 0.1 mm in the two others. The powder pattern, obtained on a Norelco diffraction unit using Nickel filtered Copper K α radiation, served to establish the stability ranges of basic antimony sulfates in sulfuric acid of different molarities at room and boiling temperature of the solutions. It was used further to determine if an equilibrium state actually had been attained and a single pure phase had been formed or if the reaction product consisted of more than one solid phase. Finally, it served a reference pattern to confirm whether the washing procedure instigated any structural changes of the salt formerly in equilibrium with its solution. Single crystals, representative of each structure type that was stable in a given acid range, were used for microscopical investigations and for the determination of the density by the wet pycnometer method using methyl-benzoate ($\rho = 4.69$ g/cm^3) at 27°C. The unit cell dimensions, the space group, the number of asymmetric units per unit cell, and the x-ray reflections for each structure type were established by single crystal x-ray diffraction methods.

The remaining residue was washed either in cold water or absolute methanol while still in the crucible and dried in air. Samples from this product were chemically analyzed. The solvents for Sb_2O_3 found in the literature (1, 8) could not be applied to the basic antimony sulfates. These were neither completely soluble in NH_4Cl, NH_4NO_3, nor in molten Na_2CO_3. They were soluble in HCl; however, an insoluble basic chloride precipitated simultaneously. Addition of tartaric acid almost completely prevented basic chloride formation. Nevertheless, a slight turbidity of the solution could not be avoided. All basic antimony sulfates investigated were found entirely soluble when heated in a slightly alkaline solution of Na_2S or $(NH_4)_2S$. Acidifying this solution with HCl precipitated antimony as Sb_2S_3 which could be determined gravimetrically as such. The $SO_4^=$ content was determined in the filtrate as $BaSO_4$, the water of hydration as the balance. The mean error of determination of Sb and $SO_4^=$ carried out on blanks was smaller than $\pm$ 2 and $\pm$ 4%, respectively.

Results and Discussion

From the unit cell dimensions, space group, number of asymmetric units per unit cell, and the density it was possible to calculate the molecular weight of the compound according to

$$M = \frac{a_o \cdot b_o \cdot c_o \cdot \rho}{z \cdot 1/N}$$

where M = molecular weight of one asymmetric unit in the unit cell; a_o, b_o, c_o = unit cell dimensions in Angstrom units (Å); ρ = density of the pure phase in g/cm^3; N = Avogadro's number; $1/N = 1.6606 \cdot 10^{-24}$ = weight of g in a hypothetical atom of atomic weight 1.000; and z = number of asymmetric units in the unit cell. Combining these results with those obtained from the chemical analyses, *i.e.*, the Sb/SO_3 ratio of the molecule, the actual chemical formula of the compound could be derived. Thus five distinct basic antimony sulfates were identified in the H_2SO_4 range $O < M < 12.7$. These sulfates are tabulated in Table I together with some crystallographic, chem-

Table I. Chemistry and crystallography of basic antimony sulfates

Structure type	A	B	C	D	E
Crystal system	Orthorhombic	Orthorhombic	Orthorhombic	Orthorhombic	Orthorhombic
Space group	Pmmn—D_{2h}^{13}	Pmmn—D_{2h}^{13}	Pmmn—D_{2h}^{13}	Pmmn—D_{2h}^{13}	Pmmn—D_{2h}^{13}
Asymmetric units	4	8	4	4	8
Unit cell dim, Å. a_o	14.83	14.26	12.03	13.23	15.35
b_o	11.42	14.16	18.89	16.21	14.61
c_o	5.80	8.98	6.00	13.50	9.23
Unit cell vol, cm^3	$0.982280 \cdot 10^{-21}$	$1.813256 \cdot 10^{-21}$	$1.363480 \cdot 10^{-21}$	$2.895210 \cdot 10^{-21}$	$2.069952 \cdot 10^{-21}$
Density, g/cm^3	4.30 ± 0.05	4.82 ± 0.05	5.16 ± 0.05	4.87 ± 0.05	4.69 ± 0.05
Weight of unit cell, g	$4.22380 \cdot 10^{-21}$	$8.73989 \cdot 10^{-21}$	$7.03965 \cdot 10^{-21}$	$14.10 \cdot 10^{-21}$	$9.811573 \cdot 10^{-21}$
Multiple of M, cU	2544.0	5264.0	4240.0	8500	5909.51
Actual M	636.0	658.0	1060.0	2125	738.69
Observed % Sb	71.5	72.8	70.8	65.5	65.3
Observed % $SO_4^=$	14.5	14.1	18.5	23.7	25.8
Observed $Sb/SO_4^=$	3.99:1	3.96:1	3.02:1	2.16:1	1.999:1
Derived chem. formula	$Sb_2O_3 \cdot [(SbO)_2SO_4]$ or $2Sb_2O_3 \cdot SO_3$	$Sb_2O_3 \cdot [(SbO)_2SO_4]$ or $2Sb_2O_3 \cdot SO_3$	$Sb_2O_3 \cdot [(SbO)_2SO_4]_2$ or $3Sb_2O_3 \cdot 2SO_3$	$[(SbO)_2 \cdot SO_4]_6$ or $(Sb_2O_3 \cdot SO_3)_6$	$[(SbO)_2SO_4]_2$ or $(Sb_2O_3 \cdot SO_3)_2$
Theoretical M	663.11	663.11	1034.70	2229.54	743.18
Theoretical % Sb	73.5	73.5	70.6	65.5	65.5
Theoretical % $SO_4^=$	14.5	14.5	18.6	25.85	25.85
Theoretical $Sb/SO_4^=$	4:1	4:1	3:1	2:1	2:1
BET, m^2/g	0.3	0.1	1.1	1.3	<0.1

Table II. Stability ranges for basic antimony sulfates in H_2SO_4 at room temperature and the temperature of the boiling solution

	Structure type formed	Proposed chemical formula	H_2SO_4 molarity range, M: At room temperature	H_2SO_4 molarity range, M: At boiling temperature
I	—	Sb_2O_3, cub	0-0.4	0-0.25
II	A and/or B	$Sb_2O_3 \cdot [(SbO)_2SO_4]$ or $2Sb_2O_3 \cdot SO_3$	0.5-2.5	0.25-2.0
III	A	$Sb_2O_3 \cdot [(SbO)_2SO_4]$ or $2Sb_2O_3 \cdot SO_3$	2.6-4.2	
IV	C	$Sb_2O_3 \cdot [(SbO)_2SO_4]_2$ or $3Sb_2O_3 \cdot 2SO_3$	4.3-6.9	2.0-6.5
V	D	$[(SbO)_2SO_4]_n$ or $(Sb_2O_3 \cdot SO_3)_n$	7.0-10.2	6.5-9.6*
VI	E	$[(SbO)_2SO_4]_2$ or $(Sb_2O_3 \cdot SO_3)_2$	10.9-12.7	10.2-12.7
—	K	$Sb_2(SO_4)_3$	—	≥17.9

* A mixture of D and E is formed at $9.6 < M < 10.2$.

ical, and physical properties. The stability ranges for the basic antimony sulfates at room temperature and at the boiling point of the acid are reported in Table II.

At boiling temperatures, the basic antimony sulfates form larger crystals and purer reaction products than at room temperature. In the acid range II (Table II) seeds of the structure-type A preferentially formed at room temperature, those of the type B in the boiling acid. Thus the activation energy for the formation of nuclei of the A-type basic sulfate is smaller than for the B-type sulfate at room temperature and *vice versa* at the boiling point of the solutions. A mixture of both salts is formed at intermediate temperatures. Once nuclei of one kind are formed, however, the crystals grow in the crystal habit of the seed, independent of temperature changes that occur during the reaction. Hence the free enthalpy of formation of both salts must be very similar.

The molarity range $12.7 < M < 15.3$ was not investigated. The normal antimony sulfate $Sb_2(SO_4)_3$ was obtained on heating Sb_2O_3 in an acid 18.7M, *i.e.*, concentrated H_2SO_4. No experiments were carried out to hydrolyze this salt in successive steps.

In conclusion, within the sulfuric acid molarity range $O < M < 12.7$ none of the five sulfates isolated contains any water of crystallization. This result was confirmed also by thermal decomposition analysis of these salts at 550°C in a He-stream. The reaction products were Sb_2O_4, Sb_2O_3, and SO_2 in each instance; no water was found. Earlier experimental findings suggesting large amounts of crystallization water in these sulfates are thus disproved; the water must have been just adsorbed in the form of a sulfuric acid film on the surface of the crystals not properly removed during separation. This is supported by the proposed chemical formulas of the basic antimony sulfates reported by other authors which show that the Sb/SO_3 ratios of compounds obtained in acid concentrations equal to ours are consistently smaller than corresponds to the formulas proposed in this work. This can be explained again in terms of adsorbed layers of dilute H_2SO_4 at the crystal surfaces of the reaction product.

Acknowledgment

The authors wish to thank Dr. R. A. Schaefer for his continuous support and for permission to publish this paper, Mr. R. T. Angstadt for his contribution in the analytical chemical work, Dr. T. H. Doyne of Villanova University for the single crystal studies, and Dr. P. Rüetschi for his valuable advice during the course of this study.

Manuscript received Aug. 18, 1967.

Any discussion of this paper will appear in a Discussion Section to be published in the December 1968 JOURNAL.

REFERENCES

1. R. H. Adie, *J. Chem. Soc.*, **57**, 540 (1890).
2. I. V. Tananaev and I. B. Mizetskaya, *Suz. ANSSSR*, **4**, 391.
3. R. L. Veller and S. I. Sobol, *Sbornik Nauch. Trudov, Gosudarat Nauch-Issledovatel Inst. Isvetnylsh Metal*, **13**, 123 (1957).
4. P. Rüetschi, U.S. Pat. 3,265,534.
5. M. J. Buerger and S. B. Hendricks, *Z. Krist.*, **98**, 1 (1937).
6. Standard X-Ray Powder Data N.B.S. Cir. 539, Vol. III, 31 and ibid. Vol. X1, 6.
7. J. W. Mellor, "A Comprehensive Treatise on Inorganic and Theoretical Chemistry," Vol. IX, p 425, Longmans Green and Company, New York (1929).
8. F. P. Treadwell, "Analytische Chemie," Bd. 1,247, F. Deuticke, John Wiley & Sons, Inc., New York (1946).

The Oxidation of Iron Single Crystals at 350°C

N. Ramasubramanian,[1] P. B. Sewell, and M. Cohen*

Division of Applied Chemistry, National Research Council, Ottawa, Ontario, Canada

ABSTRACT

A comparison of the oxidation of (001) and (112) surface single crystals of iron at 350°C and 20 Torr oxygen has been made. The (001) oxidizes more rapidly than the (112). Cubic Fe_2O_3 persists for a longer time on the (001) than on the (112). The orientation of the underlying magnetite remains constant on both crystals for up to 100 min. With both orientations the α-Fe_2O_3 starts out as a highly oriented oxide, but on the (112) it becomes randomly oriented at the surface after 50 min. The oxide on the (001) is more firmly adherent than on the (112). In both cases there appears to be an intermediate layer of "γ-Fe_2O_3" between the Fe_3O_4 and α-Fe_2O_3. The cross sections of the oxides, as revealed by replica electron microscopy, are different but typical for the two orientations.

A study of the kinetics of oxidation of the various orientations of an iron single crystal in the range of 250°-550°C and 10-760 mm oxygen has been reported by Wagner, Lawless, and Gwathmey (1). The thickening of the oxide was followed by observing the interference colors, a procedure similar to that of Mehl and McCandless in their lower temperature work (2). In the temperature region studied the oxide formed is usually at least two phases, and the interference color method has certain limitations (3, 4).

[1] Former Post-Doctorate Fellow. Present address: Atomic Energy of Canada Ltd., Chalk River, Ontario, Canada.
* Electrochemical Society Active Member.

In this paper the results of some experiments on the oxidations of two single crystals of iron of widely different orientation at 350°C are reported. Weight gains were sufficiently high to measure by microbalance weighing. At this temperature both a cubic oxide and α-Fe_2O_3 are formed, and the amounts of these oxides were measured by a combination of weighing and cathodic reduction. The crystal structure and orientation of the oxides were determined by reflection electron diffraction.

Experimental

The oxidation apparatus and procedure have been described fully previously (5). All experiments were done at 350°C and a pressure of 20 Torr of oxygen. The specimens were first electropolished (6) and then brought to temperature in a vacuum of 10^{-5} to 10^{-6} Torr. Blank experiments showed that there was no visible change in the appearance of the specimens nor a measurable weight gain during this period. Oxygen was then admitted rapidly. The experiment was stopped by removing the furnace and cooling the quartz tube with water. Specimens were weighed before and after oxidation on a Mettler microbalance.

The specimens were strain-annealed Ferrovac E[2] single crystals. Two orientations, (001) and (112) were used. Surface areas were approximately 10 cm^2.

The amount of reducible oxide was measured using the electrolytic reduction method of Oswin and Cohen (7). The solution was 0.15*N* boric acid adjusted to a *p*H of 7.58 with sodium borate. A current density of approximately 10-11 $\mu a\ cm^{-2}$ was used and potentials are reported *vs.* the saturated calomel electrode. The amount of reducible oxide was determined both by weight loss and by a measurement of Fe^{++} in solution.

Reflection electron diffraction was done in a G. E. diffraction apparatus using a camera length of 50 cm and an accelerating voltage of 50 kv. Replicas for electron microscopy were made using the two-stage formvar, platinum-carbon technique.

Results

The weight gain-time curves are shown in Fig. 1. The total weight gain was determined from the difference in weight before and after oxidation. The reducible oxide was determined both by weight loss due to cathodic reduction and by colorimetric analysis of ferrous iron in solution assuming a cathodic reduction reaction of

$$Fe_2O_3 + 3H_2O + 2e \rightarrow 3Fe^{++} + 6\ OH^-$$

These two numbers were then averaged. The magnetite was determined by difference.

It can be seen that both the over-all weight gain and the final rate of oxidation are higher with (001) than the (112) surfaces. In both cases there is a rapid formation of Fe_2O_3 which then remains fairly constant in amount, while the Fe_3O_4 increases until both oxides are approximately equal in amount at 100 min. In both cases there is a very rapid weight gain in the first 4 min. After this time the curves are approximately parabolic.

Cathodic reduction curves for the two crystals oxidized for various lengths of time are shown in Fig. 2 and 3. In both cases a definite γ-Fe_2O_3 wave (—300 to —400 mv) is observed with specimens oxidized for less than 100 min. The main Fe_2O_3 wave is that for α-Fe_2O_3 at about —600 mv. The final potential drop in all the curves is toward the Fe_3O_4 potential. This drop is best defined for specimens which have been oxidized for the longer times. The amounts of reducible oxide as determined by both gravimetric and colorimetric analysis and the current efficiency of cathodic reduction are given in Table I.

The specimens were examined by both electron diffraction and electron microscopy after oxidation and

[2] Ferrovac E: C—0.007%, Mn—0.0002, Si—0.0015, Cr—0.0002, Ni—0.0009, Al—0.0005, P—0.003.

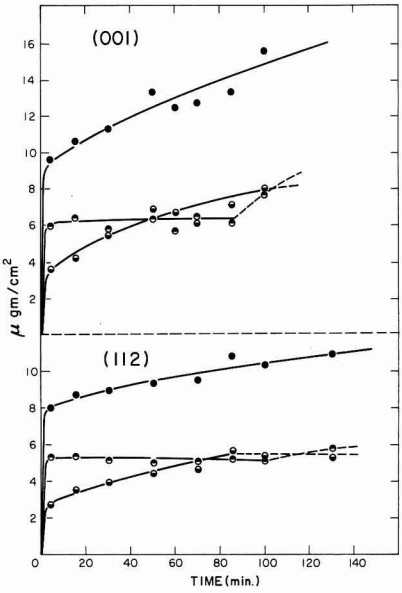

Fig. 1. Weight-gain time curves for the (001) and (112) crystals. ● Total, ◒ Fe_3O_4, ◓ Fe_2O_3.

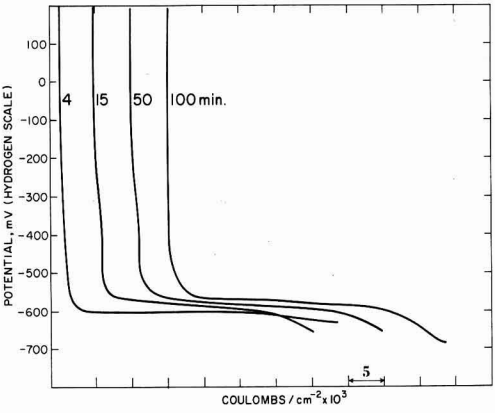

Fig. 2. Cathodic reduction curves of Fe_2O_3 on (001) after various oxidation times.

after cathodic reduction to the magnetite, Fig. 4. Once again there was a marked difference in behavior between the two orientations. In the case of the (001) surface there was some evidence for a cubic oxide in the outer layer even after oxidation for 100 min. At 4 min the pattern was predominantly cubic. On the other hand with the (112) crystal the cubic pattern was extremely weak or had disappeared after about 15 min oxidation. Even at 4 min the diffraction pattern was predominantly that of α-Fe_2O_3. In both cases the patterns from the magnetite layers were characteristic of a highly oriented microcrystalline material and were essentially unchanged from 4 to 100 min. The pattern from the outer α-Fe_2O_3 layer showed evidence of random orientation at longer times of oxidation, particularly with (112) crystals. The relative orientations are the same as those reported previously (8).

The topographical features of the oxides on the two orientations were also markedly different, as shown in Fig. 5 and 6. On the (001) surface the outer layer was essentially smooth at 4 min and there was some

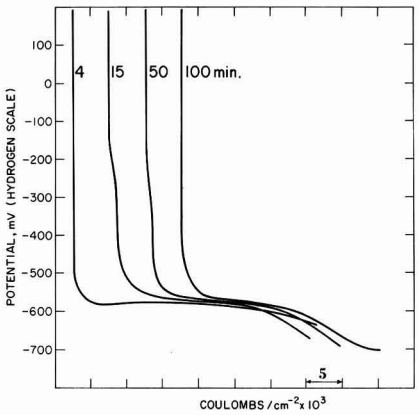

Fig. 3. Cathodic reduction curves of Fe_2O_3 on (112) after various oxidation times.

roughening at 100 min. The underlying magnetite had a cross-hatch structure, similar to that observed by Laukonis (9) for thick oxide films, from the beginning. On the (112) surface both the outer and inner layers have parallel ridges which seem to become more accentuated with increased time of oxidation. These are similar to the ridges observed by Boggs (10) on some grains of polycrystalline iron oxidized under similar conditions to these. In both cases the thickness of the outer Fe_2O_3 layer varied markedly over the surface. This is shown schematically in Fig. 7.

It was noted that the adherence of the underlying magnetite to the metal on the (112) surface was very poor after cathodic reduction of the Fe_2O_3. This led to some stripping of the oxide with the formvar replica. This is shown in Fig. 6 where the darker areas are Fe_3O_4. It can be seen that the oxide has the same structural characteristics as are shown by the replica.

A number of annealing experiments were made in which samples were heated at 350°C in a vacuum of 10^{-5} Torr after oxidation was completed. There was a marked decrease in the amount of reducible oxide and very little change in the shape of the phase boundaries. Due to the scatter in the measurements no useful kinetic data could be obtained.

Discussion

The marked effect of crystal orientation on both the over-all reaction rate and the oxide structure which was observed at 200° and 260°C (11) is even more pronounced at 350°C. In this work it is also seen that this difference is accompanied by distinct variations in the shape of the oxide-gas interface and the Fe_3O_4-Fe_2O_3 interface. The oxide on the (112) appears to be less adherent at the metal oxide interfaces than the oxide on the (001), particularly after cathodic reduction to the magnetite. Despite these differences the general kinetics is that of very rapid oxidation in the first few minutes followed by essentially parabolic kinetics for the rest of the time. The lack of adhesion on the (112) surface may indicate the formation of voids at the oxide metal interface which, in turn, would decrease the rate of transfer of metal to the oxide and, hence, decrease the oxidation rate. This factor, combined with

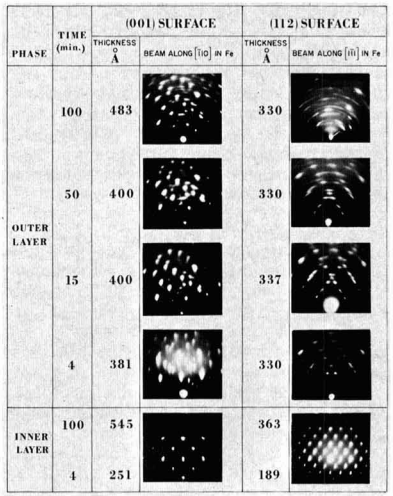

Fig. 4. Electron diffraction patterns for both surface layer and underlying magnetite on (001) and (112) after various oxidation times.

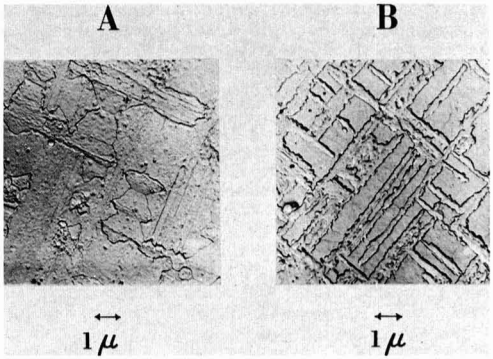

Fig. 5. Replicas of outer surface (A) and magnetite surface (B) on (001) crystal after 100 min oxidation.

Table I. Oxidation of iron single crystals, (001) and (112) surfaces, at 350°C in 20 mm oxygen

	Weight data in terms of oxygen, $\mu g/cm^2$							
	(001) Surface				(112) Surface			
		Reducible oxide		Magnetite		Reducible oxide		Magnetite
Time in min	Total, wt	Gravimetric Wr_1	Colorimetric Wr_2	Wt − $\frac{Wr_1 + Wr_2}{2}$	Total wt	Gravimetric Wr_1	Colorimetric Wr_2	Wt − $\frac{Wr_1 + Wr_2}{2}$
4	9.59	6.43	5.52	3.62	8.00	—	5.30	2.7
15	10.60	6.57	6.29	4.17	8.73	5.40	5.16	3.45
30	11.32	5.90	5.70	5.52	8.90	5.30	4.80	3.85
50	13.30	6.60	6.04	6.98	9.31	5.08	4.80	4.37
60	12.36	5.80	5.50	6.71	—	—	—	—
70	12.67	6.55	6.60	6.10	9.53	5.06	4.86	4.57
85	13.30	6.30	6.04	7.13	10.80	5.40	5.00	5.60
100	15.61	7.93	7.44	7.92	10.30	—	5.10	5.20
130	—	—	—	—	10.92	5.50	5.90	5.22

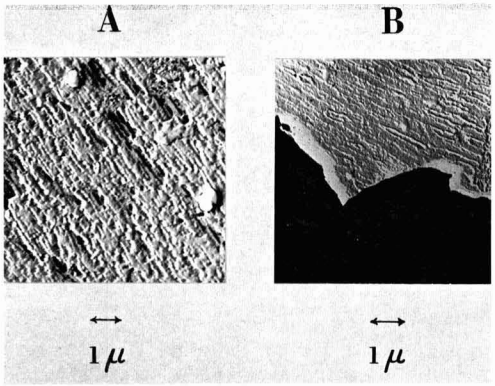

Fig. 6. Replica of outer surface (A) and magnetite surface (B) on (112) crystal after 100 min oxidation. Note dark area is transmission through stripped Fe_3O_4.

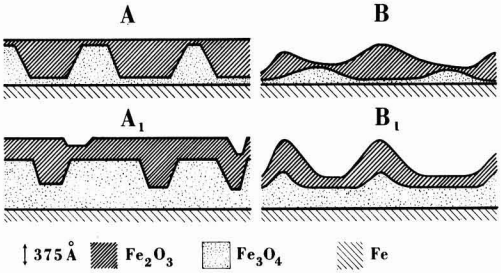

Fig. 7. Schematic of cross section through the oxides as deduced from electron micrographs, weight gains, and cathodic reduction. The Fe_2O_3 layer is "cathodically reducible oxide" and would include the γ-Fe_2O_3. A, A_1, $(001)_4$ and 100 min; B, B_1, (112).

the uneven nature of the Fe_3O_4-Fe_2O_3 boundaries renders a quantitative discussion of the diffusion rates fairly fruitless.

The cathodic reduction curves all show evidence of the presence of γ-Fe_2O_3 as part of the "reducible oxide." This is probably not on the surface but is present at the Fe_3O_4-Fe_2O_3 interface as an intermediate phase. The cathodic reduction observation is confirmed by the reflection electron diffraction. Strong spots characteristic of a cubic pattern are observed on the (001) crystal at the end of 4 min and are still discernible after 100 min of oxidation. In contrast to this no diffraction spots belonging to the cubic oxide are observed on the (112) crystal after 15 min of oxidation. This may be due to the outer layer of α-Fe_2O_3 on the (112) becoming too thick to allow penetration of the beam to the underlying γ-Fe_2O_3 or to different shapes of the oxide surface on the two crystals. This difference in shape is observed by replica electron microscopy. The outer layer of oxide on the (001) is smooth, while that on the (112) has a ridgelike structure. The difference in shape of the outer layer results in a difference in penetration of the electron beam to the intermediate cubic oxide. (In the above discussion it should not be assumed that the γ-Fe_2O_3 is a stoichiometric phase but rather something equivalent to $Fe_{3-x}O_4$ which within some composition range has the electrochemical properties of γ-Fe_2O_3.)

The sharp turnover of the weight-gain time curves at around 5 min is probably related to the formation of a continuous outer layer of α-Fe_2O_3 of sufficient thickness to lead to a change from an oxidation rate which is controlled by cation diffusion in the cubic oxide to control by anion diffusion in the hexagonal α-Fe_2O_3. As was noted in the results section both the initial and final rates of oxidation are higher on the (001) than on the (112) crystal. This may be related to two factors. First, γ-Fe_2O_3 is a larger proportion of the reducible oxide on the (001) than on the (112). The α-Fe_2O_3 is therefore thinner and the final oxidation rate would be higher. The initially higher oxidation rate is related to the more difficult transformation of cubic oxide to hexagonal oxide on the (001) surface. This was also observed at lower temperatures. The second factor leading to a lowering of rate on the (112) surface is the separation which occurs at the metal-oxide interface. Cation diffusion from the metal surface outward is accompanied by vacancy diffusion toward the metal surface. If the vacancies condense to form voids at the metal surface, separation occurs between the metal and oxide. This has been observed by metallographic techniques for oxidation at higher temperatures (12). It would appear that vacancies can be destroyed at the metal-oxide interface more easily on the (001) crystal than on the (112) crystal. This may be related to the fit of the highly oriented oxide on the metal. The condensation of vacancies to form voids would decrease the oxidation rate by decreasing the effective area of the specimen for cation diffusion. The resultant lowering of the cation flow with the (112) crystal may also result in earlier formation of α-Fe_2O_3 as well as recrystallization of the outer α-Fe_2O_3 to form polycrystalline oxide. If the final rate of oxidation is controlled by the diffusion of oxygen through the outer α-Fe_2O_3, then the decreased cation flow on the (112) crystal would lead to a smaller oxygen gradient in the oxide and a reduced final rate of oxidation.

The shapes of the Fe_3O_4-Fe_2O_3 interface appear to be characteristic for the different orientations of underlying iron. Both Laukonis (9) and Boggs (10) have observed similar structures under slightly different conditions of oxidation. The cross-hatch structure of the magnetite surface on the (001) crystal may be related to the method of nucleation or growth of the outer α-Fe_2O_3. Both oxides remain highly oriented even after 100 min of oxidation. The ridgelike structure of both the Fe_3O_4-Fe_2O_3 interface and the Fe_2O_3 surface may be related to the mechanism whereby stress is relieved in the growing oxide film.

With both orientations the combination of the shape of the phase boundaries and the different diffusion mechanisms in the two main oxides make it rather difficult or impossible to calculate diffusion coefficients with the data at hand. The attempt to measure cation diffusion in the magnetite layer by the annealing experiments was unsuccessful due to lack of reproducibility in the measurements.

Acknowledgment

The authors wish to thank Mr. E. G. Brewer for the electron microscopy.

Manuscript received May 11, 1967; revised manuscript received Sept. 7, 1967. This paper was presented at the Washington Meeting, Oct. 11-15, 1964 as Abstract No. 56.

Any discussion of this paper will appear in a Discussion Section to be published in the December 1968 JOURNAL.

REFERENCES

1. J. B. Wagner Jr., K. R. Lawless, and A. T. Gwathmey, *Trans. AIME*, **221**, 257 (1961).
2. R. F. Mehl and E. L. McCandless, *ibid.*, **25**, 531 (1937).
3. D. E. Davies, U. R. Evans, and J. N. Agar, *Proc. Roy. Soc.*, **A225**, 443 (1954).
4. E. J. Caule, *Corrosion Sci.*, **2**, 147 (1962).
5. E. J. Caule, K. H. Buob, and M. Cohen, *This Journal*, **108**, 829 (1961).
6. P. B. Sewell, C. D. Stockbridge, and M. Cohen, *Can. J. Chem.*, **37**, 1813 (1959).

7. H. G. Oswin and M. Cohen, *This Journal*, **104**, 9 (1957).
8. P. B. Sewell and M. Cohen, *ibid.*, **111**, 508 (1964).
9. J. V. Laukonis and R. J. Coleman, *J. Appl. Phys.*, **30**, 1364 (1959).
10. W. E. Boggs, R. H. Kachik, and G. E. Pellisier, *This Journal*, **112**, 539 (1965).
11. P. B. Sewell and M. Cohen, *ibid.*, **111**, 501 (1964).
12. D. Caplan and M. Cohen, *Corrosion Sci.*, **6**, 321 (1966).

The Nucleation, Growth, and Structure of Thin Ni-P Films

J. P. Marton and M. Schlesinger

Department of Physics, University of Western Ontario, London, Ontario, Canada

ABSTRACT

The nucleation, early growth, and structure of Ni-P on $SnCl_2$-$PdCl_2$ activated dielectric substrates were studied. The $SnCl_2$-$PdCl_2$ treatment was found to provide small catalytic sites on the substrate, serving as the nuclei for Ni-P growth. The average diameter of catalytic sites was estimated to be less than 10Å. The microscopic time rate of Ni-P growth on the nuclei was found to be constant and the growth to be isotropic. The resulting Ni-P deposit in the early stages of growth consists of circular islands. The surface density σ of islands were affected by activation. In later stages of growth, the circular Ni-P islands merged to form a continuous film. The critical film thickness at which continuity is attained is shown to be a function of σ. The structure of as-deposited islands, as well as that of fresh continuous film, was determined by electron diffraction to be liquidlike.

Electroless deposition of nickel on catalytic surfaces due to Brenner and Riddell (1) is well documented (1-4). The chemistry of deposition (4) and some physical properties of electroless nickel (4-6) have been reported. Deposition on dielectric (noncatalytic) surfaces has also been demonstrated (1, 2, 7). A dielectric substrate may be activated (8) by immersion in solutions of $SnCl_2$ and $PdCl_2$ for electroless nickel deposition.

Deposits from a number of electroless solutions have been determined (4) to consist of Ni and P, with $2\% \leq P \leq 12\%$ by weight. Fresh bulk deposits were stated to have either amorphous liquidlike (5) or fine polycrystalline (6) structures. Fresh film deposits were found (9) to be in a liquidlike state. The growth and film geometry of fresh Ni-P deposits have not been reported. Other electroless films (Co-P and Ni-Fe-P) deposited on activated substrates exhibit island-type growth and agglomerated structure. Judge *et al.* (10) found a "hemispherical clumpy growth" of electroless cobalt, and the surface of electroless nickel-iron films was reported by Schmeckenbecher (11) to consist of an "agglomeration of balls." Frieze and Weil (12) reported that nucleation of electroless Co-P films occurred on isolated Pd particles, followed by lateral growth to produce a continuous film.

In our work the nucleation, growth, and structure of electroless Ni-P films on activated substrates were studied. The geometry of films at various stages of growth was determined by transmission electron microscopy and the structure by transmission electron diffraction. Activation of substrates by $SnCl_2$-$PdCl_2$ method results in an island-type growth of Ni-P in the early stage, becoming continuous as the growth proceeds. The surface density of islands and the maximum size of islands varied with the method of activation and the wetting property of substrate surfaces. The structure of individual islands, ranging in size from 200 to 2000Å as well as that of continuous thin films (9), was found to be liquidlike.

Experimental

Clean substrates of glass, quartz, mica, and Formvar were activated by immersion in activating solutions at room temperature. The variations in activation of the substrates are shown in Table I. Activated substrates were immersed in electroless nickel solution for Ni-P deposition. The composition of solutions is listed in Table II. Film geometry was not affected by variations in the composition, pH, and temperature of electroless solutions; therefore only one solution of pH = 5.3 was used. Deposition temperature was adjusted to 25° ± 0.5°C, and the time of deposition was varied.

Ni-P was also deposited from the solution on electropolished solid nickel substrates and on microscope slides coated with pure nickel and palladium by vacuum evaporation. These deposits were compared with those grown on $SnCl_2$-$PdCl_2$ activated substrates.

The mass thickness and average thickness of films was determined by weighing and by the Tolansky method (13), respectively. Deposits were prepared for electron microscopy three ways. Self-supporting Ni-P films were floated off the substrates for direct transmission and diffraction measurements; discontinuous deposits were backed by Formvar and then floated off the substrates; shadowed replicas of the surface of deposits were made. Deposits grown on

Table I. Variations in activation of substrates

Method (a)	Dip clean substrates in activating solutions listed in Table II in succession.
Method (b)	Dip clean substrates as in (a) in activating solutions modified by the addition of 10 cc/l isopropyl alcohol.
Method (c)	Dip clean substrates as in (a) in activating solutions modified by the addition of 5 cc/l Kodak "Photo-Flo."

Table II. Composition of solutions used in the experiments

Activating solutions			Electroless solution	
$SnCl_2$ solution	$SnCl_2$	0.1 g/l	Nickel sulphate	29 g/l
	HCl	0.1 cc/l	Sodium hypophosphite	17 g/l
Rinse:	H_2O at pH = 7		Sodium succinate	15 g/l
			Succinic acid	1.3 g/l
$PdCl_2$ solution	$PdCl_2$	0.1 g/l	Solution pH	5.3
	HCl	0.1 cc/l	Solution temperature	25°C
Rinse:	H_2O at pH = 7			

Formvar substrates were left on the substrates and were examined directly.

For transmission and diffraction measurements, a Philips EM75C and an AEI EM6G microscope was used respectively. Both microscopes were operated at 75 kv.

Results and Discussion

Nucleation and growth.—The deposition of Ni-P on all substrates activated by method (a) in Table I, was found to be selective. Deposition appeared to start at certain points on the substrate and continue at those points only. As deposition progressed, islands formed on these nucleation points. If deposition was allowed to proceed, the islands grew in size and eventually merged to form a continuous film. Figure 1 is the transmission image of a typical deposit. Parts of the deposit are islands, other parts are already continuous. In contrast with the island-type growth, deposits that were formed on nickel substrates and on nickel and palladium coated microscope slides were homogeneous and showed no island structure. The image of a shadowed surface replica of such a deposit is reproduced in Fig. 2.

These findings show that the surface of a $SnCl_2$-$PdCl_2$ treated dielectric substrate is not completely activated. The activation is visualized to produce small catalytic sites dispersed on the surface, serving as the nuclei for Ni-P deposition. The sites are estimated to be less than 30Å in diameter, as they cannot be detected in the electron microscope having a point resolution of 30Å. A closer estimate of size of the catalytic sites was made indirectly. The diameter 2r of the growing Ni-P islands was measured and was plotted against deposition time. This is shown in Fig. 3. The diameter of catalytic sites was estimated by extrapolation (dotted line), to be less than 10Å.

Again from Fig. 3, the microscopic time rate of Ni-P growth c $(= dr/dt)$ is seen to be constant. Also, the geometry of growing islands was observed to be circular in all deposits. These findings imply isotropic growth, and one expects the islands to be half spheres situated base down on the substrate. The circular geometry is shown in Fig. 4 for islands ranging in size from 200 to 2000Å.

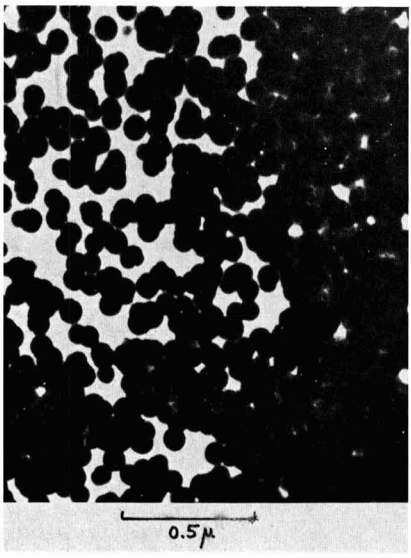

Fig. 1. Electron transmission image of a typical Ni-P deposit on $SnCl_2$-$PdCl_2$ activated substrate. Parts of the deposit are islands, other parts are continuous.

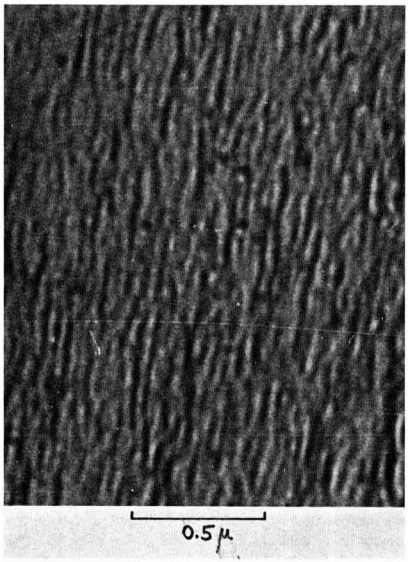

Fig. 2. Shadowed surface replica of a Ni-P deposit on a solid nickel substrate. Note the absence of islands.

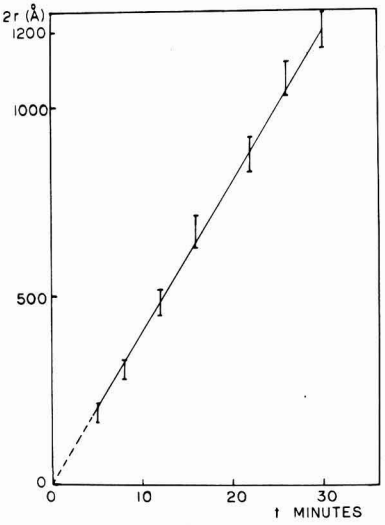

Fig. 3. Plot of diameter $2r$ of the growing Ni-P islands against time of deposition. Rate of growth $c = dr/dt$ is constant. Extrapolation (dashed line) at $t = 0$ gives average size of active sites to be less than 10Å.

The number of activation sites per unit surface area σ was found different for different substrates. The value of σ ranged from $10/\mu^2$ to $10^4/\mu^2$. The value of σ was large on substrates with hydrophilic surfaces (*i.e.*, glass), and small on those with hydrophobic surfaces (*i.e.*, Formvar). This is shown in Fig. 5. Figure 5a is the transmission image of sites on glass, and Fig. 5b is the image of sites on Formvar. The respective average values of σ are $10^4/\mu^2$ and $10^2/\mu^2$. It was found possible to decrease the difference in σ between hydrophilic and hydrophobic surfaces by activation method (b) in Table I and to eliminate it by method (c) in Table I. In both cases the small σ increased and the large σ remained constant. Attempts to increase the value of σ beyond $10^4/\mu^2$ have failed.

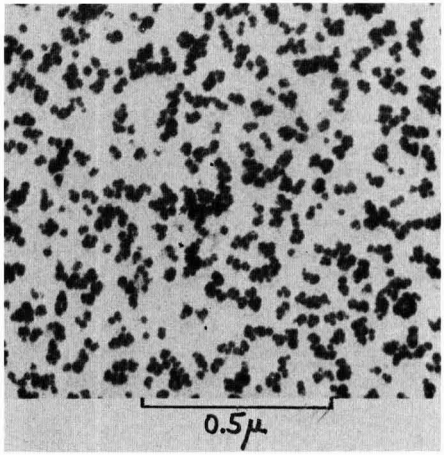

Fig. 4. Circular transmission images of islands ranging in size from 200 to 2000Å in four different deposits (a, b, c, d). The islands are visualized to be half spheres situated "base down" on the substrate in all deposits. Fig. 4a. Island size 200Å.

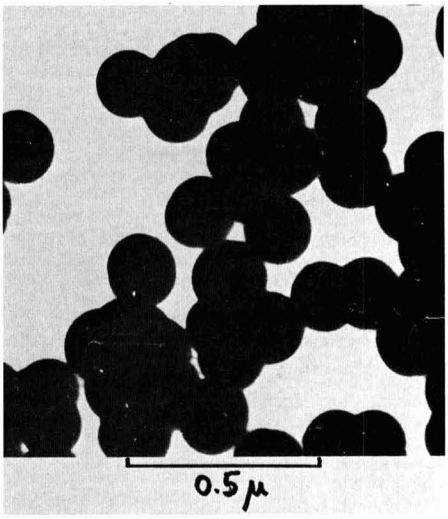

Fig. 4d. Island size 2000Å

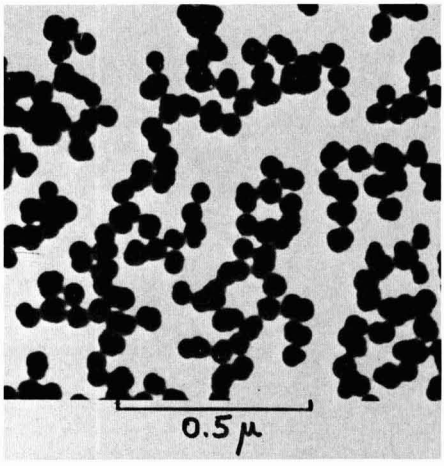

Fig. 4b. Island size 600Å

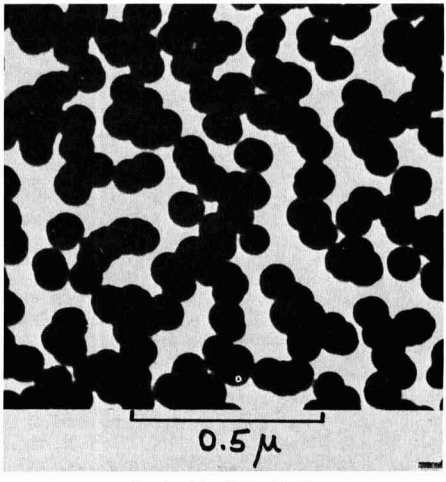

Fig. 4c. Island size 1000Å

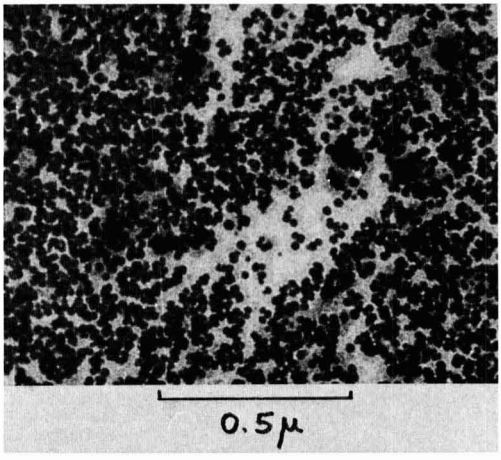

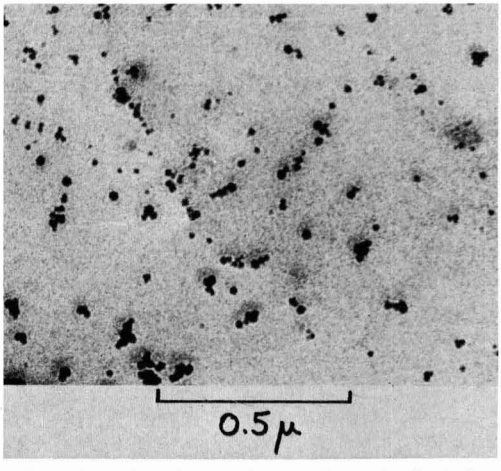

Fig. 5. Transmission images of active sites on (a) (top) glass, and (b) (bottom) Formvar substrates made visible by a slight deposit of Ni-P on them. The surface density of sites is $10^4/\mu^2$ for glass and $10^2/\mu^2$ for Formvar.

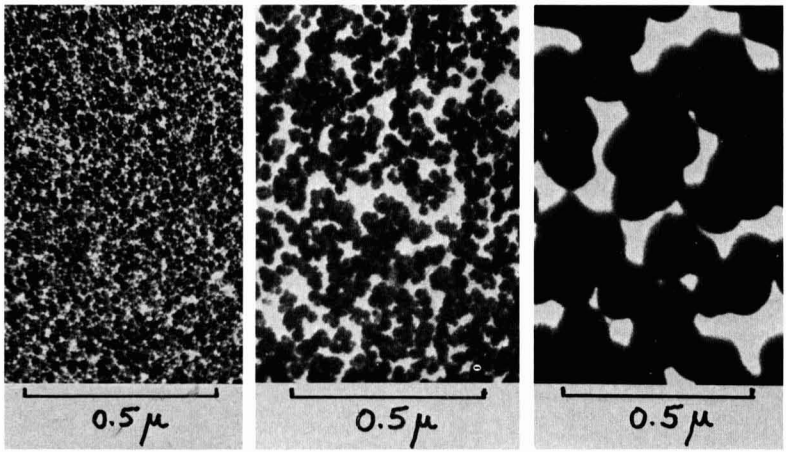

Fig. 6. Transmission images of deposits on substrates with different activation densities: (a) (left) $10^4/\mu^2$; (b) (center) $10^3/\mu^2$ and (c) (right) $10^2/\mu^2$. Note the dependence of film geometry on activation density.

Film geometry.—The natural consequence of the variation of σ is a variation in Ni-P film geometry. This is shown in Fig. 6 by the transmission image of three different deposits. The films were deposited on substrates with average σ values of $10^4/\mu^2$ (Fig. 6a); $10^3/\mu^2$ (Fig. 6b) and $10^2/\mu^2$ (Fig. 6c). From the figure it is evident that σ is an important deposition parameter. The quantitative dependence of film growth and geometry on σ may be expressed[1] as

$$d = 2\pi\sigma ct\left(r_o^2 + r_o ct + \frac{1}{3}c^2t^2\right); \qquad 0 \leq t \leq (c\sqrt{\sigma\pi})^{-1} \quad [1]$$

and

$$d = 2r_o(1 + r_o\sqrt{\sigma\pi}) - \frac{1}{3\sqrt{\sigma\pi}} + ct; \qquad t \geqq (c\sqrt{\sigma\pi})^{-1} \quad [2]$$

where d is the mass thickness of deposit (volume per unit surface area); c is the microscopic rate of deposition (increase of local thickness per unit time and/or dr/dt); σ is the activation surface density (number of active sites per unit surface area); $2r_o$ is the diameter of active sites; and t is the time of deposition. Expression [1] describes the growth of discontinuous (island-type) films and the description of growth after continuity is attained is given by expression [2]. Transition from the former to the latter configuration occurs at $t = (c\sqrt{\sigma\pi})^{-1}$.

Figure 7a is the plot of expressions [1] and [2] at $r_o = 5$Å.[2] The dashed line represents the transition between discontinuous films (below dashed line) and continuous films (above dashed line) and the solid straight line represents a linear ($d = ct$) film growth. In Fig. 7b a comparison is made between the mass thickness of growing deposits and the theoretical curves. Both solid Ni and $SnCl_2$-$PdCl_2$ activated substrates were used. With c = 20 Å/min σ was found to range between $10^4/\mu^2$ and $10/\mu^2$ for the activated substrates.

"As-deposited" structure.—The crystal structure of fresh Ni-P deposits has been investigated in the past with somewhat conflicting results. Goldenstein *et al.* (5) determined amorphous liquidlike structure for bulk deposits by x-ray diffraction, and Graham and co-workers (6) found fresh bulk deposits to be polycrystalline by electron diffraction. The present authors (9) showed that continuous, as-deposited thin films of Ni-P are in a liquidlike state. In that work

[1] See Appendix.
[2] The variation of r_o does not influence the curves appreciably, as r_o is much smaller than ct in the range of ct considered here.

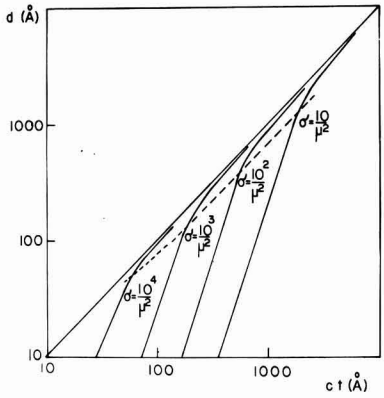

Fig. 7a. Mass thickness d of Ni-P deposits. Theoretical curves of d as a function of ct (c is rate of deposition, t is deposition time) for different activation densities σ. Dashed line represents transition between islands and continuous film.

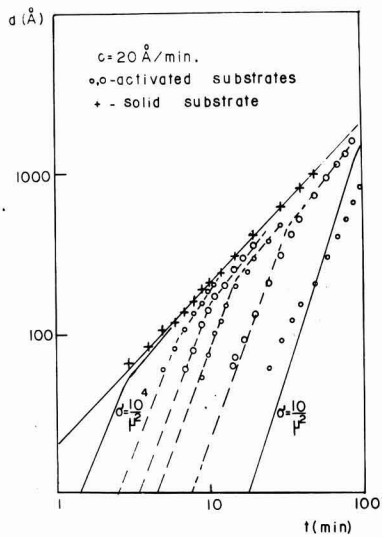

Fig. 7b. Mass thickness d of Ni-P deposits. Comparison of theoretical curves (a) and experimental values for c = 20 Å/min. Activation density is seen to range between $10^4/\mu^2$ and $10/\mu^2$.

(9) the temperature dependence of the structure of continuous films was investigated. In the present work the structural nature of as-deposited islands, ranging in size from 200 to 2000Å, as well as that of fresh continuous films of various geometry were studied.

It can be argued that, if the islands in films are single crystals, but are too small to cause proper diffraction, then the same islands grown larger would eventually reveal their crystal identity. If, however, the islands were in a liquidlike state, no size dependency should be detected in the diffraction pattern. From selected area diffraction experiments the latter case was confirmed. Islands whose size ($2r \approx 2000$Å) was comparable to the effective diameter of the electron beam (8000Å) showed an identical liquidlike structure to those with 200Å diameter. The diffraction pattern of continuous films was also the same. Figure 8 is an example of the diffraction pattern of all our (thin) Ni-P deposits.

The present findings of a liquidlike structure is in apparent contradiction with the results of Graham *et al.* (6); however the difference may be explained by the difference in sample preparation. In their experiments (bulk) deposits were prepared at 90°C for many hours, whereas our (thin) samples were grown at 25°C for only a few minutes.

Summary

It was shown that electroless deposition of Ni-P on $SnCl_2$-$PdCl_2$ activated dielectric substrates is selective and that it is homogeneous on continuous catalytic surfaces. The selective deposition is due to selective activation. The $SnCl_2$-$PdCl_2$ treatment produces catalytic sites on the substrate with less than 10Å diameter. The growth of Ni-P on these sites is isotropic, resulting in a spherical island-type film geometry. The surface density of catalytic sites σ was seen to depend on the substrate material and type of activation, with a maximum value of $10^4/\mu^2$. The importance of σ as a deposition parameter was pointed out, and its influence on film growth and geometry was shown quantitatively. Evidence of island growth of different electroless metals (10-12) suggests that the present description of nucleation, growth, and geometry may also be applicable to other electroless films deposited on activated surfaces. The structure of as-deposited Ni-P islands with variable size, as well as that of fresh continuous films, was determined to be liquidlike, and it was concluded that individual islands are not single crystals. Finally, it was suggested that different results on the structure of fresh deposits reported by other workers may have been due to differences in sample preparation.

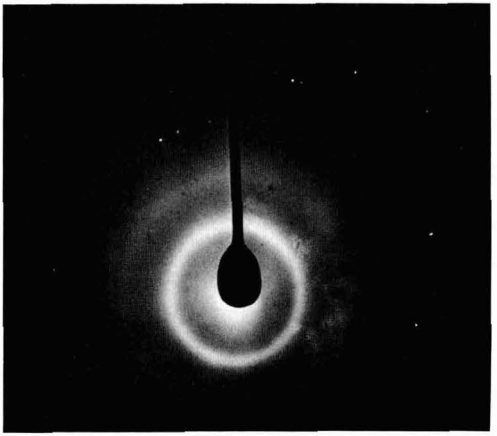

Fig. 8. Typical diffraction pattern of as-deposited Ni-P islands, and fresh thin Ni-P films (P content of 5 w/o).

Acknowledgments

The authors wish to acknowledge the valuable assistance of Dr. J. Brown in the diffraction experiments.

The present work is part of a Ph.D. Thesis to be submitted by J. P. Marton to the Graduate Faculty of the University of Western Ontario. Work was supported in part by a Defence Research Board of Canada Grant to Welwyn Canada Limited, London, Ontario, Canada.

Manuscript received July 26, 1967; revised manuscript received Oct. 12, 1967.

Any discussion of this paper will appear in a Discussion Section to be published in the December 1968 JOURNAL.

REFERENCES

1. A. Brenner and G. E. Riddell, *J. Research Natl. Bur. Standards*, **37**, 31 (1946); **39**, 385, (1947).
2. G. Gutzeit, W. J. Crehan, and A. Krieg, U.K. Pat. 761,556.
3. A. Brenner, *Metal Finishing*, **52**, 68 (1954).
4. A.S.T.M. Special Technical Publication No. 265 (1959).
5. A. W. Goldenstein, W. Rostoker, F. Schossberger, and G. Gutzeit, *This Journal*, **104**, 104 (1957).
6. A. H. Graham, R. W. Lindsay, and H. J. Read, *ibid.*, **112**, 401 (1965).
7. P. Baeyens (Philips Electrical Industries), U.K. Pat. 749,824.
8. E. A. Bergstrom, U.S. Pat. 2,702,253.
9. M. Schlesinger and J. P Marton *J. Phys. Chem. Solids*, To be published.
10. J. S. Judge, J. R. Morrison, D. E. Speliotis, and G. Bate, *This Journal*, **112**, 681 (1965).
11. A. F. Schmeckenbecher, *ibid.*, **113**, 778 (1966).
12. A. S. Frieze and R. Weil, Sixth International Conference for Electron Microscopy, Kyoto (1966) p. 533.
13. S. Tolansky, "Multiple Beam Interferometry of Surfaces and Films," Clarendon Press, Oxford (1948).

APPENDIX

Assume that the small catalytic sites are half spheres with radius r_o, situated "base-down" on the substrate. Let σ be the number of active half spheres per unit substrate area. Assume that the Ni-P deposition parameters (solution concentration and temperature) are constant in time, and that the density of Ni-P deposit ρ is constant. Let m be the mass of the deposit on each active island, and r be the radius of the growing half sphere. Then $m = 2/3\ \pi(r^3 - r_o^3)\rho$, and the time rate of change of m is

$$\frac{dm}{dt} = \frac{dm}{dr}\frac{dr}{dt} = 2\pi\rho r^2 \frac{dr}{dt}$$

Since $dr/dt = c$, (*c.f.* Fig. 3), and $r = r_o + ct$ we get

$$dm = 2\pi\rho c\ (r_o + ct)^2\, dt$$

After integration

$$m = 2\pi\rho ct\ [r_o^2 + r_o ct + (1/3)\ c^2t^2]$$

Assuming an average value of σ on the substrate, the total mass M on the substrate with surface area A is

$$M = A\sigma\ 2\pi\rho ct\ [r_o^2 + r_o ct + (1/3)\ c^2t^2]$$

With the definition of the mass thickness $d = M/A\rho$ we get

$$d(t) = 2\pi\sigma ct\ [r_o^2 + r_o ct + (1/3)\ c^2t^2] \qquad [1]$$

Further assume the islands to form a close packed surface distribution on the substrate. In this configuration each island may occupy a maximum surface area of σ^{-1}. As the islands grow in time the base of each island spreads in the available surface area of σ^{-1}. After a time t_o the islands touch and begin to form a continuous film whose surface retains the hemispherical features of the islands. At time, t_o, the area of the base of each hemisphere, $\pi r^2 \approx \sigma^{-1}$ for large values of σ. Since $r = r_o + ct$, $t_o \approx (c\sqrt{\sigma\pi})^{-1}$ for

small values of r_o. Relation [1] is therefore valid for times $0 \leq t \leq (c\sqrt{\sigma\pi})^{-1}$. For times longer than t_o the now-continuous film is visualized to grow at a constant macroscopic rate. This growth may be described by

$$d(t) = d(t_o) + c(t-t_o) = 2r_o(1 + r_o\sqrt{\sigma\pi}) - \frac{1}{3\sqrt{\sigma\pi}} + ct \quad [2]$$

$d(t_o)$ having been evaluated by setting $t = t_o = (c\sqrt{\sigma\pi})^{-1}$ in Eq. [1]. Combining [1] and [2] the final expression is

$$d(t) = \begin{cases} 2\pi\sigma ct\,[r_o^2 + r_o ct + (1/3)\,c^2t^2]; & 0 \leq t < (c\sqrt{\sigma\pi})^{-1} \\ 2r_o(1 + r_o\sqrt{\sigma\pi}) - \dfrac{1}{3\sqrt{\sigma\pi}} + ct; & t > (c\sqrt{\sigma\pi})^{-1} \end{cases}$$

The Holmium-Hydrogen System

F. C. Perkins and C. E. Lundin

Metallurgy Division, Denver Research Institute, University of Denver, Denver, Colorado

ABSTRACT

Pressure-temperature-composition data were obtained to study the nature of the holmium-hydrogen system. A Sieverts-type apparatus was employed to perform measurements in the temperature range, 250°-950°C, in the composition range, Ho to HoH_3, and at pressures from 10^{-4} to 630 Torr. The existence of three homogeneous phases was established: holmium solid solution, the dihydride, and the trihydride phases. The limits of hydrogen solid solution in each of the phases were determined from discontinuities in the isothermal plots. Equilibrium plateau decomposition relationships were determined from van't Hoff plots in the two-phase regions

$Ho_{ss} + HoH_2$,

$$\log_{10} p\ (\text{Torr}) = -\frac{11{,}520 \pm 50}{T} + 10.66 \pm 0.05$$

$HoH_2 + HoH_3$,

$$\log_{10} p\ (\text{Torr}) = -\frac{4080 \pm 50}{T} + 9.12 \pm 0.09$$

The differential heats of reaction in these two regions are, $\Delta H = -52.7 \pm 0.2$ kcal/mole of H_2 and $\Delta H = -18.7 \pm 0.2$ kcal/mole of H_2, respectively. The differential entropies of reaction are, $\Delta S = -35.6 \pm 0.2$ cal/deg · mole of H_2 and $\Delta S = -28.6 \pm 0.4$ cal/deg · mole of H_2, respectively. Relative partial molal and integral thermodynamic quantities were calculated for the system.

The dissociation pressure equation for the holmium solid solution dideuteride plateau region was determined for comparison purposes

$$\log_{10} p\ (\text{Torr}) = -\frac{11{,}420 \pm 60}{T} + 10.70 \pm 0.06$$

The enthalpy of reaction to form the dideuteride phase in $\Delta H = -52.3 \pm 0.3$ kcal/mole of D_2, and the entropy of reaction is $\Delta S = -35.8 \pm 0.3$ cal/deg · mole of D_2.

Rare-earth metals are characterized by the ability to absorb large quantities of hydrogen and to combine with hydrogen to form hydride phases. Previous investigations concerned with the heavy rare-earth metals at this laboratory defined the systems, erbium-hydrogen (1) and erbium-deuterium (2). The interest in these systems embraced the holmium-hydrogen system as well, because this latter system would be expected from chemical considerations to exhibit hydride phases with characteristics and thermal stabilities similar to the erbium hydrides.

The properties of the rare-earth-metal hydrogen systems have been reviewed in the literature (3-5). The holmium-hydrogen system has been outlined in one previous investigation (6). The present study was undertaken to broaden the temperature and compositional ranges of the above work and to extend the limits of thermodynamic data available for this system.

Experimental Procedure

The experiments were conducted in a modified Sieverts apparatus. The unit incorporated a mercury diffusion pump for evacuation and a manifold to which were connected a palladium-silver hydrogen thimble, a gas burette, a mercury manometer, a McLeod gauge (Kontes Glass Company) and a quartz reaction tube for heating to temperatures up to 950°C. High-purity hydrogen was obtained by passing hydrogen through the heated palladium-silver thimble. The 100-ml, precision gas burette was graduated to 0.1 ml divisions. Gas pressures were measured on the manometer to ±0.5 Torr and in the McLeod gauge range (10^{-4} to 1 Torr) to ±3%. The quartz reaction tube was heated by a nichrome-wound furnace controlled to a temperature cycle of ±1°C. Specimen temperatures in the quartz tube were measured independently by means of a chromel-alumel thermocouple located outside and adjacent to the tube at the vicinity of the specimen.

The specimen material was nuclear-grade holmium sponge, 99.9% purity, obtained from the Lunex Company. The large surface area of the sponge and the short diffusion paths permitted the attaining of equilibrium in relatively short periods of time. The typical specimen size was 0.3g.

The specimen of holmium sponge was contained in a tungsten foil boat to prevent contact with the quartz tube. At the beginning of each experiment, the system

with specimen in place was evacuated to less than 10^{-6} Torr and flushed several times with high-purity hydrogen, and finally evacuated again ready for the first gas addition. The specimen was then heated under vacuum to the desired temperature and exposed to a measured batch of hydrogen. After equilibrium was attained (usually in a few hours) the pressure was measured, and the hydrogen composition of the specimen calculated. Successive batches of hydrogen were added until atmospheric pressure was reached. These data were then plotted as an isothermal curve of specimen composition (hydrogen-to-holmium atomic ratio) *vs.* pressure. Other isotherms were developed in the same manner. Compositions are estimated to be accurate to ±1%. Preliminary experiments indicated that absorption of hydrogen by the specimen during flushing at room temperature was insignificant and did not change the specimen compositions beyond the limits of error.

The partial-pressure plateaus were determined by cycling suitably hydrided specimens through the temperature ranges of interest. At each temperature, time was permitted for equilibrium to be attained, and the pressure was recorded. The temperatures were cycled both up and down to detect nonequilibrium effects. The logarithm of pressure was plotted against the reciprocal absolute temperature, and the data were treated by a least squares computer analysis to obtain a mathematical van't Hoff relationship.

Results and Discussion

The holmium-hydrogen system resembles the erbium-hydrogen system, which confirms the tendency for most heavy rare-earth metals to form isomorphous systems when combined with hydrogen. As hydrogen is reacted with holmium the gas is dissolved interstitially in the hexagonal close-packed lattice. On reaching saturation, additional hydrogen reacts with holmium to form the face-centered-cubic, holmium dihydride phase (lattice parameter a_0 = 5.165Å) (7). A further addition of hydrogen produces the holmium trihydride phase, which has a hexagonal lattice with parameters a_0 = 6.308Å, c_0 = 6.560Å (8). The dihydride and trihydride phases are not stoichiometric, but exhibit compositional ranges of hydrogen solubility which broaden at high temperatures. The trihydride phase is stable only at relatively low temperatures, tending to decompose to the dihydride at temperatures above 370°C at atmospheric pressure.

Isothermal curves for the holmium solid solution-dihydride composition range are presented in Fig. 1, and a similar plot for the dihydride-trihydride range is presented in Fig. 2. More than 500 individual data points are represented by these curves. The points are not shown because of the small scale of the plot and the many points involved.

The isotherms can be correlated to the phases and solubility relationships of the holmium-hydrogen phase diagram. For example, as hydrogen initially is taken into solid solution in the holmium metal the gas pressure increases. As the metal becomes saturated, additional hydrogen initiates the formation of the dihydride phase, and the pressure remains constant in the two-phase region. This behavior is in accordance with the phase rule, which dictates that the appearance of a new phase is accompanied by the loss of one degree of freedom. Constant-pressure plateaus were observed at all temperatures investigated. Additions of hydrogen advancing the composition into the single phase dihydride region produce another increase in pressure. Experimental error accounts for the apparent crossing of some isothermal curves in this region. A second two-phase plateau region (Fig. 2) is observed between the dihydride and trihydride single-phase regions at lower temperatures. It is therefore seen that the extremities of the horizontal plateau lines demark the transitions in number

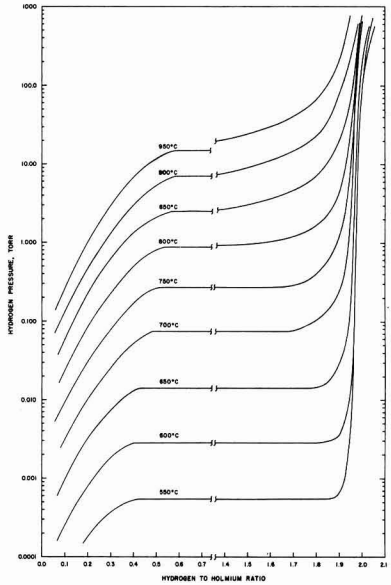

Fig. 1. Family of isotherms in the solid solution-dihydride region of the holmium-hydrogen system.

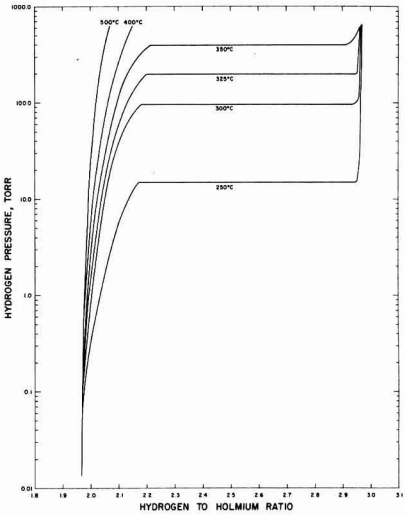

Fig. 2. Family of isotherms in the dihydride-trihydride region of the holmium-hydrogen system.

of phases and indicate the compositional solid solution limits of hydrogen in the three phases. The solubility limits of the holmium-hydrogen system are listed in Table I.

A log-log plot of composition *vs.* pressure for the various isotherms in the holmium solid solution region yielded straight lines with slopes approximating 2. This value confirms the validity of Sieverts' law for hydrogen in holmium. Sieverts' law states that the solubility of a diatomic gas in a metal is proportional to the square root of the pressure, implying that the gas is dissolved atomically in the metal.

A total of 78 independent determinations were made to establish dissociation pressures in the metal solid solution-dihydride plateau region as a function of temperature. Specimens were hydrided to 1.0 H/Ho ratio and cycled to temperatures between 550° and 900°C. Hysteresis effects were absent. The data were treated

Table I. Solubility boundaries in the Ho-H system

Temp, °C	Two-phase region Ho + HoH_3		Two-phase region HoH_2 + HoH_3	
950	0.59 H/Ho	1.20 H/Ho	Not stable	
900	0.58	1.30	Not stable	
850	0.56	1.40	Not stable	
800	0.53	1.50	Not stable	
750	0.51	1.65	Not stable	
700	0.48	1.65	Not stable	
650	0.43	1.80	Not stable	
600	0.40	1.85	Not stable	
550	0.40	1.85	Not stable	
350	—	—	2.21 H/Ho	2.91 H/Ho
325	—	—	2.20	2.95
300	—	—	2.19	2.95
250	—	—	2.17	2.95

by a least-squares computer analysis to describe the best straight line, and the following equation was obtained

$$\log_{10} p \text{ (Torr)} = -\frac{11{,}520 \pm 50}{T} + 10.66 \pm 0.05$$

where p = equilibrium hydrogen pressure and T = absolute temperature, Kelvin.

The plot of the log of plateau equilibrium pressure *vs.* reciprocal temperature is illustrated in Fig. 3. The slope of the line is related to the enthalpy of the reaction across the plateau region, and the intercept is related to the entropy of the reaction. The values for this plateau region are $\Delta H = -52.7 \pm 0.2$ kcal/mole of H_2 and $\Delta S = -35.6 \pm 0.2$ cal/deg · mole of H_2.

Dissociation pressures of the holmium solid solution-dideuteride plateau region were also determined over the same temperature range to detect differences, if any, caused by the isotopic effect. The procedure was the same as described, except deuterium was substituted for the hydrogen. A total of 57 equilibrium pressure points were employed in the least squares analysis, and the resulting equation is presented here

$$\log_{10} p \text{ (Torr)} = -\frac{11{,}420 \pm 60}{T} + 10.70 \pm 0.06$$

The enthalpy of reaction to form the dideuteride phase is $\Delta H = -52.3 \pm 0.3$ kcal/mole of D_2, and the entropy of reaction is $\Delta S = -35.8 \pm 0.3$ cal/deg · mole of D_2. The dissociation pressures for the deuterium plateaus are consistently higher than for the hydrogen system (see the deuterium plateau pressures plotted in Fig. 3). The entropy of reaction for the HoD_2 is slightly more negative than the entropy of reaction for HoH_2, which is in the right direction on the basis of theoretical considerations (2).

A similar procedure was employed for the analysis of the dihydride-trihydride plateau region. In this instance a total of 54 equilibrium pressures were obtained at temperatures between 200° and 350°C. The specimens were initially hydrided to a 2.8 H/Ho composition because the high equilibrium pressures above 300°C depleted the specimen of hydrogen. Specimens not containing an initial excess of hydrogen transformed completely to the dihydride phase at the higher temperatures. Long periods of time were required in order to attain equilibrium at each temperature. In general, the pressure values obtained on heating the specimen to the desired temperature were more reproducible than those obtained by cooling from a higher temperature. The pressures obtained by cooling were erratic and high. A plot of the log of plateau pressure *vs.* reciprocal temperature was made, and the equation obtained by computer, least-squares analysis is as follows

$$\log_{10} p \text{ (Torr)} = -\frac{4080 \pm 50}{T} + 9.12 \pm 0.09$$

The enthalpy of reaction to form the trihydride phase from the dihydride phase is $\Delta H = -18.7 \pm 0.2$ kcal/mole of H_2, and the entropy of reaction is $\Delta S = -28.6 \pm 0.4$ cal/deg · mole of H_2.

Data in the metal solid solution region were treated in this same manner. These data are presented in Fig. 3 as a series of isopleths in conjunction with the plateau data. Each solid solution isopleth was fitted by a least-squares, computer program to an equilibrium dissociation pressure equation of the van't Hoff form, $\log_{10} p = -A/T + B$. The equation constants, A and B, for each of the compositions are tabulated in Table II.

The solution reaction in the metal solid solution is

$$\tfrac{1}{2} H_2 \text{ (g)} \rightleftharpoons H$$

for which the relative partial molal free energy of solution is

$$\overline{G}_H - \tfrac{1}{2} G^\circ_{H_2} = RT \ln p^{1/2}_{H_2}$$

From this relationship, the Gibbs-Helmholtz equation is integrated to provide the van't Hoff form of the dissociation pressure equation

$$\log_{10} p = \frac{-2(\overline{H}_H - \tfrac{1}{2} H^\circ_{H_2})}{2.303\,RT} + \text{constant}$$

The relative partial molal enthalpy and entropy of solution in the holmium solid solution are calculated from the slope and equation constant, respectively. These quantities are tabulated in Table III.

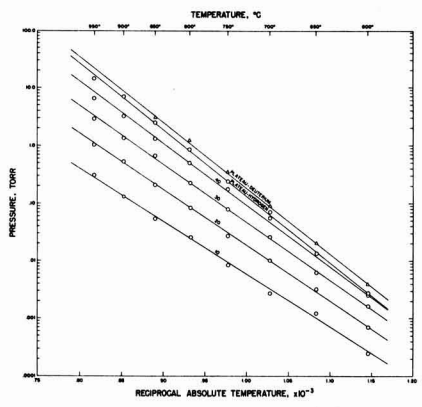

Fig. 3. Family of isopleths in the holmium-hydrogen system (included is the plateau isopleth of the holmium-deuterium system).

Table II. Equilibrium dissociation pressure equations for the holmium-hydrogen system

Atomic ratio (H/Ho)	Constants in $\log_{10} p$ (Torr) $= -A/T + B$	
	A	B
0.10	8,840 ± 240*	6.65 ± 0.24*
0.20	9,430 ± 150	7.72 ± 0.15
0.30	9,830 ± 80	8.52 ± 0.08
0.40	10,330 ± 120	9.31 ± 0.12
Plateau region	11,520 ± 50	10.66 ± 0.05

* Standard deviations.

Table III. Relative partial molal enthalpy and entropy for hydrogen in the holmium solid solution and two-phase region

Atomic ratio (H/Ho)	$\overline{H}_H - \tfrac{1}{2} H^\circ_{H_2}$ kcal/g-atom H	$\overline{S}_H - \tfrac{1}{2} S^\circ_{H_2}$ cal/g-atom H · deg
0.00	−19.8*	+∞
0.10	−20.2 ± 0.5	−8.6 ± 0.5
0.20	−21.6 ± 0.3	−11.1 ± 0.3
0.30	−22.6 ± 0.2	−12.9 ± 0.2
0.40	−23.7 ± 0.3	−14.7 ± 0.3
Plateau region	−26.4 ± 0.1	−17.3 ± 0.1

* Extrapolated value.

Table IV. Integral free energies, enthalpies, and entropies of mixing in the holmium-hydrogen system at 650°C

Composition H/Ho ratio	$-\Delta G^M$ (kcal/ g-atom soln)	$-\Delta H^M$ (kcal/ g-atom soln)	$-\Delta S^M$ (cal/ deg · g-atom soln)
0	0	0	0
0.10	1.21	1.73	0.57
0.20	2.09	3.33	1.37
0.30	2.77	4.77	2.17
0.40	3.31	6.09	3.01
0.43*	3.44	6.45	3.26
1.80*	6.05	16.20	10.10

* Solubility boundaries of the two-phase region, Ho_{ss} + $HoH_{1.80}$.

The relative partial molal quantities were used to calculate the integral free energy, entropy, and enthalpy of mixing in the holmium-hydrogen system. The equation for determining the integral enthalpy of mixing per g-atom of solution is

$$\Delta H^M = \frac{1}{1 + n_H/n_{Ho}} \int_0^{n_H/n_{Ho}} (\overline{H}_H - \tfrac{1}{2} H^o_{H_2})\, d\,(n_H/n_{Ho})$$

The integral entropies and free energies of mixing were obtained in the same manner. A graphical integration was necessary to determine the appropriate thermodynamic quantity for each level of n_H/n_{Ho}. Data are presented in Table IV for the temperature 650°C.

Acknowledgment

The writers are grateful for the support of the Sandia Corporation, Albuquerque, New Mexico (prime contractor to the Atomic Energy Commission) in the conduct of this work. Appreciation is expressed for the help of Mr. Russell A. Nye, who served as laboratory technician.

Manuscript received July 27, 1967; revised manuscript received Sept. 14, 1967.

Any discussion of this paper will appear in a Discussion Section to be published in the December 1968 JOURNAL.

REFERENCES

1. C. E. Lundin, Final Report, Sandia Contract No. 16-2524, August 1965, accepted for publication in *Trans. AIME*.
2. C. E. Lundin, Final Report, Sandia Contract No. 16-4115, December 1966, to be published.
3. J. C. Warf and W. L. Korst, *Inorganic Chem.* **5**, 1719 (1966).
4. W. G. Bos and K. H. Gayer, *J. Nucl. Matls.*, **18**, 1 (1966).
5. G. G. Libowitz, "The Solid State Chemistry of Binary Metal Hydrides," W. A. Benjamin, New York (1965).
6. P. M. S. Jones, J. Southall, and K. Goodhead, AWRE Report No. 0-22/64, United Kingdom Atomic Energy Authority, June 1964, (C. A., **61**, 7728g, 1964).
7. A. Pebler and W. E. Wallace, *J. Phys. Chem.*, **66**, 148 (1962).
8. M. Mansmann and W. E. Wallace, *J. Phys. (Paris)*, **25**, 454 (1964).

Chemistry of Electrical Wire Explosions in Hydrocarbons

Richard L. Johnson and Bernard Siegel

Laboratories Division, Aerospace Corporation, El Segundo, California

ABSTRACT

This paper describes the types and extents of high-temperature reactions that can proceed when metals are electrically exploded into atmospheres of various hydrocarbons. Pyrolyses to other hydrocarbons are readily initiated by the electrical wire explosions, forming both equilibrium and nonequilibrium products to relative extents depending on the reaction energetics and kinetics of the individual hydrocarbon reactants. A surprising aspect of these reactions is the extremely high chemical abstraction of the imparted electrical energy. The principal volatile pyrolysis product is always either acetylene or methane. Thermally labile organometallics and metal hydrides do not form in such explosions. However thermally stable metal carbides form readily during wire explosions in highly endothermic unsaturated hydrocarbons, while the saturated hydrocarbons are more inert.

The physical mechanisms of electrical wire explosions have been investigated widely (1), but it is only recently that chemists have begun to investigate the utility of this technique for chemical synthesis (2-5). An electrical wire explosion can be achieved by transferring the stored energy of a bank of capacitors to a metal conductor in a time interval so short that the energy is conserved in the conductor until explosive vaporization or liquefaction results. If the imparted electrical energy exceeds the thermodynamic heat of vaporization, it can be assumed that initially the exploded metal is mainly in the vapor state. In the presence of a surrounding gas of considerably higher total heat capacity the metal vapor will rapidly transfer energy to the surrounding gas. At this point two processes are possible. Either the cooling metal vapor will react chemically with the heated gas to form products containing metal atoms, or the heated gas molecules may react independently of the vapor by undergoing pyrolytic reactions. Alternatively, if the imparted electrical energy is only sufficient to explosively liquefy the metal, one can only observe liquid-gas reactions.

Our laboratory has been engaged in an effort to determine whether conditions can be established for predicting the reaction products of wire explosions in various gases from simple thermodynamic and kinetic factors, and thus to elucidate the scope of this method of synthesizing inorganic and organic compounds. In ref. (2) we showed the effect of reaction energetics on the ultimate yield of products arising from metal explosions in sulfur hexafluoride. In ref. (6) we studied the pyrolysis of methane that is initiated by exploding a number of metals. It was shown that energy is very efficiently transferred from the exploding wire to the surrounding methane molecules, raising portions of these molecules to transient temperatures of 3200°-3500°K. At such temperatures methane is rapidly pyrolyzed to the equilibrium products, acetylene and hydrogen, the predominant volatile products which

we found experimentally. About 70% of the imparted electrical energy was absorbed chemically by the system to effect this pyrolysis. The remaining 30% of the imparted electrical energy was transferred ultimately to the reactor walls and lost to the outside environment. This wastage of energy is believed to have resulted from the rapid temperature quenching that accompanies the endothermic pyrolysis reaction, coupled with the relative inertness of methane at temperatures much below 2500°K.

In the present paper we extend the study of pyrolyses initiated by electrical wire explosions to more reactive hydrocarbons. It was desired to ascertain whether such reactants would lead to the formation of significant amounts of nonequilibrium products in cooler regions of the wire explosion, thus raising the fraction of the imparted electrical energy which is transformed to chemical energy of pyrolysis. Another objective was to ascertain which types of hydrocarbons would react chemically toward the exploding metals, forming products such as metal carbides, organo-metallics, or metal hydrides; it was shown in ref. (6) that methane is essentially inert in this respect.

Experimental

Wire explosions.—The wire explosions were carried out in a stainless steel bomb shown in Fig. 1. This bomb was machined from a solid block to a wall thickness of ¼ in. to withstand the anticipated shock waves from the exploding wires. The bomb is in two sections so that the wires to be exploded can be mounted conveniently. There are four O-ring seals to keep the bomb vacuum tight. The largest of these O-rings is readily seen on the circumference of the upper section. The other three O-rings, which are not visible, seal between the upper plate surface and the swagelock fittings. The bomb can be evacuated to a pressure of 2×10^{-5} Torr. However, since initial pressures of 10^{-3} Torr produced extraneous gases at levels too low to be observed gas chromatographically within the time limits of our experiments, this level of vacuum was used frequently. Teflon insulators separate the ¼ in. copper pole electrodes from stainless steel parts. Wires to be exploded are fastened to the lower ends of the electrodes by set screws. The distance between electrodes is 1½ in., and they are positioned to hold the wire 1¾ in. from the top of the cylinder if the wire is placed linearly between the electrodes, the only position used in our experiments. The internal diameter of the bomb is 4 in., and the internal volume is 833 cc. The entire bomb assembly was connected to a vacuum line by a steel ball joint so that the bomb could be filled with gases and volatile products could subsequently be transferred.

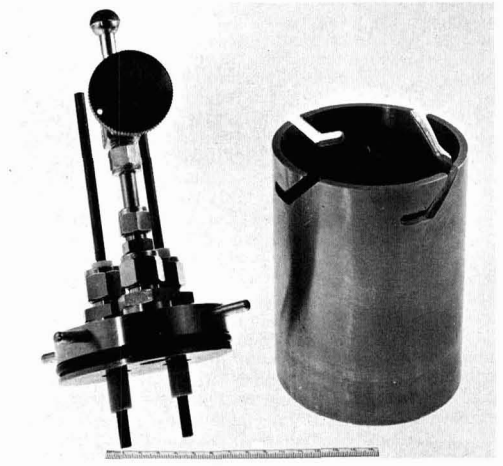

Fig. 1. Exploding wire apparatus

Two electrical discharge systems were used. For those runs in which the delivered electrical input energy was 148 or 466 joules a mechanical Jennings vacuum switch was used to discharge three 14-μf capacitors, which were rated for a maximum of 20 kv and connected in parallel. For those runs in which the delivered energy was 2188 joules this capacitor arrangement was discharged by a GE model 7703 ignitron tube. The reported energies are those energies that were actually delivered to the reactor rather than the nominal energies stored in the capacitors. Since a considerable fraction of the nominally stored energy is lost to the external circuitry on discharging the capacitors, it was deemed necessary to determine experimentally the fraction delivered to the exploding wire. This was done by calorimetry.

Wire explosions were carried out as follows. Weighed wires were connected to the electrodes, and the reactor was then sealed and evacuated. The hydrocarbon gas was then introduced to the desired pressure, the valve closed, and the wire exploded by the firing system described above. After firing, the final gas pressure was measured and the volatiles were transferred to a sample bulb for gas chromatographic analysis. The reactor was then opened in a nitrogen atmosphere enclosure for recovery of the nonvolatile products.

The wire masses that had actually been exploded are given in Table I. These masses were determined by weighing the unexploded residues still attached to the electrodes after the wires had been fired. From high-temperature heat capacity data (7,8) we have computed the fractions of exploded wires that were either explosively liquefied or vaporized. For those runs in which 0.3g Pt was exploded, sufficient energy was imparted for vaporization of only 29.4% of the exploded material at an input energy of 466 joules, while the initially exploded Pt was completely liquid at 148 joules. In each of the experiments in which 0.01g Pt or 0.05-0.06g Al were exploded, sufficient energy had been imparted to vaporize the metal fully by a large margin. In the iron explosions there could not have been any appreciable vapor at 466 joules, but sufficient energy had been imparted in the 2188 joule runs for complete vaporization of the iron.

It might be noted that experimentation with explosions of various metals into methane had demonstrated that neither the identity of the metal nor its mass over a wide range of mass ratios affected appreciably the degree of pyrolysis or the ratios of the volatile products (6). Therefore, in studying the pyrolysis reactions of higher hydrocarbons in the present paper it was deemed unnecessary to use mass or identity of the metal as a control factor for pyrolytic reactions. Because we were primarily interested in the chemical reactions resulting from the wire explosion, rather than the electrical explosion itself, the current-time characteristics of the wire explosions were not measured routinely. However there is no question but that explosions did occur. Measurements of the rate of change of current in the conductors being exploded were carried out in this laboratory under conditions somewhat similar to many of the explosions reported herein. These data indicated that current rose to a maximum within several microseconds and then damped out to zero over periods up to 100 μsec. Further, examination of the bomb contents after firing of the wire showed that the original wire had disappeared and the metal was found in the form of a fine powder, which was distributed relatively uniformly over all of the walls of the reactor.

Product analysis.—Gas chromatographic analysis of the volatiles was made on a dual-column, programmed-temperature instrument with katharometer detection, using a flow rate of 120 ml/min. For earlier runs, hydrocarbons were determined on a 6 ft x ¼in. column of 120/150 mesh Porapak Q, temperature programmed

Table I. Hydrocarbon pyrolysis data

Reactants[a]	Imparted energy,[c] joules	Per cent pyrolysis[d]	Volatile products[g] 1st	2nd	3rd	4th	5th
Methane, 0.3g Pt	148	2.4 (1.5)	C_2H_2 100	C_2H_6 3.3	C_4H_4 2.4	C_2H_4 1.9	
Methane, 0.3g Pt	466	7.8 (2.5)	C_2H_2 100	C_2H_6 3.4	C_4H_4 2.0	C_2H_4 0.7	
Methane, 0.06g Al	2188	16.4 (18.6)	C_2H_2 100[f]	C_2H_6 3.1	C_2H_4 2.8	C_4H_4 2.6[e]	C_2H_6 2.0
Ethane, 0.3g Pt	148	3.6	C_2H_2 100	CH_4 19	C_2H_6 11		
Ethane, 0.06g Al	2188	25.7 (8.2)	C_2H_2 100[f]	CH_4 47	C_4H_4 2.7[e]	C_2H_6 1.7	C_2H_4 1.4
n-Butane, 0.3g Pt	148	2.1	C_2H_2 100	CH_4 29	C_2H_6 7.4	C_2H_4 5.4	C_3H_8 2.7
Isobutane, 0.3g Pt	148	1.7	C_2H_2 100	CH_4 54	C_2H_6 23	C_3H_8 8.0	C_2H_4 4.4
Isobutane, 0.3g Pt[b]	148	5.0	C_2H_2 100	CH_4 44	C_2H_6 21	C_3H_8 7.6	C_2H_4 5.1
Isobutane, 0.3g Pt	466	5.7	C_2H_2 100	CH_4 52	C_2H_6 18	C_3H_8 7.7	C_2H_4 2.5
Isobutane, 0.05-0.06g Al	2188	11.8 (5.4)	CH_4 100	C_2H_2 98[f]	C_2H_6 30	C_2H_4 0.8	C_2H_6 0.5
Ethylene, 0.3g Pt	148	2.8	C_2H_2 100	C_4H_4 60	CH_4 3.6	C_4H_2 3.2	C_6H_6 0.2
Ethylene, 0.01g Pt	466	9.3 (1.9)	C_2H_2 100[f]	C_4H_4 4.8	CH_4 1.8	C_4H_2 1.5	C_6H_6 0.3 C_6H_6 0.3
Butadiene-1,3,0.01g Pt	466	3.9 (1.6)	C_2H_2 100[f]	CH_4 6.6	C_3H_4 2.8	C_6H_6 1.1	
Cyclopentadiene, 0.25g Fe	466	4.7	C_2H_2 100[f]	CH_4 20	C_3H_4 5.0	C_6H_6 3.9	C_4H_4 2.2 C_4H_2 2.2
Cyclopentadiene, 0.2g Fe	2188	8.6 (82.8)	CH_4 100	C_2H_2 8.1[f]	C_2H_6 1.1	C_6H_6 1.8	
Acetylene, 0.01g Pt	148	0.6 (96.3)	CH_4 100	C_2H_6 2.9	C_6H_6 1.0		
Allene, 0.01g Pt	466	10.7 (86.1)	CH_4 100	C_2H_2 14.5[f]	C_2H_6 1.5	C_3H_6 1.5	C_6H_6 2.5
Propyne, 0.01g Pt	466	7.8 (89.0)	CH_4 100	C_2H_2 19[f]	C_2H_6 2.0	C_3H_6 2.0	C_6H_6 0.5

[a] Unless specified otherwise initial hydrocarbon pressures were in range 400-450 mm.
[b] Initial isobutane pressure was 100 mm.
[c] All runs except those using input energies of 2188 joules were with Jennings mechanical switch; 2188 joule runs used ignitron switch.
[d] Values listed first are for per cent decomposition to volatiles; those given in parentheses are the per cent decomposition to nonvolatile solids.
[e] Aggregate of C_4H_4 + C_4H_2.
[f] In these runs small amounts of ethylene were not separated from acetylene.
[g] The products have been normalized to a scale of 100 for the most prevalent species.

from 50° to 250°C at 4°/min, and hydrogen was determined on a molecular sieve or on a column of coconut charcoal, 6 ft x ¼ in. at 50°C. In later runs all compounds were determined on a 12 ft x ¼ in. Porapak Q column, programmed, after a 4-min delay, at 4°/min from 40° to 250°C. Samples were taken from a glass bulb reservoir through a gas valve with a 5-ml sampling loop. Values reported in Table I are averages of 6 to 12 multiple runs.

In those runs where platinum alkyls were suspected nonvolatile products, the nonvolatile solids were extracted with benzene and the extract tested for a platinum compound. Similarly in the iron-cyclopentadiene explosions, the nonvolatiles were extracted with diethyl ether and the extract tested for ferrocene. Aluminum alkyls are volatile, and these were sought in the Al explosions by mass spectrometric analysis of the volatile products. Carbides were sought by x-ray diffraction. There has never been a reported platinum carbide (9), and x-ray diffraction patterns of our products failed to demonstrate the existence of a platinum carbide in those runs which involved explosions of platinum wires.

The carbon and hydrogen contents of the nonvolatile residues were obtained by the usual combustion procedure, after extraction with organic solvents for those runs in which organometallic products were sought. These residues were not investigated further. Our main purpose in determining the carbon contents was to compute the per cent decomposition of the hydrocarbons to nonvolatile solids for those wire explosions where thermochemical calculations were desired. In those runs where the over-all pyrolysis was very small an experimental uncertainty of several per cent in the gas chromatographic data prevented direct calculation of the yields from data on the lowering of the concentration of the hydrocarbon reactants. The yield of volatile products was obtained by summing carbon atoms from all the volatile product data, and the yield of nonvolatile hydrocarbons (or carbon) was obtained from the carbon content of the residues.

Results and Discussion

Hydrocarbon pyrolyses.—Saturated hydrocarbons higher than methane have increasingly higher rate constants for pyrolytic reactions (10-13). Our prediction that this would lead to more complex pyrolysis products for such hydrocarbons in wire explosions, as compared to methane, with larger proportions of nonequilibrium products and lesser proportions of acetylene, is supported by the product data in Table I.

The pyrolyses of ethane and the butanes resemble that of methane in that much of the acetylene is undoubtedly formed in the 3200°-3500°K temperature range. This temperature range is undoubtedly achieved in a significant portion of the hydrocarbon molecules surrounding the exploding wire as soon as sufficient numbers of molecules abstract energy from the exploded material to reduce the very much higher temperatures that would characterize the previously smaller heated portion. In the case of hydrocarbons higher than methane, further reactions are possible when the temperature falls below even 2000°K, after temperature quenching caused by the endothermicity of acetylene formation and further heat conduction to cold regions of the surrounding gas. At these lower temperatures the speed of the over-all process requires that pyrolyses fall short of equilibrium, and one obtains the nonequilibrium products shown in Table I for the ethane, n-butane, and isobutane reactions.

This additional reactivity at lower temperatures is reflected in the degree to which chemical energy is abstracted from the imparted electrical energy. Whereas the methane pyrolyses carried out at energy levels at 148 to 466 joules waste approximately 30% of the imparted energy, there is essentially no wasted energy in the ethane pyrolysis at 148 joules. From thermochemical data we compute that 110.7% of the imparted energy was transformed into chemical energy of pyrolysis in the ethane run. In view of the 6% uncertainty in calorimetric measurement of the imparted energy to the wire and the experimental uncertainties in the gas chromatographic analyses of products, this is believed to represent essentially complete energy abstraction. There is no conflict between these data and the apparently lower efficiencies of energy abstraction in the methane and ethane runs at 2188 joules. We have observed that the more rapid explosion that accompanies the use of an ignitron firing circuit, rather than a Jennings mechanical switch, leads to a lower degree of energy abstraction with the ignitron system. Because the latter was used in the 2188 joule runs, we compute lower values of 57.3 and 41.6%, respectively, for the degree of energy abstraction in the ethane and methane pyrolyses. However the relative efficiencies of methane and ethane extraction of electrical energy for chemical purposes remain unchanged.

Since saturated hydrocarbons are themselves exothermic, their pyrolysis to acetylene and hydrogen, or even to carbon and hydrogen, is always endothermic.

One would thus expect that the yield of pyrolysis products would be directly proportional to the imparted electrical energies in wire explosions. This is essentially verified by the data for methane and isobutane. At constant pressure, variation of the electrical energy from 148 to 466 joules, a 3.15-fold increase, leads to measured 3.25 and 3.35-fold increases in the yields of volatile products. The data for runs at 2188 joules cannot be compared with these runs because a different firing circuitry was used. Somewhat surprising is the fact that ethylene behaves similarly to the saturated hydrocarbons, both in type of products formed, and in exhibiting a 3.32-fold increase in volatile products when the input energy is increased from 148 to 466 joules. One might expect that ethylene would pyrolyze directly to graphite and hydrogen since the latter reaction is exothermic. Further, the yield of an exothermic reaction should not be directly proportional to the imparted energy.

The explanation for the ethylene data is based on reaction kinetics. It is known that the pyrolysis of ethylene to carbon and hydrogen proceeds through a mechanism that includes Eq. [1] (14); the heats of reaction cited in this paper were computed from

$$C_2H_4(g) \rightarrow C_2H_2(g) + H_2(g), \Delta H^\circ_{25^\circ} = +41.5 \text{ kcal/mole} \quad [1]$$

data in ref. (15). The relatively high endothermicity of this step increases the dependence of the type of product formed on the amount of electrical energy imparted to the exploding wire. At lower energy input levels the endothermicity of Eq. [1] reduces the over-all gas temperature to a point where acetylene is kinetically trapped and precludes the exothermic pyrolysis of acetylene to carbon and hydrogen. This should be readily overcome at higher energy levels, as is seen by the data for cyclopentadiene, which is similar to ethylene in the energetics of these pyrolytic reactions. At the higher energy level one obtains a drastically different pyrolysis. The yield approaches completion, unlike any of the pyrolyses of saturated hydrocarbons at such conditions, and the principal volatile hydrocarbon product becomes methane rather than acetylene.

This trend continues in the more highly endothermic alkyne molecules. Comparison of Eq. [1] with Eq. [2] and [3] indicates

$$C_3H_4(g) \text{ (propyne)} \rightarrow C_2H_2(g) + \tfrac{1}{2}C_2H_4(g), \quad \Delta H^\circ_{25^\circ} = +16.1 \text{ kcal/mole} \quad [2]$$

$$C_3H_4(g) \text{ (propyne)} \rightarrow C_2H_2(g) + H_2 + C(s), \quad \Delta H^\circ_{25^\circ} = +9.9 \text{ kcal/mole} \quad [3]$$

a much lesser tendency toward kinetic trapping of acetylene for wire explosions carried out in propyne (allene has very similar energetics), and explains the very high yields of pyrolysis products and volatile product distributions in propyne or allene explosions at lower energy input levels than had been required for comparable pyrolyses of cyclopentadiene. Acetylene, of course, cannot form permanently stable volatile intermediates by endothermic processes and should pyrolyze exothermically at energy input levels even lower than those required for the higher alkynes. Virtually complete pyrolysis of acetylene was observed at the lowest energy input level used in our experiments.

Metal-hydrocarbon reactions.—Metal alkyls were not formed by any of the explosions of aluminum or platinum into saturated hydrocarbons. The aluminum alkyls are well-known compounds, and both $(CH_3)_4Pt$ and $(CH_3)_6Pt_2$ have been reported to be reasonably stable compounds (16-19). A qualifying note might be added in regard to the platinum alkyls since doubt has recently been cast on the authenticity of the reported syntheses of these compounds (20). Yet it must be concluded that it appears unlikely that metal alkyls can be prepared by this technique. We next studied the possible formation of ferrocene by iron wire explosions in cyclopentadiene. This pi-bonded organometallic compound has been reported to have an unusually high thermal stability for this class of compounds since it is not extensively decomposed even at 470°C (21). Yet ferrocene was not formed, at either 466 joules where the over-all reaction of the cyclopentadiene was relatively small or at 2188 joules where the cyclopentadiene reacted extensively.

The difficulty in preparing organometallics by the present technique can be attributed to the limited thermal stabilities of such compounds and the competing pyrolysis reactions of the hydrocarbon reactants. Similar considerations apply to thermally labile hydrides, such as AlH_3, which also did not form in these experiments.

On the other hand many metal carbides are extremely stable thermally and should be capable of synthesis by the technique described in the present paper. Although Al_4C_3 was not observed in the methane explosion at 2188 joules, this carbide was observed among the products of the aluminum explosions in ethane and isobutane at 2188 joules. This was established by the presence of the x-ray diffraction spectrum characteristic of Al_4C_3 in the spectrum of the nonvolatile products of the ethane and isobutane explosions and its absence in the products of the methane explosion. Yet even when Al_4C_3 was found among the products of Al explosions in the higher saturated hydrocarbons, the intensities of the Al lines were considerably larger than those of Al_4C_3. Thus the reaction does not go very far toward completion, even at 2188 joules. These results reflect the energetics of Eq. [4] to [6]. Cook and Siegel showed (2) that

$$4Al(s) + 3CH_4(g) \rightarrow Al_4C_3(s) + 6H_2, \quad \Delta H^\circ_{25^\circ} = +22.8 \text{ kcal/mole} \quad [4]$$

$$4Al(s) + 3/2\ C_2H_6(g) \rightarrow Al_4C_3(s) + 9/2\ H_2, \quad \Delta H^\circ_{25^\circ} = -0.6 \text{ kcal/mole} \quad [5]$$

$$4Al(s) + 3/4\ C_4H_{10}(g) \rightarrow Al_4C_3(s) + 15/4\ H_2, \quad \Delta H^\circ_{25^\circ} = -7.3 \text{ kcal/mole} \quad [6]$$

for kinetic reasons endothermic reactions in which the metal reacts chemically with the surrounding gas are very inefficient in abstraction of electrical energy in wire explosions. Therefore Eq. [4] could be predicted to proceed to a lesser extent than would Eq. [5] or [6], if all other conditions were equal. Further, the marginal exothermicities of Eq. [5] and [6] would indicate poor yields. On this basis the endothermic unsaturated hydrocarbons should be superior to the exothermic saturated hydrocarbons as reactants leading to metal carbide formation. This is substantiated by the ready formation of $Fe_{20}C_9$ by iron explosions in cyclopentadiene at 2188 joules. Acetylene should be better still, and Al_4C_3 was found to be a product of aluminum explosions in acetylene, at energy input levels as low as 148 joules.

Future studies.—The application of the exploding wire technique in a small volume bomb is particularly efficacious for the synthesis of transition metal carbides. Cook (22) of this laboratory has expanded on the results of the present study by showing that titanium wire explosions into acetylene diluted with an inert gas can lead to the preparation of TiC samples in high yield and in purity at least equal to 98.6% by weight. The general applicability of the method is indicated by the successful synthesis of LaC_2, TiC, ZrC, NbC, Nb_2C, Ta_2C, MoC, Mo_2C, and W_2C. Although the utility of wire explosions in a small volume bomb for the synthesis of thermally labile compounds appears dim, in view of the results of the present paper, we believe that there is a possible solution to this problem. What is evidently required is the introduction of an additional mode of temperature quenching superimposed on the temperature quenching processes oc-

curring naturally in wire explosions carried out in a limited volume bomb. We are now trying to develop a technique in which the wire explosion is coupled to a device similar to a shock tube. This would provide both extra temperature quenching and longer path lengths at lower temperatures.

Acknowledgment

The authors gratefully acknowledge the general laboratory assistance of Miss C. G. Johnson who obtained all the gas chromatography data. Messrs. T. L. North and S. B. Mason assisted with the electrical discharge systems, while S. Hotta, P. Marsh, and E. S. Elliott obtained analytical data.

Manuscript received June 26, 1967; revised manuscript received Sept. 18, 1967.

Any discussion of this paper will appear in a Discussion Section to be published in the December 1968 JOURNAL.

REFERENCES

1. "Exploding Wires," W. G. Chace and H. K. Moore, Editors, Vol. 1-3, Plenum Press, New York (1959, 1962, 1964).
2. E. Cook and B. Siegel, *J. Inorg. Nucl. Chem.*, In press.
3. F. Mahieux, *Compt. rend.*, **257**, 1083 (1963).
4. M. J. Joncich, J. W. Vaughn, and B. F. Knutsen, *Can. J. Chem.*, **44**, 137 (1966).
5. M. J. Joncich and D. G. Bleu, "Exploding Wires," pp. 353-359, W. G. Chace and H. K. Moore, Editors, Plenum Press, New York (1964).
6. B. Siegel and R. L. Johnson, *A Thermal Model of Wire Explosions in Methane*, presented at the Fourth International Symposium on the Exploding Wire Phenomenon, Boston, October 1967, and will be published in the proceedings.
7. H. L. Schick, "Thermodynamics of Certain Refractory Comopunds," Vol. II, Academic Press, New York (1966).
8. D. R. Stull and G. C. Sinke, "Thermodynamic Properties of the Elements," American Chemical Society, 1956.
9. W. A. Frad, Carbides, A.E.C. Report IS-722, August 1963.
10. G. B. Skinner and W. E. Ball, *J. Phys. Chem.*, **64**, 1025 (1960).
11. C. P. Quinn, *Proc. Roy. Soc. (London)*, **275A**, 190 (1963).
12. J. H. Purnell and C. P. Quinn, *ibid.*, **270A**, 267 (1962).
13. G. I. Kozlov and V. G. Knorre, *Zhur. Fiz. Khim.*, **37**, 2082 (1963).
14. G. B. Skinner and E. M. Sokoloski, *J. Phys. Chem.*, **64**, 1028 (1900).
15. F. D. Rossini, Selected Values of Properties of Hydrocarbons, API Research Project 44, Nat. Bur. Stand., 1947.
16. H. Gilman and M. Lichtenwalter, *J. Am. Chem. Soc.*, **60**, 2085 (1938).
17. R. E. Rundle and E. J. Holman, *ibid.*, **71**, 3264 (1949).
18. G. Illuminati and R. E. Rundle, *ibid.*, **71**, 3575 (1949).
19. R. E. Rundle and J. H. Sturdivant, *ibid.*, **69**, 1561 (1947).
20. F. A. Cotton and G. Wilkinson, "Advanced Inorganic Chemistry," 2nd ed., p. 1036, Interscience Publishers, Inc. New York (1966).
21. G. Wilkinson, M. Rosenblum, M. C. Whiting, and R. B. Woodward, *J. Am. Chem. Soc.*, **74**, 2125 (1952).
22. E. Cook and B. Siegel, Unpublished results.

On the Activity of Platinum Catalysts in Solution

II. Kinetics of the Pt-O Reaction with Hydrogen and of Pt-H Deposition Using a Double Pulse Technique

Theodore B. Warner* and Sigmund Schuldiner*

Naval Research Laboratory, Washington, D. C.

ABSTRACT

Surface coverages of oxygen and hydrogen were determined on electrodes of differing activities as a function of time and of voltage in the potential decay curve following an anodic pulse. The electrolyte was 1M H_2SO_4 containing dissolved hydrogen. No important difference, other than rate, is found in the way Pt-O is removed from surfaces of differing activity; however, a significant difference is noted in the way hydrogen resorbs. The rate of Pt-O removal is of apparent first order in adsorbed oxygen when the initial fraction of the surface covered is about 1.0; it is zero order in adsorbed oxygen and in amount reacted when the initial surface coverage is <0.8. The rate of the decay reaction is probably not limited by mass transport of solution H_2 to the surface, by obstruction of active surface sites by sorbed product molecules, or by slow chemisorption of solution H_2 on the electrode prior to reaction with Pt-O.

In Part I of this series (1) and in a preceding paper (2), the rate of the reaction of oxygen, chemisorbed on smooth platinum, with hydrogen dissolved in 1M H_2SO_4 and in the Pt derma (the Pt-O/hydrogen reaction) was monitored by observing potential decay on open circuit after an anodic current pulse. The purpose in Part I was to examine how different thermal or chemical treatments affected the intrinsic catalytic activity of smooth platinum, using this reaction rate as a measure of activity. It was found that this intrinsic activity could be modified by several orders of magnitude. The purpose of this work was to determine if surfaces known to have different catalytic activities for the Pt-O/hydrogen reaction exhibited significant differences (other than rate) in the way oxygen was removed or hydrogen resorbed.

Breiter (3) has previously studied the chemical reduction of chemisorbed oxygen with H_2. His results should not be compared directly with these due to important differences in experimental procedure, as previously discussed (2). Sawyer and Seo (4) have also studied this system. Their oxygen generation rates were very low, however, so the electrodes would be presumed to contain some oxygen absorbed in the lattice. The presence of such oxygen affects the hydrogen/oxygen interaction markedly (2). The oxygen

* Electrochemical Society Active Member.

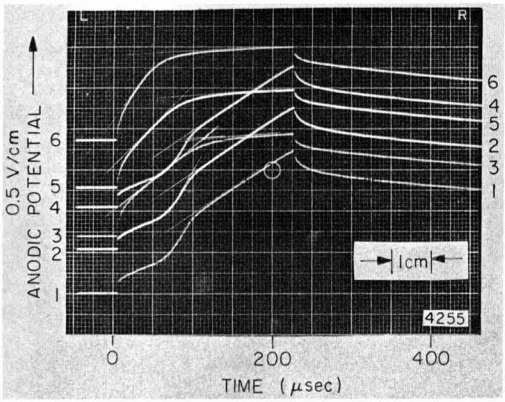

Fig. 1. Double pulse electrode polarization. First pulses (oxidation of H_{ad} followed by oxidation of H_2O to O_{ad}) are traces 1, 2, and 4; second pulses (oxidation of H_2O to O_{ad}) are traces 3, 5, and 6 taken after reaction (Pt-O_{ad} + hydrogen) times of 10, 6, and 3 msec, respectively, on an electrode with a monolayer decay time of 21 msec. Current density is 2.92 amp/cm².

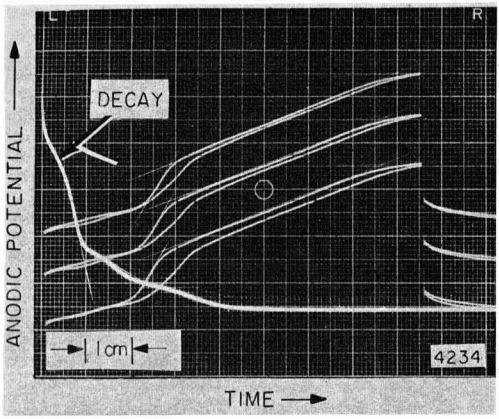

Fig. 2. Double pulse polarization of electrode on which some hydrogen had resorbed, and typical full decay curve. Pulses are 20 μsec/cm and 0.5 v/cm; decay is 50 msec/cm and 0.2 v/cm. Reaction times between pulses were 200, 230, and 260 msec reading from bottom to top on an electrode whose t_0 was 48 msec. Current density is 4.56 amp/cm².

generation rates used in this work were adjusted such that oxygen was deposited on the platinum surface without concurrent absorption of oxygen into the lattice.

Experimental

Apparatus and procedures were the same as in Part I except that two precisely spaced galvanostatic pulses were used.[1] A Hewlett-Packard 5214L Electronic Counter (clock rate 100 kc) provided two trigger pulses separated by a time known within 1 μsec. These pulses triggered a pulse generator (either an EH Model 132A or an Electropulse 3450D), sending two identical current pulses through the cell. The pulses were adjusted so that the first ended after a known amount, usually one monolayer, of chemisorbed oxygen atoms had been deposited on the electrode (Fig. 1). Current densities were from 2.9 to 4.5 amp/cm².[2]

The anodic charging curves are conceptually divided into the usual regions, called the "H ionization region" and the "O sorption region." In the subsequent decay, the first region is called the "O removal region," and the second the "H deposition region." These regions are diagrammed in Fig. 1a of ref. (2) and they are apparent in Fig. 2 here. In the O removal region, hydrogen is reacting with the oxygen chemisorbed on the electrode. This hydrogen can come from the H_2 dissolved in the bulk of the solution, from H_2 bubbles at the surface and from dermasorbed H (H absorbed in the top 2 or 3 atomic layers of Pt). After a known time into the decay, t, called at different times either the "reaction time" or the "decay time," the second pulse was triggered to determine how much charge was required to bring Pt-O coverage up to one monolayer. Knowing the initial coverage and this, the amount reacted could be computed. When the voltage decayed below 0.3v, the second pulse gave both the charge required to form the oxygen region and the charge due to oxidation of adsorbed hydrogen.

It was assumed that in the oxygen regions, $q_O = q_{measured} - q_{dl}$, and in the hydrogen regions, $q_H = q_{measured} - q_{dl}$. For the first pulse, the significance of the various terms is well understood. For the second pulse, the assumption is made in what follows that all of the charge designated q_O went to form Pt-O_{ad} via a net 2-electron oxidation, and all charge designated q_H went to oxidize Pt-H to H^+. The validity of these assumptions will be supported later. The charge due to double layer charging was subtracted from the various $q_{measured}$ using previously reported (5) double layer capacitance *vs.* potential data integrated over the potential region of interest.[3]

The "foot" of each charging curve in Fig. 1 (the horizontal trace to the left of time zero) gives the potential of the electrode prior to each pulse. The first of each pair of pulses started at the normal equilibrium hydrogen potential (0.000v). The foot of the second pulse then defined the potential, $E(t)$, in the decay from which the second pulse was taken.

Two bright platinum bead electrodes were used, one with a monolayer decay time, t_o, of 47.8 ± 0.5 msec, and one with t_o of 21.3 ± 1.5 msec. The monolayer decay time is the time required for the reduction of a monolayer of chemisorbed oxygen with hydrogen. The electrode areas were about 0.1 cm². For convenience, the more active electrode (activity defined by the rate of the Pt-O/hydrogen reaction) with $t_o = 21$ will be termed electrode A, and the less active one, electrode L. It was important to confirm that each measurement of voltage and redeposited charge was made on an electrode whose t_o was unchanged. This was done by plotting measurements of potential *vs.* reaction time, t, from a number of full decay curves taken before, during, and after the double pulse studies, and then comparing these data with the voltage/time information obtained from the foot of the second pulse. The t_o for the electrodes used did not change during the course of the experiments.

Results

Oxygen removal region: Pt-O + *Hydrogen* = Pt + H_2O.—*Voltage-time relation.*—To facilitate comparison of results on electrodes with different intrinsic activities, the results for each electrode have been expressed in terms of relative decay times, t/t_o, where t is the reaction time, and t_o the monolayer decay time.

[1] Unless otherwise specified, potentials are given *vs.* the normal hydrogen electrode, all measures of precision are standard deviations of an individual measurement, and electrode areas are "true" (5) areas based on the assumption that $q_{O+dl} = 456$ μcoul/cm² when one monolayer of oxygen is deposited at a current density of 3 amp/cm.² Precision of an individual area measurement was ±3.2%.

[2] At these current densities, the IR drop in the solution is a large fraction of the total cell voltage. The IR drop was at times removed from the display by using a Tektronix Type 547 oscilloscope with a Type 1A1 dual trace preamplifier. The rectangular pulse at the generator output was applied to input 1 and appropriately attenuated; the cell voltage was applied to input 2 and the difference signal was displayed.

[3] For the second pulse this treatment involved the assumption that q_{dl} (which includes a contribution from pseudocapacitance near 0.000v) under the nonsteady-state conditions prevailing was not significantly different from that measured in (5). Consideration of the physical situation prevailing shows that this is reasonable; further, the q_{dl} terms are small compared to total q.

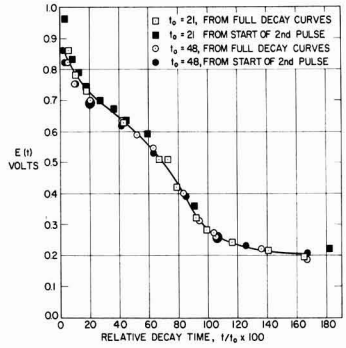

Fig. 3. Basic decay curve: potential vs. relative decay time

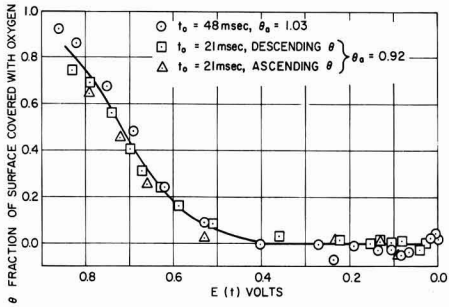

Fig. 4. Fraction of surface covered with O_{ad} vs. potential during decay. The initial coverages are denoted θ_a.

Plots of electrode potential during the decay, $E(t)$, vs. t/t_o (Fig. 3) for data obtained on electrodes with t_o = 21 and 48 msec show no important difference nor are differences noted for the relation between voltage in the decay curve and fraction θ of surface covered with oxygen (Fig. 4). It must be kept in mind that the actual times of reaction, however, differed by a factor of 2.2. From repeated measurements on electrodes whose t_o ranged from 17 to 180 msec, the potential at the end of the decay plateau, at $t = t_o$ was found to be 0.283 ± 0.004v.

Oxygen coverage vs. voltage and time.—Let a be the initial oxygen coverage of the electrode in μcoul/cm^2 deposited by the first pulse, and let $(a-x)$ be the coverage at any later time t. Let q_O be the amount of oxygen used in the second pulse to reform one monolayer of O_{ad}. We assume that $q_O + (a-x) = 420$ μcoul/cm^2; *i.e.*, the electrode is once again polarized up to the O_2 evolution region when its total oxygen coverage is brought back to one monolayer. The fraction θ of the surface covered with oxygen is

$$\theta = \frac{420 - q_O}{420} \qquad [1]$$

It is necessary to maintain a clear distinction between a, the initial concentration in μcoul/cm^2 of oxygen on the surface; θ_a, this initial concentration expressed as the fraction of Pt surface sites covered with O_{ad} ($\theta_a = a/420$ μcoul/cm^2), and θ, the fraction of the surface covered with oxygen at time t after some of the oxygen initially deposited has reacted with hydrogen.

The results in Fig. 5 and 6 show that the relationships between θ and t/t_o for the cases where $\theta_a \sim 1$ and for $0.32 \leq \theta_a \leq 0.77$ are quite different. For $0.32 \leq \theta_a \leq 0.77$, Fig. 6a shows that the rate of oxygen removal is zero order in the initial concentration a and in the amount reacted x. The slopes are independent of a and average 700 μcoul/cm^2. Converting into units

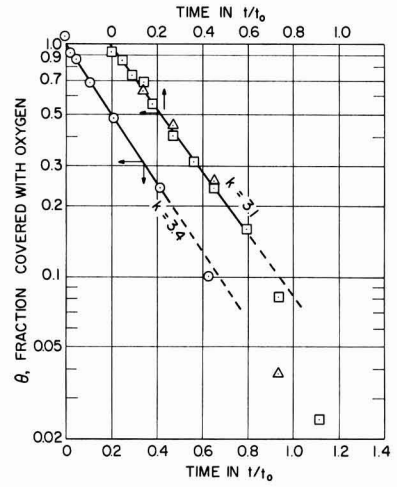

Fig. 5. Rate of removal of oxygen for case where fraction of surface initially covered is near unity. The symbols have the same meaning as in Fig. 4.

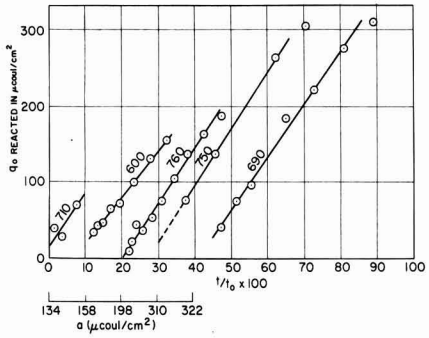

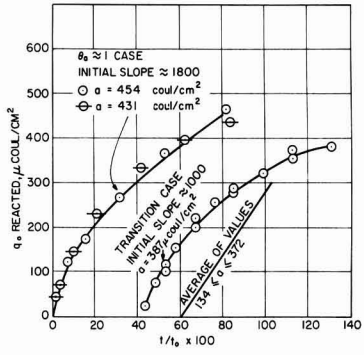

Fig. 6.(a, top) Rate of removal of oxygen for case where fraction of surface covered initially is <0.8. The initial coverage a for each curve is indicated on abscissa below t/t_o x 100 values. The origin of each succeeding curve is displaced 10 time units to the right of the preceding curve. The numbers on the curves represent the slopes in μcoul/cm^2. Fig. 6 (b, bottom) Comparison of cases where $\theta_a \approx 1$ with ones where $\theta_a < 0.8$. The origins for the two curves to the right have been displaced by 40 and 60 (t/t_o x 100) units.

of θ, the rate of oxygen removal is

$$\theta = \theta_a - 1.67\frac{t}{t_o} \qquad [2a]$$

However, for $0.92 \leq \theta_a \leq 1.03$, the rate of oxygen re-

moval is given by a first order relation

$$\theta = \exp\left(-k\frac{t}{t_o}\right) \qquad [2b]$$

over the range $1 \leq \theta \leq 0.15$ where k is the first order rate constant of about 3.2. The curves, plotted separately, show logarithmic relations; the slopes are not considered to be significantly different. (The slopes are strongly dependent on the average values used for t_o and $q_{O\ monolayer}$, as well as the extent to which some hydrogen may or may not be oxidized in the oxygen region.)

Hydrogen redeposition region: Pt + H = Pt — H. —The measured quantities were q_{H+dl}, q_{O+dl}, $E(t)$, and time since the end of the first pulse, t. The time available for hydrogen sorption was taken as $(t - t_o)$. Since charging curves at times up to $t = t_o$ gave little or no indication of any sorbed hydrogen, it was assumed that all hydrogen reaching the electrode up to this time was consumed in reaction with Pt-O, which was known to be present up to $t = t_o$. The validity of this assumption is examined in the Discussion Section. After correction for double layer charging, the resulting q_H *vs.* $E(t)$, q_O *vs.* $E(t)$, and $E(t)$ *vs.* $(t - t_o)$ data are shown in Fig. 7 and 8.

Discussion

Hydrogen redeposition region.—The factors that affect rate of potential decay in the Pt-O removal region exert no influence on the rate of potential change in the hydrogen resorption region. However, the amount of hydrogen found sorbed on the electrode after decay to a given potential does vary with the intrinsic activity of the electrode. The more active electrode, A, shows faster hydrogen reappearance in the hydrogen ionization region and no excess charge in the oxygen region whereas electrode L shows less q_H in a given time while the q_O measured simultaneously is anomalously high. It appears that the over-all rate of the hydrogen resorption is not greatly different in the two cases, but on L considerably more time is required for hydrogen to be sorbed in a form detected below 0.8v in a charging curve. Therefore, on L some hydrogen not yet sorbed in the usual ways is oxidized in the O sorption region, adding to the charge measured there. The slow process impeding hydrogen sorption could be either diffusion to a suitable chemisorption site, sorption of H into the derma, or the act of strong chemisorption itself. An alternate possibility is that it is not the sorption of the hydrogen that governs the potential at which it oxidized, but the kinetics of its subsequent oxidation. Then tiny amounts of unremoved oxygen in the Pt could act as a catalytic poison, impeding the oxidation of hydrogen sorbed near it. It is reasonable that the L electrode would hold oxygen more firmly in the H resorption region just as it did in the O removal region. The fact that oxygen coverage measured on L returns to the normal 1 monolayer at long times assures that no error in electrode area distorts these data.

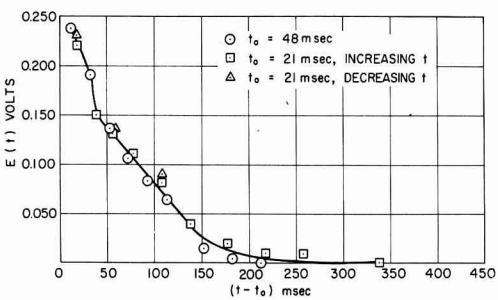

Fig. 7. Decay potential *vs.* time allowed for hydrogen resorption

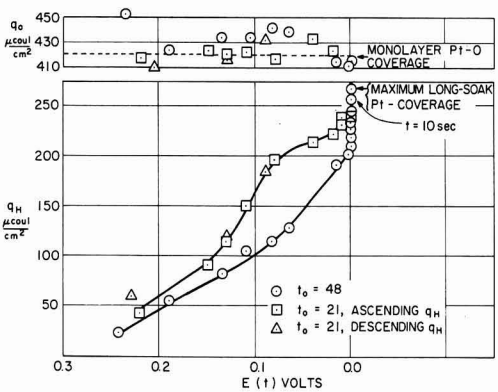

Fig. 8. Amounts of hydrogen found in the hydrogen region, and "oxygen" found in the oxygen region *vs.* potential attained in decay curve.

A very long time, much greater than 10 sec, is required to cover the electrode with full steady-state H coverage, although the equivalent of one monolayer (210 μcoul/cm^2) is sorbed in about 0.2 sec on each electrode. This is fully consistent with the view repeatedly expressed by this Laboratory that hydrogen sorbed on the surface is present in various forms, namely, weakly and strongly bonded H and dermasorbed hydrogen (hydrogen present in the Pt atomic layers just below the surface layer). It is probable that resorption of hydrogen into the derma is the slow process governing uptake of the last portion of the hydrogen sorbed.

The difference between A and L, which affects the rate of Pt-O_{ad} reaction with hydrogen, also affects the manner in which hydrogen resorbs on the electrode. It does not, however, affect the $E(t)$ *vs.* time relation or the over-all rate of sorption materially.

Oxygen removal region.—Oxygen coverage vs. potential.—It is apparent from Fig. 3 and 4 that the intrinsic difference between the reaction rates on the two electrodes is removed by normalization, giving voltage/time and oxygen coverage/time behaviors that are essentially the same. The data for $0.3v > E(t) > 0.0v$ (Fig. 4), in which the oxygen coverage of L appears to drop below zero, results from the anomalously high "oxygen" coverages found in the second pulse at certain times (*c.f.* Fig. 8 and discussion in preceding section). It appears that true zero Pt-O coverage may be more closely related to the point of inflection in the decay curve at 0.35v and $t/t_o = 0.90$. Conclusions previously drawn based on comparisons of decay times would not be influenced materially by a 10% change in the decay time used.

Rate of oxygen removal.—The rate of oxygen removal was previously (2) shown to be zero order in hydrogen partial pressure (from 1.0 to 0.1 atm), in stirring rate (from quiescent to vigorously gas-stirred), and in amount of oxygen removed from ½ monolayer to 2 monolayers. Hence, mass transport of solution H_2 to the surface is not rate-limiting. There is no indication that bare surface must be available for H_2 to chemisorb prior to reaction with Pt-O, for the integrated rate of removal of oxygen was the same for initial coverages ranging from less than a monolayer to two monolayers (2). In this study the kinetics of the removal were essentially the same for initial coverages of 0.92 and 1.03 monolayer.

The changes observed both in reaction order and in rate when initial Pt-O concentration was less than 0.8 monolayer indicate that the mechanism of the oxygen removal reaction changes. For this reason, the cases

where the initial coverage θ_a is less than 0.8 and where it is about 1.0 are discussed separately.

Case where $\theta_a < 0.8$.—The rate of oxygen removal is independent of θ_a and x. This behavior is to be expected if the surface contains sites with widely differing activities, and if the over-all rate of the reaction v_R is determined by the rapid rate v_R^* at relatively few "active sites" that comprise fraction l of the surface, and that are supplied (rate of surface diffusion v_D) as rapidly as necessary from the reservoir of oxygen atoms sorbed on the rest of the surface. Recognizing that in fact there is probably a whole spectrum of sites of differing activity on the surface, we may for simplicity consider the surface to have two kinds of sites, active and inactive (or less active), of fractions l and m with the fraction of l and m covered with oxygen being θ_l and θ_m. If l is quite small, say less than 0.05, and if $v_D >> v_R^*$, then as long as Pt-O is still present on inactive sites, l remains fully covered until θ_m becomes very low. Hence the rate of the reaction of the species on l, which is the only area catalytically significant, will be zero order in reactant. This model would make reasonable the very wide variations in v_R that have been observed as a result of thermally annealing or chemically etching the surfaces (1), for if l is sufficiently small, then addition or subtraction of relatively few active sites can change l substantially.

For several reasons, it is improbable that active sites are obstructed by product molecules as the reaction proceeds. First, the product will either be H_2O, the same as the solvent, or, if it is an intermediate, it is likely unstable with a short lifetime. Second, if active sites were obscured, then reaction rate would decrease with amount reacted, contrary to the data in Fig. 6. Finally, when all of the O_{ad} was reduced, the second charging curve in the O sorption region showed $q_O = 420\ \mu coul/cm^2$, the amount required for adsorption of 1 monolayer of O_{ad}. If during decay a significant amount of O_{ad} were reduced to a product that required only 1 electron per O_{ad} atom reformed, then recharging to full O_{ad} coverage would require $< 420\ \mu coul/cm^2$.

Case where $\theta_a \approx 1.0$.—The rate of oxygen removal was found to be first order in oxygen coverage. The reason for this difference in reaction order and the increase in initial rate at $a \approx 1.0$ is obscure. It is not the same sort of apparent reaction order change frequently noted in catalytic reactions, where as concentration of the reactant on the active surface increases, the reaction order decreases from unity to zero. Here, in the $\theta_a < 0.8$ case, the active surface is thought to be fully covered at the lowest initial concentrations used, yet in the $\theta_a \approx 1$ case the additional adsorbed oxygen somehow causes a change in the reaction order.

Tucker (6) has reported that when oxygen at 2×10^{-6} Torr interacts with Pt at 400°C, the results may be interpreted in terms of surface Pt atoms being displaced from their normal positions. If the high activity of the oxygen generated electrochemically in this work is a sufficiently large driving force, then perhaps a related rearrangement occurs here. In such a case, at high coverages the electrode surface would be quite different from that at lower coverages and a different mechanism would be reasonable. It is also conceivable that at very high coverages, additional sites on the surface become catalytically important and hence the initial rate becomes larger. However, it is then not clear why, when coverage has declined to 0.8, the other sites do not control the course of the reaction. In such a case, a zero order reaction rate should be observed for the removal of the remaining oxygen.

Conclusions

1. This work verifies that in H_2-saturated solution the time required for potential decay to about 0.300v, after a preceding anodic pulse, is also the time required for removal of the chemisorbed oxygen deposited by that pulse.

2. The rate of removal of O_{ad} is of apparent first order in adsorbed oxygen when the initial fraction of surface covered is about 1.0; it is zero order in adsorbed oxygen and in amount reacted when the initial fraction of surface covered is <0.8. It is zero order in hydrogen partial pressure in both cases.

3. Several alternative rate-determining steps in the decay reaction were considered, one being the rate of surface diffusion of O_{ad} or H_{ad} to the active sites, another being the actual rate of reaction at these active sites. The latter is favored as somewhat more probable, for it appears that active sites are involved rather than the whole surface, at least for $\theta_a < 0.8$. Steps probably excluded as rate-limiting are: (*a*) mass transport of solution H_2 to the surface, (*b*) obstruction of active surface sites by adherent product molecules, (*c*) chemisorption of solution H_2 on electrode prior to reaction with Pt-O.

4. For electrodes of differing activities, a significant difference is found in the way hydrogen resorbs on recently stripped electrodes; no difference other than rate is found in the way the Pt-O is removed.

Manuscript received June 22, 1967; revised manuscript received Sept. 27, 1967.

Any discussion of this paper will appear in a Discussion Section to be published in the December 1968 JOURNAL.

REFERENCES

1. T. B. Warner, S. Schuldiner, and B. J. Piersma, *This Journal*, **114**, 1120 (1967).
2. S. Schuldiner and T. B. Warner, *ibid.*, **112**, 212 (1965).
3. M. W. Breiter, *ibid.*, **109**, 425 (1962).
4. D. T. Sawyer and E. T. Seo, *J. Electroanal. Chem.*, **5**, 23 (1963).
5. S. Schuldiner and R. M. Roe, *This Journal*, **110**, 332 (1963).
6. C. W. Tucker, Jr., *J. Appl. Phys.*, **35**, 1897 (1964).

Thermodynamic Properties of LiCl in Dimethyl Sulfoxide

William H. Smyrl and Charles W. Tobias*

Inorganic Materials Research Division, Lawrence Radiation Laboratory, and Department of Chemical Engineering, University of California, Berkeley, California

ABSTRACT

EMF measurements were performed at 25°, 30°, and 35°C on the cell

$Pt(s)/Li(s)/LiCl(\text{solution in DMSO})/TlCl(s)/Tl_{(Hg)}(l)/Pt(s)$

For concentrations up to 0.12*M*, the activity coefficients at each temperature may be represented satisfactorily by Guggenheim's extension of the Debye-Hückel equation. The partial molal Gibbs free energy, entropy and enthalpy of transfer of LiCl from DMSO to water have been calculated to be —4.93 kcal/mole, +24.8 cal/°K-mole and +2.61 kcal/mole, respectively.

Because of its high dielectric constant and stability, dimethyl sulfoxide has been of interest as an ionizing solvent for some time (Table I). Although the chemistry of the solvent has been the subject of numerous investigations, very few thermodynamic data are available for its solutions. The only thermodynamic data which have been reported for electrolytic solutions in DMSO are some solubilities (1, 2), some acid-base equilibria (3), cryoscopic data on electrolytes in the solvent (4-6), and the heats of solution of several iodides (7). In addition, Cogley and Butler (8) have reported some qualitative thermodynamic results from measurements on the cell to be described below.

The present work is based on EMF measurements on the cell

$$Pt(s)/Li(s)/LiCl(\text{solution in DMSO})/TlCl(s)/Tl_{(Hg)}(l)/Pt(s) \quad [1]$$

The paucity of information relevant to the behavior of inorganic salts, and of reactive metals in nonaqueous media, as well as the potential usefulness of the solvent in voltaic cells, and in electrosynthesis, justify this choice. A halide system was chosen because of the low solubility of other salts in the solvent medium for which a reference electrode with a common anion could be found. Previous work in this laboratory established the advantages of the thallium amalgam-thallous chloride reference electrode (9). The nature of the reference electrode restricted the choice of the anion to chlorides and the metal cation to one of those rather high in the oxidation potential series. The lithium electrode was in part selected because of the opportunity to obtain direct thermodynamic measurements on a metal-metal ion couple which, along with the other alkali and alkaline earth metals, reacts spontaneously with most other ionizing solvent media. The potential usefulness of a lithium electrode in galvanic cells was also considered.

Experimental

The vacuum-tight Pyrex cell constructed for this purpose (Fig. 1) consisted of five approximately 2-cm diameter tubes arranged in radial positions, each connected to a central tube by 6 mm glass tubing. Reference electrodes and the counter electrodes (Li) were placed in the peripheral compartments, while the central tube served to introduce the solutions. In each experiment, two reference electrodes and three lithium electrodes were used. The cell was designed so that solutions did not come in contact with stopcocks.

The solvent (Matheson, Coleman, and Bell, spectrographic grade) was purified by distillation under reduced pressure at 80°C. The product was found to contain less than 50 ppm water by Karl Fischer titration and had a melting point of 18.58°C.

Lithium chloride (Baker and Adamson) was dried by refluxing thionyl chloride over it for 2 hr. The dried salt was stored in a vacuum dessicator under an atmosphere of dry argon.

The lithium metal (Lithium Corporation of America, 99.9%) was obtained commercially and stored under oil.

Solutions were made either by direct weighing of solute and solvent or by dilution of more concentrated solutions. The solutions were prepared and stored in a glove box under an atmosphere of dry argon. The lithium electrodes were prepared by etching the surface in an HCl solution in DMSO, carefully rinsing with solvent, and then rinsing with a portion of the solution to be used in the cell. The cell was

Table I. Selected physical properties of DMSO

		Reference
Molecular weight	78.13	†
Melting point	18.58°C	(10)
Boiling point	189.0°C	(10)
Dielectric constant, 25°C	48.05	
Density	1.0956 g/cm³	(11)
Entropy of vaporization, 189°C	25.8 cal/mole-°K	
Dipole moment	3.9 Debye	(12)
Debye-Hückel constant, 25°C	2.57 (kg/mole)$^{1/2}$	
30°C	2.57 (kg/mole)$^{1/2}$	
35°C	2.59 (kg/mole)$^{1/2}$	

† Present work.

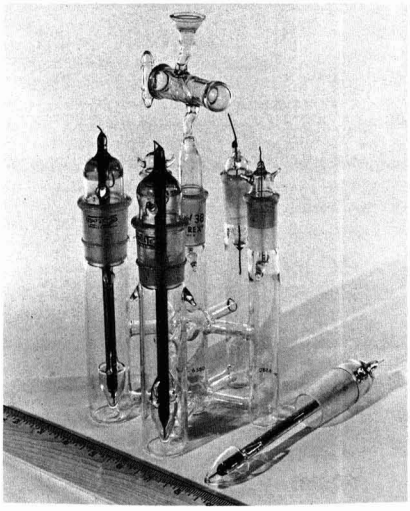

Fig. 1. Five-compartment cell used for emf measurements

* Electrochemical Society Active Member.

assembled, the solution introduced, and the cell was removed from the glove box and suspended in a grounded water bath. Temperature was controlled within ±0.01°C.

On each cell the measuring procedure began 15 min after thermal equilibrium at 25°C had been attained. The measurements were made with an L&N K-3 potentiometer, using carefully calibrated standard cells. The second set of measurements at 25°C was made 1 hr later and, if there was less than 0.1 mv difference between the readings, the temperature was raised to 30° and 35°C, respectively, where the measurements were repeated. The temperature was then reduced to 25°C, and another set of measurements was made. The last measurement at 25°C always agreed within less than 0.1 mv with the earlier measurements at 25° if the temperature cycle was shorter than 12 hr. The bias potential between the reference electrodes was always less than 0.05 mv and for the lithium electrodes was less than 0.1 mv.

The thallium amalgams used in the present studies were all in the concentration order of 10^{-2} mole fraction thallium. The voltage of the cell [1], was "corrected" to solid thallium metal by using the emf data on thallium amalgam concentration cells of Richards and Daniels (14). The relative potentials of the amalgams employed are given in Tables II, III, and IV.

In Tables V, VI, and VII are given the results of the cell measurements at 25°, 30°, and 35°C, respectively. In the first column is given the molality of LiCl in solution. The measured cell voltage, E, and the amalgam are listed in the second and third columns, respectively. The cell voltage "corrected" to solid thallium, E', is given in the fourth column. E' is related to the standard cell potential and the solution concentration by

$$E' = E^{\circ} - \frac{2RT}{\mathbf{F}} \ln m_{\mathrm{LiCl}}\, \gamma_{\mathrm{LiCl}} \qquad [2]$$

where both E° and γ_{LiCl} are unknowns. The usual arbitrary definition is adopted: the activity coefficient of lithium chloride approaches unity as the concentration of lithium chloride approaches zero. The limiting equation proposed by Guggenheim (13) is employed to facilitate extrapolation to infinite dilution, *i.e.*

$$\ln \gamma_{\mathrm{LiCl}} = -\frac{\alpha z_+ |z_-| I^{1/2}}{1 + I^{1/2}} + 2\beta_{\mathrm{LiCl}}\, m_{\mathrm{LiCl}} \qquad [3]$$

Table II. Relative potentials of thallium amalgams at 20°C

Mole fraction Tl[a]	Amalgam	$\mathcal{E}^b$
9.67×10^{-3}	1	0
9.32×10^{-3}	3	−0.00107
1.035×10^{-2}	2	+0.00193
9.71×10^{-3}	4	+0.00012
1		+0.14690

Table III. Relative potentials of thallium amalgams at 30°C

Mole fraction Tl[a]	Amalgam	$\mathcal{E}^b$
9.67×10^{-3}	1	0
9.32×10^{-3}	3	−0.00107
1.035×10^{-2}	2	+0.00199
9.71×10^{-3}	4	+0.00012
1		+0.15091

Table IV. Relative potentials of thallium amalgams at 40°C

Mole fraction Tl[a]	Amalgam	$\mathcal{E}^b$
9.67×10^{-3}	1	0
9.32×10^{-3}	3	−0.00111
1.035×10^{-2}	2	+0.00203
9.71×10^{-3}	4	+0.00012
1		+0.15483

[a] Calculated using molecular weights based on $C^{12} = 12.000$.
[b] Absolute volts.

Table V. Results of cell potential measurements at 25°C

m (moles/kg)	E (volts)	Amalgam	E' (volts)	$E^{o\prime}$ (volts)
0.87877	2.47341	1	2.32451	2.25398
0.30177	2.52252	3	2.37255	2.26417
0.16389	2.54697	4	2.39819	2.26722
0.12450	2.55971	3	2.40974	2.26825*
0.12213	2.56064	3	2.41067	2.26843*
0.08803	2.57327	1	2.42437	2.26930*
0.08775	2.57324	1	2.42434	2.26915*
0.07592	2.57932	4	2.43054	2.26956*
0.05821	2.59230	3	2.44233	2.27055*
0.05821	2.59110	4	2.44232	2.27054*
0.02821	2.62266	4	2.47388	2.27156*
0.01775	2.64319	1	2.49429	2.27164*
0.00988	2.66970	1	2.52080	2.27163
0.00891	2.67465	1	2.52575	2.27182
0.00884	2.67500	1	2.52610	2.27180
0.00768	2.67933	2	2.53236	2.27157
0.00677	2.68436	2	2.53739	2.27072
0.00456	2.70491	1	2.55601	2.27115
0.00383	2.71131	2	2.56434	2.27075
0.00356	2.71687	1	2.56797	2.27099
0.00332	2.71830	2	2.57133	2.27060
0.00275	2.72604	2	2.57907	2.26958
0.00190	2.74340	2	2.59643	2.26900
0.00178	2.74803	1	2.59913	2.26849
0.00089	2.77455	2	2.62758	2.26288
0.00084	2.77662	2	2.62965	2.26208
0.00045	2.79921	2	2.65224	2.25358

* Data used in least squares analysis.

Table VI. Results of cell potential measurements at 30°C

m (moles/kg)	E (volts)	Amalgam	E' (volts)	$E^{o\prime}$ (volts)
0.30177	2.52102	3	2.36904	2.25885
0.16389	2.54550	4	2.39471	2.26154*
0.12450	2.55880	3	2.40682	2.26296*
0.12213	2.55951	3	2.40753	2.26291*
0.07592	2.57825	4	2.42746	2.26378*
0.05821	2.59156	3	2.43958	2.26492*
0.05821	2.59039	4	2.43960	2.26494*
0.02821	2.62241	4	2.47162	2.26591*
0.00988	2.67002	2	2.52110	2.26576
0.00768	2.67988	2	2.53096	2.26575
0.00677	2.68496	2	2.53604	2.26488
0.00456	2.70393	2	2.55501	2.26489
0.00383	2.71222	2	2.56330	2.26474
0.00357	2.71765	1	2.56674	2.26478
0.00275	2.72716	2	2.57824	2.26352
0.00190	2.74477	2	2.59585	2.26315
0.00178	2.74936	1	2.59845	2.26226
0.00089	2.77639	2	2.62747	2.25661
0.00084	2.77798	2	2.62906	2.25529
0.00045	2.80111	2	2.65219	2.24679

* Data used in least squares analysis.

Table VII. Results of cell potential measurements at 35°C

m (moles/kg)	E (volts)	Amalgam	E' (volts)	$E^{o\prime}$ (volts)
0.30177	2.51946	3	2.36550	2.25310
0.16389	2.54423	4	2.39148	2.25581*
0.12450	2.55773	3	2.40377	2.25726*
0.12213	2.55842	3	2.40446	2.25717*
0.07592	2.57747	4	2.42472	2.25810*
0.05821	2.59072	3	2.43676	2.25902*
0.05821	2.58964	4	2.43689	2.25915*
0.02821	2.62214	4	2.46939	2.26013*
0.00988	2.67039	1	2.51752	2.25989
0.00768	2.68038	2	2.53032	2.23987
0.00677	2.68587	2	2.53581	2.25950
0.00383	2.71319	2	2.56313	2.25879
0.00357	2.71865	1	2.56578	2.25878
0.00275	2.72829	2	2.57823	2.25747
0.00190	2.74617	2	2.59611	2.25683
0.00178	2.75068	1	2.59781	2.25603
0.00089	2.77775	2	2.62769	2.24637
0.00084	2.77939	2	2.62933	2.24515
0.00045	2.80276	2	2.65270	2.23982

* Data used in least squares analysis.

Here, α = Debye-Hückel constant, I = ionic strength $= \frac{1}{2} \sum_i z^2_i m_i$, and β_{LiCl} = constant, independent of molality. From [2],

$$E' - \frac{\alpha z_+ |z_-| I^{1/2}}{1 + I^{1/2}} \left(\frac{2RT}{\mathbf{F}} \right) + \frac{2RT}{\mathbf{F}} \ln m = E^{o\prime} = E^{\circ} - \frac{4RT}{\mathbf{F}} \beta_{\mathrm{LiCl}}\, m \qquad [4]$$

where Eq. [4] defines $E^{o\prime}$. The function $E^{o\prime}$ is listed in the fifth column of Tables V, VI, and VII.

By constructing a plot of $E^{o\prime}$ *vs.* m, according to Eq. [4], one should obtain a straight line. Extrapolating to $m \rightarrow 0$, one can obtain E^{o} and then γ_{LiCl}, for other concentrations at which the cell emf is measured.

$E^{o\prime}$ is plotted *vs.* molality in Fig. 2, 3, and 4. The emf-s of the cells were found to be well behaved for concentrated solutions of lithium chloride. As the concentration is decreased, the function $E^{o\prime}$ becomes a linear function of molality. The sharp decrease of $E^{o\prime}$ at concentrations below $2 \times 10^{-2} M$ was quite unexpected. This behavior could not be explained by random scatter of data; the decrease persisted at all three temperatures. Several independent sets of solutions, made by both methods, were used, and the data was found to be reproducible and not due to errors in solutions concentration. A reaction in the cell could not have caused this behavior because the cell voltage was constant over the period of the temperature cycle. After 12-hr the lithium electrodes became discolored, and the cell potential began to decrease steadily due to the reaction

$$Li(s) + TlCl(soln) \rightarrow Tl(s) + LiCl(soln) \quad [5]$$

The unexpected decrease of $E^{o\prime}$ occurred in solutions where the concentration of LiCl was approaching that of TlCl. The solubility product of TlCl in dimethyl sulfoxide is 5×10^{-7} (8). Since TlCl must be kept away from the lithium electrode, where it will react, a concentration gradient of TlCl exists in the cell. The cell potential will be lower than expected when there is diffusion of the sparingly soluble salt from the reference electrode. At higher concentrations of LiCl, it would be expected that the nonuniform concentration distribution would be of no effect, and the effect should become greater as the solution concentration of LiCl decreases. The departure of the potential from the linear extension of the line obtained by least squares fit of the data at higher concentrations can be, to a good approximation, explained by quantitative consideration of the effect of diffusion of TlCl (15).

With the foregoing consideration in mind, the extrapolation to infinite dilution was made by fitting a least squares line to the data in the linear region. The results of the data analysis are summarized in Table VIII for the 95% confidence level. From these results were calculated ΔG^{o}, ΔH^{o}, and ΔS^{o} for the cell reaction. These thermodynamic functions are given in Table IX.

The same calculations may be carried out for aqueous solutions. The quantity $\Delta\bar{G}^{o}$ for the transfer at 25°C,

$$LiCl(\text{soln in DMSO}, \gamma_{\pm} = 1) + 55.55 \text{ moles } H_2O \rightarrow LiCl(\text{soln in } H_2O, \gamma_{\pm} = 1) + 12.799 \text{ moles DMSO} \quad [6]$$

is found to be

$$\Delta\bar{G}^{o} = -4.93 \text{ kcal/mole}$$

The entropy of transfer at this temperature is calculated to be +24.8 cal/°K-mole, after correcting for the difference in partial molal volume of the two solvents.

Activity coefficients were determined as a function of concentration at the measured temperatures. Activity coefficients obtained from the smoothed data are given in Table X at rounded concentrations.

The behavior of the activity coefficient of LiCl indicates that it is a completely dissociated salt in very dilute solutions. We arrive at this interpretation from the value of β_{LiCl} which is positive, as in aqueous solutions. In aqueous solutions, a negative value of β is interpreted as an indication of ion pairing (18). Although the magnitude of β_{LiCl} in dimethyl sulfoxide is larger than in water, we attach less significance to the magnitude than to the sign. Further interpretation

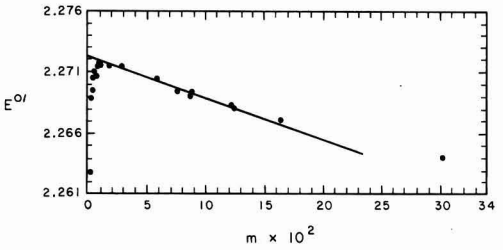

Fig. 2. Extrapolation of emf data to infinite dilution at 25°C.

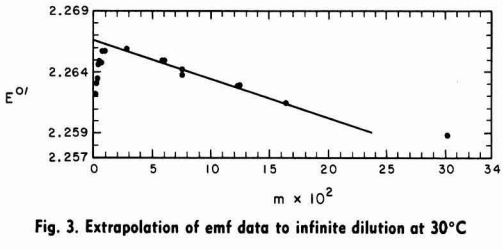

Fig. 3. Extrapolation of emf data to infinite dilution at 30°C

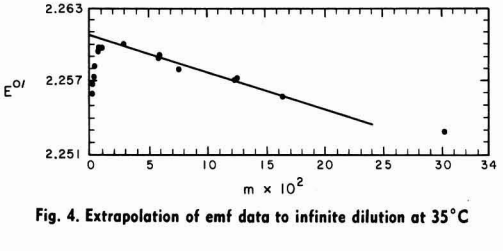

Fig. 4. Extrapolation of emf data to infinite dilution at 35°C

Table VIII. Standard cell potentials at 25°, 30°, and 35°C

T (°K)	E^{o} (volts)	β_{LiCl} (kg/mole)
298.15	2.27234 ± 0.00045	0.325 ± 0.040
303.15	2.26665 ± 0.00072	0.298 ± 0.052
308.15	2.26083 ± 0.00064	0.286 ± 0.045

Table IX. ΔG°, ΔS°, and ΔH° for the reaction

$\gamma_{\pm}=1$

Li(s) + TlCl(s) + 12.799 moles DMSO ⇄ LiCl (soln in DMSO) + Tl(s)

T (°K)	ΔG^{o} (kcal/mole)	ΔS^{o} (cal/°K-mole)	ΔH^{o} (kcal/mole)
298.15	−52.40 ± 0.01	−26 ± 2	−60.2 ± 0.6
303.15	−52.27 ± 0.02	−26 ± 4	−60.2 ± 0.6
308.15	−52.14 ± 0.01	−26 ± 2	−60.2 ± 0.6

Table X. Activity coefficients of lithium chloride at 25°, 30°, and 35°C

m moles/kg	$-\ln \gamma_{LiCl}$ 25°	30°	35°
0.005	0.152	0.160	0.165
0.010	0.220	0.230	0.230
0.015	0.270	0.275	0.275
0.020	0.306	0.310	0.310
0.025	0.335	0.339	0.340
0.030	0.360	0.364	0.365
0.035	0.383	0.385	0.392
0.040	0.404	0.405	0.414
0.045	0.422	0.423	0.430
0.050	0.440	0.440	0.447
0.060	0.470	0.470	0.475
0.080	0.511	0.520	0.525
0.100	0.548	0.560	0.565
0.120	0.582	0.592	0.600

must await further data on other electrolytes in dimethyl sulfoxide.

The activity coefficients from the present study (25°) are consistently higher than those reported by Dunnett and Gasser (18.5°) obtained from freezing point depression studies (4). According to our measurements, correction for temperature would increase the discrepancy. Analysis of the results of Dunnett and Gasser according to the method suggested by Brown and Prue (16)[1] yields a value $\beta_{LiCl} = -2.11$. The reasons for the disagreement with the present study are not understood. It seems possible that traces of water may have caused anomalous freezing point readings in the dilute solutions, those most important for the determination of β_{LiCl}. Also, the value of the cryoscopic constant (4.36) used by Dunnett and Gasser is subject to question. This value reported by Lindberg, Kenttämaa, and Nissema (17) is based on cryoscopic measurements on solutions of benzene in dimethyl sulfoxide, but the most dilute solution used was 0.88*M*. If one used the cryoscopic constant of Skerlak *et al.* (5), *i.e.*, 3.97, for the above analysis, the value of β_{LiCl} becomes positive. The value of 3.97 is also consistent with the data of Lindberg *et al.*

According to the present results the free energy and entropy of transfer of LiCl from dimethyl sulfoxide to water are in the direction one would predict from the relative dielectric constant of the two solvents. Calculations of the dielectric constant effect according to the Born equation do not account quantitatively for the free energy and entropy of transfer. Similar conclusions were reached for several other solvents by Strehlow (19). The heat of transfer of LiCl from DMSO to H_2O is calculated to be +2.61 kcal. This may be compared to the recent measurements of the heats of transfer of several iodides from DMSO to H_2O (7), for which the heats of transfer, as expected, are larger, in the order of +10 kcal.

Acknowledgment

This work was supported in part by the Electrochemistry Branch Naval Ordnance Laboratory, Corona, and in part by the Atomic Energy Commission.

[1] In these calculations we used for the dielectric constant 49.15 (10), 18.55°C as the melting point of the solvent (4), 1.1000 g/cm³ for the density (11), and 4.36 (17) for the molal cryoscopic constant.

Manuscript received Aug. 28, 1967; revised manuscript received Oct. 16, 1967. This paper was presented at the Dallas Meeting, May 7-12, 1967, as Abstract 133.

Any discussion of this paper will appear in a Discussion Section to be published in the December 1968 JOURNAL.

REFERENCES

1. J. Kenttämaa, *Suomen Kemistilehti,* **B33**, 180 (1960).
2. C. Melendres (Dissertation), University of California, September, 1965.
3. I. M. Koltoff and T. B. Reddy, *Inorg. Chem.*, **1**, 189 (1962).
4. J. S. Dunnett and R. P. H. Gasser, *Trans. Faraday Soc.*, **61**, 922 (1965).
5. T. Skerlak, B. Ninkov, and V. Sislov, *Bull. Soc. Chim. Sarajevo,* (Yugoslavia), **11**, 34 (1962).
6. M. D. Archer and R. P. H. Gasser, *Trans. Faraday Soc.*, **62**, 3451 (1966).
7. E. M. Arnett and D. R. McKelvey, *J. Am. Chem. Soc.*, **88**, 2598 (1966).
8. D. R. Cogley and J. N. Butler, *This Journal,* **113**, 1074 (1966).
9. W. H. Smyrl and C. W. Tobias, *ibid.*, **113**, 754 (1966).
10. H. L. Schläfer and W. Schaffernicht, *Angew. Chem.*, **72**, 618 (1960).
11. R. G. LeBel and D. A. I. Goring, *J. Chem. Engr. Data,* **1**, 100 (1962).
12. F. A. Cotton and R. Francis, *J. Inorg. Nuclear Chem.*, **17**, 62 (1961).
13. E. A. Guggenheim, *Phil. Mag.*, **19**, 588 (1935).
14. T. W. Richards and F. Daniels, *J. Am. Chem. Soc.*, **41**, 1732 (1919).
15. W. H. Smyrl and C. W. Tobias, "The Effect of Diffusion of a Sparingly Soluble Salt on the EMF of a Cell without Transference," *Electrochim. Acta,* **13** (1968).
16. P. G. M. Brown and J. E. Prue, *Proc. Roy. Soc. (London)*, **A232**, 320 (1955).
17. J. J. Lindberg, J. Kenttämaa, and A. Nissema, *Suomen Kemistilehti,* **B34**, 98 (1961).
18. E. A. Guggenheim, "Thermodynamics," 4th ed., p. 361, North-Holland, Amsterdam, (1959).
19. H. Strehlow, *Z. Elektrochem.*, **56**, 827 (1952).
20. W. H. Smyrl (Dissertation), University of California, Berkeley, 1966.

Technical Note

Effects of Probe Position on Potentiostatic Control during the Breakdown of Passivity

D. C. Mears[1] and G. P. Rothwell

Department of Metallurgy, University of Cambridge, Cambridge, England

The breakdown of passivity of stainless steels with the formation of brightened pits in chloride-containing solutions has received considerable attention since the observations of Brennert(1). More recently, similar breakdown of passivity has been recorded for a wide variety of passive alloys in solutions in which the anion concentration and anode potential are sufficiently high(2). It is of practical interest to assess the natural resting potential of such alloys, and to compare it with the breakdown potential determined during the measurement of polarization curves in deaerated solutions. If the breakdown potential is considerably higher than the highest natural resting potential of an alloy in a given chloride solution, the alloy is unlikely to undergo chloride breakdown in use in that solution(3). It is essential, however, to know and to control the anode potential precisely during the polarization measurements. We have measured anode potentials simultaneously with two Luggin probes in different positions and find that electrode geometry strongly influences

[1] Present address: Nuffield Department of Orthopaedic Surgery, University of Oxford, Oxford, England.

the potential recorded at different points on the anode. Furthermore, prior to and during breakdown of passivity the electrode potential of the pitting region may fall rapidly to *ca.* 100 mv more negative than the controlled electrode potential at the passive anode surface.

Electrical analogues have also illustrated these and other problems of electrode geometry(4). Somewhat similar observations have previously been made on the localization of attack on naturally corroding specimens (5-7).

Electrochemical Experiments

Specimens of stainless steel (18Cr-10Ni-3Mo) and of Vitallium (30Cr-5Mo, bal.Co) were prepared by masking the borders with Picien wax or Lacomit stopping-off lacquer. The anode potential was controlled potentiostatically using a Luggin probe at the center of the specimen. Additional probes were positioned at the masked edge and at the center of the specimen (Fig. 1); the pd between these two saturated calomel reference electrodes was measured using an electronic millivoltmeter. The area of the anode was *ca.* 1 cm^2, and that of the concentric cathode *ca.* 10 cm^2. Solutions of 0.2M and 1M sodium chloride, and 4M magnesium chloride were deaerated(8) until the specimen potential had fallen below *ca.* — 350 mv(nhe). Potentiostatic anodic polarization curves were then measured in 50 mv, 10 min steps for both alloys, in the three solutions; at each step the pd between the two non-controlling probes was also measured.

While a specimen is passive, the pd between the probes at edge and center is negligible (< 2 mv), except during the current transient after each increase in potential, when the current initially rises, then falls due to film thickening(9), and the pd between the probes may rise to *ca.* 20 mv (the edge probe being positive), falling rapidly to zero. As the specimen undergoes film breakdown, the transient and steady potential differences between the two probes increase to *ca.* 100 mv and 40 mv, respectively. Breakdown of passivity, with the formation of hemispherical brightened pits, occurs predominantly at the masked edge of the specimen. As the anode cd increases further the pd between middle and edge probes ceases to rise, and may decrease, falling below zero in many cases. Figure 2 shows a typical polarization curve for Vitallium in 0.2M sodium chloride solution, with a probe pd/potential curve superimposed. For anode potentials below *ca.* 200 mv, corresponding to passive current densities of less than 10 $\mu A/cm^2$, the pd between the edge and the middle is negligible. At higher potentials, rapid breakdown occurs with a large increase in current. The pd between edge and middle rises rapidly to *ca.* 60 mv. At still higher anode potentials, the steady pd decreases rapidly and ultimately changes sign.

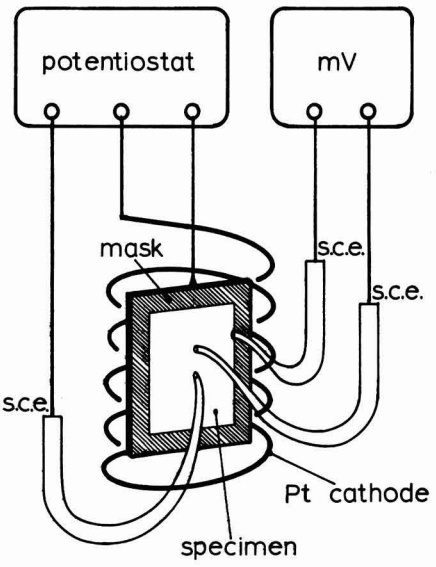

Fig. 1. Apparatus for electrochemical experiments

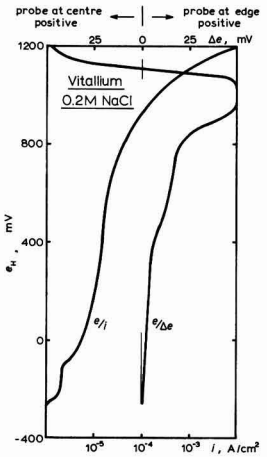

Fig. 2. Anodic polarization curve (*e/i*) and curve for edge/center potential difference (*e/Δe*) for Vitallium in 0.2M sodium chloride solution.

The edges of some specimens were coated with Picien wax so that the wax was flush with the face of the specimen. Polarization curves and pd measurements gave results similar to those for earlier experiments.

The above experiments were repeated with the potential of the edge, rather than that of the middle controlled potentiostatically. With specimens at potentials at which they exhibit passive behavior, the pd from middle to edge is negligible. At higher anode potentials chloride breakdown occurs primarily at the center of the specimen. The probe at the middle of the specimen becomes positive to that at the edge by *ca.* 60 mv.

Anodic polarization curves and pd measurements were repeated in rapidly stirred solutions: breakdown of passivity occurred with random pitting, and the electrode potentials at different points on the anode differed by less than 5 mv.

Discussion

Potential variations in natural corrosion environments have been measured by previous workers for many different systems. The work of Bianchi(10) deserves particular attention. In the present work, the polarization experiments with measurement of potential variation across the controlled anode show that electrode geometry may strongly influence the observed behavior of specimens under potentiostatic control. For specimens with surface area of *ca.* 1 cm^2 determinations of the breakdown potential may be in error by ± 50 mv; for larger specimens, greater error could occur. The site of breakdown may be altered from random pitting to preferential edge attack. Very high rates of flow tend to minimize the effects of electrode geometry and may cause a return to random pitting behavior. These effects may also be minimized when the anode and counter electrode are opposed parallel surfaces of the same extent, such as two plates or two concentric cylinders, with an insulating barrier extending perpendicularly between their ends, as has been suggested by Piontelli(11).

For film growth on a passive metal under potentiostatic conditions, in a cell giving anything other than perfect uniformity of potential, the rate of the anodic

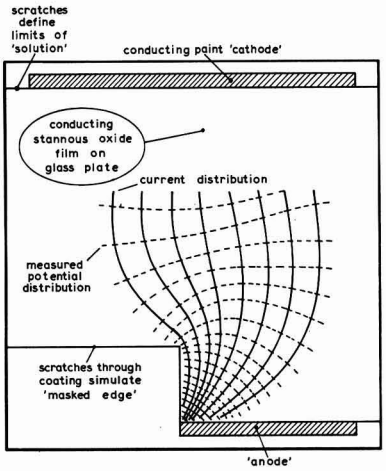

Fig. 3. Potential and current distributions for an electrical analogue of the masked edge on a passive specimen.

process is correspondingly nonuniform. Figure 3 shows the current distribution in an electrical analogue of the masked edge of a passive specimen(4). When the electrode potential, controlled by a probe at the center of the specimen is increased abruptly, the cd at the central region also increases abruptly, then decreases as the passive film thickens. At regions remote from the controlling probe, in which the current distribution leads to current densities higher than those on the bulk of the specimen, the transient cd must also be greater than that near to the probe, although the electrode potential appears to be lower (*i.e.*, potential in the solution more positive), until the equilibrium film thickness has been reached. The transient metal dissolution and film formation processes also occur faster in these regions. This variation in rates of formation may itself lead to structural variations in the film in different regions of the specimen, and to enhanced take-up of aggressive anions into the film, leading ultimately to the observed initial breakdown in these regions. Very high rates of flow of solution then lead to more random attack by increasing the (diffusion controlled) cd near the probe during the transient period, shortening the transient and minimizing differences of potential across the specimen. Similarly, if the controlling probe is placed at the masked edge of the specimen, where the natural current distribution leads to the highest transient current densities, the effect of such transients in determining the site of breakdown is minimized, and random attack is usually observed.

After high potential breakdown of passivity in natural environments, the corrosion process is under cathodic control, and the potential in the pit decreases (b Fig. 4). Consequently, at the lowered mixed potential the pit may be gradually repassivated. If the pit becomes repassivated, the mixed potential may again rise until breakdown of passivity occurs elsewhere on the specimen. Once a pit has formed breakdown in the adjacent area is less likely because of the change in potential distribution. Random breakdown is thus observed in this case.

If the potential is under the control of a cathodic reaction which is not readily polarized, the potential at the pit site falls only slightly after the breakdown of passivity (c Fig. 4), so that adjacent, and ultimately general breakdown can ensue.

For passive specimens under potentiostatic control, with this type of nonuniform current distribution the potentiostat supplies to the center of the specimen the cd required by the anode, and to the edge areas a cd proportionally higher, as dictated by the geometry

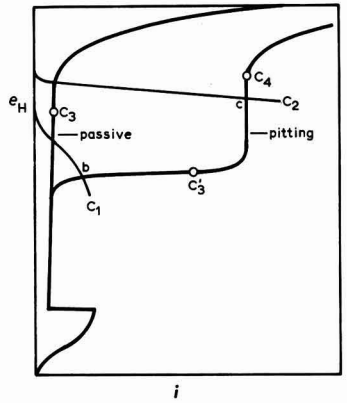

Fig. 4. Schematic anodic polarization curves for a typical passive alloy which undergoes high potential breakdown. Curve C_1 represents the behavior of a natural cathode and C_2 that of a less polarizable cathodic reaction. Points C_3, C'_3 represent the behavior under potentiostatic control of a system with small pits, and C_3, C_4 the behavior of the same system when the pits have become large enough to affect current distribution at the probe.

of the system. When pitting starts, provided that the total current in this area is less than that available in the distribution the pitting can proceed at its limiting cd at the same potential as the bulk of the specimen. However when the pitting area increases so that the current requirement exceeds that available, then the potential and the pitting cd fall so that the total current requirement can be maintained. Thus the electrode potential may fall during pitting to a point such as C'_3 while the bulk of the specimen may be at C_3. The fact that the film resistance decreases greatly with the onset of pitting may lead to a decreased iR drop across the film, leading to a still lower measured electrode potential of the metal.

As the pitting area grows larger it may influence the current distribution at the center of the specimen. If this occurs, the pitting current may increase by drawing from the main current distribution, the potentiostat supplying more current as required to maintain the passive potential. Once the pitting current density again reaches the limiting cd, the pitting potential, which is virtually under galvanostatic control, may continue to rise toward C_4, giving ultimately the observed change in sign of the difference in potential between the pitting and passive regions. We stress therefore that potentiostatic control does not necessarily insure uniformity of potential at the surface of the working electrode.

Manuscript received Aug. 1, 1966; revised manuscript received Sept. 19, 1967.

Any discussion of this paper will appear in a Discussion Section to be published in the December 1968 JOURNAL.

REFERENCES

1. S. Brennert, *Korros. Metallsch.*, **12**, 46 (1936).
2. T. P. Hoar, D. C. Mears, and G. P. Rothwell, *Corros. Sci.*, **5**, 279 (1965).
3. T. P. Hoar and D. C. Mears, *Proc. Roy. Soc.*, **A294**, 486 (1966).
4. D. C. Mears, Ph.D. Thesis, University of Cambridge 1965.
5. U. R. Evans, *J. Iron St. Inst.*, **141**, 219P (1940).
6. U. R. Evans and T. P. Hoar, *Proc. Roy. Soc.*, **A137**, 343 (1932).
7. R. H. Brown and R. B. Mears, *Trans. Electrochem. Soc.*, **74**, 495 (1938).
8. D. C. Mears and G. P. Rothwell, *J. Sci. Inst.*, **42**, 446 (1965).
9. T. P. Hoar, "Anodic Behaviour of Metals" in "Modern Aspects of Electrochemistry," No. 2, J. O'M. Bockris, Editor, Butterworths, London (1954).
10. G. Bianchi, *Metallurg. ital.*, **45**, 123, 323 (1953).
11. R. Piontelli, *Z. Elektrochem.*, **59**, 778 (1955).

JOURNAL OF THE ELECTROCHEMICAL SOCIETY

SOLID STATE SCIENCE

JANUARY 1968

Journal of The Electrochemical Society *is the fundamental research journal serving the interdisciplinary interests of chemistry, physics, electronics, biology, medicine, and engineering as they pertain to electrochemistry and to electrochemical phenomena. Written for the research scientist in industry, government, the independent laboratory and the university, it publishes contributed Technical Papers, Technical Notes and Brief Communications describing current basic research of original character, and is edited in two sections: 1)* ***Electrochemical Science*** *including such areas as batteries, fuel cells, corrosion and corrosion mechanisms, electrothermics and metallurgy, electrodeposition, electroorganic reactions and phenomena, and allied work of theoretical electrochemical nature. 2)* ***Solid State Science*** *including such areas as dielectrics and insulation, electrothermics and metallurgy, semiconductors, luminescence and related solid state investigations.*

Electret Phenomenological Theory Presented in Linear Systems Formalism

Donald E. Tilley

Department of Physics, Collège militaire royal de Saint-Jean, Saint-Jean, Québec, Canada

ABSTRACT

Standard techniques for the analysis of linear systems are applied to the phenomenological theory of the electret effect, as developed by Wiseman and Feaster and extended by Perlman and Meunier. A generalized electric susceptibility is introduced which allows electret behavior at constant temperature to be characterized by two functions, the impedance and the short-circuit current. Asch's electret theory is shown to be equivalent to the assumption that the generalized susceptibility is an exponential function.

A phenomenological theory of electrets, based on Gross's two-charge theory (1) and the superposition principle used by Wiseman and Feaster (2) as well as by Perlman and Meunier (3), has been given by the author in a previous paper (4) in a form which allows a simple and unified treatment of several electret problems. In the present paper, this theory is reviewed and amplified with the presentation now given using the most familiar tool for the analysis of linear systems, the Laplace transform. Natural generalizations of the electric susceptibility and the dielectric constant are introduced, and the role of these quantities in electret phenomenological theory is emphasized. Finally, it is shown that this theory includes, as a very special case, the electret theory of Asch (5).

Generalized Electric Susceptibility

The polarization of a dielectric with a time dependent internal electric field $E(t)$ depends not only on the present value of the field but also on the history of the dielectric. It is convenient to regard the polarization $P(t)$ as a sum

$$P(t) = P_i(t) + P_s(t) \qquad [1]$$

where $P_i(t)$ is the polarization which responds practically instantaneously to the applied field, and $P_s(t)$ is the slow response that is determined by fields that have existed at all previous instants up to the time t. The method of measurement will determine in a given experiment what response should be classified as instantaneous. In any case, in a linear isotropic dielectric the fast response is given by

$$P_i(t) = \chi_i E(t) \qquad [2]$$

where χ_i/ϵ_0 is the electric susceptibility characterizing the instantaneous response. (MKS units are used throughout this paper.)

The experiments of Wiseman and Feaster (2) and of Perlman and Meunier (3) show that, at constant temperature, the polarization of Carnauba wax is a linear superposition of the contributions furnished by electric fields applied in the past. This superposition principle can be expressed in several different but equivalent ways. The formulation of the superposition principle given in this paper allows the introduction of natural generalizations of the electric susceptibility and the dielectric constant. We assume that the slow polarization response of a dielectric maintained at constant temperature can be characterized by a response function $\chi_s(t)$ such that a field $E(t)$ applied between the times T and $T + dT$ produces a polarization which, at a later time t, is $\chi_s(t-T)E(T)dT$. The linear superposition of contributions from all previous electric fields gives the polarization

$$P_s(t) = \int_{-\infty}^{t} \chi_s(t-T)E(T)dT \qquad [3]$$

It is assumed that $\chi_s(t) = 0$ for $t < 0$ and that $\chi_s(t) \to 0$ as $t \to \infty$. The response function $\chi_s(t)$ is to be determined empirically and is often assumed to be a sum of exponential decays. Equations [1]-[3] yield, for the total polarization, the expression

$$P(t) = \int_{-\infty}^{t+} \chi(t-T)E(T)dT \qquad [4]$$

where

$$\chi(t) = \chi_i\delta(t) + \chi_s(t) \qquad [5]$$

and $\delta(t)$ is the Dirac delta function [$\int_{-\infty}^{+\infty} \delta(t) = 1$ and $\delta(t) = 0$ for $t \neq 0$]. The relationship between $\chi(t)$ and the response function $\pi(t)$ used by previous workers (2, 3) is $\chi(t) = d\pi/dt$. In a pioneering paper on dielectric after-effects (6), Gross expressed the after-current as a superposition of contributions from previous voltage changes and used a response function $\phi(t)$ which is proportional to $\chi_s(t)$.

It is the function $\chi(t)/\epsilon_0$ which merits the name "the generalized electric susceptibility." The corresponding generalized dielectric constant is $K(t)/\epsilon_0$ where

$$K(t) = \epsilon_0\delta(t) + \chi(t) \qquad [6]$$

as can be seen by examining the relationship between the electric displacement $D(t)$ and the electric field. The electric displacement is defined by

$$D(t) = \epsilon_0 E(t) + P(t) \qquad [7]$$

Now using Eq. [4], [6], and [7] we obtain

$$D(t) = \int_{-\infty}^{t+} K(t-T)E(T)dT \qquad [8]$$

which shows that it is the function $K(t)$ which enables the electric displacement to be expressed as a superposition of contributions from previous electric fields.

The convolution relationships given by Eq. [3], [4], and [8] in the time domain take on a particularly simple form when one takes either the Fourier transform or the two-sided Laplace transform to pass to the domain of complex frequency s. Since the transform of the convolution of two functions is the product of the transforms, the transform of the polarization is simply the product of the transform of the generalized electric susceptibility with the transform of the electric field.

In initial value problems, it is convenient to use the one-sided Laplace transform with the lower limit $0-$ (7). Using the bar notation for such transforms we define

$$\bar{E}(s) = \int_{0-}^{\infty} E(t)e^{-st}dt \qquad [9]$$

It is necessary to single out the part, $P_b(t)$, of the slow polarization response that arises from electric fields which have existed before $t = 0$. Equation [3] gives

$$P_b(t) = \int_{-\infty}^{o-} \chi_s(t-T)E(T)\,dT \qquad [10]$$

Equations [4] and [10] now yield the simple algebraic relation between Laplace transforms

$$\overline{P}(s) = \overline{P}_b(s) + \overline{\chi}(s)\overline{E}(s) \qquad [11]$$

and Eq. [5], [6], [8], and [10] give

$$\overline{D}(s) = \overline{P}_b(s) + \overline{K}(s)\overline{E}(s) \qquad [12]$$

Equations [11] and [12] show that, in the complex frequency domain, except for the appearance of the term $P_b(s)$, the relationship between the fields and the generalized susceptibility and dielectric constant is the same as the relationship in time domain between the fields and the usual susceptibility and dielectric constant when the response is considered to be instantaneous.

Electret Impedance

The formalism introduced in the preceding section can be used to present the solution to the electret field equations in the familiar language of circuit analysis. At the interface of an electrode carrying a real surface charge density $\sigma(t)$ with a dielectric within which there is an electric displacement $D(t)$, Gauss's law gives

$$D(t) = \sigma(t) \qquad [13]$$

Differentiation of Eq. [13] yields

$$dD(t)/dt = J(t) - cE(t) \qquad [14]$$

where $J(t)$ is the conduction current density within the electrode and $cE(t)$ is the ohmic conduction current within the dielectric.[1] Taking Laplace transforms we obtain from Eq. [14]

$$s\overline{D}(s) - D(\mathrm{O}-) = \overline{J}(s) - c\overline{E}(s) \qquad [15]$$

Using Eq. [12], the solution to Eq. [14] can be written in the transparent and useful form

$$\overline{E}(s) = \overline{z}(s)[\overline{J}(s) - \overline{J}_b(s)] \qquad [16]$$

where

$$\overline{z}(s) = 1/[c + s\overline{K}(s)] \qquad [17]$$

and

$$\overline{J}_b(s) = s\overline{P}_b(s) - D(\mathrm{O}-) \qquad [18]$$

The electret impedance, in the complex frequency domain, is determined by $\overline{z}(s)$ which is seen to be a simple function of the conductivity c and the generalized dielectric constant $\overline{K}(s)$.

The quantity $\overline{J}_b(s)$ is the value of $\overline{J}(s)$ when $\overline{E}(s) = 0$ and therefore is named the short-circuit current density. All the effects of the past history (at constant temperature) of the dielectric are included in this term. A useful expression for the evaluation of $\overline{J}_b(s)$ is obtained by using Eq. [1], [2], [7], and [10], together with Eq. [18] to yield

$$\overline{J}_b(s) = s\overline{P}_b(s) - P_b(\mathrm{O}-) - [\epsilon_0 + \chi_i]E(\mathrm{O}-) \qquad [19]$$

In Eq. [19], the quantity $s\overline{P}_b(s) - P_b(\mathrm{O}-)$ is simply the Laplace transform of $dP_b(t)/dt$.

Several applications of Eq. [16]-[18] are given in ref. (4). An important special case arises when the generalized susceptibility function is assumed to involve a sum of two exponentials

$$\chi_s(t) = Ae^{-\alpha t} + Be^{-\beta t} \qquad [20]$$

for $t \geq 0$. Such a function, with constants A, B, α, and β determined empirically, has been found adequate to give good agreement with experimental measurement of the charge decay at constant temperature of Carnauba wax electrets (2-4). For such a $\chi_s(t)$, it is easy to give a simple equivalent circuit for a dielectric slab (4).

Asch's Theory as a Special Case

Instead of assuming a superposition principle, Asch (5) postulates that the polarization $P_s(t)$ satisfies the first order linear differential equation

$$dP_s(t)/dt = -\alpha[P_s(t) - kE(t)] \qquad [21]$$

with an initial condition,

$$P_s(\mathrm{O}) = P_o \qquad [22]$$

It is interesting to notice that Asch's equations, Eq. [21] and [22], are equivalent to a very special case of the general theory developed in this paper, the case where $\chi_s(t)$ is (for $t \geq 0$) the single exponential function

$$\chi_s(t) = \alpha k e^{-\alpha t} \qquad [23]$$

with the initial polarization given by

$$P_b(\mathrm{O}) = P_o \qquad [24]$$

In this case Eq. [3] and [10], together with Eq. [23] and [24] yield

$$P_s(t) = e^{-\alpha t}P_o + \int_o^t k\alpha e^{-\alpha(t-T)}E(T)\,dT \qquad [25]$$

Now using the familiar rules for the differentiation of an integral it is easy to verify that the $P_s(t)$ given by Eq. [25] is the solution to Asch's Eq. [21] and [22].

In applying his equations to the case of an electret which is polarized at one temperature and then cooled and maintained, for times $t \geq 0$, at a constant final temperature, Asch implies that the effect of the temperature change can be described very simply as follows. For a given value of the initial polarization P_o at the final temperature, the subsequent electret behavior is independent of the temperatures encountered before $t = 0$ and therefore is the same as if the electret had been maintained always at the final temperature. With this assumption, the polarization $P_s(t)$ given by Eq. [25] is, for $t \geq 0$, the common prediction of both Asch's theory and the special case of the superposition principle, Eq. [3], which arises when $\chi_s(t)$ is the exponential function given in Eq. [23].

Acknowledgment

The author wishes to thank Professor M. M. Perlman for stimulating discussions and for reading the manuscript.

Manuscript received Aug. 30, 1967. This paper was presented at the Electrets Symposium at the Chicago Meeting, Oct. 15-19, 1967, as Abstract 120.

Any discussion of this paper will appear in a Discussion Section to be published in the December 1968 JOURNAL.

[1] It is assumed that the dielectric is homogeneous and that, within the dielectric, the fields E, D, P are uniform.

REFERENCES

1. B. Gross, *Phys. Rev.*, **66**, 26 (1944).
2. G. Wiseman and G. Feaster, *J. Chem. Phys.*, **26**, 521 (1957).
3. M. M. Perlman and J. L. Meunier, *J. Appl. Phys.*, **36**, 420 (1965).
4. D. E. Tilley, *ibid.*, **38**, 2543 (1967).
5. G. Asch, *C. R. Acad. Sci. (France)*, **256**, 5302 (1963).
6. B. Gross, *Phys. Rev.*, **57**, 57 (1940).
7. F. F. Kuo, "Network Analysis and Synthesis," p. 121, John Wiley & Sons, Inc., New York (1962).

The Electret Effect in Ice

J. D. Cross

University of Manchester, Institute of Science and Technology, Manchester, England

ABSTRACT

The electret behavior of polycrystalline and single crystal ice is investigated by means of measurements of the dipole moment of the samples, the currents flowing during charging and discharging, and the potential distribution within the sample. For comparison, measurements are made of the persistent dipole moment of tetradecanol, carboxylic acid C_{20}, and paraffin wax. The results show that in these substances the build-up and decay of space charges contribute to the volume polarization.

The electret effect has been mainly studied in complex materials; although such materials have shown the electret effect very strongly their complexity is a severe hindrance to workers hoping to identify the mechanisms of the electret effect. A suitable material for a study of the mechanisms of electret formation should have a known simple structure, the normal conduction processes should be known, and it should be possible to produce samples of high purity in both polycrystalline and single crystal states. All these conditions are fulfilled by ice, and therefore it was chosen as the principal subject for this investigation. To determine the effect of internal structure on the electret effect behavior measurements were also made on samples of 1-tetradecanol, carboxylic acid C_{20}, and paraffin wax.

Experimental Methods

The quantities measured in this investigation were the macroscopic dipole moment of the electrets, the currents flowing during charging and discharging of the electrets, and the potential distribution within the electrets. All samples were disks 12 mm in diameter and 3 mm thick. Polycrystalline samples were made by allowing materials to solidify in a mould. Single ice crystals were grown by a method described by Jaccard (1), and disks were cut from these. All measurements were carried out at a temperature of −70°C in a nitrogen atmosphere. In all cases the polarizing field was applied for 30 min. The water used had an impurity content of 7 ppm.

Dipole moment measurements.—Measurement of the macroscopic dipole moment of an unshielded electret provides a sensitive method of observing changes in the polarization of the electret without the disturbance produced by the removal and replacement of surface electrodes involved in the usual lifted electrode measurements of the surface charge. The dipole moments were measured with a torsion balance similar to that described by Cross and Hart (2).

A schematic diagram of the balance is shown in Fig. 1. The sample, in the form of a disk, is suspended by a gold ribbon between two parallel plates referred to as the field plates. The upper end of the gold ribbon is attached to a torsion head free from backlash. Mirrors M_1 and M_2 are used in conjunction with a lamp and scale to determine the angular position of the sample with respect to the field plates. When the sample holder is clamped the sliding electrodes can be used to apply the required polarizing field; these electrodes are withdrawn when dipole moment measurements are made.

When a potential difference is applied to the field plates the field so produced interacts with the dipole moment of the sample to produce a torque, τ, given by $\tau = \mu \times E$ where E is the field applied and μ is the dipole moment of the sample. By rotating the head of the suspension on opposing torque is applied to the sample to position the axis of the sample at right angles to the applied field. The field is then reversed, and the suspension is again rotated to position the axis of the sample at right angles to the field. Readings of the torsion head are taken for each field direction. The angular difference between these two readings is twice the angle of twist necessary to counteract the torque due to the field. The dipole moment can be calculated if the torsional properties of the suspension and the field strength are known. The suspension used had a torsion constant of 0.1 dyne cm/radian, the torsion head could be read to 1 min of arc, the applied field was 0.5 esu/cm and therefore dipole moments of approximately 10^{-4} esu could be measured. To study the electret behavior of a material with this balance a sample is prepared in the form of a disk 12 mm in diameter. The sample is fitted into the holder and the sliding electrodes moved to the required position with respect to the sample, and the polarizing field is applied. After a suitable time interval the polarizing field is removed, the sliding electrodes are withdrawn, and the dipole moment is measured as described above.

Current measurements.—When a potential difference is applied to electrodes in contact with an electret material a current flows through the circuit. This current decreases with time to a small constant value. If the source of potential difference is removed and electrodes connected together, a current, which decreases with time, flows in the reverse direction.

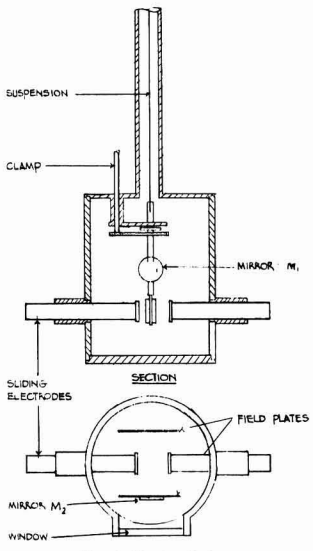

Fig. 1. Torsion balance

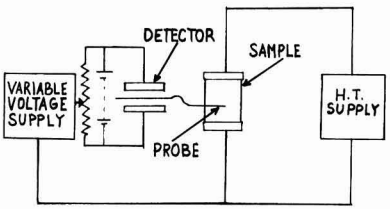

Fig. 2. Schematic diagram of the probe circuit

In this investigation measurements were made of these charging and discharging currents for polycrystalline ice.

Potential distribution measurements.—The potential distribution within polycrystalline ice disks, after the application of an electric field by means of electrodes on the surface, was measured by means of three platinum probes inserted at distances of 0.5, 1.3, and 2.5 mm from the cathode. The potential of the probes was determined by a null method. The circuit is shown schematically in Fig. 2. The null detector designed by Hart and Mungall (3) is essentially a robust equivalent of the string electrometer and can easily be constructed to produce a detector with extremely high leakage resistance so that off balance the current drawn by the probe is negligible and at balance there is no current drawn. The sensitivity of the detector was ±5v.

Results and Discussion

Figure 3 shows the variation of the charging and discharge currents for a sample of ice electrified by applying 3 kv to brass electrodes in contact with the surface. The currents fall off with time reaching almost constant values within 6 min. The total charge liberated on discharging is approximately 150 esu. Figure 4 shows the variation with time of the dipole moment of ice electrified by applying 3 kv to brass electrodes in contact with the sample. The dipole moment corresponds always to a homocharge, the magnitude of which decreases with time. As ice has a low-frequency dielectric constant of approximately 100 the field in the region between an electrode and the sample it is nominally in contact with will be very high, and therefore a considerable amount of charge transfer is to be expected; this may therefore mask any volume effect. To avoid this, samples of ice were electrified by applying a potential difference to electrodes 1 mm from the surface of the samples. Figure 5 shows the dipole moment of ice electrified in this manner as a

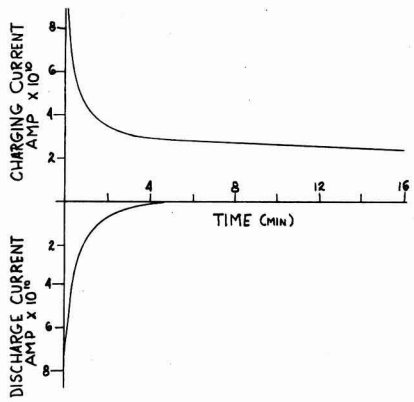

Fig. 3. Charge and discharge currents as a function of time for polycrystalline ice electrified between brass electrodes in contact with the surface: applied potential 3 kv.

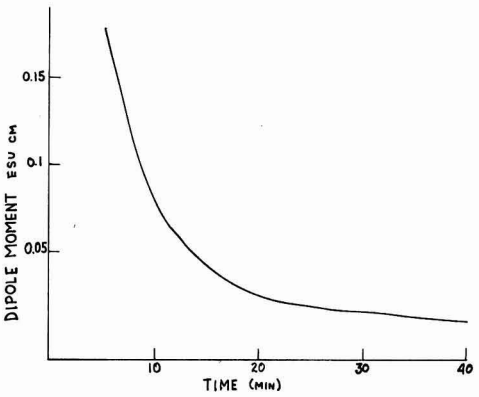

Fig. 4. Dipole moment as a function of time for polycrystalline ice electrified between brass electrodes in contact with the surface: applied potential 3 kv.

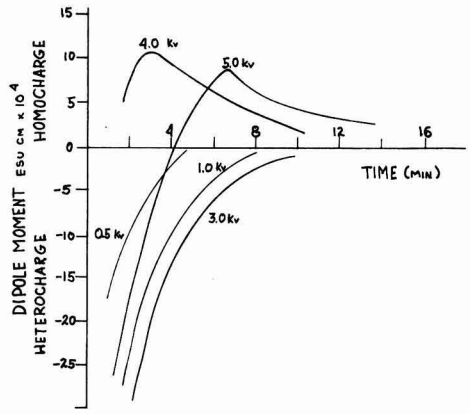

Fig. 5. Dipole moment as a function of time for polycrystalline ice electrified between electrodes 1 mm from the surface: applied potentials 0.5, 1.0, 3.0, 4.0, and 5.0 kv.

function of time after removal of the polarizing field. For applied potentials of 0.5 1.0, and 3.0 kv the dipole moment corresponds to a volume polarization which decays to zero. For an applied potential of 4 and 5 kv the dipole moment is initially equivalent to a heterocharge, it falls to zero, rises to a maximum value in the opposite direction, and then falls slowly toward zero. This is an electret effect similar to that observed in carnauba wax, the only difference being in time scale. The behavior is explicable in terms of the two-charge theory: ice has a low frequency constant of 100 and therefore with applied potentials of 0.5, 1.0, and 3.0 kv the fields in the air gap between the electrodes and the samples are 2.5, 5.0, and 15 kv/cm, respectively. These fields are too low to cause breakdown in the gap, and therefore no surface charge is deposited, and the dipole moment is due to a heterocharge. With applied potentials of 4 and 5 kv the fields in the air gap are 20 and 25 kv/cm; enhancement by uneven surfaces will produce breakdown, and the observed dipole moment will be the resultant of the volume polarization and a real surface charge.

It should be noted that the dipole moment for samples polarized with "contact" electrodes is approximately one hundred times that for samples electrified with 1 mm air gap. This supports the suggestion that in the case of contact electrodes the high field at the dielectric-electrode interface caused a large transfer of

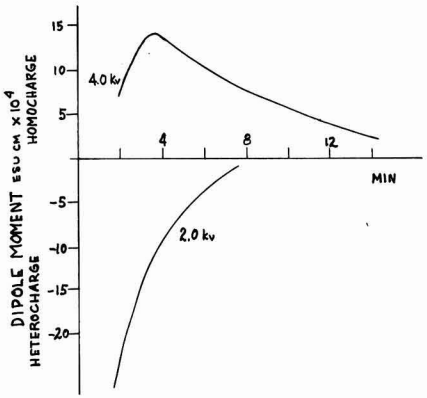

Fig. 6. Dipole moment as a function of time for single crystal ice electrified between electrodes 1 mm from the surface: applied potentials 2.0 and 4.0 kv.

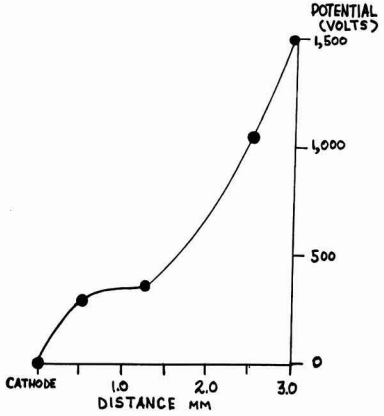

Fig. 8. Potential distribution within a 3 mm thick sample of polycrystalline ice, 30 min after the application of 1500v to electrodes on the surface.

charge which would have masked the volume polarization present.

Figure 6 shows the dipole moment for single crystal ice electrified between electrodes 1 mm from the surface. The behavior of the single crystal is almost identical to the polycrystalline sample.

The nature of the volume polarization has been a point of dispute in electret studies. The choice lies between a space charge mechanism, a uniform volume polarization, or a combination of the two. All measurements of the internal potential distribution with probes have shown the existence of space charges near the surfaces. X-ray studies of polarized and nonpolarized electrets have failed to show any increased ordering in the polarized electrets. From this evidence it seems that a space charge effect must exist. Objections have been made [Gerson (4)] to the apparent independent decay of a space charge in close proximity with a real surface charge of opposite polarity. This behavior can be explained by a simple model. It is necessary to assume that the surface charges are trapped so that they are not discharged by the approach of a charge carrier forming the space charge, then the situation at the moment the external field is removed is illustrated by Fig. 7. As a simplification the space charges are assumed to exist as a thin uniform layer of charge near each electrode, the charge per unit area being Q. The trapped surface charge has a density σ per unit area. The electric field at a point in the space charge layer is equal to $\sigma - Q/KE_0$ where K is the dielectric constant of the medium. For $\sigma > Q$ the surface charge initially predominates, and the internal field holds the space charge to the surface layer. The change in dipole moment is controlled then by the decay rate of the surface charge, the dipole moment reaching zero when $\sigma = Q$. This is the behavior shown in Fig. 4 for the sample electrified with electrodes in contact with the sample.

If $\sigma < Q$ the internal polarization predominates initially, and the internal field results in a migration of the space charge layers to the center of the sample. This migration reduces the contribution of the space charge to the dipole moment, causing the surface

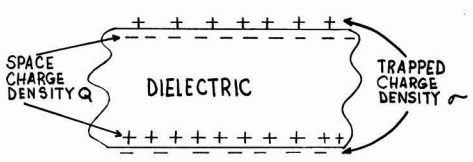

Fig. 7. Schematic diagram of a polarized electret

charge to predominate. The maximum value of the positive dipole moment is reached when the space charges of opposite sign meet. From then on the change in dipole moment is controlled by the decay of surface charge. This is the behavior shown in Fig. 5 and 6 for ice samples electrified between electrodes spaced 1 mm from the surface.

The potential distribution within ice with an applied potential difference of 1.5 kv, measured by the probes, is shown in Fig. 8. The potential distribution shows the existence of a strong positive space charge near the cathode and a very weak negative space charge near the anode. This is to be expected from the theory of electrical conduction in ice proposed by Jaccard (5) in which conduction is attributed to the migration of protons and H_3O^+ ions.

The main experimental evidence against a space charge mechanism is the work by Gross (6) in which measurements were made of the discharge current released when an electret, that had been cooled during polarization, was reheated. The discharge current liberated by sections cut from the electret was found to be independent of the thickness of the sections and of the position in the electret from which the section was taken. This indicated that a uniform polarization was responsible for the current. However, experiments on tetradecanol by Cross and Hart (2) showed that discharge currents are not dependent on internal polarization alone, and the results shown in Fig. 3 and 4 support this view. The surface charge on the ice electret electrified between contact electrodes completely obscures any volume effect and the decay of this major charge concentration must effect the discharge current. Measurements of the discharge current cannot be taken as evidence in favor of a uniform volume polarization unless the contributions of surface effects can be shown to be zero in that experiment.

A uniform volume polarization would arise from a mechanism such as dipole orientation or the short range movements of charges. Such mechanism should be sensitive to the internal structure of the dielectric. To check the dependence of the internal polarization on structure, samples of ice, tetradecanol, carboxylic acid C_{20}, and paraffin wax were polarized by applying a potential difference of 3 kv to electrodes 1 mm from the surfaces of the samples. The results of these measurements are shown in Fig. 9. All four materials show similar behavior, that is, a slowly diminishing dipole moment corresponding to a volume polarization, yet the structure of the materials differ widely: ice is a purely hydrogen bonded solid. In tetradecanol long hydrogen bonded chains are formed. In carboxy-

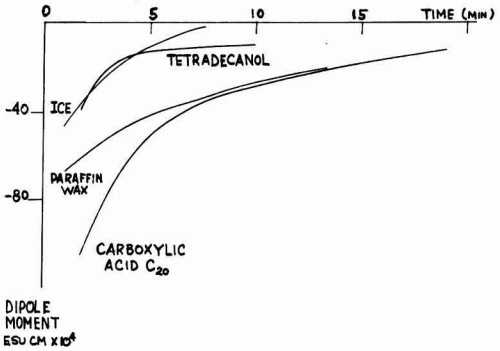

Fig. 9. Dipole moment as a function of time for ice, tetradecanol, carboxylic acid C_{20}, and paraffin wax, electrified between electrodes 1 mm from the surface. Applied potential 3.0 kv.

lic acid C_{20} hydrogen bonded dimmers form and in paraffin as there is no hydrogen bonding.

As the polarization is so little affected by differing structure and crystalline state it is improbable that uniform volume polarization is involved. All dielectrics used in electret studies have a finite electrical conductivity. In any dielectric with a finite electrical conductivity space charges will accumulate near the electrodes applied to the surface if there is any hindrance to the complete discharge of the charge carriers at the electrode. It is impossible to attach removable electrodes to a solid dielectric in such a way that there is perfect electrical contact over the whole dielectric-electrode interface and, if the surface charge or dipole moment is to be measured, and hence a volume polarization detected, the electrodes must be removable. Therefore in any electret study space charges must accumulate; and in fact whenever they have been directly sought by probe techniques, as in this work and in tetradecanol by Cross and Hart (2) or in carnauba wax [Gemant (7), Antennan (8), Van der Linde (9)], they have been detected.

The conclusion to be drawn is that the persistent volume polarization in electrets must be, at least in part, due to space charges and in simple materials it is wholly due to space charges.

Manuscript received June 29, 1967; revised manuscript received *ca.* Sept. 27, 1967. This paper was presented at the Electrets Symposium at the Chicago Meeting, Oct. 15-19, 1967, as Abstract 125. This work was supported by a Science Research Council Grant, reference B/SR/4382.

Any discussion of this paper will appear in a Discussion Section to be published in the December 1968 JOURNAL.

REFERENCES

1. C. Jaccard, *Helv. Phys. Acta*, **32**, 89 (1959).
2. J. Cross and J. Hart, *Brit. J. Appl. Phys.*, **17**, 311 (1966).
3. J. Hart and A. G. Mungall, *J. Sci. Instr.*, **33**, 411 (1956).
4. R. Gerson and J. Rohrbaugh, *J. Chem. Phys.*, **23**, 2381 (1955).
5. C. Jaccard, *Ann. N. Y. Acad. Sci.*, **125**, 390 (1965).
6. B. Gross and R. J. DeMoraes, *J. Chem. Phys.*, **34**, 2061 (1962).
7. A. Gemant, *Phil. Mag.*, **20**, 929 (1935).
8. K. Antennan, *Z. Angew Math. Phys.*, **7**, 478 (1955).
9. L. Van der Linde, *Z. Physik*, **155**, 413 (1959).

Production and Charge Decay of Film Electrets

Martin M. Perlman[1]

Department of Physics, Collège militaire royal de Saint-Jean, Saint-Jean, Québec, Canada

and Cornelis W. Reedyk

Northern Electric Research and Development Laboratories, Ottawa, Ontario, Canada

ABSTRACT

The object of this work has been to obtain charged dielectric films, electrets, that retain their charge over periods of years when left open circuited. Such films are receiving increasing attention because of their potential use in practical devices such as condenser microphones, electrostatic recorders, air filters, etc. Procedures have been devised to form highly charged thin films and to measure their decay rates. Charge decay comparisons are made among different materials at various temperatures, charged in different ways. A procedure is developed that enables long lifetimes of electrets at room temperature to be predicted by extrapolating short charge decay times at elevated temperatures. A number of materials are identified as suitable for very long-lived electrets.

Production of Electrets with a Large Net Homocharge

The decay lifetime of the homocharge of an electret is generally much longer than that of the heterocharge. It is desirable therefore to obtain samples with a large net homocharge. The films used in this work vary in thickness between 0.25 and 5 mils. If such a film be charged in the usual way, *i.e.*, by sandwiching between two metal electrodes, applying heat and a field, net heterocharged electrets result. If one attempts to create net homocharged samples by increasing the applied field, the film soon arcs through at a weak point, dust spot, or microscopic inhomogeneity in the surface of the electrodes.

Electrets with a large net homocharge may be produced, without arcing, by inserting an appropriate dielectric between metal electrodes and film (1). The dielectric, air gaps, and film then form a 5-layer capacitor, Fig. 1. (The dielectric inserts are metallized on their surfaces remote from the film to eliminate dielectric-electrode air gaps.) The electric fields in the various layers can be determined by applying Maxwell's equations. The expression for the electric fields in the air gaps enables one to explain why electrets with a large net homocharge are obtained using dielectric inserts.

Assuming that the air gaps behave as ideal dielectrics of dielectric constant equal to unity, using the line integral law for electric field, Gauss's law, and

[1] Consultant at Northern Electric Research and Development Laboratories, Ottawa, Ontario, Canada.

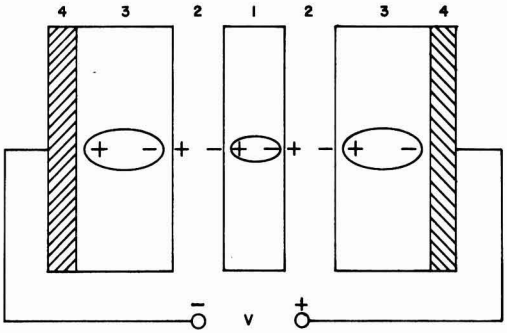

Fig. 1. Five-layer capacitor with dielectric inserts: 1, film; 2, air gaps; 3, inserts; 4, metal electrodes.

the expression connecting electric displacement, field, and polarization, one has (2)

$$E_2 = \frac{V + [d_1(P_1 - \sigma_{r1}) + 2d_3(P_3 - \sigma_{r3})]/\epsilon_0}{d_1 + 2d_2 + 2d_3} \quad [1]$$

where E_2 is the field in the air gaps; V is the applied charging voltage; subscripts 1, 2, and 3 refer to the film, air gaps, and inserts, respectively; d is the thickness; σ_r is the real homocharge; and P is the volume polarization or heterocharge.

At $t = 0$, there is no homocharge, *i.e.*, $\sigma_{r1} = \sigma_{r3} = 0$. During charging, the heterocharges P_1 and P_3 increase, and so does the field in the gaps. Eventually, this field will exceed the breakdown strength of the air in the gap, and spray discharges (*i.e.*, homocharge deposition) will occur, increasing σ_{r1} and σ_{r3}. The numerator in Eq. [1] then decreases, and the field in the gap falls to a value below breakdown, quenching the discharges. The heterocharge then continues to increase, and the cycle repeats.

Both heterocharge and homocharge should be present on charging with or without dielectric inserts. However, with inserts, the contribution to the field in the air gap due to the polarization of the inserts relative to that due to polarization of the film is $2d_3P_3/d_1P_1$. In these experiments, the latter quantity ranges between 500 and 25, since the insert is 1/16 in. thick, the films are 0.25 to 5 mils thick, and P_3 and P_1 are of the same order. Comparing Eq. [1] with the expression for the field in the air gaps when the inserts are not present (put $d_3 = 0$ in the numerator of Eq. [1]; $2d_2 + 2d_3$ in the denominator is now the thickness of the air gap), one can see that the gaps will break down many more times during the course of polarization with inserts than without, and one may expect a much larger homocharge in the former case. In Fig. 2, typical voltages across the air gaps are plotted as a function of time in the two cases. Note that the breakdown frequency is much greater in the former case. V_o is the breakdown voltage of the gaps.

If one attempts to charge an ideal dielectric without inserts, $d_3 = 0$ in the numerator of Eq. [1], the gap is $2d_2 + 2d_3$, $\sigma_{r1} = 0$ and P_1 is constant; thus the field in the gap is a constant, and repetitive breakdown cannot occur. With inserts, P_3 varies, and the heterocharge-homocharge cycle takes place. One can of course use a sufficiently high field to create a corona or Townsend discharge and produce homocharge on all films (ideal or not). Charging with inserts produces a large homocharge simultaneous with a volume polarization in nonideal dielectrics, which is desirable for the long-lived electrets considered here.

Most samples were charged with 6 kv applied across the electrodes for 0.5 hr at 120°C. The initial fields were of order 30 kv/cm in the films, 100 kv/cm in the air gaps, and 20 kv/cm in the inserts. Initial charges obtained were about 5 x 10^{-8} coul/cm^2. All films were

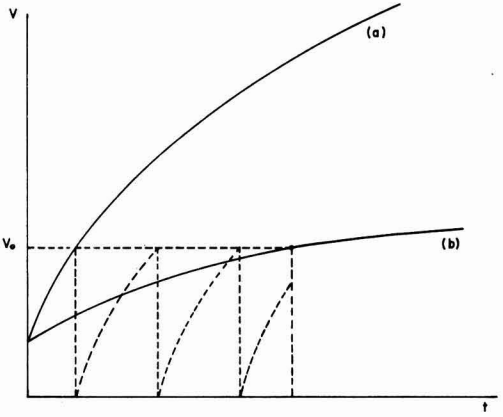

Fig. 2. Voltage V across the air gap as a function of time t; (a) with inserts (b) with inserts replaced by air gaps.

metallized on one side and stored in microphones, with the charged surface in contact with a metallic backplate. The films were only partially shielded because the average gap between surface and backplate was of the same order as the thickness of the film.

The charges were measured by applying sound pressure to vibrate the film, displaying the output signal on a C.R.O., and applying a d-c bias across the metallized side of the film and backplate sufficient to produce zero output signal (3).

The net surface charge $(\sigma_r - P_s)$ and bias V_B are related by

$$(\sigma_r - P_s) = K\epsilon_0 V_B/d_1 \quad [2]$$

where K is the dielectric constant of the film, and ϵ_0 is the permittivity of free space.

Typical Homocharged and Heterocharged Film Electrets

All films acquired a large net homocharge when polarized using the inserts; those polarized without the inserts were mainly net heterocharge. Both homocharge and heterocharge were simultaneously present whether samples were charged with inserts or not. This is illustrated in Fig. 3 and 4. In Fig. 3, a 5-mil Mylar sample polarized without inserts had an initial bias of 1200v net heterocharge. (Values stated for the bias V_B may be converted to net surface charge density, $\sigma_r - P_s$, using Eq. [2] with appropriate values for dielectric constant and thickness of the films.) The charge was allowed to decay at room temperature and fell to 200v in about 20 days. The sample was then heated to 80°C to increase the rate of decay. Within 4 hr the net heterocharge decayed to zero and reversed its sign to 48v net homocharge. In Fig. 4, a 5-mil Mylar sample polarized with inserts had an initial bias of 500v net homocharge. The charge was allowed to decay

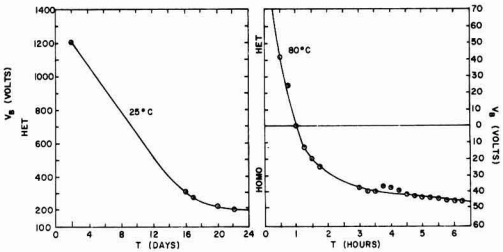

Fig. 3. Charge decay of a net heterocharged electret (5-mil Mylar charged without inserts).

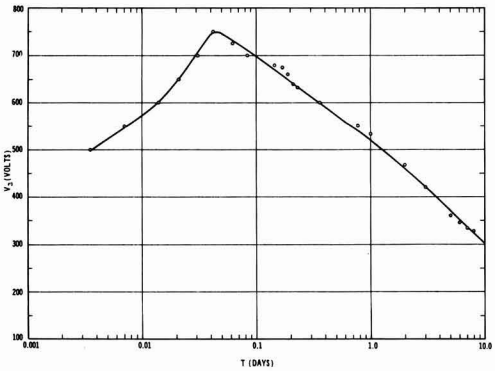

Fig. 4. Charge decay of a net homocharged electret (5-mil Mylar charged with inserts).

at 80°C. An increase in net homocharge to 750v took place in about 1 hr and then a decay over the next ten days. The initial increase in net homocharge is due to the decay of the heterocharge and is just what one expects if both heterocharge and homocharge are present in a net homocharge sample. The real homocharge in the sample polarized with inserts was at least 15 times greater than in the sample polarized without inserts.

To demonstrate that air breakdown is necessary to produce a homocharge in film electrets, a sample of 0.25-mil Mylar was polarized in a vacuum of 10^{-5} Torr at room temperature. The charge was measured during the polarization process using a dissectible capacitor. A slowly increasing heterocharge was observed over a period of ten days. The sample was then heated and the net heterocharge decayed to zero, rather than reversing the sign of its charge, demonstrating that heterocharge only was present in a vacuum.

The above experiments show that we are dealing with the decay of two coexisting charges, resulting in the decay of a net surface charge, *i.e.*, with a true electret phenomenon in films.

Charge Decay Comparisons at Various Temperatures

Charge decay comparisons were made, both at room temperature and at elevated temperature, among many different film materials. The most interesting of the charge decay curves are those of Fig. 5, taken at room temperature. Here, the 1-mil K-1 polycarbonate[2] electret (4) shows no measurable charge decay over a period of 7½ months. These measurements have now been extended. The charge on K-1 polycarbonate shows no measurable decay after 1½ years of storage at room temperature. There are variations of ±6% in the experimental points about an initial bias of 375v. Figure 6 compares the charge decay of various electret films at 95°C, and Fig. 7 compares K-1 polycarbonate and FEP Teflon[3] at 130°C.

The K-1 polycarbonate electrets are the best of all films tried. They are very long-lived and have the desired mechanical characteristics over a wide temperature range for use in our application, *i.e.*, microphones. Figures 5 and 7 show that whereas K-1 polycarbonate is longer lived than FEP Teflon at room temperature, it is slightly inferior at 130°C. FEP Teflon electrets are the next best choice. They are longer-lived than Mylar[4] and most other films, but tend to flow under stress at elevated temperature.

H-film[3] is poorer than Mylar at room temperature, but better at 95°C. Makrofol KG-polycarbonate[4] and

[2] Supplied by and registered trademark of Tennessee Eastman Co., Kingsport, Tennessee.
[3] Supplied by and registered trademarks of E. I. Du Pont de Nemours and Co., Wilmington, Delaware.
[4] Supplied by American Dielectrics Division of American Anodizing Corp., Quincy, Massachusetts.

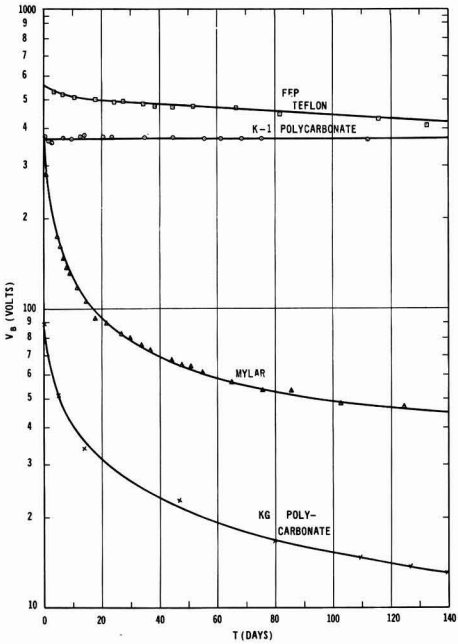

Fig. 5. Charge decay of various film materials at 25°C

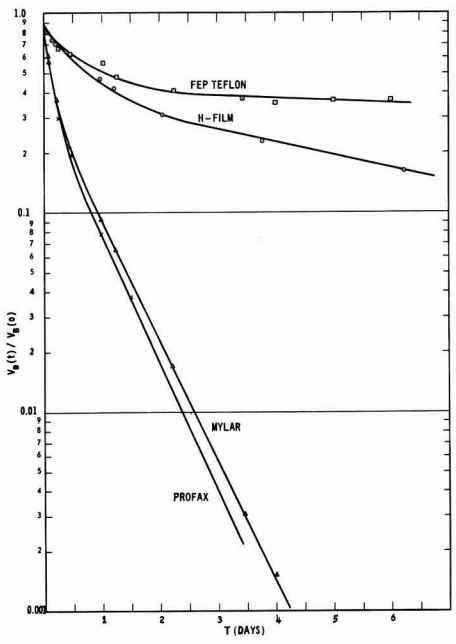

Fig. 6. Charge decay of various film materials at 95°C

Profax[5] form short-lived electrets. Two other films with promising electrical properties are polystyrene[6] and Surlyn.[3] While both have high volume resistivities, they have low service temperatures. Surlyn was longer-lived at room temperature than all other films, with the exception of K-1 polycarbonate. However, its

[5] Supplied by and registered trademark of C.I.L. Montreal, Canada.
[6] Supplied by Natvar Corp., Woodbridge, New Jersey.

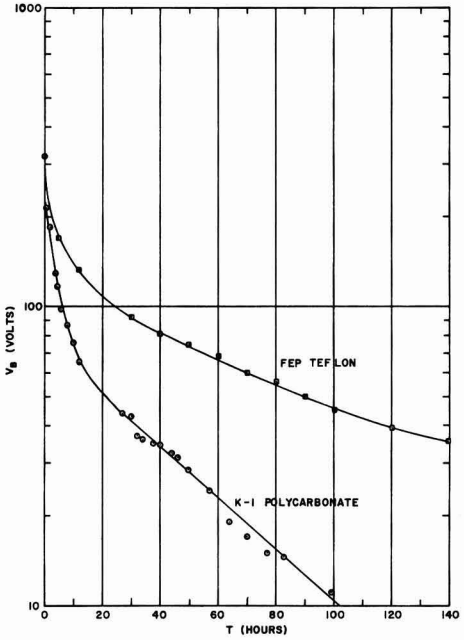

Fig. 7. Charge decay of 1 mil films at 130°C

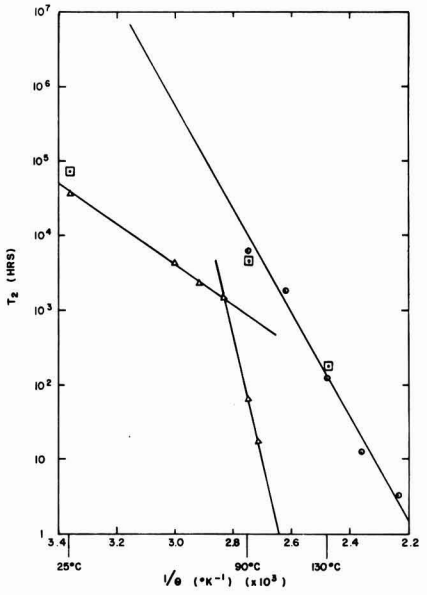

Fig. 8. Arrhenius plot of charge decay lifetimes; △, 0.25 mil Mylar; ⊙, 1 mil K-1 polycarbonate; ⊡, 1 mil FEP Teflon.

decay just 10°C above room temperature proved to be more rapid than even that of Mylar.

Extrapolation Procedure on Arrhenius Plots

An extrapolation procedure on measurements of short charge decay lifetime at elevated temperature has been developed, which enables a prediction of the long lifetimes at room temperature. In many dielectrics, after decay has taken place for some time, the subsequent decay can be characterized by a single relaxation time T_2. The dependence of this time on the absolute temperature θ is often of the form (5)

$$T_2 = \alpha e^{\epsilon/k\theta} \qquad [3]$$

where ϵ is an activation energy, α is constant, and k is Boltzmann's constant. An "Arrhenius" plot of ln T_2 *vs.* $1/\theta$ usually yields one or more straight lines of different slope. The change in slope takes place at the glass transition temperature.

Figure 8 shows an experimental Arrhenius plot for ¼-mil Mylar over the temperature range 25°-100°C. Mylar has a glass transition temperature of 80°C. It is amorphous below this temperature and partly crystalline above it. Two straight lines above and below 80°C are evident. Measurements on 1-mil K-1 polycarbonate at 5 different temperatures, and on 1-mil FEP Teflon at 3 temperatures are also plotted in Fig. 8. K-1 polycarbonate is amorphous, and cannot be crystallized at any temperature (6). Thus, hopefully, one straight line can be drawn through the 5 points and extrapolated back to room temperature. This yields a useful life at room temperature in the thousands of years. As stated above, room temperature measurements on the charge of electreted K-1 polycarbonate show no measurable decay over a period of 1½ years. It should also be noted that activation energies may be determined from the slopes of the Arrhenius plots.

Parameters Optimizing Lifetime

A theory that relates the net surface charge of electrets to internal field and constants of the material, when the dielectric is polarized at one temperature and decays at another, is not available at present. One can, however, make some guesses as to the parameters that influence lifetime.

The long charge decay lifetimes of net homocharge electrets are due to the presence of two charges of opposite polarity, each of which decays. If both homocharge and heterocharge were to decay at the same rate, the net charge, their difference, would remain constant. Thus comparable rates of decay of homocharge and heterocharge are desirable.

In net homocharge electrets the internal field during decay is in the same direction as that during charging. In general, the volume resistivity must be large ($> \sim 10^{18}$ ohm-cm) or the homocharge would disappear by conduction in a short time unless the air gaps are zero. The internal field would then be opposite to that during charging, and the decay of the remaining heterocharge would take place in a relatively short time. Since a large resistivity implies a slow rate of decay of the homocharge, one must have a material with a comparable slowly varying polarization, for a long-lived electret.

An imperfectly shielded charged thick sample has a smaller internal field and experimentally, a longer life than a thin sample (2). Crystallinity of the material has an adverse effect on longevity. It may be possible to extend the life of the homocharge by charging under corona at high temperature to produce deep penetration and trapping, and to control the life of the heterocharge by the addition of various ionic impurities to ideal dielectrics.

Acknowledgment

The authors wish to thank Professor D. E. Tilley of Collège militaire royal de Saint-Jean, Saint-Jean, Québec for reading and correcting the manuscript, and P. Fatovic, M. Hutchison, and C. Lafrance of Northern Electric Research and Development Laboratories, Ottawa, Ontario for their help with the experiments. This work was supported in part by the Department of Defence Production of Canada under Contract 9PJ4-40 and in part by the Defence Research Board of Canada under Grant 5501-33.

Manuscript received Aug. 17, 1967; revised manuscript received Sept. 25, 1967. This paper was pre-

sented at the Electrets Symposium at the Chicago Meeting, Oct. 15-19, 1967, as Abstract 133.

Any discussion of this paper will appear in a Discussion Section to be published in the December 1968 JOURNAL.

REFERENCES

1. P. Fatovic, Fixture for Use During the Polarization of an Electret, Pat. pend.
2. M. M. Perlman and C. W. Reedyk, Northern Electric Co. Final Report on Condenser Microphone Contract 9PJ4-40. The Department of Defence Production, Canada.
3. C. W. Reedyk and M. M. Perlman, *This Journal*, **115**, 49 (1968).
4. M. M. Perlman and C. W. Reedyk, Long-lived K-1 Polycarbonate Electrets, Pat. pend.
5. P. H. Sutter and A. S. Nowick, *J. Appl. Phys.*, **34**, 734 (1963).
6. R. G. Devaney, Proceedings of the Sixth Electrical Insulation Conference, Sept. 13-16 (1965).

The Measurement of Surface Charge

Cornelis W. Reedyk

Northern Electric Research and Development Laboratories, Ottawa, Ontario, Canada

and Martin M. Perlman[1]

Department of Physics, Collège militaire royal de Saint-Jean, Saint-Jean, Québec, Canada

ABSTRACT

A new method of measuring the charge density on a dielectric surface has been developed. An electrode is vibrated in the surface field to produce a signal that is displayed on an oscilloscope, or measured with a VTVM. A bias is then applied across the vibrating and fixed electrodes sufficient to produce zero output signal. The value of this bias and a simple calculation yields the surface charge and its polarity. The method is simple, nondestructive, gives reliable results when compared with other techniques, and has few disadvantages. Measurements may be made at atmospheric pressure without fear of discharges at a wide range of surface-to-electrode gaps. The measurement of the surface charge is independent of circuit parameters.

In 1959, Gubkin *et al.* (1) reviewed various methods of measuring the charge of electrets. This paper outlines the advantages and disadvantages of the various techniques and suggests a new method that is simple and has proven to be reliable.

One of the earliest techniques is that of electrostatic induction, as in Gross (2). The electret is made the dielectric in a dissectible capacitor, whose upper electrode is moveable. To measure the surface charge, the upper electrode is grounded and lowered to induce a charge on it, and then disconnected from ground and raised to transfer this charge to a known capacitor. The voltage across this capacitor is measured and the charge calculated in a simple manner. An inherent disadvantage in the use of the dissectible capacitor is that, except for low surface charge densities, measurements must be made in vacuum to prevent discharges. The discharges in air arise because the field strength in the gap, between the surface of the dielectric and the movable upper electrode, can exceed the breakdown strength of the air, as the electrode is raised for a measurement (3). Another disadvantage is that charges are often generated on contact of the induction electrode and the dielectric (4).

Gubkin (1), Freedman (5), and also Gross (6) have suggested vibrating an electrode or rotating a wafer (10) in the field of the electret, measuring short-circuit alternating current or open-circuit voltage, and relating these quantities to surface charge. While measurements may be conveniently made at atmospheric pressure, ideal short- or open-circuit conditions can never be achieved, and the results must be corrected for circuit parameters.

The charge may of course be determined by applying heat and measuring the resultant thermal depolarization current (9), but this method destroys the sample.

[1] Consultant, Northern Electric Research and Development Laboratories, Ottawa, Ontario, Canada.

Other methods such as the mechanical displacement of a moveable electrode (1), or the deflection of an electron beam (7) in the field of the electret are cumbersome and have not been widely applied.

New Method

In the method suggested here, an electrode is vibrated in the field of the electret to produce a signal that is displayed on an oscilloscope, or measured with a VTVM. A bias is then applied across the vibrating and fixed electrodes (Fig. 1) sufficient to produce zero output signal. The surface charge of the electret is simply related to this bias, the dielectric constant of the sample and its thickness, and is independent of the gap and electrical circuit parameters, as shown below. The polarity of the charge is identical to that of the bias. This method was first used by the authors to study the rate of decay of thin electret films in microphones, as described by Sessler and West (8). Here, an electret film, metallized on one side, was vibrated by sound, and the backplate (electrode) held fixed. The bias was applied as in Fig. 1.

Theory

To calculate the electric field in the air gap, apply the line integral law to the two layer capacitor of

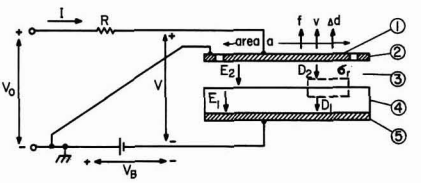

Fig. 1. Electrical circuit: 1, vibrating electrode; 2, guardring; 3, air gap d_2; 4, dielectric d_1, K; 5, fixed electrode.

Fig. 1, *i.e.*

$$d_1E_1 + d_2E_2 = V \quad [1]$$

where d_1 and d_2 are the thicknesses of sample and gap, respectively, E_1 and E_2 are the electric fields in sample and gap, respectively, and V is the potential difference between the electrodes. From Gauss's law, one has

$$D_1 - D_2 = \sigma_r \quad [2]$$

where D_1 and D_2 are the electric displacements in sample and gap, respectively, and σ_r is the real charge on the surface of the sample. By definition

$$D_1 = P_1 + \epsilon_0 E_1 \quad [3]$$

where P_1 is the polarization response of the sample to the applied field, and ϵ_0 is the permittivity of free space. The polarization response $P_1(t)$ is resolved into two components

$$P_1(t) = P_i(t) + P_s(t) \quad [4]$$

where $P_s(t)$ is the component that responds slowly to changes in the internal field $E_1(t)$, and $P_i(t)$ is the component that responds practically instantaneously to changes in the internal field and can be characterized by a dielectric constant K, *i.e.*

$$P_i(t) = \epsilon_0(K-1)E_1(t) \quad [5]$$

In the air gap, $P_s(t) = 0$, and thus combining Eq. [3], [4], and [5] one has

$$D_2 = \epsilon_0 E_2 \quad [6]$$

and

$$D_1 = K\epsilon_0 E_1 + P_s \quad [7]$$

Finally, combining Eq. [1], [2], [6], and [7], the field in the air gap is

$$E_2 = \frac{KV - \left(\frac{\sigma_r - P_s}{\epsilon_0}\right) d_1}{d_1 + Kd_2} \quad [8]$$

where $(\sigma_r - P_s)$ is the net surface charge density. If now one applies a bias $V = V_B$ so that $E_2 = 0$, Eq. [8] yields

$$(\sigma_r - P_s) = K\epsilon_0 V_B/d_1 \quad [9]$$

Thus the net surface charge of the sample is simply related to the bias that produces zero field in the air gap, and hence zero output signal when the upper electrode is vibrated.[2] The value of the net surface charge, obtained by this method, is also independent of the air gap d_2. The polarity of the net surface charge (heterocharge or homocharge) is automatically given by the polarity of V_B.

While the suggested method of measurement is completely independent of the signal voltage and current, it is useful to relate these to surface charge to obtain some idea of the orders of magnitude of the signals involved. Gubkin (1) and Sessler (8) have related the absolute value of the net surface charge to the short-circuit current amplitude and open-circuit voltage amplitude, respectively. The polarity of the charge must be determined independently.

In this paper, a harmonic analysis is made on the electrical mesh of Fig. 1. A general expression is obtained for the output voltage amplitude V_o in terms of circuit parameters. This result contains Eq. [9] and Gubkin's and Sessler's equations as special cases.

In Fig. 1, applying the principle of continuity at the vibrating electrode, one has

$$I - a\frac{\partial D_2}{\partial t} = 0 \quad [10]$$

where I is the current in the external circuit and a is the cross-sectional area of the sample.

[2] It is assumed that during the time the bias is applied the slowly varying polarization P_s remains constant.

The voltage V across the electrodes is

$$V = V_B + V_o - V_1 \quad [11]$$

where $V_1 = IR$ is the voltage drop across resistance R.

The air gap d_2 is given by

$$d_2 = d_{2o} + x \quad [12]$$

where d_{2o} is the equilibrium thickness of the gap and x is the variation about d_{2o} as the electrode is vibrated.

Combining Eq. [6], [8], [10], [11], and [12], one obtains an equation relating current I to x, V, and their time derivatives. Assuming that the variables x, V_o, V_1 can be expanded in a Fourier series, *i.e.* as

$$A = \tfrac{1}{2} A_1 e^{j\omega t} + \tfrac{1}{2} A^*_1 e^{-j\omega t} \quad [13]$$

and keeping only first order terms, one has the following solution for the fundamental frequency mode of operation

$$V_o = (R + 1/j\omega C_o)I + \frac{[V_B - (\sigma_r - P_s)d_1/(\epsilon_0 K)]C_o}{j\omega\epsilon_0 a} v \quad [14]$$

C_o is the static value of the capacitance of the system, *i.e.*

$$C_o = \epsilon_0 a/(d_2 + d_1/K) \quad [15]$$

and

$$v = j\omega\Delta d \quad [16]$$

where v is the velocity of the vibrating electrode, and Δd is the amplitude of vibration.

There is no output signal under short-circuit or open-circuit conditions when the bias has reduced E_2 to zero so that Eq. [9] applies, since then the coefficient of v in Eq. [14] is zero. The electromechanical coupling is reduced to zero, and the motion of the system is a function of the mechanical constants only.

Using Eq. [14] with $R = 0$, $V_o = V_B = 0$, $I = I_o$, one obtains the following relation between the net surface charge and the short circuit current amplitude I_o:

$$(\sigma_r - P_s) = (Kd_2/d_1 + 1)^2 d_1 I_o/(Ka\Delta d\omega) \quad [17]$$

This result agrees with Gubkin (1). Combining Eq. [9] and [17]

$$I_o/\Delta d = \epsilon_0 a\omega V_B/(d_2 + d_1/K)^2 \quad [18]$$

Using Eq. [14] with $I = 0$, $V_B = 0$, one obtains the following relation between the net surface charge and the open-circuit voltage amplitude V_o

$$(\sigma_r - P_s) = -(Kd_2/d_1 + 1)\epsilon_0 V_o/\Delta d \quad [19]$$

This result agrees with Sessler (8).

Combining Eq. [8] or [9] and [19]

$$V_o/\Delta d = E_2 = -V_B/(d_2 + d_1/K) \quad [20]$$

Plots of $I_o/\Delta d$, $V_o/\Delta d$ *vs.* gap d_2 using Eq. [18] and [20] are shown in Fig. 2 and 3 for a typical polycarbonate electret film with $K = 2.9$, $d_1 = 1/4$ mil, $V_B = 50$v, $a = 10$ cm^2, $f = 100$ Hz. Note that with gaps ranging from 1 to 4 mm, signals of the order of 1 to 0.3 v/mil of vibration are obtainable.

Experimental

A preliminary apparatus (Fig. 4) was built to test this idea. It consisted of an electrode made to vibrate by alternating current fed to a solenoid. The assembly was placed over a charged sample that was metallized on one side and provision made to vary the gap d_2. The electrodes were connected to an oscilloscope, and the bias applied as in Fig. 4. Signals of the order of those predicted were observed. We verified that Eq. [9] is independent of gap (from 0 to 10 mm) and electrical circuit parameters to an accuracy of better than 1%. The charge given by Eq. [9] also agrees with that determined using a dissectible capacitor to bet-

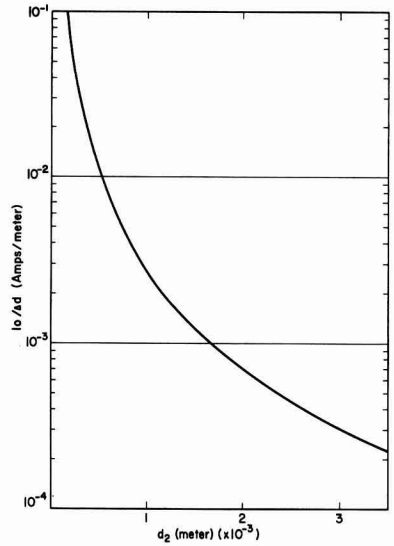

Fig. 2. Short circuit current/amplitude of vibration vs. gap

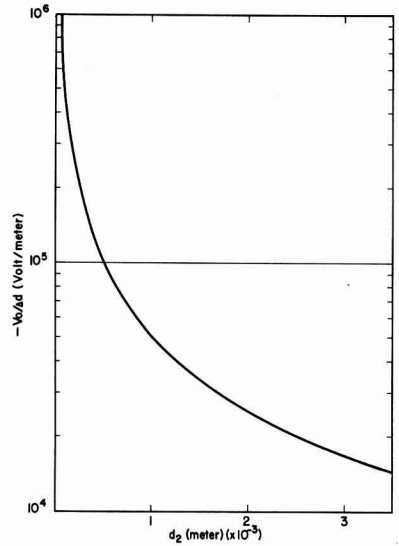

Fig. 3. Open circuit voltage/amplitude of vibration vs. gap

ter than 1%. A sturdier apparatus is shown in Fig. 5. Here, a motor drives a horizontal rod, eccentrically connected to its shaft. This motion is then translated into a vertical vibration of the upper electrode.

Conclusions

A new method of measuring the charge density on a dielectric surface has been developed. The method is simple, nondestructive, gives reliable results when compared with other techniques, and has few disadvantages. A voltage measurement and a simple calculation yield the surface charge and its polarity. Measurements may be made at atmospheric pressure without fear of discharges, at a wide range of gaps, and the surface charge is independent of electrical circuit parameters.

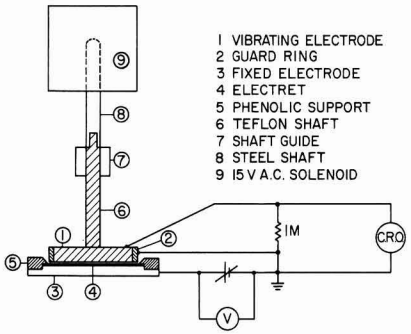

Fig. 4. Vibrating electrode apparatus

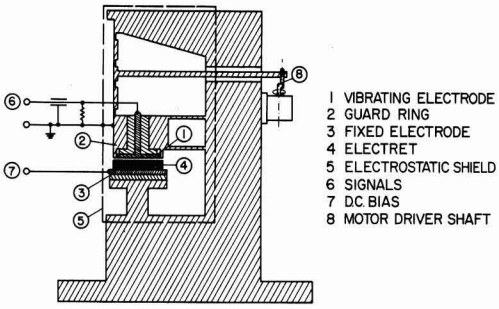

Fig. 5. Vibrating electrode apparatus

Acknowledgments

The authors wish to thank P. Fatovic, C. Lafrance, and B. Creswell for their help with the experiments and F. Stokes for the design of the vibrating electrode apparatus, all of Northern Electric Research and Development Laboratories, Ottawa, Ontario, Canada.

Manuscript received Sept. 5, 1967; revised manuscript received *ca.* Oct. 15, 1967. This paper was presented at the Electrets Symposium at the Chicago Meeting, Oct. 15-19, 1967, as Abstract 137. Work on this paper was supported in part by the Department of Defence Production of Canada under Contract 9PJ4-40 and in part by the Defence Research Board of Canada under Grant 5501-33.

Any discussion of this paper will appear in a Discussion Section to be published in the December 1968 JOURNAL.

REFERENCES

1. A. N. Gubkin *et al., Instrum, exper. tech.* (*USA*), June 1960.
2. B. Gross, *J. Chem. Phys.*, **17,** [*10*] Oct. 1949.
3a. M. M. Perlman and J. L. Meunier, *J. Appl. Phys.*, **36,** [2] Feb. 1965. b. B. Gross, *Brit, J. Appl. Phys.*, **1,** Oct. 1950.
4. G. G. Wiseman and G. R. Feaster, *J. Chem. Phys.*, **26,** [3] March 1957.
5. L. A. Freedman and L. A. Rosenthal, *Rev. Sci. Inst.*, **21,** [11] Nov. 1950.
6. B. Gross, Private communication.
7. H. Saito, *Jap. J. of Appl. Phys.*, **4,** [11], Nov. 1965.
8. G. M. Sessler and J. E. West, *J. Acoust, Soc. Am.*, **35,** 1354 (1963).
9. B. Gross and L. Ferreira Denard, *Phys. Rev.*, **67,** [7 and 8] (Apr. 1945).
10. S. Kojima and K. Kato, *J. Phys. Soc. Jap.*, **6,** 207 (1951).

Preparation and Properties of Vanadium Dioxide Films

J. B. MacChesney, J. F. Potter, and H. J. Guggenheim

Bell Telephone Laboratories, Incorporated, Murray Hill, New Jersey

ABSTRACT

Phase equilibria of the vanadium-oxygen system have been restudied in the composition range VO_2-V_2O_5 in order to establish the conditions required for stable existence of the VO_2 phase. Using this knowledge, it was possible to prepare films of VO_2 exhibiting transition in conductivity between semiconducting and metallic states. Films of V_2O_5 were first prepared by vapor deposition of vanadyl trichloride at temperatures below 127°C in 1 atm of CO_2. Reduction of these to VO_2 was accomplished by heating in controlled atmospheres of appropriate partial oxygen pressure at temperatures between 500° and 550°C. The resulting thin film (0.1-1.0μ) exhibited a sharp drop (greater than two orders of magnitude) in resistance at the expected transition temperature, 67°C.

A flurry of interest greeted Morin's discovery in 1959 (1) of unusual semiconducting to metallic transitions in the conductivities of VO_2, V_2O_3, and VO. Although, for a time, actively pursued by investigators intent on understanding the mechanism of the conduction anomaly, this interest was largely spent until revived recently. The recent emphasis has been directed toward utilizing this phenomenon in devices. However, difficulties have been encountered in the preparation of the VO_2 phase in a form applicable to device fabrication. Although methods for the growth of single crystals had been developed (2-4), single crystals were found to be undesirable for this purpose since they tend to disintegrate on cycling through the transition temperature. On the other hand, preparation of dense, sound ceramic bodies has proved difficult (5) due to inability to sinter this oxide by conventional means. Methods for preparing thin films, probably the most desirable form for utilization of VO_2 in devices, have only recently been reported (6).

In the present work the phase equilibria of the vanadium oxygen system are studied for the range of compositions between VO_2 and V_2O_5. This knowledge was then utilized to reduce amorphous vanadium pentoxide films to polycrystalline vanadium dioxide films. Resistance measurements of these showed an abrupt change at the appropriate transition temperature which was comparable in magnitude to that of single crystals.

Experimental Procedures

Although the phase relations of the vanadium oxygen system are generally known (7-10) the conditions of temperature and oxygen partial pressure necessary for the stable existence of vanadium dioxide are uncertain. Since knowledge of these parameters is indispensable to the purpose of this investigation, our first step was to determine representative oxygen isobars for the liquidus region of the diagram VO_2-V_2O_5. For this study both the quenching technique and weight changes, measured by means of a recording Chevrand thermobalance, were employed. In both cases, controlled atmospheres consisting of carbon dioxide or mixtures of carbon monoxide and carbon dioxide were used. Desired mixtures were obtained using commercially available flowmeters; compositions of these were determined using a gas chromatograph (L&N Chromolax II) which had been calibrated by gas mixtures of known composition. The phase assemblage of each quenched specimen was determined by x-ray diffraction.

Thin films of crystalline V_2O_5, suitable for reduction to VO_2 were prepared by vapor deposition on polished single crystal sapphire substrates. The apparatus used for deposition is shown in Fig. 1. It consists only of a bell jar with a side arm to permit introduction of CO_2 and a heater. Vaporization was carried out in 1 atm of CO_2 by heating $VOCl_3$ to near its boiling point while maintaining the substrates at temperatures between 60° and 120°C. Vaporization was continued until films of desired thickness (approximately 1μ) were attained. Subsequent annealing was carried out at temperatures sufficiently below the melting point of V_2O_5 to prevent the formation of a liquid phase which would separate into globules on the substrate surface. Resistance measurements of these specimens were made using indium-gallium stripes drawn on their surface as electrodes. These films were further characterized by electron microscopy, and electron and x-ray diffraction.

Results and Discussion

We should like to preface discussion of our results by a brief description of the phase equilibria of the vanadium oxygen system. It will be appreciated that these can be studied as either a closed or an open system. Most previous studies have been made on the closed system. By this technique various mixtures of vanadium oxides whose total composition is that desired are equilibrated in sealed containers. As such, the amount of oxygen in the container is fixed, and at equilibrium the total composition of the condensed phase or phases will be essentially that of the initial mixture, with only a small pressure of oxygen present in the gas phase filling the volume of the container. Our studies have been made on the open system. Here the total composition of the condensed vanadium oxide phase assemblage changes in response to the oxygen

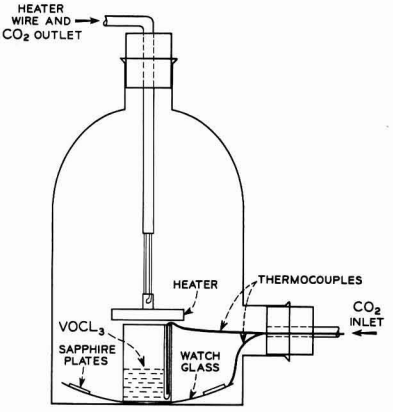

Fig. 1. Experimental apparatus used for deposition of amorphous V_2O_5 coatings from $VOCl_3$.

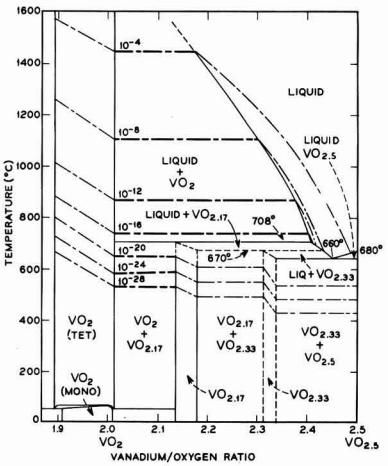

Fig. 2. Phase diagram for vanadium-oxygen system reconstructed from Kachi and Roy (10). Heavy dash-dot lines are oxygen isobars which have been determined for the Liquid + VO_2 and VO_2 + $VO_{2.17}$ phase regions. Estimates of the positions of those in adjoining areas of the diagram are shown by light dash-dot lines.

partial pressure of the furnace atmosphere until equilibrium is attained.

Such changes can be visualized by the use of oxygen isobars. These show the change in total composition taking place at fixed partial oxygen pressure in response to changes in temperature. In Fig. 2, a portion of the vanadium-oxygen phase diagram is shown for compositions from VO_2-V_2O_5. The diagram is based on that of Kachi and Roy's (10), but has been modified to show the existence of $VO_{2.33}$ (9) and also by the imposition of representative oxygen isobars obtained from the present study. Dashed portions of these show expected trends of such curves in phase regions not extensively studied in the present work.

The significance of these isobars to the present work will become obvious if one recalls the phase rule

$$P + F = C + 2$$

where C is the number of components of a system, F is the number of degrees of freedom, and P represents the number of phases present at equilibrium.

In the present system there are two components, vanadium and oxygen, so that $P + F = 4$. First let us consider that portion of the diagram representing a single liquid phase. At equilibrium, in addition to the condensed phase, a gas phase is present containing oxygen at a pressure of 1 atm or less. In this situation, two degrees of freedom remain so that, within limits, both temperature and oxygen partial pressure can be changed without altering the phase assemblage.

But what happens when these limits are exceeded? Specifically, what happens when the temperature or the oxygen pressure is fixed such that the composition of the system is changed so as to cross the liquidus curve separating the liquid phase region from that of crystalline VO_2? Now three phases are present, and only one degree of freedom remains. In order to maintain two condensed phases (crystalline VO_2 and liquid) in equilibrium, the temperature and oxygen pressure can no longer be independently varied. Instead, VO_2 and liquid are stable only at a single oxygen partial pressure at a single temperature. In practice then, reduction of the oxygen partial pressure at fixed temperature or increasing temperature at fixed oxygen partial pressure will ultimately bring about the complete precipitation of the liquid phase as VO_2. It can be shown by similar reasoning that VO_2 can be obtained from other crystalline phases in the same manner at lower temperatures.

With this in mind we can simplify the diagram of Fig. 2 to describe more readily the conditions necessary for the stable existence of VO_2 at equilibrium. Since temperature and oxygen pressure are not independently variable when two condensed phases are present, the two-phase region of the diagram of Fig. 2, will become a line on the diagram of log P_{O_2} *vs.* $10^4/T$ ($°K^{-1}$). Such a diagram, Fig. 3, has been constructed from the data of the present study. Here, phase fields of VO_2-liquid and VO_2-$VO_{2.17}$ are separated by the solid line representing the conditions necessary for the existence of these phases at equilibrium. Dashed lines again are used to represent estimates of conditions giving rise to univariant equilibria involving other vanadium oxide phases.

Before proceeding to describe preparation of films it is important to point out that the oxygen pressures referred to in this discussion are calculated from the standard free energy change for the reaction

$$2CO_{2(g)} = 2CO_{(g)} + O_{2(g)}$$

An equilibrium constant can be written for this reaction

$$K = \frac{P_{O_2} \cdot P^2_{CO}}{P^2_{CO_2}}$$

from which the oxygen partial pressure is defined by the familiar expression:

$$\Delta F° = -RT \ln K$$

$$= -RT \ln \left(\frac{P^2_{CO}}{P^2_{CO_2}} \cdot P_{O_2} \right)$$

In its evaluation, standard free energy values of Couglin (11) were used, and experimental CO/CO_2 ratios were provided by gas chromatograph readings.

Preparation of Thin Films

Vapor deposition was attempted using several halide and metallo-organic compounds of vanadium. Among these $VOCl_3$ (vanadyl trichloride) proved to be satis-

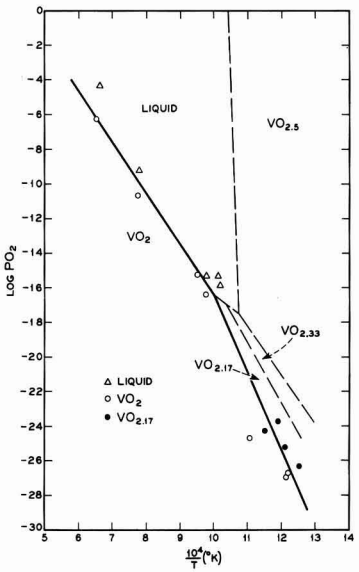

Fig. 3. Diagram of Log P_{O_2} *vs.* $10^4/T°K^{-1}$ showing boundary between VO_2-liquid and VO_2-$VO_{2.17}$ phase fields. Dashed lines are sketched to illustrate positions of phase boundaries of adjacent phases.

factory. Not only is its boiling point low, but also its vapor is decomposed at low temperatures to yield V_2O_5. We conceive of this decomposition taking place by the reaction

$$2VOCl_3 + 3CO_2 = 3COCl_2 + V_2O_5$$

This supposition is strengthened by chromatographic analysis which found phosgene among the effluent gases.

Thin films can be deposited quite rapidly (greater than 1μ/hr), even using the rather crude apparatus described which was not intended to optimize the rate. The films produced were amber and transparent. Electron diffraction patterns showed these films to be crystalline V_2O_5. A typical electron micrograph of the surface (Fig. 4) shows a poorly developed microstructure composed of grains between 0.01 and 0.1μ.

In reducing these films to VO_2 it was found necessary to remain well below liquidus temperatures. Apparently the liquid oxide phase does not wet the sapphire surface so that the film separated into droplets on the surface whenever reduction was attempted above 550°C. At the same time lowering the annealing temperature very much below this temperature presents a problem. Here, at the relatively high CO/CO_2 ratios needed to accomplish reduction of these films, carbon monoxide will be decomposed to graphite according to the reaction.

$$CO = C_{(graphite)} + CO_2$$

Thus there is a lower limit to the temperature range over which reduction can be accomplished using these gas mixtures.

After reduction under the conditions described in Table I, these films were again viewed by electron microscopy. Figure 5 shows a typical surface. Individual crystallites measuring up to 500Å can be recognized. The micrograph also shows blistering which is probably caused by release of volatile components during annealing. Talysurf measurements of this film show its thickness to range between 6500 and 9000Å. X-ray diffraction patterns from the surface show the film to be VO_2. No other phases can be recognized.

Resistance measurements over the range of 25° to approximately 100°C are shown by Fig. 6. Here resistance (ohms/square) is plotted *vs.* reciprocal temperature ($10^3/T°K^{-1}$). It is to be observed that, on heating to 65°C (2.96 on the reciprocal temperature scale), there is a drop in resistance of more than three orders of magnitude. A hysteresis amounting to between 7° and 8°C is observed in the cooling curve of this figure.

Another experiment which may be of interest to persons concerned with this subject was carried out in conjunction with Rozgonyi and Polito. They prepared polycrystalline V_2O_5 films of 2000Å thickness by oxi-

Table I. Conditions employed in preparation of VO_2 films by vapor deposition from $VOCl_3$, and from oxidized vanadium films

	Vaporization of $VOCl_3$			Annealing				
	Substrate Temp, °C	$VOCl_3$ Temp, °C	Time, hr	Atmosphere Temp, °C	CO_2 vol. %	CO vol. %	Time, min.	Film thickness, μ
Fig. 6	64	134	2	526	50	50	33	0.9
Fig. 7	—	—	—	482	50	50	15	0.2

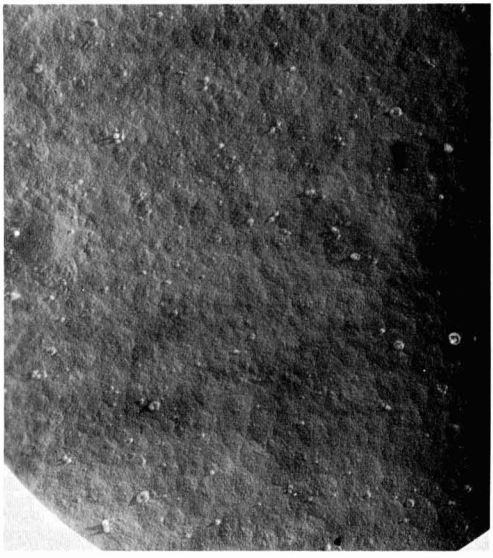

Fig. 4. Electron micrograph of a V_2O_5 film on sapphire at *ca.* 7600X.

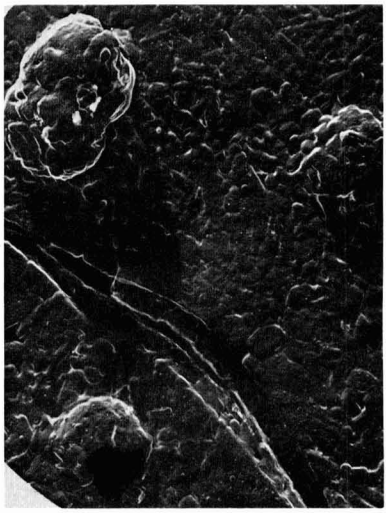

Fig. 5. Electron micrograph, at *ca.* 7600X, of a typical film after annealing in CO/CO_2 mixture to convert it to vanadium dioxide.

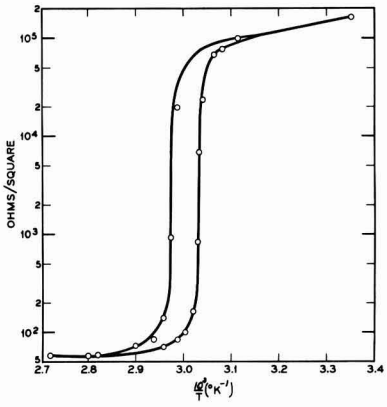

Fig. 6. Resistance *vs.* reciprocal temperature of vapor deposited film applied on a single crystal sapphire substrate and annealed in 1:1:CO:CO_2 at 526°C.

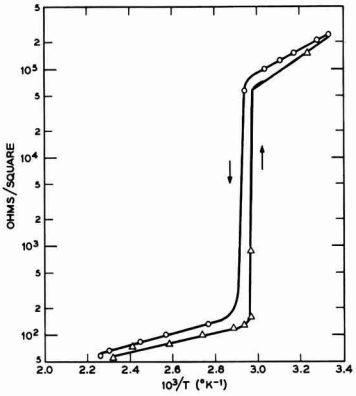

Fig. 7. Resistance vs. reciprocal temperature of a metallic vanadium film first oxidized to V_2O_5 and then reduced to VO_2 in a mixture of 1:1 :CO:CO_2 at 482°C.

dizing sputtered vanadium deposits.[1] These were then reduced in mixtures of CO/CO_2 as also described in Table I. Resistance measurements for one such film are shown in Fig. 7. It will be observed that the character of the curves are similar to those shown in the preceding figure. However the transition temperature is slightly higher, 67°C (2.93 on the reciprocal temperature scale). Also it appears that the material behaves as a semiconductor both above and below the transition.

Discussion

The reader has probably observed that we have taken some pains in our annealing experiments always to approach the VO_2 phase from an oxygen rich composition. This was done to take advantage of the favorable kinetics provided by carrying out the reductions at temperatures only 100°C below the eutectic temperature in the system VO_2-V_2O_5. This is also thought to provide an additional advantage by retarding the rate at which reduction of VO_2 to phases of lower oxygen content takes place. We have shown in another paper (12) that reduction, even when carried out at oxygen partial pressures appreciably below that in equilibrium with VO_2 phase, can still yield this phase provided that the annealing is not too prolonged.

Another comment on this work concerns the purity of vapor deposited films. After completing the work described above we performed an additional evaporation, employing the same conditions but depositing on a large graphite plate. This provided enough specimen for semiquantitative spectrographic analysis. Results given in Table II show the deposit to be contaminated. These impurities are thought not to be derived from the graphite plate, rather, we think, they result from attack by the vapor species of the nichrome heating elements and its support which were suspended in the bell jar. Obviously this can be eliminated by a different experimental arrangement. However, it is surprising that the properties of these films are not appreciably degraded by high levels of impurities. Although

[1] See "Preparation of Thin Films of Vanadium (Di-, Sesqui-, and Pent-) Oxide" by G. A. Rozgonyi and W. J. Polito, *This Journal*, 115, 56 (1968).

Table II. Impurity levels of vapor deposited thin films

	w/o		w/o
Aluminum	0.X	Copper	0.00X
Iron	0.0X	Titanium	0.00X
Silicon	0.0X	Lead	0.00X
Nickel	0.00X	Magnesium	0.00X low
Tin	0.00X	Manganese	0.000X low

the impurities may contribute to the slight lowering of the transition temperature of the vapor deposited films compared to that of the sputtered vanadium film, and single crystals (1), they have not drastically "smeared" the transition or affected the apparent resistivity of these films.

Conclusions

Investigation of the phase equilibria of the vanadium-oxygen system has resulted in a further definition of the limits of temperature and oxygen pressure for the stability of the VO_2 phase field. Using these data it was possible to prepare specimens exhibiting a sharp drop in resistivity characteristic of the phase transition between the monoclinic and tetragonal polymorphs of that phase.

Thin films of amorphous V_2O_5 were first prepared on sapphire substrates by vapor deposition. Here, $VOCl_3$ was vaporized by decomposing $VOCl_3$ vapor in 1 atm of CO_2 and then converting this to VO_2 by suitable annealing at low oxygen partial pressure. Thin films produced in this manner were shown to have electrical properties typical of the vanadium dioxide and comparable to single crystals of that phase.

Acknowledgments

The authors are indebted to Miss S. E. Koonce for electron micrographs and to D. L. Nash for spectrographic analysis. They also wish to thank M. D. Rigterink for helpful comments on the text, and to acknowledge useful discussion with W. R. Sinclair, P. J. Fillingham, and G. A. Rozgonyi.

Manuscript received July 25, 1967. This paper was presented at the Dallas Meeting, May 7-12, 1967, as Abstract No. 19.

Any discussion of this paper will appear in a Discussion Section to be published in the December 1968 JOURNAL.

REFERENCES

1. F. J. Morin, *Phys. Rev. Letters*, **3**, 34 (1959).
2. H. J. Guggenheim, "Solid State Physics," vol. 12, p. 209, F. Seitz and D. Turnbull, Editors, Academic Press, Inc., New York, (1961).
3. H. Sasaki, *J. Phys. Soc. Japan*, **19**, 1748 (1964).
4. P. F. Bongers, *Solid State Com.*, **3**, 275 (1965).
5. T. Ohashi and A. Watanabe, *J. Am. Ceram. Soc.*, **49**, 46 (1966).
6. S. Koide and H. Takei, *J. Phys. Soc. Japan*, **22**, 946 (1967).
7. G. Anderson, *Acta Chem. Scand.*, **8**, 1599 (1954).
8. F. Aebi, *Helv. Chim. Acta*, **31**, 8 (1948).
9. J. Tudo and G. Tridot, *Compt. rend.*, **261**, 2911 (1965).
10. S. Kachi and R. Roy, Second Quarterly Report, Materials Research Laboratory, The Pennsylvania State University, (Contract DA-28-043-AMC-01304E U. S. Army Electronics Laboratory) 1966.
11. J. P. Couglin, U.S. Bureau of Mines Bull. #542 (1954).
12. J. B. MacChesney, J. F. Potter, and H. J. Guggenheim, *J. Am. Ceram. Soc.*, in press.

Preparation of Thin Films of Vanadium (Di-, Sesqui-, and Pent-) Oxide

G. A. Rozgonyi and W. J. Polito

Bell Telephone Laboratories, Incorporated, Murray Hill, New Jersey

ABSTRACT

Polycrystalline thin films of V_2O_3, VO_2, and V_2O_5 have been prepared in the thickness range from 500 to 4000Å. The films are obtained by a post-deposition heat-treatment of sputtered V or V-O films. The quality of the films has been studied by x-ray diffraction techniques and by measuring resistivity as a function of inverse temperature to check the magnitude of the metal to semiconductor transition. Electrically the films compare favorably with bulk crystals, and in addition the films are extremely stable during repeated cycling through the transition temperature.

Since Morin (1) reported on the metal to semiconductor transition in certain oxides there has been considerable interest in the preparation and properties of single crystals of the oxides of vanadium. Vanadium dioxide, VO_2, which gives rise to a conductivity change of up to 10^4 at 338°K has received the most attention (2-7) due to the very convenient transition temperature. However, for fundamental studies and some more restricted device applications vanadium sesquioxide, V_2O_3, with a conductivity change of greater than 10^6 at 168°K, is also of great interest (8-10). A serious problem encountered with both V_2O_3 and VO_2 is a tendency for bulk crystals to fracture. This fracture, plus the need for material in configurations compatible with modern device technology, has stimulated our effort to deposit thin films of the above oxides.

Previous work on thin films has been restricted to the deposition of VO_2 films. The films were obtained either by vapor deposition techniques (11, 12) using $VOCl_3$ or by reactive sputtering of vanadium in argon and oxygen mixtures (13). Since difficulties have been encountered in obtaining consistently reproducible results on these films simple postdeposition annealing of films was attempted. Considerable success was achieved in obtaining uniform large area films of V_2O_5 and V_2O_3, as well as VO_2, by choosing a suitable oxidizing or reducing atmosphere while treating sputtered V or V-O films.

Apparatus and Procedures

Experimentally the vacuum system is identical to that used previously for the sputtering of ZnO (14) with the ZnO cathode replaced by V_2O_5. However, due to the complexity of the oxidation states of vanadium it was not possible to deposit crystalline films reproducibly and directly, as was accomplished with ZnO. Therefore, postdeposition treatments were devised which recrystallized the films such that their properties were comparable to bulk single crystals. Vanadium films sputtered in conventional bell jar systems were also studied. Substrate materials included single crystal sapphire and amorphous Pyrex glass slides with the best results obtained on the sapphire.

Depending on the oxide desired the films were annealed in the presence of three different flowing gases in three separate open tube furnaces. The gases were water vapor, a mixture of 90% N_2-10% O_2, and H_2 which had been bubbled through water. The optimum conditions for obtaining the V-O composition of interest are presented in Table I. No attempt has been made in this study to determine the exact conditions of temperature and oxygen partial pressure necessary for the stable formation of a particular V-O phase. The choice of gas was based simply on its expected oxidizing (N_2-O_2, H_2O) or reducing (H_2) properties. Attempts at varying the conditions of the wet H_2 treatment to obtain a crystalline phase intermediate to V_2O_3-V_2O_5, specifically VO_2, were not successful. This is consistent with the work of Gel'd *et al.* (15) who found that, although VO_2 and V_6O_{13} were detected during the reduction of powders of V_2O_5 in H_2, single phases of these compositions could not be formed.[1] In order to obtain VO_2 films the water vapor treatment was used to provide a slightly oxidizing atmosphere for the sputtered V-O films. The exact composition of the thin (500-4000Å), as-sputtered films could not be determined because of the small amount of material and its amorphous nature. However, since they were sputtered in pure argon it is expected that the V_2O_5 cathode material converted to $V_2O_3 + O_2$ and that the resulting film stoichiometry was of a phase lower in oxygen than VO_2.

Results and Discussion

The films were evaluated crystallographically by x-ray powder diffraction techniques and electrically by plotting the resistivity as a function of inverse temperature. A standard four-point probe with 0.010 in. separation was used for the resistivity measurements. Figure 1 shows the ρ *vs.* $1/T$ data for the phases of interest. The metal-to-semiconductor transitions in V_2O_3 and VO_2 films are of the same magnitude as those reported for bulk material (1) and occur at approximately the same temperatures. The semiconductor behavior of V_2O_5 films over the entire temperature range studied is also consistent for that material (2). The width of the hysteresis and the relatively soft behavior at the transition is most likely due to the polycrystalline nature of the films, and the resulting grain boundary effects, although strain introduced at the film-substrate interface, may also be important. Slight chemical inhomogeneities are also possible, and, in certain films, an extra x-ray diffraction line was observed at d = 2.25. This line could not be unequivocally assigned to any one phase, but it is suspected to be a reflection from $VO_{1.87}$. However, the metallic behavior and positive temperature coefficient of resistance in the high temperature regions indicate that the electrical behavior is not seriously effected by extraneous phases. X-ray photographs were taken with Ni filtered Cu-K_α radiation at a fixed beam incidence of 16°, treating the polycrystalline film as if it were a powdered sample. The x-ray results are presented in Table II and compared with the ASTM data for the various phases. The grain size of all films was estimated to be less than 100Å.

The resistance of these films to fracture was checked by cycling the VO_2 samples from room temperature to ~100°C on a hot plate and dipping the V_2O_3 sam-

[1] It should be noted that MacChesney (11) has reduced our V_2O_5 films to VO_2 using a CO/CO_2 reducing atmosphere.

Table I. Optimum conditions for preparation of vanadium oxide films

Desired film	Initial sputtered or recrystallized film	Annealing conditions: Atmosphere	Temp, °C	Time, hr
V_2O_5	Amorphous V-O or Polycrystalline V	90% N_2-10% O_2	500	4
V_2O_3	Recrystallized V_2O_5	Wet H_2	550	1
VO_2	Amorphous V-O Recrystallized V_2O_5*	Water vapor	450	4

* See (11) for details.

ples in and out of liquid nitrogen at least 12 times. The samples would undergo repeated resistance changes of $>10^3$ ohms for VO_2 and $>10^7$ ohms for V_2O_3 as measured with a simple ohmmeter. A point-by-point measurement after the above cycling did not reveal any change in performance.

It has been demonstrated that polycrystalline films of V_2O_5, VO_2, and V_2O_3 can be prepared by a suitable postdeposition heat-treatment of sputtered V or V-O films. The VO_2 and V_2O_3 films exhibit metallic-semiconductor behavior characteristic of bulk vanadium oxides with the added feature of stability and resistance to fracture during repeated temperature cycling. It is expected that these films will prove to be reproducible and stable samples for further investigations into the properties of vanadium oxides and the mechanism of the metal-to-semiconductor transition.

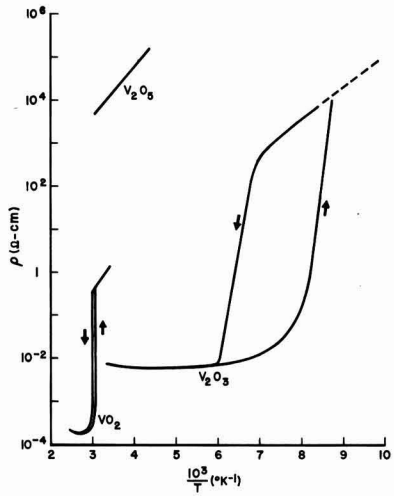

Fig. 1. Resistivity vs. reciprocal temperature for V_2O_5, VO_2, and V_2O_3 films. Arrows indicate direction of temperature change.

Table II. X-ray diffraction data for vanadium oxide films

Phase	ASTM index: d, Å	Relative intensity	hkl	Thin film: d, Å	Relative intensity, estimated
V_2O_5	4.38	100	001	4.4	100
	4.09	35	101	4.1	15
	3.40	90	110	3.4	80
	2.88	65	400	2.9	10
	2.76	35	011	2.8	10
	2.147	11	102	2.14	15
	1.757	30	601	1.75	20
V_2O_3	2.70	80	104	2.7	60
	2.47	60	110	2.45	100
	2.18	20	113	2.15	10
	1.69	100	116	1.65	40
VO_2	3.20	100	011	3.2	100
	2.430	40	$\bar{2}02$	2.43	80
	2.422	60	$\bar{2}11$		
	2.139	50	$\bar{2}12$	2.13	40
	2.131	50	$\bar{2}10$		
	1.657	30	$\bar{2}13$	1.65	50
	1.654	30	$\bar{2}22$		
	1.650	60	220, 211		

Acknowledgment

The authors wish to thank G. Mahoney for making the four-point probe measurements, J. Sosniak and D. Hensler for providing sputtered V films, and to acknowledge helpful discussions with J. B. MacChesney, H. J. Guggenheim, G. E. Smith, and P. Fillingham.

Manuscript received July 25, 1967.

Any discussion of this paper will appear in a Discussion Section to be published in the December 1968 JOURNAL.

REFERENCES

1. F. J. Morin, *Phys. Rev. Letters*, **3**, 34 (1959).
2. S. Kachi, T. Takada, and K. Kosuge, *J. Phys. Soc. Japan*, **18**, 1839 (1963).
3. K. Kosuge, T. Takada, and S. Kachi, *ibid.*, **18**, 318 (1963).
4. S. Minomura and H. Nagasaki, *ibid.*, **19**, 131 (1964).
5. H. Sasaki and A. Watanabe, *ibid.*, **19**, 1748 (1964).
6. P. F. Bongers, *Solid State Commun.*, **3**, 275 (1965).
7. H. J. Guggenheim, To be published.
8. G. Goodman, *Phys. Rev. Letters*, **9**, 305 (1962).
9. I. G. Austin, *Phil. Mag.*, **7**, 961 (1962).
10. D. Adler and J. Feinleib, *Phys. Rev. Letter*, **12**, 700 (1964).
11. J. B. MacChesney, J. F. Potter, and H. J. Guggenheim, *This Journal*, **115**, 52 (1968).
12. S. Koida and H. Takei, *J. Phys. Soc. Japan*, **22**, 46 (1966).
13. E. N. Fuls, D. H. Hensler, and A. R. Ross, *Appl. Phys. Letters*, **10**, 199 (1967).
14. G. A. Rozgonyi and W. J. Polito, *Appl. Phys. Letters*, **8**, 220 (1966).
15. P. V. Gel'd, S. I. Alyamovskii, and I. I. Matveenko, *Russ. J. Inorg. Chem.*, 5, 815 (1960).

The Measurement of Ionic Mobilities in the Anodic Oxides of Tantalum and Zirconium by a Precision Sectioning Technique

J. L. Whitton[1]

Research Chemistry Branch, Chalk River Nuclear Laboratories, Chalk River, Ontario, Canada

ABSTRACT

The technique of removing thin sections of anodic oxides by vibratory polishing has been used in conjunction with implantation of anion, cation, and inert gas radiotracers to measure the mode of anodic oxide formation on Zr and Ta. The measured transport number for metal during the growth of Ta_2O_5 (0.28) is in good agreement with previous work. ZrO_2 is shown to grow by oxygen migration and preliminary experiments suggest that the process occurs by rapid movement of the oxygen along defects. Comparison of the movement of anion and cation radiotracers with that of an inert gas provides additional evidence that xenon and krypton may be regarded as immobile markers for use in oxidation studies.

The transport mechanism responsible for oxide film growth on metals, *i.e.*, whether growth occurs by metal or oxygen migration or both, can best be measured by the use of inert markers. These markers can be placed initially on, or just beneath the surface of the specimen, and any change in their location, due to subsequent oxidation, is then directly related to the transport mechanism involved.

The best type of marker for thin anodic films is an inert radiotracer injected at a known depth by means of an isotope separator (the conventional embedded Pt wire method is not suitable for oxides of thicknesses less than a few microns). This radiotracer method, using ^{125}Xe as the radioactive marker has been used previously [(1) and references cited therein] to study the anodic oxidation mechanisms of several "valve" metals, including Zr and Ta, the position of the Xe before and after oxidation being determined by β-ray spectroscopy.

A detailed pictorial illustration of the method of obtaining transport numbers from these radiotracer measurements is shown in Fig. 1. The initial location of injected Kr atoms in an oxide layer is shown. In the case where the oxide grows by oxygen migration alone, the marker atoms stay at the same distance from the outer surface; where only metal migration occurs the marker atoms remain at the same distance from the metal-oxide interface; and where a combination of metal-oxygen migration occurs, the marker atoms are buried to an intermediate depth which depends on the ratio of metal to oxygen ion mobility.

As noted in the previous work (1), the ideal marker atoms should be immobile and should not significantly change the properties of the oxide in which they are embedded. Hence, they should be: (*i*) uncharged, so that no movement occurs due to the applied electric field, (*ii*) large in size, so that diffusion within the oxide is not a significant factor, and (*iii*) present in trace amount, so that the macroscopic properties of the oxide remain unaltered. Inert gas isotopes, such as ^{125}Xe, ^{133}Xe, ^{85}Kr etc., are expected to fulfill rather closely these requirements of the ideal marker.

Although it is difficult to devise an experiment to show unambiguously that the inert gas markers are or are not immobile, some indication of this can be expected by comparison of the behavior of inert gas atoms with that of anions and cations. This type of experiment can best be performed by injecting two or more radiotracers in the same specimen, then locating simultaneously their positions relative to each other. The results of such experiments are reported here.

A new method of determining the locations or depth distributions of the radiotracers before and after oxidation has been used. This is a method of precise sectioning using a vibratory polisher which allows layers as thin as 20Å to be removed. As successive layers are removed, the fraction of tracer remaining is determined by measurement of the residual activity, thus providing a direct measure of the location and depth distribution of the markers.

Experimental Method

The sectioning technique makes use of a commercial vibratory polisher[2] and has been described previously (2). Briefly, the specimens to be sectioned are prepared in the form of right cylinders $\sim$ ½ in. diameter by $\sim$ ¾ in. long. These have one face mechanically polished on carborundum paper, then on successively finer diamond grit down to 0.25 μm before being finally vibratory polished in an aqueous slurry of 0.05 μm Linde A Al_2O_3 for 72 hr. It has been shown (2) that this treatment leaves a virtually undeformed mirror-like surface.

The anodic oxide films required for the sectioning procedure were prepared by anodizing vibratory polished surfaces of Ta and Zr at 1 ma/cm², using 0.1M

[2] Syntron Company, Homer City, Pennsylvania.

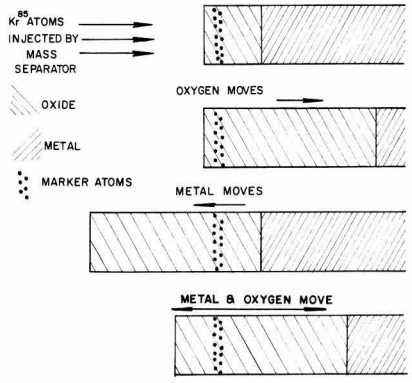

Fig. 1. A schematic representation of the effect of metal and oxygen migration on the final position of an inert marker in an oxide film.

[1] Present address: Department of Electrical Engineering and Electronics, The University of Liverpool, Liverpool, England.

H_2SO_4 as the electrolyte for tantalum and saturated ammonium borate for zirconium.

The rate of removal of Ta_2O_5 and ZrO_2 was calibrated by observing optically the residual oxide thickness after each layer was removed, and plotting this thickness *vs.* the polishing time. The oxide thicknesses were measured on a u.v. spectrophotometer, using the interference minima-oxide thickness calibration data of Young (3) for Ta_2O_5 and of Wilkins (4) for ZrO_2. The rate of removal of Ta_2O_5 is shown in Fig. 2; the slopes correspond to a rate of 50Å/min of vibratory polishing. The ZrO_2 removal rate (Fig. 3) is not so uniform initially but becomes reasonably constant after the first 100Å. As the removal rate is less than 5 atom layers per minute of vibratory polishing, it is perhaps not too surprising to find that the rate differs somewhat from one experiment to the other. It means,

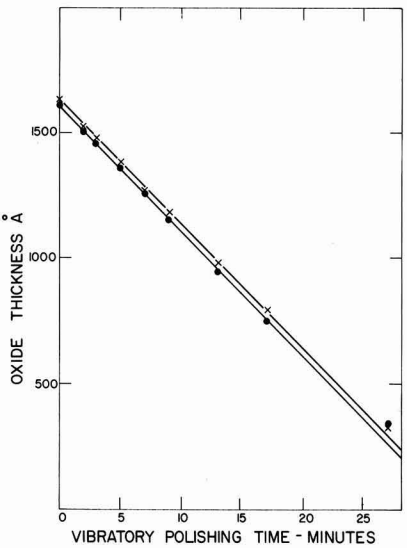

Fig. 2. Spectrophotometric calibration of sectioning method for Ta_2O_5: X, specimen 1; ●, specimen 2.

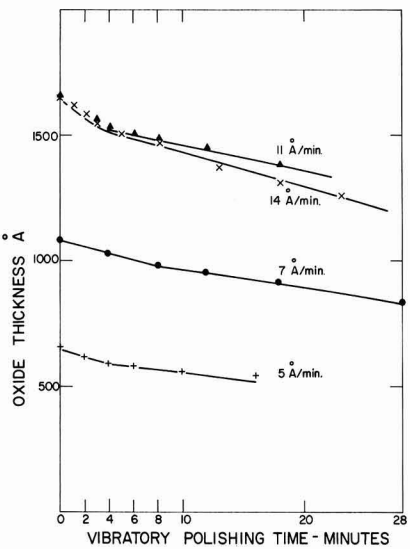

Fig. 3. Spectrophotometric calibration of sectioning method for ZrO_2: △, X, ●, +, specimens 1, 2, 3, and 4.

however, that a more careful spectrophotometric control is required for ZrO_2 than for Ta_2O_5.

The choice of radiotracers was governed by the need to have (*i*) an anion, a cation, and an inert gas, (*ii*) such a trio having approximately the same mass so as to have the same initial depth distribution, and (*iii*) having activities that could be determined independently by a combination of radioactive measuring techniques.

The trio ^{82}Br, ^{85}Kr, and ^{86}Rb fulfill these requirements. Conditions (*i*) and (*ii*) are obviously met and condition (*iii*) also, as ^{82}Br and ^{86}Rb emit β^- particles and gamma rays while ^{85}Kr is an almost pure β^- emitter. These properties, therefore, make it possible for the inert gas and the anion or the inert gas and the cation to be injected in the same specimen and the precise location of each isotope determined by a combination of sectioning, measuring the β and γ activities and comparing these measurements to a standard source of each isotope.

In a typical experiment, two specimens of Ta, anodized to 20v in order to form an oxide layer ~ 400Å thick, were used. The Chalk River isotope separator (5) was utilized to inject 30 kev ^{85}Kr and ^{86}Rb into one and 30 kev ^{85}Kr and ^{82}Br into the second. The depth distributions of these embedded atoms were then measured by removing successive thin layers on the vibratory polisher and using the isotope-selective β- and γ-counting technique to determine at each stage the residual activity of both radiotracers independently.

The anodizing and injection procedure was then repeated but the oxide layer was increased to a total thickness of 1600Å (80v) before the depth distribution was measured. The depth distributions of each isotope were again obtained by β- and γ-counting.

Results and Discussion

The distribution of the three isotopes in Ta_2O_5 before and after oxide growth is shown in Fig. 4. It is assumed at this point that Kr is a truly immobile marker, so the abscissa scale for the initial distribution (upper scale) has been displaced to make the two Kr peak positions coincide. The fraction of oxide growth by metal migration outward is then immediately seen. Of the extra 1200Å of oxide grown, 340Å are due to metal migrating outwards, and hence 860Å are due to oxygen moving inwards. This gives a transport number for the metal of 0.28 ± 0.03 in good agreement with the previous values of 0.31 ± 0.03 by β-ray spectrometry (1) and of 0.255 ± 0.004 by a chemical stripping method (6).

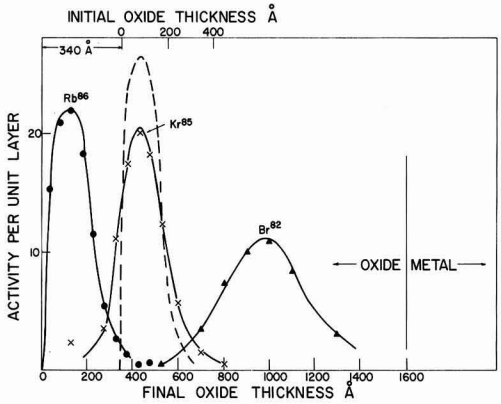

Fig. 4. Differential distribution of 30 kev ^{86}Rb, (●), ^{85}Kr (x) and ^{82}Br (△) in Ta_2O_5 before (- - - -) and after (———) additional anodizing. The abscissa scale for the initial distribution has been shifted by 340Å (upper scale) in order to make the ^{85}Kr peak positions coincide.

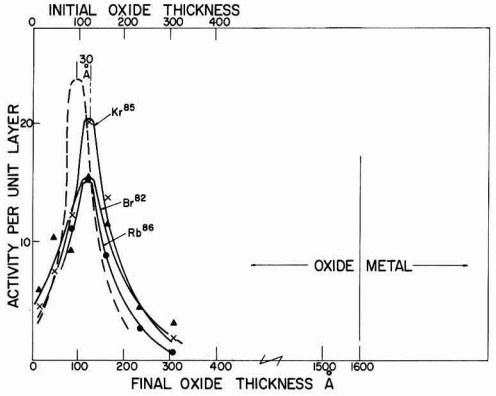

Fig. 5. Differential distribution of 30 kev ^{86}Rb, (●), ^{85}Kr (x) and ^{82}Br (△) in ZrO_2 before (- - -) and after (———) additional anodizing.

The final locations of ^{82}Br and ^{86}Rb indicate that bromine migrates inwards, but with two thirds the mobility of the oxygen, and that the rubidium migrates outwards with two thirds the mobility of the Ta. Qualitatively, this behavior is what would be predicted from simple chemical considerations, *viz.*, that Br migrates as an anion, and Rb as a cation. The broadening of the Br peak may be attributed to the combination of (*i*) a random walk broadening due to movement of the ions during oxide growth and (*ii*) the preferential removal of oxide from the edges of the specimen [c.f. ref. (2)].

The location of Kr, Br, and Rb in ZrO_2 after anodic oxidation is shown in Fig. 5, where again the initial distribution of the three isotopes is shown by the dotted line. In this case the final distribution curves are virtually the same as the initial one (except for a slight broadening), indicating that no new oxide has been formed on the surface, and that therefore all the oxide formation is by oxygen migrating inwards. This is in agreement with the previous work (1).

However, it is interesting to note that although zirconium oxide grows almost completely by oxygen migration, the Br anion does not move appreciably as it does during the growth of tantalum oxide (Fig. 4). This would indicate that in ZrO_2, a large monovalent ion such as ^{82}Br has a negligible mobility compared to the oxygen ion. An alternative possibility is that oxygen movement in ZrO_2 is by way of holes, grain boundaries, defects, etc. Such a transport mechanism might not be available to the marker atoms because these are embedded uniformly at a depth of about 100Å in the oxide lattice.

It is known that anodically formed Ta_2O_5 is amorphous (7) while ZrO_2 formed anodically in saturated ammonium borate is crystalline (8) and may contain defects such as holes, cracks, etc. This information strengthens the latter explanation but a more direct method of testing it would be to add ^{82}Br atoms to the electrolyte and then measure their uptake into a growing ZrO_2 film, and their final depth distribution within the ZrO_2 layer.

Preliminary experiments of this type indicate that an appreciable amount of ^{82}Br does in fact penetrate deeply into the growing ZrO_2 layer. The measurements were made by first growing a 400Å (20v) oxide in inactive electrolyte then increasing the oxide thickness to 700Å (35v) in Br^- doped electrolyte. Sectioning and measurement of the residual Br^- activity showed that it was distributed throughout the complete oxide, old and freshly formed. The experiment was repeated but in this case the initial undoped oxide was formed to a thickness of 400Å (20v) then immersed in the Br^- doped electrolyte at 10v. Again, on sectioning, the Br^- was found distributed through the oxide. As a control, a 400Å oxide was formed in inactive electrolyte then immersed in the Br^- doped electrolyte with no voltage applied. Sectioning showed that the Br^- had not penetrated into the oxide.

These results, together with the observation (Fig. 2) that none of the radiotracers moves appreciably during the anodic formation of ZrO_2, suggests that defects, holes, grain boundaries etc. may contribute significantly to the mode of oxygen movement through the growing oxide. This has been postulated previously by Cox and Roy (9) who measured the diffusion of oxygen into growing oxide films of zirconium, and concluded that the measured rates represented diffusion along easy paths which were "probably crystallite boundaries."

Additional evidence that ZrO_2 grows by oxygen migration was obtained by injecting 30 kev ^{133}Xe into a 400Å ZrO_2 layer, increasing the oxide thickness to 1600Å and finally injecting 30 kev ^{125}Xe. The depth distributions of the two Xe isotopes were then measured simultaneously by the sectioning technique and the separation of the gamma ray peaks of ^{133}Xe (81 kev) and ^{125}Xe (243 kev). Since the ranges of 30 kev ^{125}Xe and ^{133}Xe are virtually the same (10), their final depth distributions in ZrO_2 should be identical provided that the oxide grows by oxygen migration alone. The results (Fig. 6) illustrate that the ^{133}Xe and ^{125}Xe have almost exactly the same location, the extent of metal ion transport, if any, being evidently less than 1%.

Summary

The comparison of cation and anion movement with the location of krypton in the anodic oxides of tantalum and zirconium, and the measurement of different isotopes of xenon in ZrO_2 has provided additional evidence that xenon and krypton are immobile markers for use in oxidation studies. The lack of measurable broadening of the krypton distribution tends to confirm this.

The transport number of metal in the anodic oxidation of tantalum has been measured as 0.28 ± 0.03, in good agreement with other workers' results. The anodic oxidation of zirconium has been shown to proceed almost entirely by oxygen migration, probably by some defect mechanism.

The technique of removing thin sections of anodic oxides by vibratory polishing has been shown to be suitable for the measurement of ionic transport numbers in Ta_2O_5 and ZrO_2. This type of measurement may in principle be extended to any other metals on which coherent oxides can be formed. A large number of isotopes may be used as radiotracers as shown and, if chosen carefully, may be used simultaneously.

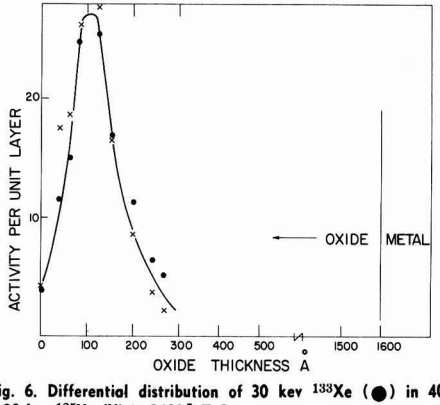

Fig. 6. Differential distribution of 30 kev ^{133}Xe (●) in 400Å and 30 kev ^{125}Xe (X) in 1600Å ZrO_2.

Acknowledgment

The author is grateful to Dr. J A. Davies for many useful discussions and to J. P. S. Pringle for the use of his spectrophotometric calibration data.

Manuscript received July 17, 1967.

Any discussion of this paper will appear in a Discussion Section to be published in the December 1968 Journal.

REFERENCES

1. J. A. Davies, B. Domeij, J. P. S. Pringle, and F. Brown, *This Journal*, **112**, 675 (1965).
2. J. L. Whitton, *J. Appl. Phys.*, **36**, 3917 (1965).
3. L. Young, *Proc. Roy. Soc.*, **A244**, 41 (1958).
4. N. J. M. Wilkins, *Corrosion Science*, **5**, 3 (1965).
5. J. A. Davies, F. Brown, and M. McCargo, *Can. J. Phys.*, **41**, 829 (1963).
6. J. P. S. Pringle, Private communication.
7. P. H. G. Draper and J. Harvey, *Acta Met.*, **11**, 873 (1963).
8. J. N. Wanklyn, A.S.T.M. S.T.P. 368, 58 (1963).
9. B. Cox and C. Roy, *Electrochem. Technol.*, **4**, 121 (1966).
10. P. Jespersgaard and J. A. Davies, Private communication.

Property Changes in Pyrolytic Silicon Nitride with Reactant Composition Changes

V. Y. Doo,* D. R. Kerr,* and D. R. Nichols[1]

IBM Components Division, East Fishkill Facility, Hopewell Junction, New York

ABSTRACT

Property changes in pyrolytic silicon nitride were investigated as a function of the reactant composition (silane:ammonia ratio). The potential of developing cracks in films deposited on silicon was greatly reduced by decreasing the ammonia injection rate. However, all films in this work with low ammonia and the films in the previous work with high ammonia were amorphous. Decreasing the ammonia injection rate increases the index of refraction and the electronic leakage while decreasing the dissolution rate (in 48% HF). The deposition rate, the dielectric constant, and the flat-band charge density are not significantly affected by the ammonia injection rate.

In pyrolytic deposition of amorphous silicon nitride films by the reaction of silane and ammonia (1-4), an excess quantity of ammonia is normally injected into the reaction chamber to ensure that the silane will react completely. The properties of the films deposited with silane:ammonia injection ratios in the range of 1:20-40 and under given conditions (temperature, deposition rate, etc.) are essentially the same (1). As the ammonia injection rate is gradually reduced to approach the silane injection rate, the ammonia becomes scarce around a silane molecule. One expects part of the silane to decompose and then be deposited on the substrate without reacting with ammonia, thus causing deficient Si-N bonds in Si_3N_4 films. In other words, the composition of the silicon nitride films would become silicon rich, thereby affecting the film properties. This paper reports the findings on the property changes of amorphous silicon nitride films as a function of the reactant composition.

Experimental Procedures

The amorphous silicon nitride films were prepared by the pyrolytic reaction of silane and ammonia in a hydrogen atmosphere (1-4). The reaction occurred in a fused quartz tube in which a surface treated high-purity graphite susceptor was used to couple with an rf coil placed outside of the quartz tube. The injection rates of silane and hydrogen were maintained at 1 ml min^{-1} and 4 liters min^{-1}, respectively, throughout this work, while the injection of ammonia was regulated to the predetermined rate.

The substrates were n-type silicon wafers of about 1.5 ohm-cm. The wafers were chemically polished in $HF\text{-}HNO_3$ solution. Prior to deposition, the substrate surface was *in situ* cleaned by heating in hydrogen at about 1225°C. The substrate temperature was then lowered to the predetermined deposition temperature. After the substrate temperature, which varied from 800° to 1000°C, was stabilized, the deposition of nitride film proceeded.

The film thickness of the amorphous silicon nitride was measured by the interference fringes under sodium light and checked by a Tolansky (5) interferometer. The index of refraction was determined by the differential interfringe spacing method (1) with sodium light (λ = 5900Å) on samples with the nitride films deposited on thermally oxidized silicon substrates. Estimated accuracy is ±0.05.

Electrical properties of the films were investigated using MIS (metal-insulator-silicon) capacitors. After deposition of the silicon nitride films (typically 6000Å thick), circular aluminum electrodes (20 mil diameter) were evaporated to form the MIS structures. Surface charge was determined from the well-known capacitance-voltage measurement (6, 7) using a frequency of 10 kHz. Dielectric constant and electronic leakage measurements were made on the same structures.

Results and Discussion

The structure of the pyrolytic silicon nitride films was studied by the transmission electron diffraction and electron microscopy. The results of all the films studied confirmed earlier reports (1) that the films were amorphous. A typically broadly diffused diffraction pattern is shown in Fig. 1. In one sample prepared at 800°C with the silane to ammonia injection, ratio of 1:1, however, a thin layer of fine polycrystallites was detected at the film-substrate interface. Figures 2 and 3 show the transmission electron diffraction and the transmission electron microscopy, respectively, of the polycrystalline material identified as silicon crystallites. The deposit of silicon crystallites may have been caused by the sudden surge of silane at the beginning of deposition. Other samples grown at the same substrate temperature and silane:ammonia ratio with silane injection started 15 sec after ammonia showed no evidence of the presence of polycrystalline silicon.

[1] Present address: Materials Research Corporation, Orangeburg, New York.

* Electrochemical Society Active Member.

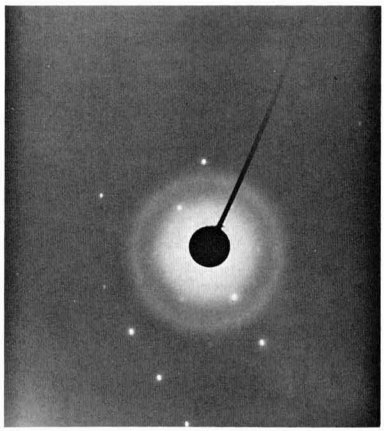

Fig. 1. Typical transmission electron diffraction pattern of pyrolytic amorphous silicon nitride. Spots are from single crystal silicon substrate.

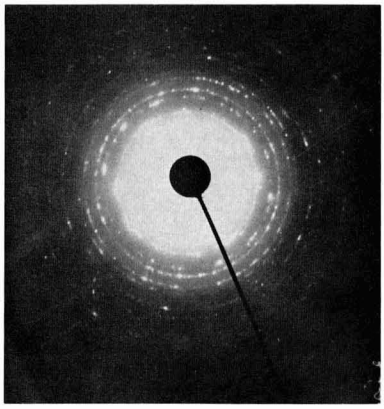

Fig. 2. Transmission electron diffraction pattern of polycrystalline silicon detected at the interface of silicon nitride-substrate.

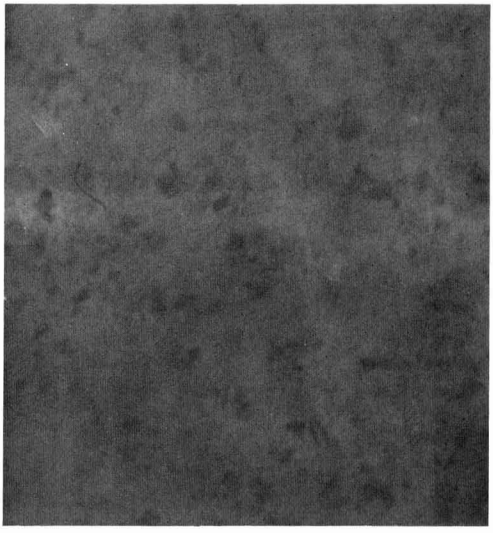

Fig. 3. Transmission electron microscopy of the same sample as Fig. 2.

Earlier work (1) reported that cracks are often observed on thick (>1μ) silicon nitride films grown on silicon substrates. The density of cracks increased with increasing film thickness and growth rate (>500Å min^{-1}). Thick silicon nitride films were grown at a silane:ammonia injection ratio of 1:40. The potential of developing cracks in silicon nitride films (on silicon) is greatly minimized for ratios of 1:1 to 1:5 even though the growth rate is a factor of three greater (1500Å min^{-1}) as shown in Fig. 4. These results indicate that the composition of the reactants has a profound effect on the stress and strain in the silicon nitride-silicon interface.

The growth rate of the silicon nitride is plotted as a function of the silane to ammonia injection ratio as shown in Fig. 4. Note that at a given deposition temperature, the deposition rate is practically independent of the ammonia injection rate when the silane to ammonia injection ratio is in the range of 1:1 to 1:10. The scattering of results was caused primarily by the experimental error in controlling low injection rates of the reactant gases and the error in thickness measurements.

The index of refraction of the pyrolytic silicon nitride was investigated as a function of the silane to ammonia injection ratio. In general, the index of refraction increases with decreasing ammonia injection rates at all the deposition temperatures (from 800° to 1000°C). At the highest ammonia injection rates the refractive index was in the range 2.0-2.1. When the ammonia injection rate equals the silane injection rate, the index of refraction of the amorphous silicon nitride films exceeds the index of refraction of the crystalline α-Si_3N_4 (RI = 2.1) (8). These results strongly indicate that the composition of the pyrolytically deposited films change gradually toward silicon rich silicon nitride as the ammonia injection rate is reduced to approach the silane injection rate. Since the film structure is amorphous, the excess silicon atoms must be dispersed randomly within the silicon nitride.

The dissolution rate of the silicon nitride in 48% HF (at room temperature) was determined. Figure 5 shows the dissolution rate plotted as a function of the silane to ammonia injection ratio. The dissolution rate of the silicon nitride films grown at a given silane to ammonia injection ratio decreases as expected with increasing deposition temperature. The 800°C films dissolved much faster than the 900° and 1000°C films.

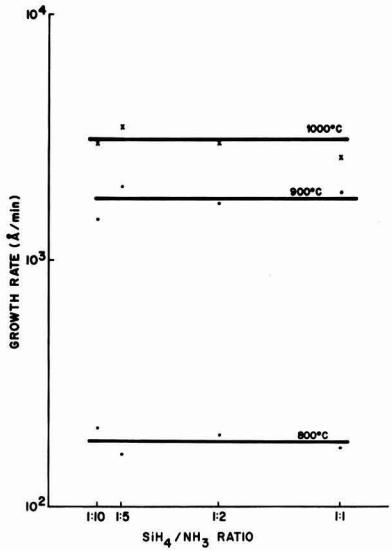

Fig. 4. Growth rate *vs.* silane to ammonia injection ratio

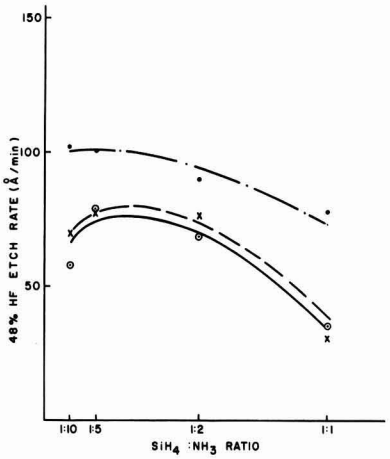

Fig. 5. Dissolution rate in 48% HF vs. silane to ammonia injection ratio. ●, 800°C films; X, 900°C films; ⊙, 1000°C films.

This suggests that the 800°C films are substantially less tightly bound than the 900° and 1000°C films. The dissolution rate of the films grown at a given temperature decreases with decreasing ammonia injection rate as it approaches the silane injection rate. This can be due to the film composition changing toward the silicon rich silicon nitride.

In all capacitance-voltage measurements a negative bias is required on the aluminum to observe the flat-band capacitance. Flat-band surface charge is defined by $N_{FB} = C_N V_{FB}/q$ where C_N is the nitride film capacitance per square centimeter, V_{FB} is the flat-band bias, and q is electronic charge. In Fig. 6 the surface charge is plotted *vs.* silane:ammonia ratio for films deposited at 800°, 900°, and 1000°C. It is seen that the magnitude of N_{FB} varies with deposition temperature (900°C giving lowest values) but has little dependence on the silane:ammonia ratio. The surface charge has the same sign as that found with thermally grown SiO_2 but is an order of magnitude larger (7). The dielectric constant of the films was obtained by measuring capacitance per square centimeter in the accumulated portion of the C-V characteristic and thickness by the Tolansky technique (5) after etching a step with HF. Uncertainties in the film thickness, electrode area, and capacitance indicate an absolute error in the dielectric constant of, at most, 3%. This permits more accurate dielectric constant measurements than

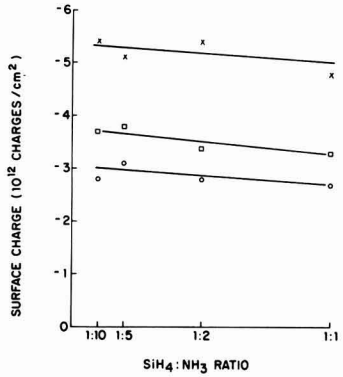

Fig. 6. Flat-band surface charge from C-V measurements on pyrolytic silicon nitride films deposited on silicon. Measurement frequency is 10 kHz. □, 800°C films; ○, 900°C films; X, 1000°C films.

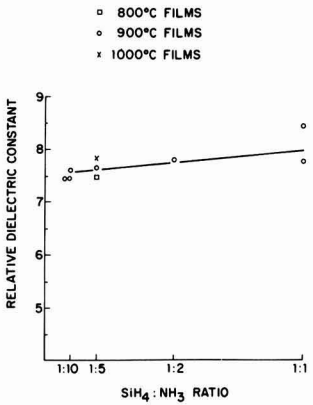

Fig. 7. Relative dielectric constant of pyrolytic silicon nitride films. Measurements are at 25°C and 10 kHz. Each data point represents an individual wafer. □, 800°C films; ○, 900°C films; X, 1000°C films.

those previously reported (1, 9). Figure 7 shows that the relative dielectric constant (measured at 10 kHz) has little dependence on the deposition temperature or the silane:ammonia ratio and approaches a value of 7.6 as the ammonia fraction increases. Dielectric constant measurements over the range 100 Hz to 1 MHz show no variation with frequency.

At high fields ($E > 10^6$ V/cm), electronic leakage currents were observed at room temperature in the MIS devices. These currents are characterized as being reproducible between devices on a given wafer, being symmetrical with respect to polarity of the d-c bias, showing no decay with time, and having a nonohmic I-V characteristic. Note that log (I/A) is a linear function of the square root of the applied field as shown in Fig. 8 and that doubling the field results in a current increase by several orders of magnitude. Figure 8 also shows a strong dependence of the conductivity on the silane:ammonia ratio. Increasing the ammonia fraction causes a shift of the curve to higher fields with little change of slope. Increasing the ammonia fraction beyond the 1:10 ratio causes very little additional shifting of the characteristic. The slopes of

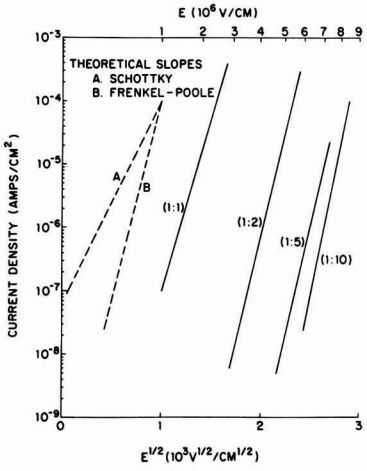

Fig. 8. Electronic leakage of pyrolytic silicon nitride films deposited at 900°C. Measurements are at 25°C, and the silane:ammonia ratios are given in parentheses on each curve. Theoretical slopes are shown for Schottky barrier injection and Frenkel-Poole emission from traps.

the curves permit a tentative identification of the conduction mechanism. Schottky barrier injection from the electrodes gives a current dependence on the field of $I \sim \exp(q^3E/\pi\epsilon)^{1/2}/2kT$ where E is the field, and ϵ is the optical dielectric constant of the insulator. A Frankel-Poole mechanism (10) in which carriers are emitted from traps in the bulk of the film gives the dependence $I \sim \exp(q^3E/\pi\epsilon)^{1/2}/kT$, which has twice the slope of the Schottky equation. These theoretical slopes are shown in Fig. 8 using a dielectric constant of $\epsilon/\epsilon_0 = 4$ (refractive index squared) and $T = 300°K$. The slopes of the experimental curves and the symmetry with bias polarity are evidence for the bulk-limited, Frenkel-Poole mechanism. A detailed study of the conduction mechanism is being conducted.

Conclusion

In the pyrolytic deposition of the amorphous silicon nitride films with the reaction of silane and ammonia, the film property changes were investigated as a function of the reactant composition. The reactant composition was changed by gradually reducing the ammonia injection rate while the silane injection rate was kept constant. The potential of developing cracks in silicon nitride films deposited on silicon substrates is greatly reduced by decreasing the ammonia injection rate to 1-5 times greater than the silane. However, the structure of all films in this work grown with low ammonia and in the previous work (1) with high ammonia ratios is amorphous. The index of refraction increases while the dissolution rate in 48% HF decreases with a decreasing ammonia junction rate. These results indicate that silicon nitride films grown with reduced ammonia (approaching the silane rate) are silicon rich in film composition. The electronic leakage current increases rapidly with decreasing ammonia. The film deposition rate, the dielectric constant, and the flat-band charge density are not significantly affected by the ammonia injection rate.

Acknowledgment

The authors wish to thank Dr. S. Dash for the electron microscopy and diffraction analysis, Mr. J. R. Petrak for the electrical measurements, and Dr. G. A. Silvey for valuable discussion. This work was supported in part by the National Aeronautic and Space Administration, Electronic Research Center under Contract NAS 12-105.

Manuscript received April 19, 1967; revised manuscript received Sept. 21, 1967. This paper was presented in part at the Philadelphia Meeting of the Society, Oct. 9-14, 1966, as Abstract 146. The research reported in this paper was sponsored by the Electronics Research Center of the National Aeronautics and Space Administration under NASA Contract No. 12-105.

Any discussion of this paper will appear in a Discussion Section to be published in the December 1968 JOURNAL.

REFERENCES

1. V. Y. Doo, D. R. Nichols, and G. A. Silvey, *This Journal*, **113**, 1279 (1966).
2. K. E. Bean, P. S. Gleim, and W. R. Runyan, Paper presented at the Philadelphia Meeting of the Society, Oct. 9-14, 1966, as Abstract 147.
3. J. H. Scott and J. A. Olmstead, *ibid.*, Abstract 151.
4. C. H. Lee, T. L. Chu, and G. A. Gruber, *ibid.*, Abstract 154.
5. S. Tolansky, "Multiple-Beam Interferometry of Surfaces and Films," Clarendon Press, Oxford, England (1948).
6. D. R. Kerr, *IBM Journal*, **8**, 385 (1964).
7. A. S. Grove, B. E. Deal, E. H. Snow, and C. T. Sah, *Solid-State Electronics*, **8**, 145 (1965).
8. W. D. Forgeng and B. F. Decker, *Trans. Met. Soc. AIME*, **47**, 343 (1958).
9. S. M. Hu, *This Journal*, **113**, 693 (1966).
10. S. M. Hu, D. R. Kerr, and L. V. Gregor, *Appl. Phys. Letters*, **10**, 97 (1967).

Computer Programs for Quantitative and Semiquantitative Analysis with the Electron Microprobe Analyzer

S. S. So and H. R. Potts*

Systems Development Division, International Business Machines Corporation, Endicott, New York

ABSTRACT

A description of two FORTRAN IV computer programs is presented to simplify quantitative and semiquantitative analysis with the electron microprobe analyzer. The first program, EPMP1, determines the weight fraction of each element in a specimen from the characteristic x-ray intensity measurements of the specimen and the standards. The second program, EPMP2, calculates the relative characteristic x-ray intensities of all the elements in a specimen by assuming the composition of the specimen to be known. The correction procedure includes dead time correction, one of two background corrections (either constant background or background depending on composition), Philibert's absorption correction modified by Duncumb and Shields, one of three fluorescence corrections (either Birks', Castaing's, or Reed's), and a compound standard correction. The effects of the absorption and the fluorescence of each element in the specimen are easily seen from the output results. Versatility, efficiency, and ease of operation are emphasized in the programs.

Two FORTRAN IV computer programs[1] have been written to facilitate quantitative and semiquantitative analysis with the electron microprobe analyzer. The first program, EPMP1, calculates the weight fraction of each element in the specimen from the characteristic x-ray intensity measurements of the specimen and the standards. The second program, EPMP2, which is essentially the inverse of the first program, calculates the relative characteristic x-ray intensities of all

* Present address: IBM, Components Division, East Fishkill, New York.

[1] The program package is available from the IBM Program Information Department, Hawthorne, New York.

the elements in the specimen by assuming the composition of the specimen to be known.

Many correction procedures for electron microprobe analysis are available in literature (1-13). Each procedure has it merits and deficiencies, depending on the system being analyzed. Because of the complex, tedious, and time-consuming process of these correction procedures, computer techniques have been used to make proper correction for a more accurate quantitative analysis (14-18). The present programs include the following corrections: (*i*) dead time correction, (*ii*) a background correction (either constant background or background dependent on composition), (*iii*) Philibert's absorption correction modified by Duncumb and Shields, (*iv*) Birks', Castaing's, or Reed's fluorescence correction, and (*v*) a compound standard correction. However, there is no correction provided in the programs for the errors contributed by the following: atomic number effect, fluorescence excitation by the continuum, or contamination of the specimen and the standards.

The programs emphasize versatility and ease of operation. The large combinations of input data indicate the flexibility of the programs; this flexibility allows use of experimental data from various commercial electron microprobes. Codes for the various corrections are provided to eliminate unnecessary input data and computations; these codes thus enhance the efficiency of the programs.

Theory of Corrections

The theory of electron microprobe analysis is based on relating the weight fraction of an element in a specimen to a ratio. This ratio is defined as the characteristic x-ray intensity generated in the specimen to that generated by a pure standard of the same element under the same experimental conditions. The characteristic x-ray intensity measured by the electron microprobe analyzer is affected by the following: finite resolving time of the detector, background x-ray spectrum, absorption of the emerging characteristics radiation in the specimen, and the fluorescence excitation by the characteristic radiations of other elements in the specimen. The program considers the previous effects in order to have an accurate quantitative analysis.

Due to the finite resolving time of the detector, the measured x-ray intensity, I_M, is less than true intensity, I_T. If the dead time, DT, is known, the program will make a dead time correction for all measured x-ray intensities as given by

$$I_T = \frac{I_M}{1 - I_M \cdot DT \cdot 10^{-6}} \qquad [1]$$

where DT is in microseconds. If no dead time correction is necessary, set $DT = 0$, and the program will bypass above calculation.

Two types of background intensity corrections are provided in the program, the constant background and the background depending on the composition. If the continuum x-ray intensity, I_B, is small compared with the measured characteristic intensity, I_T (corrected for dead time), a constant background may be used. The corrected x-ray intensity for the i^{th} element in a matrix or the i^{th} standard element is simply given by

$$\begin{aligned} I_i &= I_T - I_B \\ I_{std} &= I_{Tstd} - I_{Bstd} \end{aligned} \qquad [2]$$

However, for very small weight fractions (where the characteristic intensity approaches that of the continuum) the background intensity must be measured for each characteristic radiation and for each element in the specimen. Then the background intensity for the i^{th} element is given by

$$(I_B)_i = \sum_j W_j I_{ji} \qquad [3]$$

where W_j is the weight fraction of the j^{th} element and I_{ji} is the background intensity of the i^{th} element due to the j^{th} element. The summation is carried over all the elements in the specimen.

The characteristic radiation is generated beneath the surface of the target and undergoes absorption when it emerges from the target before being detected by the spectrometer. Philibert's absorption correction (4), modified by Duncumb and Shields (11), is used in the program. The true weight fraction of the i^{th} element in the specimen, with absorption correction, is given by

$$W_i = I_{rel}\left[\frac{F_{std}(\chi)}{F_i(\chi)}\right] \qquad [4]$$

where the relative x-ray intensity, I_{rel}, is defined as the ratio of measured characteristic x-ray intensity from the specimen to that of the standard (corrected for dead time and background)

$$I_{rel} = \frac{I_i}{I_{std}} \qquad [5]$$

and $F_{std}(\chi)$ and $F_i(\chi)$ are the absorption correction factors for the standard and the specimen, respectively. The absorption correction parameter is given by

$$F(\chi) = \frac{1}{\left(1 + \frac{\chi}{\sigma}\right)\left[1 + h\left(1 + \frac{\chi}{\sigma}\right)\right]} \qquad [6]$$

where

$$\chi = \operatorname{cosec}\psi \cos\theta \sum_j \mu_{ij} W_j \qquad [7]$$

$$h = 1.2\frac{\sum_j A_j W_j}{\left[\sum_j Z_j W_j\right]^2} \qquad [8]$$

$$\sigma = \frac{2.39 \times 10^5}{V^{1.5} - V_c^{1.5}} \qquad [9]$$

with μ_{ij} as the mass absorption coefficient for characteristic radiation generated from the j^{th} element absorbed by the i^{th} element, ψ as x-ray emerging angle with respect to the surface of the target, θ as incident electron beam angle with respect to the normal of the target, A as the atomic weight, Z as the atomic number, V as the incident electron beam potential, and V_c as the critical excitation potential. Note that the parameter χ has been modified to account for the inclination of the target to the electron beam.

When the characteristic radiation of the j^{th} element is shorter in wavelength than the absorption edge of the i^{th} element, it is able to enhance the characteristic radiation of the i^{th} element. The true weight fraction of the i^{th} element in a specimen, with both absorption and fluorescence corrections, is then given by

$$W_i = I_{rel}\left[\frac{F_{std}(\chi)}{F_i(\chi)}\right]\left[\frac{1}{1 + K_{fi}}\right] \qquad [10]$$

where K_f is the fluorescence correction factor. Three methods are available in the program to calculate the fluorescence correction parameter, K_f.

Birks' equation (7) is given by

$$K_{fi} = 0.6 \sum_j E_{ij} W_j \left(\frac{\mu_{ij}}{\mu_j}\right)\left(\frac{V - V_{cj}}{V - V_{ci}}\right)^{1.65} \qquad [11]$$

where E_{ij} is the excitation efficiency of the i^{th} element by the characteristic radiation of the j^{th} element, and μ_j is the mass absorption coefficient of the specimen for characteristic radiation generated from j^{th} element.

Castaing's equation (1) is given by

$$K_{fi} = 0.5\left(\frac{r_i - 1}{r_i}\right)\sum_{j \neq 1} W_j \omega_j(K)\left(\frac{\lambda_j}{\lambda_i}\right)\left(\frac{\mu_{ij}}{\mu_j}\right)\left(\frac{A_i}{A_j}\right) \cdot \left[\frac{\ln(1+u)}{u} + \frac{\ln(1+v)}{v}\right] \qquad [12]$$

where

$$u = \left(\frac{\mu_i}{\mu_j}\right) \operatorname{cosec} \psi \qquad [13]$$

$$v = \left(\frac{\sigma}{\mu_j}\right) \sec \theta \qquad [14]$$

with r_i as the absorption edge jump ratio (12), $\omega(K)$ as the K-shell fluorescence yield (19), and λ as the characteristic wavelength.

Reed's equation (9) is a modified form of Castaing's equation; it considers all cases involving K and L characteristic radiations and may be written as

$$K_{fi} = 0.5\, P_{mn} \left(\frac{r_i - 1}{r_i}\right) \sum_{\substack{j \\ j \neq i}} W_j\, \omega_j(K) \left(\frac{U_j - 1}{U_i - 1}\right)^{1.67} \cdot \left(\frac{\mu_{ij}}{\mu_j}\right)\left(\frac{A_i}{A_j}\right) \left[\frac{\ln(1+u)}{u} + \frac{\ln(1+v)}{v}\right] \qquad [15]$$

where $P_{KK} = P_{LL} = 1$, $P_{KL} = 0.24$, $P_{LK} = 4.2$, and

$$U_i = \frac{V}{V_{ci}} \qquad [16]$$

If a compound of known composition is used as a standard for the i^{th} element instead of a pure standard, then the measured x-ray intensity of that element from the compound standard (I_{cs}) must be adjusted to be equivalent to the pure standard form (I_{std}). Namely,

$$I_{std} = \frac{I_{cs}}{\xi_i} \qquad [17]$$

where the compound standard correction factor is calculated from

$$\xi_i = W_i \left[\frac{F_i(\chi)}{F_{cs}(\chi)}\right] (1 + K_{fcs}) \qquad [18]$$

to include both absorption and fluorescence effects of the compound standard.

Programs

Quantitative analysis.—The first program, EPMP1, calculates the weight fraction of each element in the specimen from the characteristic x-ray intensity measurements of the specimen and the standards. Figure 1 outlines the basic operation of EPMP1. Many features are built into the program to handle various situations in data compilation. Any number of problems can be analyzed in the same run of the program by simply stacking each set of input data one after another. The program treats each set of input data as a separate analysis. However, in the analysis of a system of specimens consisting of the same elements but different compositions, the standard intensity measurements may change from one specimen measurement to another because of the stability of the electron microprobe. In this case, the input data for the successive problems may be simplified by the continuation code. Other codes are provided for dead time, background, fluorescence, and compound standard corrections to enhance the efficiency of the program. If any of these corrections are not necessary, then input data is not required for that correction and the program will bypass the execution of that correction. (See List of Input Data.)

The incident electron beam of variable energy may be inclined at any angle with respect to the target. The x-ray emerging angle may be varied from element to element in the specimen. Each element in the specimen has its own compound standard code, so that any number of compound standards may be used as the standard of the specimen. The elements in the specimen may be analyzed in any order. Furthermore, if there is an uncertainty in any of the specimen x-ray intensity measurements, that intensity may be set to zero in the input data. The program will calculate the weight fractions of all other elements in the specimen and will set the remaining weight fraction in the specimen equal to the weight fraction of the uncertain element. This is the only case where the quantitative analysis will yield normalized weight fractions.

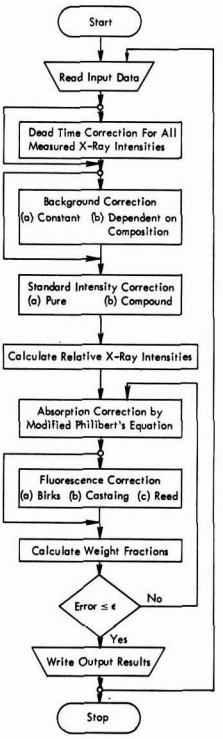

List of Input Data

1. Codes for dead time correction, background correction, compound standard correction, and fluorescence correction.
2. Instrument parameters V, θ, ψ, DT.
3. Element parameters Z, A, V_c.
4. Intensity measurements I_M, I_B, I_{std}.
5. Mass absorption coefficient matrix, μ_{ij}.
6. (a) Excitation efficiency matrix, E_{AB} (b) Absorption edge jump ratio, r_K, and fluorescence yield, ω_K.

Fig. 1. Flow chart of EPMP1

Note that the background (dependent on composition), absorption, fluorescence, and compound standard corrections are all dependent on the weight fractions of each element in the specimen. However, these weight fractions are the unknowns of the quantitative analysis. Therefore, the normalized relative x-ray intensities are taken as a first approximation for the weight fractions in calculating the correction terms. This is the only place where any normalization occurs in the iterative approximation. After having made the proper correction, the unnormalized weight fractions obtained from the previous approximation are then used to recalculate the correction terms for the successive approximations. This sets up the iterative procedure which is satisfied by either: (*i*) the successive approximations of the weight fractions do not change by more than a specified error, ϵ, or (*ii*) the specified number of iterations has been reached. In the latter case, a warning message will be printed out to indicate the slow convergence or the divergence of the iterative steps.

All input data are printed out for easy reference, and they also serve as a record of the problem analyzed. In the output data, the measured relative x-ray intensity and the unnormalized weight fractions (with absorption correction or with both absorption and fluorescence corrections) are printed out. From these values, the effect of the absorption and the fluorescence of each element in the analyzed system is clearly seen. The value of the total unnormalized weight fractions gives an indication of the accuracy of the experimental data.

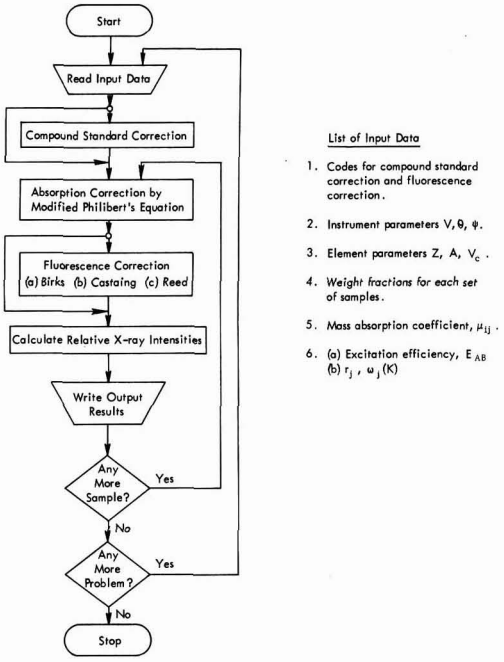

Fig. 2. Flow chart of EPMP2

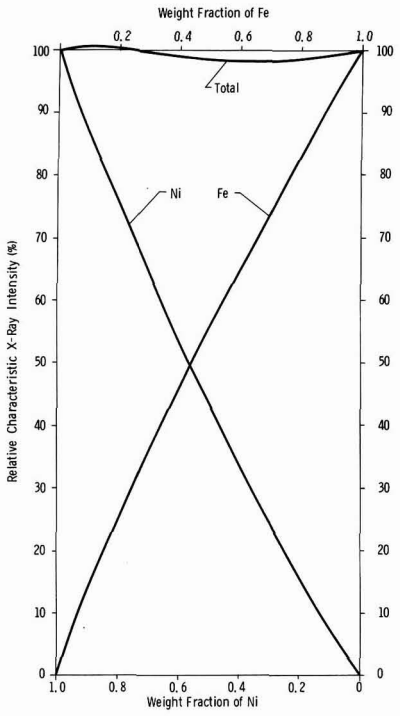

Fig. 3. Calculation of relative x-ray intensity by EPMP2 for FeNi binary alloys.

Semiquantitative Analysis.—The second program, EPMP2, is particularly useful in a quick semiquantitative analysis, especially for binary alloys. By assuming various combinations of the weight fractions of a specimen, this program calculates the relative x-ray intensity of each element in the specimen. Figure 2 outlines the basic operation of EPMP2. The correction procedure is the same as the first program, EPMP1 (for the quantitative analysis), except no iterative approximation is necessary since the weight fractions of the specimen are assumed to be known. The calculated results may be plotted on a graph. Then, from the measured relative x-ray intensity (taken with the electron microprobe analyzer), the graph directly gives the weight fraction of that element (Fig. 3). Furthermore, it gives an indication of the degree of accuracy of the x-ray intensity measurements by noting: (*i*) how near the measured relative intensities approximate a vertical line, or (*ii*) how close the total measured relative x-ray intensity compared with the total calculated relative x-ray intensity.

Examples

Table I and Fig. 3 are included to illustrate quantitative and semiquantitative analysis with the electron microprobe analyzer on a system of FeNi alloys over a wide range of compositions. The data[2] used in each alloy correspond to the averaged values of three different locations on the alloy, with ten consecutive measurements over each location. The measured relative intensities (in per cent) of Table I are calculated by Eq. [5].

By assuming various combinations of weight fractions of Fe and Ni, the relative characteristic x-ray intensities are calculated by EPMP2. These results are plotted on a graph as shown in Fig. 3. Using the values of measured, relative, characteristic x-ray intensities from Table I (column 3), Fig. 3 directly yields the weight fractions which are shown in column 4 of Table I. This gives a quick semiquantitative analysis of FeNi alloys. If more accurate results are required, the raw data from the electron microprobe analyzer measurements can be fed into EPMP1. Since three methods of fluorescence correction are available in the program, the differences between Birks', Castaing's, and Reed's equations are easily detected by comparing their results as shown in columns 5, 6, and 7 of Table I. The weight fractions of the FeNi alloys were determined by chemical analysis, and listed in column 8 of Table I.

By comparing column 4 of Table I with columns 5, 6, and 7, one can see that the results of EPMP2 are a good approximation to the quantitative analysis. Furthermore, by comparing columns 5, 6, and 7, one should note that the fluorescence corrections by Birk's,

Table I. Quantitative analysis of FeNi alloys

1	2	3	4	5	6	7	8
		Measured relative intensity, %	EPMP2	EPMP1			Chemical analysis*
Set			Weight fraction	Weight fraction[a]	Weight fraction[b]	Weight fraction[c]	Weight fraction
I	Fe	14.06	0.105	0.09810	0.10005	0.10607	0.106
	Ni	86.28	0.895	0.88945	0.88988	0.89125	0.888
	Total	100.34	1.000	0.98755	0.98993	0.99732	0.994
II	Fe	43.42	0.375	0.37907	0.36623	0.37804	0.370
	Ni	54.32	0.610	0.60810	0.60635	0.60799	0.628
	Total	97.74	0.985	0.98717	0.97258	0.98603	0.998
III	Fe	49.42	0.435	0.44155	0.42675	0.43862	0.437
	Ni	48.92	0.555	0.55706	0.55525	0.55674	0.564
	Total	98.34	0.990	0.99861	0.98200	0.99536	1.001
IV	Fe	95.00	0.940	0.94693	0.94484	0.94590	0.939
	Ni	2.51	0.030	0.03278	0.03278	0.03278	0.051
	Total	97.51	0.970	0.97971	0.97762	0.97868	0.990

[a] Birks' fluorescence correction.
[b] Castaing's fluorescence correction.
[c] Reed's fluorescence correction.
* G. Fisher, INCO.

[2] Measurements were taken by Electron Microprobe Analyzer, Model 400, Materials Analysis Company, at an electron beam voltage of 30 kv.

Table II. Correlation of relative intensities calculated from weight fractions by EPMP2 and weight fractions calculated from these intensities by EPMP1

	Input to EPMP2 = Output from EPMP2			Input to EPMP1 = Output from EPMP1	
	Weight fractions		Relative intensity (%)*		Weight fractions*
Set	P	Cu	P	Cu	P	Cu
1	0.1	0.9	3.71182	89.45734	0.10001	0.90000
2	0.2	0.8	7.99170	79.00667	0.20002	0.79999
3	0.3	0.7	12.97807	68.65514	0.30005	0.69999
4	0.4	0.6	18.85751	58.41150	0.40008	0.59999
5	0.5	0.5	25.88731	48.28600	0.50011	0.49999
6	0.6	0.4	34.43199	38.29140	0.59999	0.40000
7	0.7	0.3	45.02460	28.44341	0.70012	0.29999
8	0.8	0.2	58.47522	18.76149	0.80007	0.20000
9	0.9	0.1	76.07399	9.27002	0.89999	0.10000

* Modified Philibert's absorption correction and Reed's fluorescence correction.

Castaing's, and Reed's equations differ more significantly for small weight fraction of Fe but tend to agree for larger weight fraction of Fe.

One way to check the accuracy of the iterative approximation of EPMP1 is to use the output from EPMP2 as the input of EPMP1. Then by comparing the output from EPMP1 with the original input to EPMP2, the difference gives a direct indication of the accuracy of the iterative approximation used in EPMP1. Table II illustrates this check with a system of PCu alloys. Nine sets of weight fractions of P and Cu are assumed and used in the input data to EPMP2. The relative characteristic x-ray intensities calculated by EPMP2 are then used as the input data to EPMP1. The weight fractions calculated by EPMP1 may be compared with the original assumed weight fractions. The difference, less than $\pm 0.03\%$, is the error of the iterative approximation of EPMP1.

Similarly, the uncertainty in any parameter of the correction procedure may be detected by varying that parameter. By comparing the output results, one gets an indication of the resultant effect on the quantitative analysis due to that particular parameter.

Conclusions

Two FORTRAN IV computer programs have been used to facilitate quantitative and semi-quantitative analysis with the electron microprobe analyzer. These programs emphasize versatility, efficiency, and ease of operation. A primary advantage of these programs is the freedom of the user to utilize many alternative forms of correction to coincide with the data available. The efficiency of the programs is enhanced by the codes provided, so that unnecessary input data and computations are eliminated. All input data are printed out for easy reference, and they also serve as a record of the problem analyzed. From the output results, the effect of the absorption and the fluorescence of each element in the analyzed system is clearly indicated.

The over-all accuracy of the quantitative and the semiquantitative analysis with the electron microprobe analyzer is still limited by many factors. It not only depends on the system of elements being analyzed, but also depends on the correction procedures, the uncertainty in their parameter values, and the over-all experimental error. As better theories for the electron microprobe analysis are developed, the present programs can be easily modified to give more accurate results.

Acknowledgments

The authors wish to thank Mr. H. R. MacQueen for experimental data measurements; Metropolitan New York section of The Electron Probe Analysis Society of America for supplying the FeNi specimens and the wet chemistry data on them; and Mr. J. E. Riedy for his assistance in preparing the manuscript.

Manuscript received March 28, 1967; revised manuscript received Sept. 28, 1967.

Any discussion of this paper will appear in a Discussion Section to be published in the December 1968 JOURNAL.

REFERENCES

1. R. Castaing, Ph.D. Thesis, Univ. of Paris, 1951; O.N.E.R.A. Publication No. 55 (1952); Report No. WAL 142/59-7 (English).
2. D. B. Wittry, Univ. of S. California Engineering Center, Rept. 84-204 (1962).
3. D. M. Poole and P. M. Thomas, *J. Inst. Metals*, **90**, 228 (1962).
4. J. Philibert, "X-Ray Optics and X-Ray Microanalysis," p. 379, Pattee *et al.*, Editors, Academic Press, New York (1963).
5. G. Archard and T. Mulvey, "X-Ray Optics and X-Ray Microanalysis," p. 398, Academic Press, New York (1963).
6. M. Green, "X-Ray Optics and X-Ray Microanalysis," p. 361, Pattee *et al.*, Editors, Academic Press, New York (1963).
7. L. S. Birks, "Electron Probe Microanalysis," Interscience Publishers, New York (1964).
8. T. O. Ziebold and R. E. Ogilvie, *Anal. Chem.*, **36**, 322 (1964).
9. S. J. B. Reed, *Brit. J. Appl. Phys.*, **16**, 913 (1965).
10. R. Theisen, "Quantitative Electron Microprobe Analysis," Springer-Verlag, New York Inc. (1965).
11. P. Duncumb and P. K. Shields, "The Electron Microprobe," p. 284, McKinley *et al.*, Editors, John Wiley & Sons, Inc, New York (1966).
12. K. F. J. Heinrich, *ibid.*, p. 296.
13. J. W. Colby, *ibid.*, p. 95.
14. J. D. Brown, *Anal. Chem.*, **38**, 890 (1966).
15. J. W. Criss and L. S. Birks, "The Electron Microprobe," p. 217, McKinley *et al.*, Editors, John Wiley & Sons, Inc., New York (1966).
16. E. Davidson, W. E. Fowler, H. Neuhans, and W. G. Shequen, *ibid.*, p. 454.
17. D. R. Beaman, Second National Conference on Electron Microprobe Analysis, Boston, Mass. (1967).
18. H. E. Bishop, *Brit. J. Appl. Phys.*, **18**, 703 (1967).
19. R. W. Fink, R. C. Jopson, H. Mark and C. D. Swift, *Rev. Modern Phys.*, **38**, 513 (1966).

Crystal Growth of a New Laser Material, Fluorapatite

R. Mazelsky,* R. C. Ohlmann, and K. Steinbruegge

Westinghouse Electric Corporation, Research and Development Center, Pittsburgh, Pennsylvania

ABSTRACT

Neodymium-doped calcium fluorophosphate is an efficient laser crystal. The growth method, chemistry, spectroscopy, and some pulsed laser results are presented.

The growth of laser technology has resulted in the need for crystals of large size which can perform at higher efficiencies than currently existing materials. A material that meets these specifications is neodymium-doped calcium fluorophosphate, $Ca_5(PO_4)_3F$. This material doped with manganese and antimony is known to be an efficient phosphor and is, in fact, used in

* Electrochemical Society Active Member.

fluorescent lamps. Johnson (1) has been successful in pulling large crystals of fluorapatite, pure and manganese-doped, from the melt. We have succeeded in preparing crystals by the Czochralski method which, when doped with neodymium, show laser oscillations at low threshold. This paper describes the method and apparatus for growth of the crystals and the pertinent spectroscopic data.

Experimental

The pulling apparatus was designed such that pull rates between 1 and 40 mm/hr and rotation speeds of 10-110 rpm can be used. The furnace is surrounded by a quartz cylinder attached to the apparatus by means of a neoprene gasket and a brass flange. There are inlet holes for the introduction of appropriate atmospheres and a temperature sensing device. An iridium crucible is used to contain the fluorapatite. Insulation is provided by ½-in. thick zirconia quadrants stacked to form a cylinder. A circular zirconia plate with an access hole caps the furnace and serves as a reflector for minimizing thermal losses from the surface of the melt.

Heating is accomplished using a 30 kw motor-driven 10 kc generator, the a-c power driving water-cooled copper induction coils. It has been found that the lower frequencies give fairly uniform heating even though there are irregularities present in the iridium susceptor. Even with large irregularities no "hot spots" have been observed.

Temperature is controlled by using the output of a sapphire-light-pipe radiomatic detector and feeding it into an L&N Azar recorder controller. The voltage from the recorder controller in association with an L&N current adjusting type relay supplies the input circuit of a Norbatrol linear power controller. The Norbatrol output voltage supplies the necessary field excitation required by the 10 kc generator.

The seed holder consists of a pin vise or a water-cooled copper shaft which is threaded to accommodate a tantalum chuck. The seed is pinned to the tantalum chuck which is then threaded onto the water-cooled shaft such that the seed butts against the shaft. A schematic of the apparatus is shown on Fig. 1.

The fluorapatite crystals are grown in an argon atmosphere. The temperature at the surface of the melt as determined by optical pyrometer readings uncorrected for emissivity is 1705°C during growth. Pull rates of 3-8 mm/hr are used, and the seed crystal is rotated between 30-100 rpm. The melt is quite viscous, and the rapid rotation rate creates a visible swirl pattern on the surface of the melt.

Crystals obtained using rapid pull rates had visible feathery imperfections along the center of the boule. These were described by Johnson (1) as "opalescent inclusions." However, these "feathers' can be minimized or removed by utilizing slower pull rates in the range of 3-5 mm/hr. By using a seed crystal in which the feathers are present, it is possible to propagate these imperfections along the length of the crystal. Rapid changes in the diameter of the growing crystal results in large numbers of these imperfections. Under these conditions the preferred direction for the propagation of imperfections is along the "c" axis of the crystal. It is believed that these imperfections are associated with fluoride vacancies.

Neodymium-doped crystals can be obtained by simple substitution of neodymium for calcium in the melt. Since neodymium is a trivalent ion substituting for divalent calcium, some charge compensation is necessary. There is a self-compensating mechanism by which a fluoride ion may be replaced by an oxide ion. This can also be accomplished by the creation of a vacancy. The chemical formulas for crystals compensated in these ways can be represented by the following

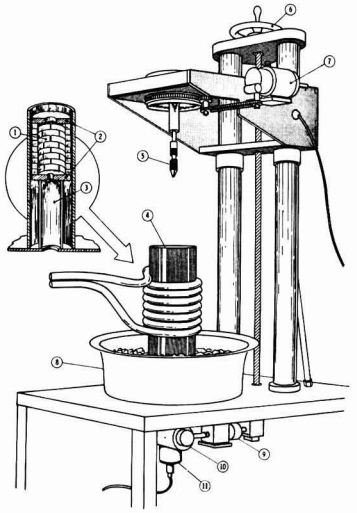

Fig. 1. Schematic of crystal puller. 1, Stabilized zirconia quadrant bricks; 2, stabilized zirconia quadrant plates; 3, stabilized zirconia quadrant cylinder; 4, 90 mm Vycor tube; 5, seed chuck; 6, manual feed; 7, rotator motor; 8, stainless steel basin; 9, electrically operated clutch; 10, pull motor; 11, sapphire rod radiomatic detector.

$$Ca_{5-3x/2}\,Nd_x\,(PO_4)_3\,F$$

$$Ca_{5-x}\,Nd_x\,(PO_4)_3\,F_{1-x}\,O_x$$

Both mechanisms are possible although it is not clear which predominates during growth.

Calcium fluorophosphate is a complicated chemical system in which it is necessary to consider at least four chemical entities, Ca^{+2}, PO_4^{-3}, $O^{=}$, and F^{-}. It is indeed fortuitous that the combination is congruently melting. The substitution of neodymium in the melt is an additional complication. Calcium fluorophosphate is prepared by combining the appropriate weights of $CaHPO_4$, $CaCO_3$, and CaF_2. The substitution of neodymium for calcium can be accomplished by the replacement of any of these compounds with Nd_2O_3. Crystals were grown with Nd_2O_3 replacing $CaCO_3$, CaF_2, and combinations of the two. In all cases crystals of fair quality were obtained but they had a pronounced tendency to form color centers under ultraviolet radiation. The problem of color centers in halophosphate crystals has been discussed by Swank (2). Substitution of neodymium can also be accomplished by charge compensation; *i.e.*, Na^{+1}, Nd^{+3} pairs being introduced into the divalent sites. No differences were observed in the Nd emission spectra or in the laser properties, whether the crystals were ion-compensated or allowed to self-compensate.

The segregation coefficient of neodymium in calcium fluorophosphate was determined by x-ray fluorescence analysis. Standard concentrations of neodymium in the host were prepared by solid-state reaction and analyzed. Then small crystals were grown from charges of several concentrations of neodymium varying from 0.5 to 5%. Crystals of the same concentration were pulled at different rates and analyzed to insure that the system was near equilibrium. In each case the mass of the crystals pulled were less than 1% of the total charge. The crystals, ground into powders, were analyzed for neodymium by x-ray fluorescence and compared to the standards. In this manner the concentration of neodymium in the pulled crystal as compared to the melt was determined. A plot of atomic per cent (a/o) neodymium in the melt versus atomic per cent neodym-

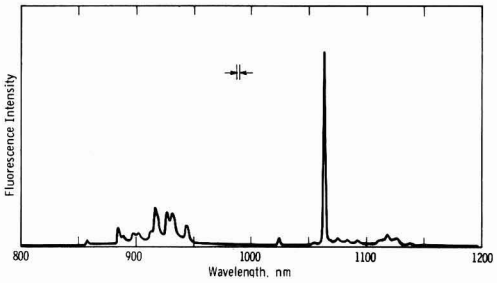

Fig. 2. Relative quanta rate of fluorescence of Nd doped $Ca_5(PO_4)_3F$ at room temperature and 523 nm excitation. Corrected spectrum.

ium in the solid was prepared and a segregation coefficient of 0.52 was determined.

Optical properties.—The fluorescence spectrum of Nd^{3+} in calcium fluorophosphate at room temperature is shown in Fig. 2. This spectrum has been corrected for sensitivity so that the amplitude is proportional to quanta/sec nm. A larger fraction of the Nd^{3+} emission is present in a single line (at 10629Å) than is found in the Nd^{3+} spectra in most other host crystals. The fluorescence decay time of the Nd^{3+} fluorescence is 180 μsec at room temperature in a crystal containing 1 a/o neodymium by analysis.

The spectral quantum efficiency, *i.e.*, the number of quanta emitted per unit wavelength interval for each quantum absorbed, particularly at the peak of an emission line, is an important parameter for laser materials. The room temperature line width of the principal line in calcium fluorophosphate is 6Å, about the same as in yttrium aluminum garnet (YAG). The greater concentration of the emission in a single line in fluorapatite implies a greater spectral quantum efficiency than in YAG for the same over-all efficiency. A direct comparison of a YAG:Nd and fluorapatite:Nd crystal was made by measuring both the amount of energy absorbed and the peak emission intensity for each crystal. It was found that the spectral quantum efficiency at room temperature is 2 ± 0.2 times larger for Nd^{3+} in fluorapatite than in YAG for 0.5 a/o Nd in each. This implies that the stimulated emission gain for a given rate of absorbing energy is correspondingly greater for fluorapatite than YAG. The Nd^{3+} absorption and excitation spectra are similar for the two materials although fluorapatite has broader absorption bands which are more intense in the visible region of the spectrum. One would expect, therefore, that the threshold for the fluorophosphate should be considerably less than for the same size YAG:Nd rod for the same distributed losses. This has been borne out by laser tests.

Crystals of fluorapatite with 1 a/o neodymium have ben fabricated into rods 6.3 mm in diameter and 37 mm long. In the laser testing only a moderately efficient cylindrical pumping cavity was used. A typical rod was excited by a xenon flash lamp with an 800 μsec pulse length. The laser rod had flat polished and parallel ends which were uncoated. Flat external mirrors were used as resonators. The threshold with reflectivities of 99% at one end and 35% at the other was 8 joules, a factor of two lower than YAG:Nd in the same apparatus. The crystal measured appeared of poor optical quality by visual inspection and the loss coefficient was fairly large. However, slope efficiencies in excess of 1% were obtained.

Conclusion

Fluorapatite is by no means optimized with respect to either crystal quality or doping. However, sufficient data have been obtained to indicate potential superiority with respect to threshold and efficiency over existing crystalline lasers.

Acknowledgment

The authors wish to acknowledge the assistance of W. E. Kramer and E. P. H. Metz, helpful discussions with Dr. R. C. Miller and A. J. Venturino, and the analytical work of J. Rudolph.

Manuscript received Aug. 23, 1967.
Any discussion of this paper will appear in a Discussion Section to be published in the December 1968 JOURNAL.

REFERENCES

1. P. D. Johnson, *This Journal*, **108**, 159 (1961).
2. R. K. Swank, *Phys. Rev.*, **135**, 1A, 266 (1964).

Microscopic Rates of Growth in Single Crystals Pulled from the Melt: Indium Antimonide

August F. Witt* and Harry C. Gatos*

Department of Metallurgy and Center for Materials Science and Engineering, Massachusetts Institute of Technology, Cambridge, Massachusetts

ABSTRACT

Vibrations of known frequency introduced into a melt during crystal growth appear as impurity "vibrational" striations in the grown crystal. The growth-characteristics of crystal pulling under rotation (instantaneous microscopic growth rates and growth interface topography) were determined from the spacing and direction of introduced vibrational striations. It was demonstrated that periodic growth rate fluctuations (including local remelting) in the "off-facet" region are associated with rotational crystal pulling in the presence of thermal asymmetry. As a result of local remelting the average microscopic growth rate was shown to be significantly greater than the corresponding pulling rate. "Facet" growth is unaffected by rotation and proceeds at a rate which is identical with the pulling rate, although impurity heterogeneities have been identified in "facet" growth regions.

The effects of growth rates and their variations on crystalline perfection and the distribution of impurities during solidification have been treated extensively in a large number of theoretical studies (1-7). The related experimental investigations do not provide the necessary information regarding instantaneous rates of growth and impurity concentrations (8-15). In these

* Electrochemical Society Active Member.

investigations the instantaneous microscopic growth rates could not be directly determined. By necessity, the assumption has been made in some instances that the growth rate is equal to the pulling rate. Very often this assumption is not valid on the microscale. Thus, the formation of impurity striations (rotational and nonrotational) is generally attributed to periodic or random variations of the microscopic growth rate which imply deviations from the pulling rate. The origin of these growth rate fluctuations is attributed to short time temperature variations at the growth interface, caused by rotation of the growing crystal in a thermally asymmetric surrounding (rotational striations) (15), or alternately by random thermal convections due to unavoidable temperature gradients in the system (nonrotational striations) (12).

Recently a technique has been developed (16) which permits the determination of microscopic growth rates and the evaluation of interface morphology with high precision. This technique is presently applied to the investigation of InSb single crystal growth by the Czochralski technique.

Experimental Procedure

A standard Czochralski crystal puller was modified to permit the introduction of vibrations with controlled and known frequency into the melt during crystal growth (Fig. 1). The incorporation of these vibrations in the form of impurity vibrational striations was achieved by doping the InSb melt with tellurium (15 mg of Te per 50g of InSb). All crystals were grown in a <111> B direction (14) and subsequently cut along the growth axis to expose a (211) plane. The cut crystals were then mounted in plastic and polished. The final polish was obtained with a Linde "B" abrasive on a rotating wheel with the polishing direction parallel to that of the growth axis. It was found to be important that alumina abrasive particles be carefully removed from the InSb surface by means of a cotton pad under running water. The InSb crystal while still wet was immersed in a permanganate etchant for 2 min (17). The etched specimens were then rinsed in tap water, washed with soap, and dried in hot air. The etching process revealed impurity heterogeneities including the vibrational striations as elevations and depressions since the rate of etching is a function of the impurity concentration in the semiconductor. The presence of Te in InSb decreases the rate of etching. The microscopic investigation was performed with an interference contrast microscope (Normarski interferometer).

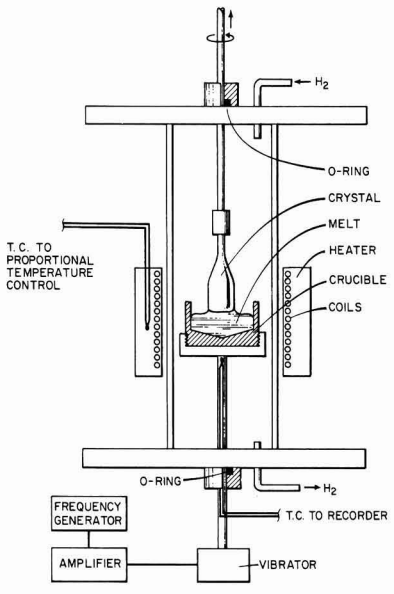

Fig. 1. Schematic representation of crystal growth arrangement

Experimental Results and Discussion

Effects of thermal asymmetry on rotational crystal growth.—A recent investigation (15) of crystal growth under rotation revealed that in the presence of thermal asymmetry the instantaneous microscopic growth rate should be subject to sinusoidal fluctuations and follow the relationship

$$V = V_0 - \frac{2\pi\Delta TR}{G}\cos 2\pi Rt \qquad [1]$$

where V is the instantaneous rate of growth, V_0 is the pulling rate, ΔT is the temperature variation during a 360° seed rotation, R is the rate of rotation, G is the temperature gradient in the melt, and t is the time.

Figure 2 is a section near the periphery of a single crystal which was pulled at a rate of 22 mm/hr and rotated at a rate of 8 rpm. The vibrational frequency was 3.5/sec. The thermal asymmetry was measured by a rotating thermocouple in the melt (without the seed present) at a distance of 6 mm from the rotational axis and was found to be 1.8°C for a full rotation. It is, of course, expected that the thermal asymmetry during actual growth (ΔT in Eq. [1]) is somewhat different from the one measured. The changing spacing of the vibrational striations clearly reveals periodic growth rate changes with a periodicity of V_0/R. The so-called rotational striations (indicated by arrows) can be clearly identified here as the result of a decreased microscopic growth rate (decreased spacing in vibrational striations) which took place in the "hot" region of the thermally asymmetric melt (15). The actual in-

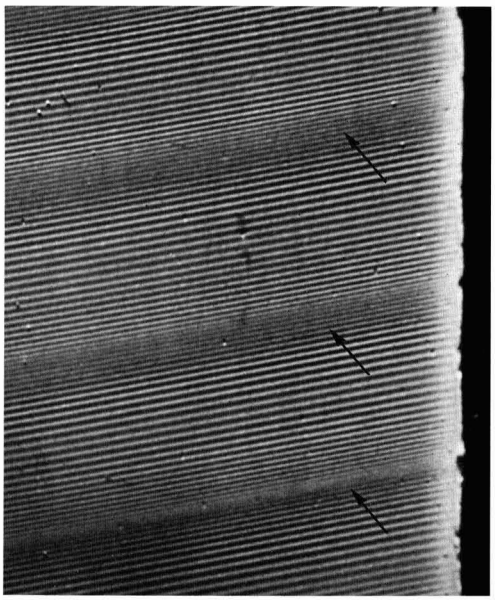

Fig. 2. Peripheral (off-facet) section of a Te doped InSb single crystal. The variations in the spacing of the vibrational striations reflect fluctuations in the microscopic rate of growth. Rotational striations appear as areas of decreased growth rate (arrows). Pulling rate 22 mm/h; rate of rotation 8 rpm; vibrational frequency 3.5/sec. Magnification *ca.* 600X.

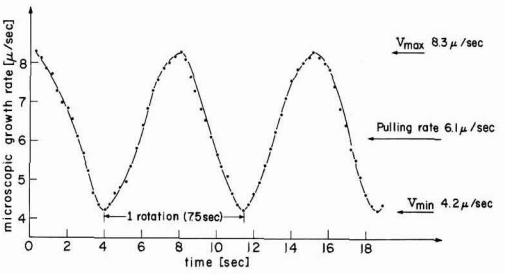

Fig. 3. Microscopic growth rates of the crystal shown in Fig. 2, as computed from the spacing of the vibrational striations measured at a distance of 15μ from the actual crystal periphery.

stantaneous growth rates, corresponding to the crystal of Fig. 2, as determined from the spacing of consecutive vibrational striations are seen in Fig. 3. The sinusoidal variations predicted in Eq. [1] are clearly shown. It should be noted that thermal conditions other than those assumed in Eq. [1] and encountered in the case of Fig. 2 can prevail in which case the variations in the microscopic rate of growth are no longer sinusoidal.

The effects of increased thermal asymmetry (ΔT 2.4°C) on the microscopic growth rate during rotational pulling are depicted in Fig. 4. The small increase of ΔT from 1.8° to 2.4°C has resulted in a change of the maximum to minimum growth velocity ratio, within one revolution, from 2.1 (Fig. 3) to 7.4. The small but readily observable change in direction of the vibrational striations in going from the minimum to the maximum spacing reflects a change in the radius of curvature of the growth interface which is greatest in the "hot" region and smallest in the "cold" region during a given revolution. This change corresponds to the continuous relocation of the growth interface which at any point in this "off facet" region (15) is determined by the exact position of the solidification isotherm.

A further increase in thermal asymmetry (ΔT = 2.7°C) which was brought about by the lateral displacement of the tubular heating element (⅛ in. from its original position) resulted in partial remelting of the grown crystal during rotation as shown in Fig. 5. Such a remelting phenomenon is predicted from Eq. [1] and reflects negative values of the minimum microscopic growth rates. A continuous change in the shape of the growth interface can readily be observed

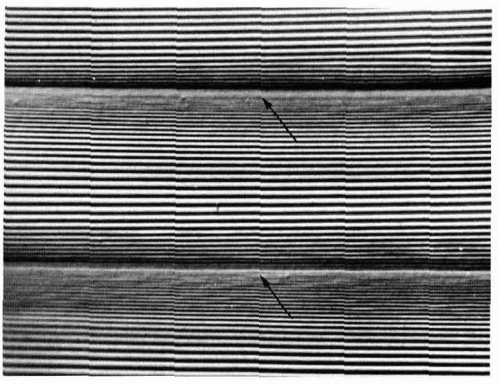

Fig. 4. InSb single crystal pulled under rotation in the presence of thermal asymmetry. Two rotational striations (arrows) can readily be observed. They reflect the onset of local remelting. Pulling rate 22 mm/hr; rate of rotation 8 rpm; vibrational frequency 8.2/sec. Magnification *ca.* 1320X.

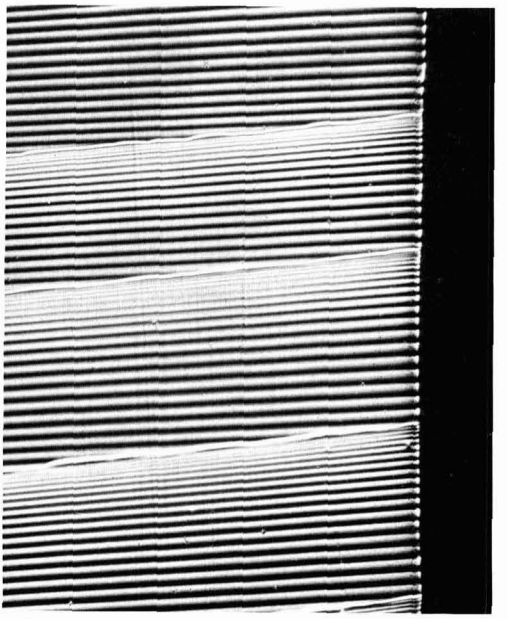

Fig. 5. Off-facet growth characteristics in InSb pulled under rotation in the presence of pronounced thermal asymmetry. The observed rotational striations are remelt lines which delineate the transitions of high to very low instantaneous growth rates (see text). The change in the direction of the vibrational striations reflects the continuous change of the radius of curvature of the growth interface during rotation. Pulling rate 22 mm/hr; rate of rotation 8 rpm; vibrational frequency 5/sec. Magnification *ca.* 675X.

here which is more pronounced than in Fig. 2 and 4. During a 180° rotation of the crystal from the hot into the cold region of the melt, the rate of growth increases steadily. This increase is accompanied by a decrease in the radius of curvature of the growth interface and reflects the relocation of the solidification isotherm deeper into the melt. Further rotation by 180° into the original hot region results in a steadily decreasing growth rate which, in turn, corresponds to an upward shift of the solidification isotherm. Concurrently with the growth rate decrease the radius of curvature of the growth interface increases. It can be observed that during this latter 180° rotation remelting takes place, *i.e.*, the microscopic growth rate assumes negative values. Such remelting is a consequence of the fact that the rate at which the crystal is pulled from the melt is less than the rate of upward relocation of the crystal-melt interface. The resulting rotational remelt striation delineates the abrupt transition from a relatively high growth rate to a growth rate which starts at zero and increases steadily to its maximum value at the coldest point in the rotational cycle. It is apparent that for impurities with an equilibrium distribution coefficient $k_0 < 1$, the rotational striations constitute regions of decreased impurity concentration.

Single crystal growth in the <111> direction generally leads to a more or less extensive facet formation at the growth interface. Figure 6 shows the transition region of a curved, nonsingular growth region (off-facet) to a flat singular facet region, which is reflected in the directional change of the vibrational striations. This transition is characterized by a rather abrupt change of the microscopic growth rate. While the growth rate varies continuously in the "off facet" region it assumes a constant value in the facet region which is identical to that of the macroscopic pulling rate. Obviously variations of the growth rate within

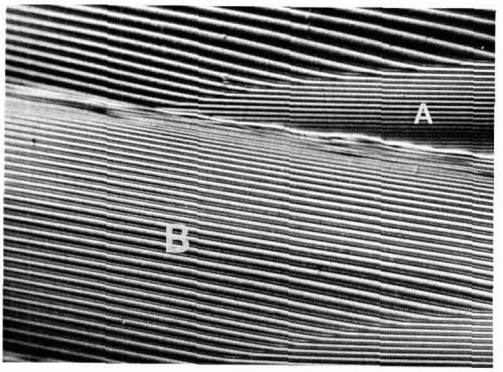

Fig. 6. Transition region of off-facet to facet growth; *A* facet region, *B* off facet region. The transition is characterized by the abrupt directional change of the vibrational striations. It can be observed that the instantaneous microscopic rate of growth varies during rotation in the off-facet region and becomes constant in the facet region. Small growth rate variations in the lower part of the facet near the off-facet region are attributed to growth on vicinal planes. Magnification *ca.* 1250X, oil immersion.

the facet region will result whenever significant temperature changes occur in the melt.

The interaction of remelt rotational striations with the facet results in its abrupt termination; the regrowth immediately following remelting is off facet growth (15). The interference of rotational remelting with the normal facet formation can clearly be observed in Fig. 7. This crystal was pulled at a rate of 35 mm/hr and rotated at a rate of 29 rpm. The frequency of the imposed vibrations was 6/sec. The upper part of the figure shows a section grown in the regular off

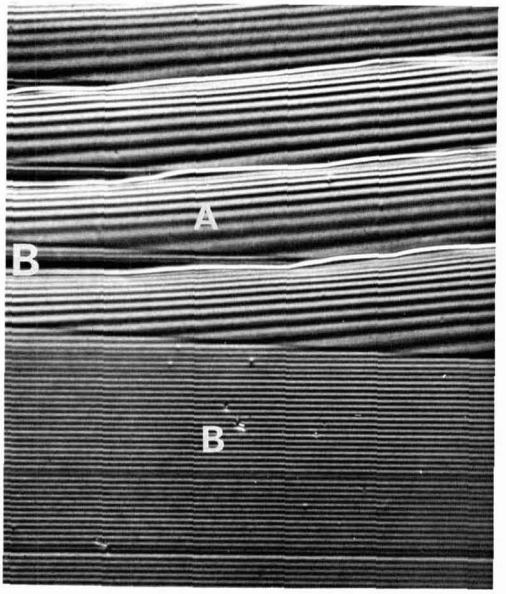

Fig. 7. Off-facet, A, and facet, B, region of an InSb single crystal. In the upper part grown under vibration, irregular growth conditions with extensive remelting are observed. Rotation has prevented the normal facet formation. Portions of the suppressed facet can be observed on the extreme left (B). After stopping rotation (lower part) the facet expands and covers the whole field shown. Pulling rate 35 mm/hr; rate of rotation 29 rpm; vibrational frequency 6/sec. Magnification *ca.* 500X.

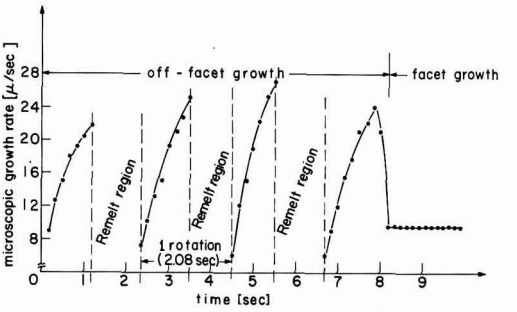

Fig. 8. Instantaneous microscopic rates of growth of the crystal shown in Fig. 7 as computed from the spacing of the vibrational striations. The duration of remelting is determined from the number of missing vibrational striations per rotation.

facet mode with the usual microscopic growth rate fluctuations and local remelting. Facet formation can barely be observed in this section since its lateral expansion is depressed by the backmelting process. Upon stopping the rotation (lower part of Fig. 7) the core or facet region expands to the right and the growth rate assumes a constant value identical with the crystal pulling rate (Fig. 8). This experimental result confirms the predicted independent and constant facet growth rate (15).

It can be clearly seen from Fig. 7 and 8 that due to local remelting the actual average microscopic growth rate is significantly greater than the pulling rate.

When, in addition to the controlled vibrations through the crucible, controlled vibrations are simultaneously introduced through the seed, then rather complex interference patterns of vibrational striations are observed in the curved, nonsingular growth sections (Fig. 9). Since this type of vibrational interference pattern is not present in the facet region, it is quite clear that singular and nonsingular planes exhibit basic differences in their growth characteristics.

It is generally assumed that off-facet growth proceeds normal to the interface without substantial kinetic supercooling since nucleation sites are provided by the curved growth interface. "Facet" growth, on the other hand, is believed to require the nucleation of growth steps (kinetic supercooling) which grow at

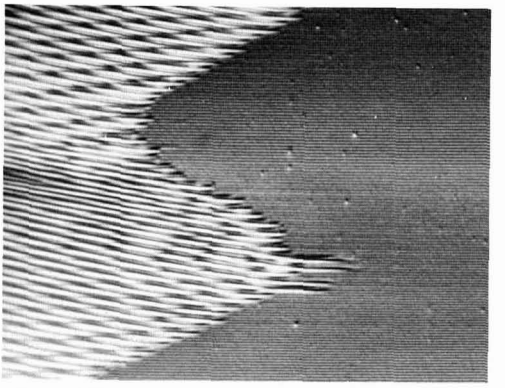

Fig. 9. Effect of the simultaneous introduction of vibrations through the crucible and the seed holder. The resulting vibrational striations exhibit pronounced interference patterns in the off-facet region. No interference patterns can be observed in the facet region. The frequency of the observed vibrational striations in the facet region shows that the seed vibrations are not incorporated in the form of vibrational striations. Magnification *ca.* 1000X, oil immersion.

high rates in a lateral direction. The width of individual vibrational lines in the facet region of Fig. 9 corresponds to approximately 1000Å. Thus, if facet growth proceeds by actual step growth, then, under the present experimental conditions, the step height cannot exceed 1000Å since a height in excess of this value would interfere with the formation of the observed striations. It is apparent that the present technique is uniquely suited for studies of the mechanism of facet growth.

The interference patterns of Fig. 9, which represent localized impurity concentration changes, are not caused by correspondingly localized growth rate fluctuations, since such fluctuations in rate would lead to continuous corrugations at the curved interface. Thus, the observed patterns must be attributed to localized perturbations (in the thickness and/or impurity concentration) of the interfacial boundary layer. Although vibrational interference effects are not observed in the facet region, impurity concentration changes (dark and light regions) under constant microscopic growth rate are observed as shown in Fig. 10. These concentration changes are, thus, most likely due to corresponding concentration changes in the boundary layer.

Impurity concentration changes unrelated to the microscopic growth rate are also shown in the facet region of Fig. 11. In this case controlled vibrations through the seed were intermittently superimposed to the regular vibrations as can readily be seen in the off facet region. The observed concentration changes in the facet region are apparently associated with rotational effects. It is not resolved as yet whether impurity heterogeneities in the facet grown region are due to changes in the thickness, the impurity concentration of the boundary layer, or other effects.

Growth rate fluctuations in a single crystal pulled from the melt without rotation are shown in Fig. 12. The resulting nonrotational heterogeneities are attributed to temperature fluctuations at the growth interface brought about by convective currents (14). From the spacing of the vibrational striations (10/sec) and its variation it can be seen that the duration of the growth rate perturbations ranges from a fraction of a second to several seconds. It was generally observed (under the present experimental conditions) that such random growth rate fluctuations are less common in crystals pulled with rotation and could not be observed in crystals pulled under high rotational rates.

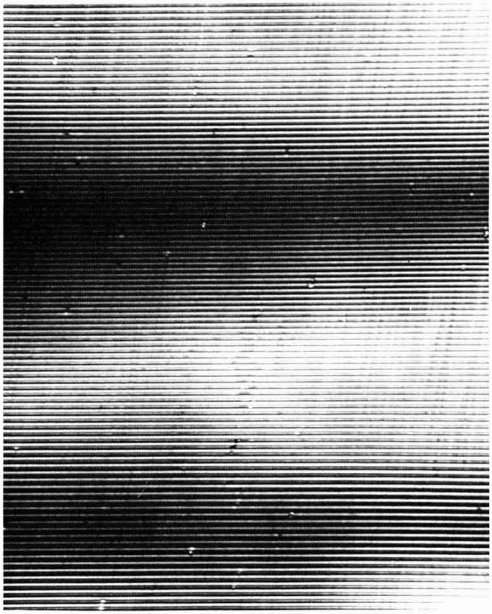

Fig. 10. Facet region in a single crystal of InSb. The observed dark regions reflect an increased impurity concentration. These impurity concentration changes are not related to growth rate changes since the spacing of vibrational striations remains constant. Magnification *ca.* 700X.

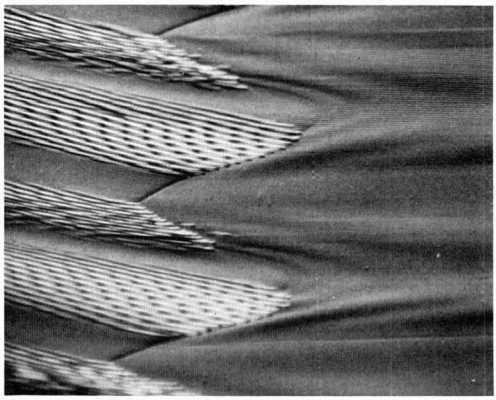

Fig. 11. Transition region (off-facet to facet) in InSb which was intermittently subjected to crucible and seed vibrations. Pronounced heterogeneities in impurity concentration are observed in the facet region. These heterogeneities exhibit the periodicity of rotation. Magnification *ca.* 1000X.

Fig. 12. Nonrotational striations in the peripheral part of an InSb single crystal. Note microscopic growth rate changes. Magnification *ca.* 600X.

Summary

Microscopic rates of growth were determined in single crystals pulled from the melt by introducing vibrations of known frequency into the melt containing small amounts of impurity. Such vibrations are incorporated into the growing crystal in the form of vibrational striations. In the investigated system (InSb doped with Te) impurity heterogeneities and superimposed vibrational striations were revealed by means of

a permanganate etchant. The microscopic rates of growth and crystal-melt-interface topography were determined from the spacing and direction of the vibrational striations.

It was shown that off-facet regions (nonsingular, curved interfaces) exhibit constant and periodic growth rate fluctuations during rotational crystal pulling. The extent of the growth rate variations (at constant pulling rate) is a function of the degree of thermal asymmetry in the system. With increasing thermal asymmetry partial remelting results, *i.e.*, the minimum microscopic growth rate assumes negative values during rotation through the hot region of the melt. The so called rotational striations were identified as the result of a decrease in the microscopic growth rate. The extent of the associated variation in impurity concentration is controlled by the rate at which the microscopic growth rate changes. Crystal growth on singular interfaces (facets) was shown to occur at a constant rate, equal to the pulling rate. Impurity heterogeneities were observed in facet regions grown under constant microscopic rate. Their origin is associated with perturbations in the boundary layer conditions.

Acknowledgment

This work was supported by the National Science Foundation Grant GK-1653 and by a grant from the Sloan Basic Research Fund administered by M.I.T. The authors wish to express their appreciation to Mr. C. J. Herman and Mr. W. J. Fitzgerald for their skillful laboratory assistance.

Manuscript received Aug. 17, 1967.

Any discussion of this paper will appear in a Discussion Section to be published in the December 1968 JOURNAL.

REFERENCES

1. J. A. Burton, R. C. Prim, and W. P. Slichter, *This Journal*, **21**, 1987 (1953).
2. R. N. Hall, *J. Phys. Chem.*, **57**, 836 (1953).
3. W. A. Tiller, K. A. Jackson, J. W. Rutter, and B. Chalmers, *Acta. Met.*, **1**, 428 (1953).
4. C. Wagner, *J. Metals*, **200**, 154 (1954).
5. A. Trainor and B. E. Bartlett, *Solid State Electr.*, **2**, 106 (1961).
6. L. S. Milevskii, *Soviet Phys. Crystallography*, **6**, 193 (1961).
7. P. J. Holmes, *J. Phys. Chem. Solids*, **24**, 1239 (1963).
8. J. A. Burton, E. D. Kolb, W. P. Slichter, and J. D. Struthers, *J. Chem. Phys.*, **21**, 1991 (1953).
9. P. R. Camp *J. Appl. Phys.*, **25**, 459 (1954).
10. H. Ueda, *J. Phys. Soc. Japan*, **16**, 61 (1961).
11. K. F. Hulme and J. B. Mullin, *Solid State Electr.*, **5**, 211 (1962).
12. A. Mueller and M. Wilhelm, *Z. Naturforschung*, **19a**, 254 (1964).
13. J. R. Carruthers, *Can. Met. Quart.*, **5**, 55 (1966).
14. A. F. Witt and H. C. Gatos, *This Journal*, **113**, 808 (1966).
15. K. Morizane, A. F. Witt, and H. C. Gatos, *ibid.*, **114**, 738 (1967).
16. A. F. Witt and H. C. Gatos, *ibid.*, **114**, 413 (1967).
17. A. F. Witt, *ibid.*, **114**, 298 (1967).

The Deposition of Silicon on Single-Crystal Spinel Substrates

P. H. Robinson* and D. J. Dumin

RCA Laboratories, Princeton, New Jersey

ABSTRACT

Single crystal silicon has been epitaxially grown on (100), (110), and (111) magnesium aluminate spinel. The Hall mobilities of films grown on (111) spinel were higher than similar resistivity films grown on (100) and (110) spinel. Typical values of mobility have been 200 cm^2/v-sec on 1 μm thick p-type films and 300 cm^2/v-sec on 15 μm thick p-type films of 0.1 ohm-cm silicon. These mobility values represent 80-100% of the mobility expected on similar resistivity bulk silicon. The autodoping of the films by the substrate was measured and compared with the aluminum autodoping of silicon-on-sapphire films. Silicon grown on spinel was doped about an order of magnitude less than silicon-on-sapphire. The deformation of the film and substrate was found to be anisotropic and the silicon was under a compressive stress of 1-4 · 10^{10} dynes/cm^2.

Recently there has been considerable interest in the growth of silicon films on insulating substrates (1-5). The major portion of this work has been done using either single crystal sapphire or quartz as the substrate material. There have also been reports (6, 7) that single crystal magnesium aluminate spinel substrates can be used for the growth of single crystal silicon.

Spinel is a solid solution of MgO and Al_2O_3 and has a cubic crystal structure with a thermal coefficient of expansion variable with composition but lower than that of sapphire. Spinel is a good insulator which is commercially available in large flame-fusion grown single-crystal boules. This paper will describe the deposition and characterization of single-crystal silicon layers on single-crystal spinel substrates.

Physical Properties

The reaction used for the growth of single-crystal silicon films was the pyrolysis of silane diluted in hydrogen and has been described in detail (8). Electron diffraction patterns obtained have consistently been those of single-crystal oriented silicon layers and it has been found that the silicon lattice was parallel to the spinel substrate orientation, *i.e.*, (111) silicon parallel to (111) spinel, (110) silicon parallel to (110) spinel, and (100) silicon parallel to (100) spinel, in agreement with previously reported results (6).

Sirtl (9) etching was used to reveal the number of dislocations present in the silicon layers. A typical film grown on (111) spinel and dislocation etched is shown in Fig. 1. The major growth imperfection appears to be stacking faults.

The deformation of silicon films between 2 and 25 μm thick on 0.025 and 0.050 cm thick spinel has been measured using a cross-section microscope. In all cases the deformations were anisotropic and exhibited a maximum deformation in one direction and a minimum deformation perpendicular to this direction. A

* Electrochemical Society Active Member.

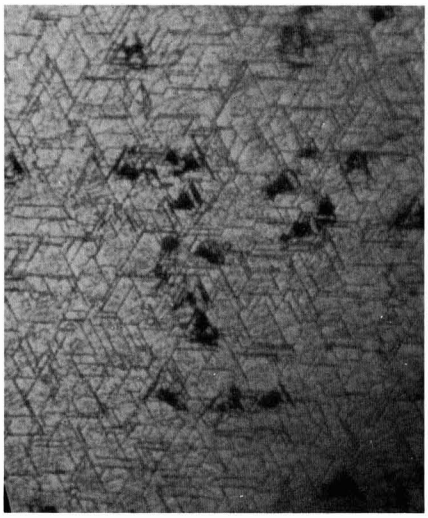

Fig. 1. Dislocation etched 15 μm thick silicon-on-spinel film

typical plot of maximum and minimum deformation of a 5 μm thick silicon film on 0.050 cm thick (111) oriented spinel is shown in Fig. 2. Removal of the silicon by chemical etching restored the spinel to a flat surface. This maximum deformation is about five times as large as the deformation of silicon grown on sapphire (10) and corresponds to a stress in the silicon of 1-4x10^{10} dynes/cm^2. Measurements of silicon grown on (100) and (110) spinel substrates have yielded similar but smaller anisotropic deformations than (111) spinel. Occasionally the deformation is accompanied by cracking of the spinel substrate as well as the exsolution of α-Al_2O_3 from the spinel.

In an attempt to lower the deformation, 0.005 in. stripes spaced 0.050 in. on centers were etched in a 5 μm thick film deposited on (100) spinel. The deformation measured in the direction of the stripes was small; however, the deformation perpendicular to this direction was relatively large. This is a further indication of the anisotropy in the spinel substrates used. Attempts to grow silicon on spinel through holes in a sapphire mask lead to spinel that was cracked along the edge of the deposited line.

Electrical Properties

Both p- and n-type silicon films have been grown via the addition of either B_2H_6 or AsH_3 during silicon growth on (100), (110), and (111) MgO·3.5 Al_2O_3 spinel. Films between 1 and 30 μm thick have been grown. Typical Hall mobilities measured on films 10-15 μm thick are shown in Table I for films grown on different orientations of spinel. The films grown on (111) spinel have consistently had higher mobilities

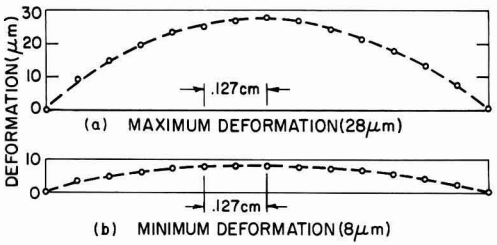

Fig. 2. Deformation of silicon-on-spinel film: (a) deformation along axis of maximum deformation; (b) deformation along axis of minimum deformation.

Table I. Hall mobility of 10-15 μm thick silicon films grown on spinel

Spinel orientation	Hall mobility (cm^2/v-sec)	Conductivity type	% of Bulk for same resistivity
(111)	250-330	p-type	80-100
(100)	162-170	p-type	48-58
(110)	50-60	p-type	16-18
(111)	410-645	n-type	53-65

than films grown on either (100) or (110) spinel. The p-type films had higher resistivity than films grown on sapphire under similar growth conditions indicating that aluminum autodoping from the substrate is less severe in silicon grown on spinel than in silicon grown on sapphire (5).

The Hall mobility and resistivity of 1-2 μm thick silicon films grown on (100) and (111) spinel at different growth temperatures were measured and are shown in Fig. 3 and 4. The highest mobility films were grown at temperatures near 1200°C where typical values of 200 cm^2/v-sec on (111) spinel and 100 cm^2/v-sec on (100) spinel were obtained on p-type films. Higher Hall mobilities have been measured on thicker films indicating an improvement in silicon structure as the film grows thicker. The increase in Hall mobility with film thickness appears to be a general characteristic of heteroepitaxially grown films (11). The mobility-growth temperature curve was more sharply peaked in (111) silicon films than on (100) silicon films, similar to the behavior of (111) silicon grown on (0001) sapphire and (100) silicon grown on (1$\bar{1}$02) sapphire (12).

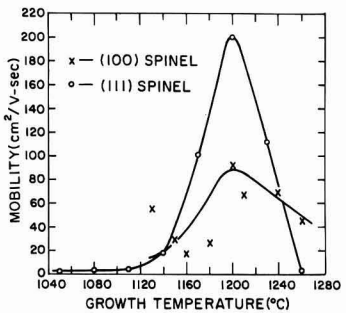

Fig. 3. Hall mobility of silicon films grown on (100) and (111) spinel as a function of growth temperature.

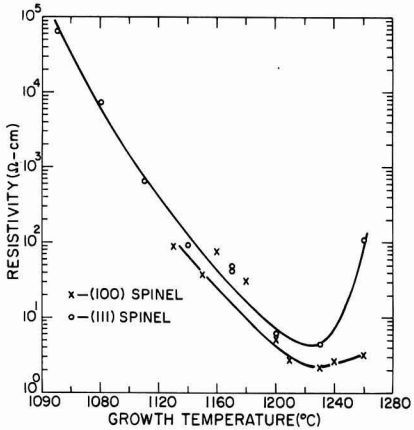

Fig. 4. Resistivity of silicon films grown on (100) and (111) spinel *vs.* growth temperature.

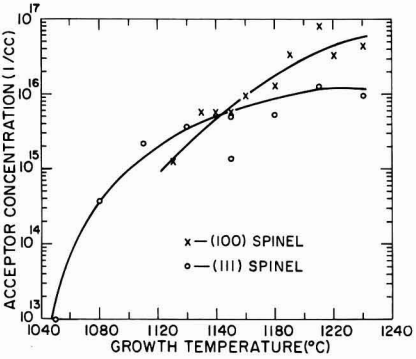

Fig. 5. Carrier concentration vs. growth temperature

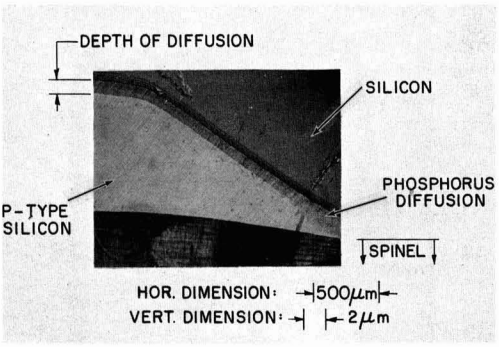

Fig. 7. Diffusion front if phosphorus into p-type silicon-on-spinel as a function of silicon thickness.

Improvement in silicon crystal quality with increasing film thickness has been directly observed. Silicon films 15 μm thick grown on (111) spinel were polished at a ½° angle to the substrate. Chemical etching of the films indicated a decrease in the incidence of crystal faults as the film became thicker. Defect densities of the order of $10^8/cm^2$ have been observed at the surface of 5 μm thick films.

The carrier concentration of the silicon films, as derived from the Hall data, is plotted in Fig. 5. The substrate autodoping raises the acceptor concentration in films grown at the higher temperatures, an effect previously observed in silicon grown on sapphire (5). At a given growth temperature the acceptor concentration (presumably due to aluminum) in a silicon film grown on spinel is approximately an order of magnitude less than the acceptor concentration in a similar film grown on sapphire. In silicon grown on sapphire the autodoping has been linked with the hydrogen reduction of sapphire releasing aluminum into the film. It is suspected that a similar reaction is releasing aluminum into the silicon films grown on spinel, but the cracking and exsolution of the α-Al_2O_3 in spinel at high temperatures have limited the high temperature experiments to determine the source of the acceptors. A comparison between the autodoping found in silicon-on-spinel films and silicon-on-sapphire films is shown in Fig. 6, where the acceptor concentration *vs.* growth temperature is plotted for 2 μm thick films grown on both spinel and sapphire.

The activation energy associated with the autodoping process has been determined from plots of acceptor concentration *vs.* reciprocal temperature. Activation energies of 170 kcal/mol and 160 kcal/mol on (111) and (100) silicon on spinel have been measured, similar to the activation energies measured in silicon-on-sapphire films.

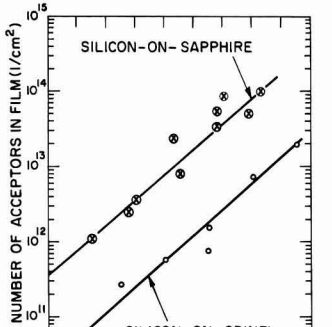

Fig. 6. Comparison of autodoping on silicon films grown epitaxially on sapphire and spinel.

Diffusion of phosphorus into angle polished surfaces has lead to a diffusion profile which was uniform in the thick silicon and a profile that contained diffusion spikes in the thin silicon. A photograph of a phosphorus diffusion front in p-type silicon as a function of film thickness is shown in Fig. 7 where the better quality of the thick film is evident from the sharp diffusion front obtained in the thicker section.

The diode characteristics obtained by phosphorus diffusion into silicon grown on (100) and (111) spinel have been compared with diodes made on similar resistivity bulk silicon. For silicon layers thicker than about 8 μm the diffusion fronts were sharp and were of the same depth as in bulk silicon. Diode breakdown voltages agreed with those predicted for bulk silicon of similar resistivity (13). The breakdowns were sharp although the reverse currents were larger than predicted (14). This could be due to the low minority carrier lifetime in these films (nano-second range) or due to high field emission in the vicinity of diffusion spikes or precipitates.

All of the work reported in this paper on the growth of silicon on spinel has been with alumina rich spinel having the composition $MgO:Al_2O_3$; 1:3.0-3.5. The major difficulty with the use of alumina rich spinel as a substrate is the exsolution of α-Al_2O_3 at dislocations and subgrain boundaries that accompanies high temperature firing of the spinel (15). This weakens the spinel often causing severe cracking of the substrate as well as deterioration of the substrate surface.

Several (111) oriented stoichiometric spinel wafers were polished and fired in hydrogen for times up to 4 hr at 1400°C. X-ray and microscopic examination of these surfaces after heating showed that no exsolution of α-Al_2O_3 had taken place. There was also no evidence of deterioration of the spinel surface or cracking after this heating. A number of polished (111) oriented stoichiometric spinel surfaces were examined by electron diffraction techniques before and after heat treatment in hydrogen. Before heat treatment the mechanically polished stoichiometric spinel surface gave a ring type Laue pattern. Figure 8 shows the electron diffraction pattern indicating poor polycrystalline surface structure representing work damage. After heating in hydrogen at 1500°C for 1 hr, the surface observed by the electron diffraction pattern is shown in Fig. 9. A much better single crystal spinel surface free of work damage was produced. Microscopic examination of the spinel surface revealed that thermal etching of the spinel was responsible for this change in surface structure.

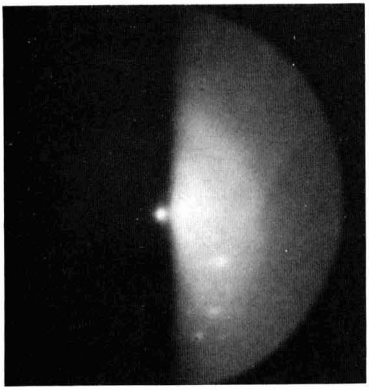

Fig. 8. Electron diffraction pattern of mechanically polished spinel wafer.

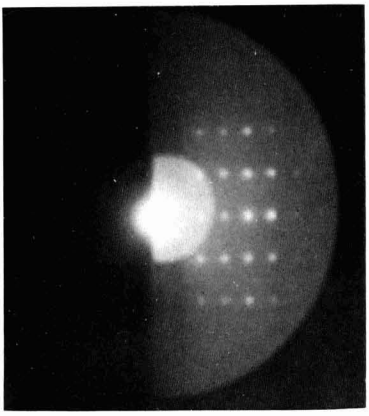

Fig. 9. Electron diffraction pattern of mechanically polished spinel wafer after heating in H_2 at 1500°C for 1 hr.

Work is underway to investigate the electrical properties of silicon on stoichiometric spinel.

Summary

The electrical and mechanical properties of silicon grown on excess Al_2O_3 spinel have been measured and compared to silicon films grown epitaxially on sapphire. The films grown on (111) spinel have in general both higher Hall mobilities and less autodoping than similar thickness films grown on $(1\bar{1}02)$ sapphire. The films on both substrates have a highly reflective surface and in thicknesses less than 4-6 μm can be used directly in device processing without the need for mechanical polishing. The temperature at which the highest mobility films were obtained on spinel was about 50°C higher than the temperature at which the highest mobility films were obtained on sapphire (12). Even at the higher growth temperature the autodoping from the substrate is less on the spinel than on the sapphire. Diodes fabricated in the silicon on spinel have yielded sharp reverse breakdown voltages of a value comparable to the breakdown found in bulk silicon.

Acknowledgments

The authors wish to acknowledge the technical assistance and encouragement of C. W. Mueller. The authors are also indebted to A. Kokkas for some of the exsolution experiments and to C. C. Wang for supplying the stoichiometric spinel. We also wish to thank R. Adams and R. O. Wance for sample preparation and electrical measurements. Thanks are also due to R. Smith, W. C. Roth, and E. Krieger for both x-ray and electron-diffraction analysis. Research reported in this paper was sponsored by the Air Force Avionics Laboratory, Research and Technology Division, Wright-Patterson Air Force Base, Ohio, under Contract No. F33615-67-C-1150, and RCA Laboratories, Princeton, New Jersey.

Manuscript received July 17, 1967; revised manuscript received Sept. 5, 1967.

Any discussion of this paper will appear in a Discussion Section to be published in the December 1968 JOURNAL.

REFERENCES

1. H. M. Manasevit and W. I. Simpson, *J. Appl. Phys.*, **35**, 1349 (1964).
2. C. W. Mueller and P. H. Robinson, *Proc. IEEE*, **52**, 1487 (1964).
3. B. A. Joyce, R. J. Bennett, R. W. Bicknell, and P. J. Etter, *Trans. Met. Soc. AIME*, **233**, 556 (1965).
4. H. M. Manasevit, Arnold Miller, F. C. Morritz, and R. Nolder, *ibid.*, **233**, 540 (1965).
5. D. J. Dumin and P. H. Robinson, *This Journal*, **113**, 469 (1966).
6. H. M. Manasevit and D. H. Forbes, *J. Appl. Phys.*, **37**, 734 (1966).
7. V. H. Seiter and C. H. Zaminer, *Z. Angew. Physik.*, **20**, 158 (1965); H. Schlotterer and C. H. Zaminer, *Phys. Stat. Sol.*, **15**, 399 (1966).
8. P. H. Robinson and C. W. Mueller, *Trans. Met. Soc. AIME*, **236**, 268 (1966).
9. E. Sirtl and A. Adler, *Z. Metallk.*, **52**, 529 (1961).
10. D. J. Dumin, *J. Appl. Phys.*, **36**, 2700 (1965).
11. B. W. Sloope and C. O. Tiller, *ibid.*, 38, 140 (1967).
12. D. J. Dumin, *ibid.*, **38**, 1909 (1967).
13. S. M. Sze and G. Gibbons, *Appl. Phys. Lett.*, **8**, 111 (1966).
14. C. T. Sah, R. N. Noyce, and W. Shockley, *Proc. IRE*, **45**, 1228 (1957).
15. H. Saalfeld and H. Jagodzinski, *Acta. Cryst.*, **7**, 666 (1954).

Phosphorus Concentration Profile and Phase Segregation in Phosphosilicate Glass on SiO_2 Films

P. F. Schmidt,* W. van Gelder,* and J. Drobek

Bell Telephone Laboratories, Inc., Allentown, Pennsylvania

ABSTRACT

The phosphorus distribution in phosphorus diffused SiO_2 films has been determined by means of neutron activation. The general shape of the profile is in good agreement with the results by Fränz *et al.* (4), who used the P^{32} isotope. In the phosphosilicate region occasional strong fluctuations of the P concentration were observed, usually accompanied by changes in the etch rate in 0.2*N* HF opposite to the expected dependence of etch rate on P concentration. The fluctuations were tentatively attributed to phase segregation in the phosphosilicate glass. Confirmation was obtained from related experiments in which polycrystalline films of composition P_2O_5 x SiO_2 (and possibly P_2O_5 x $2SiO_2$) were obtained and identified by electron diffraction.

The neutron activation of phosphosilicate layers on SiO_2 films reported here was originally undertaken in order to study the phosphorus distribution for different phosphorus diffusion and subsequent reoxidation conditions. The resulting phosphorus distributions are described.

During the course of this investigation, strong fluctuations of the phosphorus concentration in the glass region as a function of distance into the glass were discovered. It was noticed that these fluctuations often coincided with a trend of the etch rate in 0.2*N* HF opposite from that expected from the phosphorus concentration: the higher phosphorus concentration often corresponded to a slower etch rate, and vice versa.

These observations could be explained by assuming phase segregation in the glass, with formation of one or more of the compounds occurring in the P_2O_5-SiO_2 system according to Tien and Hummel (1), but there was no hard evidence for the correctness of this assumption except for some radioautographs which showed that slow etching regions of the glass contained indeed more phosphorus than the faster etching portions. Audley (2) has reported on the insolubility in HF of a SiO_2 x P_2O_5 compound. According to Eitel (3) the system SiO_2-P_2O_5 is remarkable in that its components and the binary mixtures near them form glasses readily, while the compounds crystallize well.

Independent evidence for the occasional occurrence of a SiO_2-P_2O_5 compound in the phosphosilicate glass was obtained when a polycrystalline film, insoluble in HF, was observed to form at the interface between the phosphosilicate glass and a pyrolytic SiO_2 film deposited on top of the glass. Pyrolysis had been carried out at a much lower temperature (850°C) than was used for the original phosphorus diffusion (1040°C).

It was possible to isolate this polycrystalline film, and to identify by electron diffraction alpha-SiO_2 x P_2O_5 as its main constituent, with possibly some admixture of $2SiO_2$ x P_2O_5. The surface of the phosphosilicate layer prior to the pyrolytic SiO_2 deposition showed no evidence of compound formation detectable by electron diffraction or etch rate in HF.

Fränz *et al.* (4), who used the P-32 isotope in their study, also report a scatter in the phosphorus profile [Fig. 8b of ref. (4)], which appears to be outside the error of measurement; however, they did not attempt an explanation. If the cause for the fluctuation in phosphorus concentration reported by them is also phase segregation, as appears likely, then their results would indicate that neither neutron activation nor pyrolytic deposition of SiO_2 are required to trigger the formation of SiO_2 x P_2O_5 in the phosphosilicate glass.

It is perhaps worth noting in this context that Snow and Deal (5) describe phosphosilicate layers as "behaving as though they had a very slow dipolar polarizability. The 'dipoles' involved may be physical dipoles with a concentration of 10^{19} cm^{-3}, or they may be small regions of the glass occupying about 6% of the volume which polarize by interfacial polarization."

Activation Studies

Method.—P-type silicon disks after oxidation and phosphorus diffusion, were subjected to neutron activation. The wafers were then etched in dilute HF to remove the oxide in controlled steps of about 100Å, and the phosphorus profile in the oxide was established by measuring the activity remaining on the slice after each etching step. The oxide thickness was measured by means of a spectrophotometer.

As stated above, strong fluctuations in phosphorus concentration were observed in the phosphosilicate region. In order to evaluate the reliability of the tracer data, a knowledge of all possible sources of error is necessary. The experimental technique used is given in the Appendix, together with a brief discussion of the uncertainties accompanying the measured parameters. A full account of the experimental method used for establishing the phosphorus concentration profile in the oxide is given in an extended appendix which is available from the authors on request. It is shown there that the fluctuations of the phosphorus concentration observed in the phosphosilicate region are far outside the error limits.

Results.—The over-all diffusion results are summarized in Table I. The thickness of the phosphosilicate glass is defined as that position in the oxide at which the phosphorus concentration drops steeply according to the activity data (see graphs). It can be seen that the phosphorus concentration increases with increasing temperature of diffusion, as expected. Reoxidation in steam under the conditions shown leads to a relatively small increase in glass thickness, to a slight decrease in phosphorus concentration, and to some loss of phosphorus to the ambient (total P/cm^2 of oxide, column 5).

Figures 1 and 2 show two typical phosphorus concentration and etch rate profiles observed in analyzing the samples listed in Table I. The profile shown in Fig. 1 (wafer 30-211), in which phosphorus concentration and etch rate vary in opposite direction at certain positions in the oxide was observed more often than the profile shown in Fig. 2, in which phosphorus concentration and etch rate vary in the same direction. The error bars shown include the contributions

* Electrochemical Society Active Member.

Table I. Tracer data on oxidized and phosphorus diffused silicon wafers

No.	Treatment	Final oxide thickness, Å	Thickness of P_2O_5 glass, Å	Total P/cm² of oxide	Highest conc in oxide
30-203	Ox. 900°C, 45 min Diff. PBr_3 1000°C, 20 min	1600	1200	3.7×10^{16}	3.6×10^{21} cm^{-3}
30-238	Ox. 900°C, 45 min Diff. PBr_3 1000°C, 20 min Reox. 900°C, 45 min	3350	1600	3.2×10^{16}	2.2×10^{21} cm^{-3}
30-208	Ox. 900°C, 90 min Diff. PBr_3 1000°C, 10 min	2900	600	1.4×10^{16}	3.9×10^{21} cm^{-3}
30-209	Same as 30-208	2900	Lost data	1.6×10^{16}	Lost data
30-210	Ox. 900°C, 90 min Diff. PBr_3 1000°C, 10 min Reox. 900°C, 20 min	3250	800	1.3×10^{16}	3.5×10^{21} cm^{-3}
30-211	Same as 30-210	3200	800	4.4×10^{15}	3.9×10^{21} cm^{-3}
30-215	Ox. 900°C, 90 min Diff. PBr_3 745°C, 45 min	2750	450	4.4×10^{15}	1.4×10^{21} cm^{-3}
30-216	Ox. 900°C, 90 min Diff. PBr_3 745°C, 45 min Reox. 900°C, 20 min	3150	600	2.9×10^{15}	2.1×10^{20} cm^{-3}
30-221	Ox. 1050°C, 30 min Diff. PBr_3 1000°C, 20 min	4000	1200	3.9×10^{16}	7.2×10^{21} cm^{-3}
30-222	Ox. 1050°C, 30 min Diff. PBr_3 1000°C, 20 min Reox. 900°C, 45 min	4900	1600	7.2×10^{16}	3.1×10^{21} cm^{-3}
30-223	Same as 30-222	5000	1500	3.3×10^{16}	2.6×10^{21} cm^{-3}

from all known causes. It can be seen that the fluctuations of the phosphorus concentration in Fig. 1 are far outside the errors of measurement.

The low concentration phosphorus tail extending all the way through the oxide and into the silicon substrate[1] is a result of the intense neutron irradiation, and has been described in detail elsewhere (6). An interesting series of autoradiographs is shown in Fig. 3 (wafer 30-223). In addition to the large "diffusion pipe," extending all the way through the oxide, there is a triangular "hot spot," which was initially invisible (*a*) because it was masked by the high phosphorus concentration of the surface layers. It became visible (*b*) when 800Å of the oxide had been removed by etching, and then lasted for another 800Å (*c*) before disappearing again (*d*); it is thus located in the phosphosilicate glass region (cf. Table I). This triangular spot also showed up optically as a region of increased oxide thickness. If the spot were due just to a higher local concentration of phosphorus (without compound formation), one would expect an increased etch rate and therefore a locally decreased oxide thickness, *i.e.*, the reverse of what is observed. The explanation that adsorption of some kind of protective film had occurred in the area of the triangular spot appears invalid because the oxide thickness in the area of the triangular spot did not remain constant during the series of etching steps from (*b*) to (*c*), but decreased though at a slower rate than the rest of the oxide. Unfortunately, the opportunity was missed to examine this triangular spot by electron diffraction. It will be appreciated that the exposure times in Fig. 3 increased with each etching step, so that features well visible in the long exposure autographs would be swamped in the short exposure pictures. The size of the circular diffusion pipe in radioautographs (*c*) and (*d*) is an artifact: the "pipe" has not spread in diamater, but the image of the pipe was badly overexposed at an exposure time adequate for the rest of the wafer. The overexposure caused the diffuse lateral spreading of the image of the pipe. Wafer 30-223 was also the only wafer on which a pipe of such intensity was observed. Densitometric evaluation of the radioautographs taken from other wafers showed that the contribution by pipes is unimportant relative to the phosphorus concentration in the rest of the oxide, at least in the high phosphorus concentration region. In particular, the pipes cannot be held responsible for the fluctuations of phosphorus concentration observed in the phosphosilicate glass region.

The number 30-223 appearing in (*d*) of Fig. 3 is due to phosphorus decoration of dislocations generated by scribing the Si disk. The decoration disappeared when 1200Å of silicon were removed by anodic oxidation. The lighter periphery of the disks is due to preferential loss of phosphorus from the wafers during neutron irradiation; evaporation of

[1] In addition to some P_2O_5 "pipes" not present on all wafers.

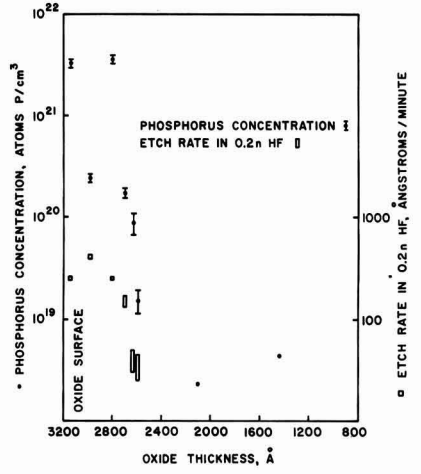

Fig. 1. Phosphorus concentration and etch rate profiles of diffused and reoxidized wafer 30-211.

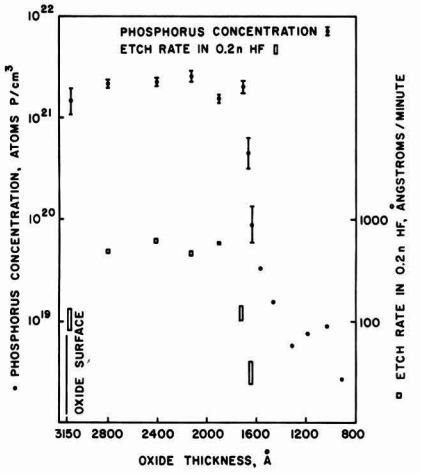

Fig. 2. Phosphorus concentration and etch rate profiles of diffused and reoxidized wafer 30-238.

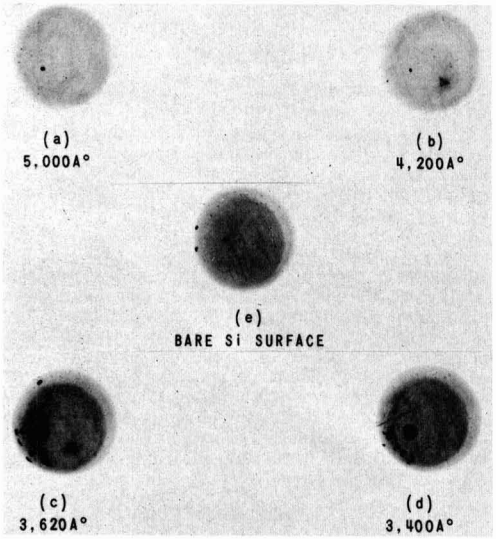

Fig. 3. Radioautographs of diffused and reoxidized wafer 30-223 at different remaining oxide thicknesses.

phosphorus from the center of the disks was suppressed by aluminum spacers inserted between each wafer.

Formation of a Polycrystalline Phosphosilicate Film Triggered by Pyrolytic Deposition of SiO_2

Experimental.—A number of chemically polished silicon slices, 50 ohm-cm P-type, {111} oriented, diameter 1 in., were oxidized in 100% steam of atmospheric pressure for 1 hr at 1100°C. The resulting oxide thickness was 6800Å, as determined from the wavelength position of the interference fringe minima. The slices were next phosphorus diffused in PBr_3 at 1040°C for 40 min, resulting in a phosphosilicate glass layer on top of the SiO_2 film. The total thickness of the dielectric layer after diffusion was 7150Å. The slices were then deposited with SiO_2 at 850°C from a gas mixture consisting of 0.15% $SiCl_4$, 0.15% O_2, and 99.7% H_2. The total thickness after deposition of the pyrolytic SiO_2 was 10,200Å. The slices were then step-etched in P-etch (14), and the remaining thickness of the dielectric layer was measured at various intervals.

Figure 4 shows that the etch rate of the oxide "sandwich" varied with depth as expected. That is, at first the etch rate was fairly constant, then increased steeply in the phosphosilicate glass region, to fall off again to a low and constant value when the phosphorus concentration had become negligible.

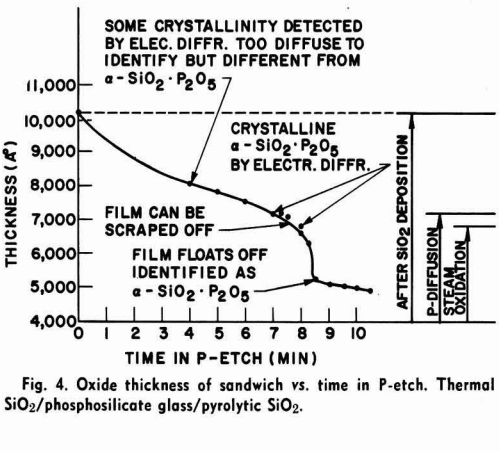

Fig. 4. Oxide thickness of sandwich vs. time in P-etch. Thermal SiO_2/phosphosilicate glass/pyrolytic SiO_2.

Table II. Comparison of electron diffraction data (this work) with the x-ray data of Tien and Hummel Identification of $SiO_2 \times P_2O_5$ by electron diffraction

X-ray data by Tien and Hummel (1)		Data calculated from electron diffraction of HF insoluble film
d (Å)	I/I_0	d (Å)
5.87	15	5.91
4.82	5	4.80
4.00	16	—
3.80	23	—
3.69	100	3.658 (strongest obs. refl.)
		3.54*
3.38	25	3.372
3.26	5	—
3.20	38	—
3.10	7	—
2.91	6	—
2.68	4	2.69
2.59	18	2.586
2.35	2	—
2.26	5	2.24
2.22	8	2.15
2.12	6	
2.09	5	2.085
2.05	8	2.02
2.00	4	—
1.977	8	—
1.888	3	—
1.863	3	1.844
1.824	3	

* 3.54 is the highest intensity d-value of $2SiO_2 \times P_2O_5$ according to Tien and Hummel (1).

After 8.5 min of etching, a thin film, apparently insoluble in the P-etch, floated off the surface. This film was removed from the solution and placed into buffered HF [2] for 3 days without dissolving. Transmission electron diffraction showed the film to be alpha-SiO_2-P_2O_5 (compare below).

No insoluble film was observed when the phosphosilicate layer was etched prior to pyrolytic SiO_2 deposition. After SiO_2 deposition, followed by 4 min of etching in P-etch, *i.e.*, still in the deposited SiO_2 layer, glancing-angle electron diffraction showed some crystallinity, too diffuse for identification (cf. Fig. 4). However, after 7 and 8 min of etching, electron diffraction showed the presence of α-$SiO_2 \cdot P_2O_5$. This diffraction pattern was distinctly different from the diffuse pattern seen after 4 min of etching. It appears likely that the $SiO_2 \cdot P_2O_5$ crystals induced conversion of SiO_2 to α-crystobalite which extended some distance into the pyrolytic SiO_2. It is known (7) that $SiO_2 \cdot P_2O_5$ is highly analogous to α-crystobalite and catalyzes this transformation.

After 8 min of etching there are also indications of the presence of traces of $2SiO_2 \times P_2O_5$ (presence of the reflection $d = 3.54$Å, cf. Table II), according to the data by Tien and Hummel (1). At 8 min the polycrystalline film was visible under an optical microscope and could be scraped with a sharp needle.

Figures 5, 6, and 7 are a series of pictures of a slice on which the left half lagged 1 min behind in etching time compared to the right hand half. This difference in etching time was brought about by masking the left half, etching the slice for 1 min, and then removing the mask. From then on the left half always lagged behind the right half by 1 min etching time. The pictures were taken under dark field illumination at a magnification of 428x.

Figure 5 shows a polycrystalline film appearing on the right hand side after 8 min of etching, while no crystallinity is yet visible on the left hand side (etched for 7 min). The high intensity light spots on both left and right hand side should be ignored as due to either pin holes or loose particles on the surface.

Figure 6 is taken from the same area of the slice as the right hand side of Fig. 5. It was also etched for 8 min and it shows the film partly scraped by means of a sharp needle.

[2] 40g NH_4F, 15 cc conc HF, 60 cc H_2O.

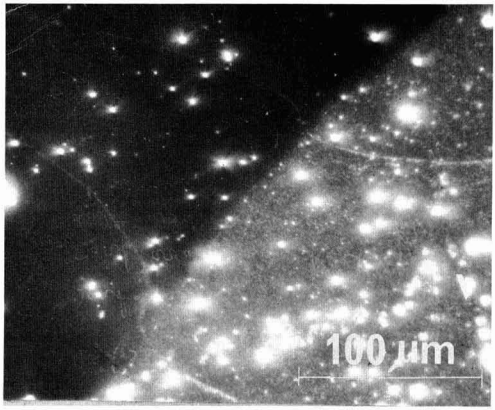

Fig. 5. Microphotograph of oxide sandwich after etching in P-etch. Right half etched for 8, left half for 7 min. Polycrystalline film visible only on right half.

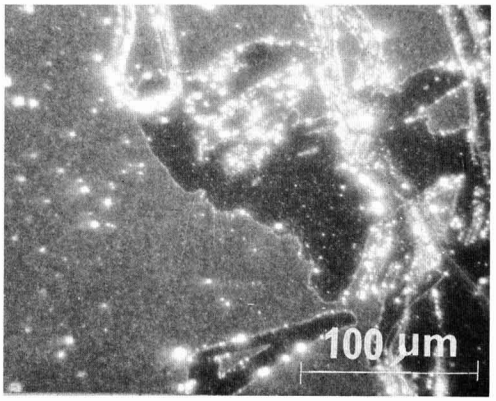

Fig. 6. Microphotograph of right half of Fig. 5, after scraping with steel needle.

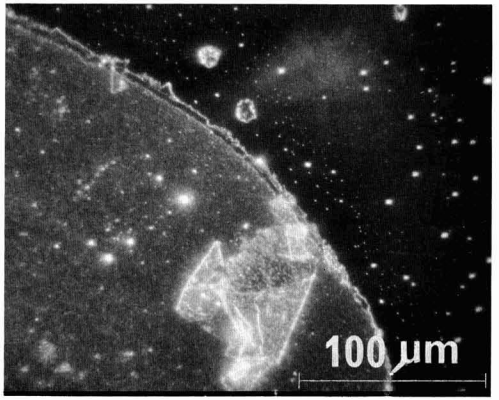

Fig. 7. Microphotograph of oxide sandwich after etching in P-etch. Right half etched for 9, left half for 8 min. Polycrystalline film has lifted from right side, but is visible on left side.

The right hand side of Fig. 7 shows an area that was etched 9 min. The film has completely lifted from this side. A part of the loose film is visible in the lower middle part of the picture. The left side of the picture shows an area that was etched for 8 min. The polycrystalline film on this side is clearly visible and is identical in appearance with the film in Fig. 6.

Identification of the Film as Alpha-$SiO_2 \cdot P_2O_5$ by Electron Diffraction

Electron diffraction patterns were obtained both from the isolated film (in transmission) and from the film on the surface (in reflection) after 7-8 min of etching. The patterns taken in transmission were more distinct, and are compared in Table II to the x-ray data by Tien and Hummel (1) for the low-temperature (= alpha) modification of SiO_2 x P_2O_5. The agreement is very satisfactory. The x-ray data contain reflections which do not show up in the electron diffraction pattern because in this latter case the sample is not being rotated so that certain crystal planes do not reflect. The observed reflections, however, match their counterparts in the x-ray data quite closely. The appearance of a reflection at $d = 3.54$Å may be considered as an indication that traces of $2SiO_2$ x P_2O_5 are present since this is the strongest reflection of this compound according to Tien and Hummel (1).

Discussion

Phase segregation is suggested by the large fluctuations in phosphorus concentration in the phosphosilicate region, and by the often opposing trends of phosphorus concentration and etch rate. The latter relationship is masked to some extent by the strong effect of the neutron irradiation on the etch rate.

The transition from phosphosilicate glass to undoped SiO_2 extends over 100-200Å. The shape of the diffusion profile in this transition region can be explained on the basis of strongly concentration dependent diffusivity. It was shown by Thurston *et al.* (8) that the diffusivity of phosphorus (pentoxide) in SiO_2 at lower concentrations than corresponds to the "glass" is strongly concentration dependent and very slow, especially at lower temperatures (below 1200°C). Thus the diffusivity in the phosphosilicate glass region, according to Sah *et al.* (9), is 2.5×10^{-13} cm^2 sec^{-1} at 1100°C, but only about 10^{-16} cm^2 sec^{-1} at the same temperature and a concentration of 3% P_2O_5 in SiO_2 according to Thurston *et al.* (8). The fast diffusion in the glass region thus ensures a practically flat concentration profile in the glass up to the point where the phosphorus concentration drops steeply. Reoxidation of the wafers leads to slight penetration of the phosphorus front under the given reoxidation conditions (2-400Å), a lowering of the maximum phosphorus concentration, and to some loss of phosphorus to the ambient (about 15% of the total originally contained in the oxide after diffusion).

Pyrolytic deposition of SiO_2 leads occasionally to the formation of a polycrystalline film across the whole surface of the phosphosilicate glass, thus facilitating its detection. The details of this (catalytic) effect have not been established. The main constituent of this film has been unambiguously established as SiO_2 x P_2O_5, possibly with traces of $2SiO_2$ x P_2O_5. The ratio of SiO_2 to P_2O_5 in the phosphosilicate glass is about 4:1, so that formation of some $2SiO_2 \cdot P_2O_5$ might be expected. According to Tien and Hummel, the 2:1 compound melts incongruently at 1120°C to a silica-rich liquid and SiO_2 x P_2O_5. Even though the system in the present case was not heated to 1120°C, the formation of the 1:1 compound was favored.

Acknowledgments

The authors wish to thank V. E. Hauser for the deposition of the pyrolytic SiO_2 films, and D. R. Wonsidler for help with the tracer experiments.

Manuscript received June 5, 1967; revised manuscript received Sept. 27, 1967.

Any discussion of this paper will appear in a Discussion Section to be published in the December 1968 JOURNAL.

REFERENCES

1. T. Y. Tien and F. A. Hummel, *J. Am. Ceram. Soc.*, **45**, 422 (1962).
2. J. A. Audley, "Silica and the Silicates," pp. 9-10, Bailliere, Tindall & Cox, London (1921).
3. W. Eitel, "The Physical Chemistry of the Silicates," Univ. Chicago Press (1954).
4. I. Fränz, W. Langheinrich, and K. H. Löcherer, *Telefunken-Zeitung*, **37**, 194 (1964).
5. E. H. Snow and B. E. Deal, *This Journal*, **113**, 263 (1966); SCP and Solid State Technology, November 1966, p. 30.
6. P. F. Schmidt, *Appl. Physics Letters*, **8**, 264 (1966).
7. G. Peyronel, *Z. Kristallographie*, **95**, 274 (1936).
8. M. O. Thurston, J. C. C. Tsai, and K. D. Kang, ASTIA Report AD 261 201 (1961).
9. C. T. Sah, H. Sello, and D. A. Tremere, *J. Phys. Chem. Solids*, **11**, 288 (1959).
10. T. M. Buck, F. G. Allen, J. B. Dalton, and J. D. Struthers, *This Journal*, **114**, 862 (1967).
11. R. O. Carlson, R. N. Hall, and E. M. Pell, *J. Phys. Chem. Solids*, **8**, 81 (1959).
12. F. Reizman, *J. Appl. Phys.*, **36**, 3804 (1965); F. Reizman and W. van Gelder, *Solid State Electronics*, **10**, 625 (1967).
13. B. R. Rex and G. H. Schneer, Private communication.
14. W. A. Pliskin and R. G. Gnall, *This Journal*, **111**, 872 (1964).
15. A. Kant, J. P. Cali, and H. D. Thompson, *Anal. Chem.* **28**, 1867 (1956).
16. Am. Inst. of Physics Handbook, 2nd edition.

APPENDIX

Activation Studies, Experimental

Float-zoned 1.3 ohm-cm P-type silicon, {111} oriented, was used throughout. The wafers were mechanically lapped and polished, and then given a chemical polish to remove surface damage. Average dislocation density of the starting material was 12,000 cm^{-2} by Sirtl etch.

Table I lists the wafers according to oxidation and diffusion treatment. Oxidation was carried out in steam, diffusion was from a PBr_3 source kept at 30°C, with part of the carrier gas bubbling through the PBr_3 source. Subsequent to diffusion the wafers were cooled directly to room temperature by pulling from the furnace.

For irradiation, the wafers were wrapped in a special high purity aluminum foil, with high purity aluminum disks inserted between each Si wafer in order to insure uniformity of neutron dose throughout the charge. The wafers were irradiated for seven days at the Brookhaven National Laboratories at a flux of $1.2 \times 10^{13} \pm 5\%$ thermal and $1.5 \times 10^{11} \pm 10\%$ fast neutrons cm^{-2} sec^{-1}, leading to a specific activity of 11.0 Curies per mol of phosphorus. The wafers were not intentionally cooled during neutron irradiation, and the temperature in the aluminum capsule may have risen about 50°C above the ambient temperature of 250°C at the place of irradiation.

Subsequent to irradiation the wafers were kept in storage for several weeks to permit decay of the Na^{24} beta and gamma activity (from the reaction Al^{27} $(n,\alpha)Na^{24}$), of the beta-activity of Si^{31} (from the reaction Si^{30} (n,γ) Si^{31}), and of the beta activity of Br^{82} (from the reaction Br^{81} (n,γ) Br^{82}). The half-lives of Na^{24}, Si^{31}, and Br^{82} are 15.05 hr, 2.62 hr, and 35.5 hr., respectively. At the end of the investigation, when the phosphorus activity had already largely decayed, the presence of S^{35} could be detected both from its decay rate and its beta-energy spectrum.[3] The S^{35} was probably introduced by neutron activation of a chlorine impurity in the PBr_3 source, by means of the reaction Cl^{35} (n,p) S^{35}.[4] The level of contamination with S^{35} was too low to affect the phosphorus determinations. The half-life of S^{35} is 86.7 days.

[3] The authors are indebted to J. D. Struthers for these measurements.

[4] Contamination with sulphur cannot be the cause since the observed surface concentrations of 8×10^{16} cm^{-3} are above the solid solubility limit for sulphur in silicon (11).

A Nuclear-Chicago gas flow detector, model D47, operated in the Geiger tube mode, in conjunction with a Nuclear-Chicago Decade Scaler, series 8703, was used to determine the activity of the samples. Since this counting system has already 1% loss at 6000 counts/min, suitable aluminum absorbers were placed over the samples. Each time an absorber was removed or exchanged against another absorber, the ratio of the counts under the two conditions was determined. It was thus possible to calculate the counting rate in the most active conditions of the wafers (*i.e.*, before step-wise stripping of the oxide in HF) by using the final counting rate without any absorber (*i.e.*, when most of the activity had been etched away) as the starting point for the calculation. It is felt that no appreciable error was introduced by this procedure, since a sufficient number of counts was taken to reduce the statistical errors to insignificant values.

The detection efficiency of the detector was measured by means of a P^{32} simulated source of 2.8×10^{-5} millicuries (supplier: Tracerlab, Waltham, Massachusetts) calibrated against standards of the NBS.

An aluminum holder served to position either the P^{32} simulated source or the Si wafers underneath the window of the Geiger tube. Measuring conditions for source and samples were kept as nearly identical as possible. Counts were taken to 10,000 for each point in the high phosphorus concentration region, and to at least 2000 above background in the low phosphorus concentration region of the oxide films.

A Perkin-Elmer model 202 visible-uv spectrophotometer was used to measure the reflectance minima as a function of wavelength (12). Oxide film thicknesses were then calculated by assuming the same refractive index for the phosphorus-doped film as for thermal SiO_2 films. This involves only a small error, of the order of 1% (4, 13); a more accurate determination of the refractive index would not have been meaningful in view of the continuously changing SiO_2-P_2O_5 composition as a function of film thickness.

Radioautographs were taken with type AA x-ray film because of its sensitivity. It is, however, a double emulsion film and rather coarse grained.

The analysis consisted in principle in measuring the activity of the silicon wafers before and after successive etching of the oxide in dilute HF in order to decrease its thickness in steps of about 100Å each. The oxide from one side of the wafer was removed completely, and the wafer was measured with active side facing the window. After each etching step the oxide thickness was remeasured. On a considerable number of wafers radioautographs were taken before, during, and after stepwise dissolution of the oxide. Controlled etching of the oxide was carried out in 0.2*N* HF until low phosphorus concentrations were reached and the strength of the etching solution had to be increased in order to have reasonable etch rates. In the phosphosilicate glass region it was not possible to use the so-called "P-Etch" (14) because of the excessively fast etch rate caused by radiation damage to the oxide.[5] It was, however, noticed that the 0.2*N* HF solution was more sensitive to variations in phosphorus concentration than a 1.0*N* HF solution, and the latter in turn was more sensitive than the P-Etch. The dissolution of the oxide was usually very uniform, and only occasionally were very weak differences in local interference color detectable by the unaided eye.

The counting rates observed were converted to phosphorus concentrations by means of the relationship

$$A = N \times f \times \sigma \times S \times e^{-\lambda t} \qquad [1]$$

where A is the activity in disintegrations sec^{-1} (corrected for the detection efficiency of the system, 13.5%), N is the number of atoms of P^{31} originally present, f is the thermal neutron flux cm^{-2} sec^{-1}, σ is the capture cross section of P^{31} for thermal neutrons, S equals $1 - e^{\lambda t_i}$; for t_i equals 1 week (6.04×10^5 sec), and the decay constant λ of $P^{32} = 5.6 \times 10^{-7}$ sec^{-1}, the saturation factor $S = 0.28$. The t in the exponent in Eq. [1] is the time in seconds elapsed since the end of irradiation.

Equation [1] must in principle be corrected for a

[5] Enhanced by a factor of ~ 2 for pure SiO_2 and of ~ 8 for phosphosilicate glass compared to the values given in ref. (14).

background activity of P^{32} introduced by the reaction (15)

$$Si^{30}\ (n, \gamma)\ Si^{31}\ (\beta-)\ P^{31}\ (n, \gamma)\ P^{32}$$

However, for phosphorus concentration above 10^{17} cm^{-3}, *i.e.*, in the phosphorus concentration range of interest here, this correction may be neglected.

Errors

The accuracy of the terms in Eq. [1] determines the precision with which a known disintegration rate can be converted into number of phosphorus atoms. The accuracy with which the disintegration rate is known depends on the knowledge of the collection efficiency of the measuring system. The following assumptions were made concerning these quantities: the slow neutron flux was assumed to be known to ±5%; the activation cross section of P^{31}, 0.19 ± 5.2% barns (16); decay constant of P^{32}, 14.30 days; accuracy of P^{32} simulated source, ±5%; statistical error inherent in the radioactive decay phenomenon was kept at 1% in the phosphosilicate glass region by taking a sufficiently large number of counts.

The phosphorus concentration profile was obtained by dividing the decrement in phosphorus activity detected on the silicon after each etching step by the thickness of the oxide slice removed. The error due to statistical fluctuations in counting rate can be kept small, as discussed above, but the determination of the oxide slice thickness introduces a considerable error. The shift in the position of the reflectance minima from one etching step to the next can be measured to about ±15Å; since a single etching step was usually of the order of 200Å, the error for each individual point in the phosphosilicate glass region due to this source of error is usually about 7.5%.

At the transition from the glass region to the weakly phosphorus-doped SiO_2, etch rates occasionally dropped to very low values and only 40-50Å were removed per step. Where the experimental points in the graphs shown are very closely spaced ($<<$100Å apart), only the general trend of the curve, rather than the absolute values of the individual points should be considered; the latter could easily be wrong by a factor of 2. The points outside the phosphosilicate region are shown only for the sake of completeness; they show very strong scatter, as is to be expected for a variety of reasons.

It is estimated that the absolute phosphorus concentrations in the phosphosilicate region are known to better than ±30%, the relative phosphorus concentrations in the glass region to better than ±20%, and the relative phosphorus concentrations in the low phosphorus region within a factor of about 2.

Effects of High Phosphorus Concentration on Diffusion into Silicon

M. C. Duffy,* F. Barson,* J. M. Fairfield,* and G. H. Schwuttke

IBM Components Division, East Fishkill Facility, Hopewell Junction, New York

ABSTRACT

Phosphorus diffusion into silicon has been explored near and above the solubility limit by radiochemical profiling and compared with crystal damage by x-ray diffraction microscopy and Sirtl etch techniques. An apparent diffusion retardation has been found for very high source concentrations that results in a shallowed junction penetration for certain higher surface concentrations. The retardation phenomenon occurs over a narrow range of surface concentrations, within which diffused junctions are nonuniform, or ragged. This effect can be correlated with large amounts of crystal disorder inside the diffused area and dislocation loops outside at the peripheries. These outside loops have been found to degrade transistor gain.

Phosphorus diffusion into silicon has been very important in the semiconductor device industry because of its use in fabricating N-P junctions, especially emitters for N-P-N transistors. Nevertheless, phosphorus diffusion from high concentrations is not well understood and many anomalous effects have been reported (1-6). An additional anomaly not reported previously has been found which manifests itself in an apparent retardation of the phosphorus diffusion under some circumstances when maximum surface concentrations are involved. This anomaly can have serious consequences upon device fabrication.

The effect can best be described by outlining the conditions under which it has arisen in typical transistor fabrication procedures. In our case, phosphorus diffusion is accomplished by a two step process, a deposition and a drive-in cycle. The system and technique are similar to that used by McDonald *et al.* (6). The deposition cycle is 35 min in length at 970°C with a controlled amount of a phosphorus source in an ambient of nitrogen with about 2% oxygen. The drive-in cycle is 5 min in dry O_2, 30 min in steam, and 40 min in dry O_2, also at 970°C. After deposition only, the diffused junction depth increases with phosphorus source concentration (in the ambient gas) up to a point and, thereafter, remains constant.

Presumably this point corresponds to the solid solubility of phosphorus at the deposition temperature. After the subsequent drive-in cycle, the junction depth initially increases with phosphorus source concentration as before, but at a certain concentration it decreases sharply as shown in Fig. 1. Also, as illustrated by the photo inserts, there is a concentration range in which the junctions are ragged, which is a serious effect for emitter diffusions. Flat junctions are obtainable above and below this ragged area, which appears to be a transition region.

An understanding of this phenomenon is important for controlling transistor fabrication procedures employing high concentration phosphorus diffusions. Other types of phosphorus diffusion techniques also result in this retardation effect at high concentrations. Furthermore, although flat emitter junctions can be made by employing phosphorus concentrations above the ragged region, certain transistor parameters are influenced and degraded (*e.g.*, gain) when the emitter diffusion is in this retarded region. Therefore, this phenomenon has been investigated with the purpose of understanding the conditions under which it arises. This report describes the investigation and discusses possible mechanisms through which the diffusion retardation and ragged junctions should occur.

Experimental Procedure

For this investigation, Czochralski grown silicon wafers (111) oriented and virtually dislocation free were used. They were lapped and chemically polished to remove all surface damage. Phosphorus diffusions

* Electrochemical Society Active Member.

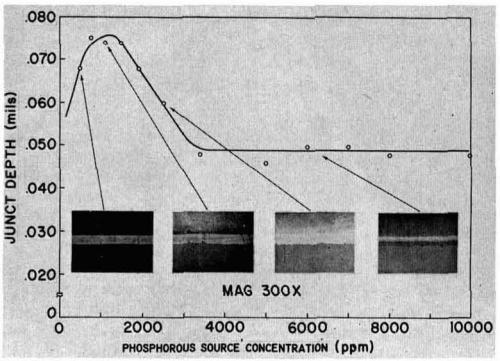

Fig. 1. Junction depth vs. phosphorus concentration; circles represent data after drive-in cycle. Photo inserts illustrate the junction depth from beveling and staining at representative points.

were done in the manner described in the introduction. Both blanket diffusions over the entire wafers and planar diffusions using standard oxide masking techniques were used; some of the planar structures were emitters of actual N-P-N transistors. Junction depths were measured by standard angle lap and copper staining techniques.

Diffused phosphorus profiles were determined on blanket diffusions by neutron activation analysis techniques similar to that employed by Tannenbaum (1) and Kooi (7). After diffusion, wafers were irradiated with neutrons to produce P^{32}. The wafers were profiled by anodizing and etching the resultant oxide to remove thin layers of silicon and employing a liquid scintillation radio-assay of the etchants to determine the amount of phosphorus atoms removed in each etching step. In some cases, the wafer itself was counted with a Geiger-Mueller type counter after each step; the two counting techniques agreed well.

The crystallographic damage of the diffused areas was determined by x-ray transmission diffraction microscopy, using the scanning oscillator technique (SOT) to record topographs of entire wafers (8); by transmission electron microscopy (9); and by Sirtl etching (10) of diffused areas. Taking advantage of the nondestructive nature of the first technique, x-ray topographs were made of both blanket and planar diffused wafers after both the deposition and the drive-in cycles. In a few cases, transmission electron microscopy was used to resolve the structure of the crystal disorder revealed by the x-ray topographs (11). Finally, diffused areas were Sirtl etched for 10-15 sec and examined for crystal disorder.

In some cases when the crystal structure around actual devices was examined, transistor gain and V_{be} were measured and correlated with the crystallographic structure of the phosphorus diffused area. If the base width is narrow compared to carrier diffusion length, V_{be} at a given low current can be used as a relative measure of total base doping (12). Since the time-temperature cycles of these diffusions were identical and the junction depths similar, small variations in V_{be} reflect similar variations in effective base width; equal V_{be}'s indicate equal base widths. For this investigation V_{be} was used only as a relative measure of effective base width and no attempt was made to relate this factor to transistor gain theoretically.

Results and Discussion

Figure 2a illustrates the phosphorus profiles prior to drive-in for two concentrations of phosphorus, one above and the other below the ragged region. As might be expected, the profiles are similar and the junction depths are almost equal. Figure 2b shows profiles for two similar wafers after drive-in. In agreement with the junction depth measurements shown in Fig. 1,

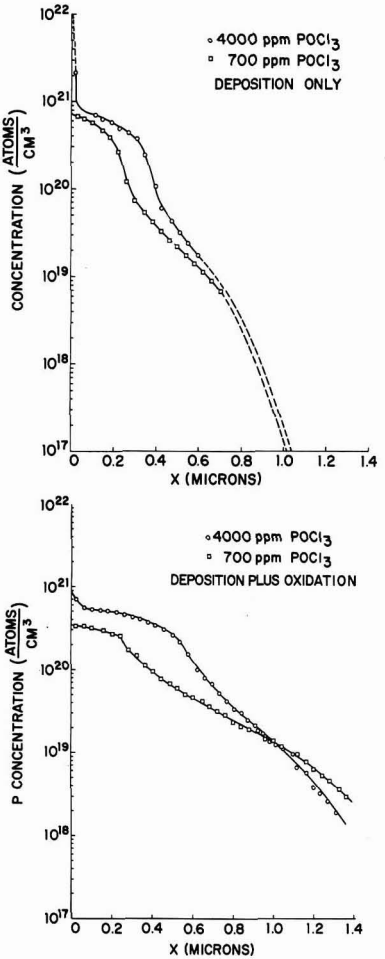

Fig. 2. Total phosphorus concentration profiles; (a) after deposition only, (b) after both deposition and drive-in.

the lower surface concentration diffused to a greater depth. Also, the concentration gradient at any depth is steeper for the higher concentration diffusion. Thus, the effective diffusion coefficient for the higher concentration appears to be reduced all along the profile.

The crystal damage in the diffused areas shows a similar relation to the process steps as the diffusion profiles in that anomalous behavior appears after the oxidizing drive-in-cycle on high concentration samples. After deposition only, the x-ray topographs show almost no evidence of dislocations or precipitation even when very high concentrations of phosphorus are used. An example of such a topograph is illustrated in Fig. 3a which shows no contrast indicative of damage. However, after drive-in, wafers deposited with high concentrations of phosphorus (*i.e.*, above the ragged region) reveal much crystal disorder as indicated by the anomalous contrast of Fig. 3b; this is the same wafer shown in Fig. 3a. It was confirmed through electron microscopy that this crystal disorder consists of dislocations and precipitates as illustrated by the electron micrographs, Fig. 3c.[1] On the other hand,

[1] It may seem surprising that no dislocations appear after deposition; however, it is possible that the rather abrupt appearance of the dislocations is the result of a threshold effect activated by the small increase in total concentration and/or an enhancement of crystal energy from the additional heat cycle and surface oxidation of the drive-in. This is supported by Shockley's model which requires a certain minimum impurity concentration for dislocation formation (see H. S. Queisser, *J. Appl. Phys.*, 32, 1776 (1961).

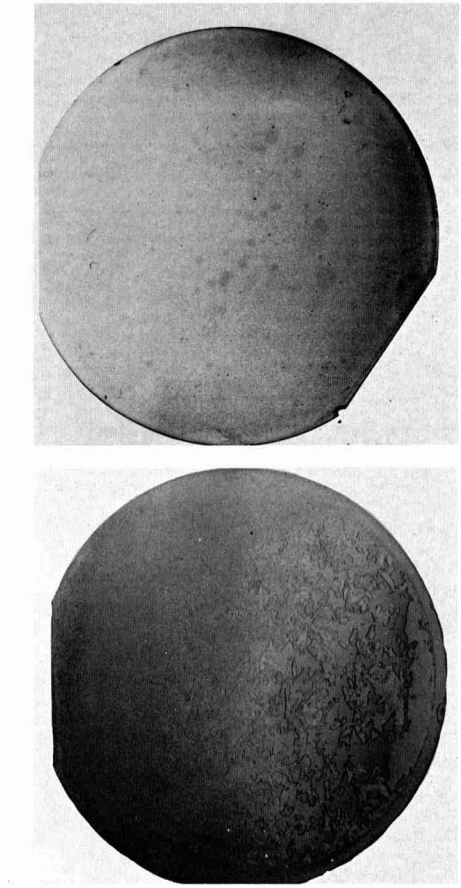

Fig. 3. X-ray topograph (SOT) and electron micrographs of blanket phosphorus diffused wafer; (a) x-ray topograph after deposition only; (b) x-ray topograph after drive-in; (c) electron micrograph illustrating dislocation networks, taken at the surface, magnification *ca.* 8000X.

wafers whose deposition phosphorus concentration was below the ragged region are still relatively free of crystal damage after drive-in. Wafers within the ragged region show a varied crystal disorder.

These observations are confirmed by Sirtl etching. After deposition only, the Sirtl etch technique reveals little surface structure. After drive-in, there is much crystal disorder for the wafers of higher phosphorus concentration as shown in Fig. 4. For the sample of 500 ppm phosphorus source, there is the beginnings of a "crow's foot" type pattern similar in nature to the slip lines reported by McDonald *et al.* (6) for similar types of phosphorus diffusion. As the concentration increases, the pattern becomes more dense until it resembles a general haze. Note that for the highest concentration there are a large number of etch pits surrounding the emitter. These pits result from dislocation loops that propagate for considerable distances outside of some high concentration phosphorus diffused planar structures. These dislocations have been described previously (13), and have been shown to be distinct from and often in addition to the diffusion induced dislocation networks within the diffused areas.

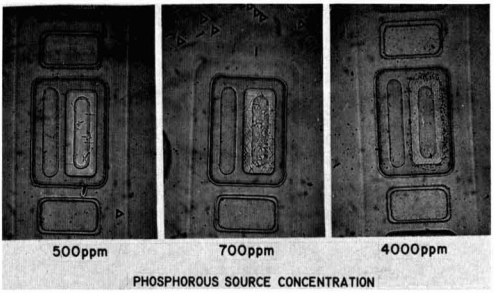

Fig. 4. Sirtl etch patterns of transistor structures with phosphorus diffused emitters. Note etch pits surrounding emitter area of unit highest phosphorus concentration. Magnification *ca.* 215X.

From the foregoing observation, it appears that the ragged junction area is a transition region in which diffusion induced dislocations and precipitates are forming. In other words, the dislocations, etc. can be directly correlated with retardation of phosphorus diffusion. When these dislocations are uniformly present or absent across a wafer, the junctions are flat. When these dislocations are not uniform, as when the phosphorus concentration is such that dislocations are just beginning to form, the diffused junctions have variable depths; or, they are ragged. This would correspond to the ragged region of Fig. 1.

The crystal damage within the diffused areas, consisting of diffusion induced dislocations and precipitation, was found to extend into the silicon for about 20-25 μin. (or about 1/3 junction depth) as determined by combining the x-ray technique with the anodic removal of thin silicon layers. Conversely, the dislocation loops around the edges of the planar structures extend to depths of 0.5 mils (and sometimes more). Thus, the former type of damage would be confined to the emitter of a transistor, whereas the peripheral dislocation loops would extend well through the base. These dislocation loops are correlated with a reduction of transistor gain; a phenomenon presumably due to carrier recombination within the base along the dislocations. For example, consider the two device wafers, of which x-ray topographs are shown in Fig. 5. The phosphorus concentrations are just about the ragged region in both cases (Fig. 1), and all junctions are flat. However, the peripheral dislocation loops around the edges appear on only one of the wafers. Note that the geometry of the units themselves are delineated by the contrast resulting from the macroscopic elastic strains around the phosphorus diffused areas. The average V_{be} for both was 0.70v ($\pm$0.005), but the transistor gain (at 2.5 ma) of those without dislocations was 52 $\pm$ 3 and of those with dislocations was 33 $\pm$ 5. This phenomenon can also be illustrated by Fig. 6 which plots transistor gain (β) *vs.* V_{be} for units whose phosphorus concentrations in the emitters were both above and below the ragged re-

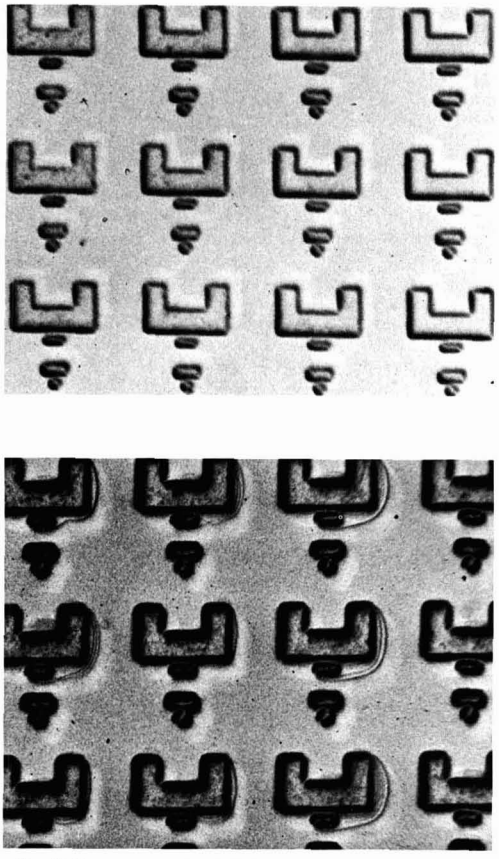

Fig. 5. X-ray topographs of device structures upon which transistor gain was subsequently measured. $V_{be} = 0.70$ at $I_e = 0.5$ ma: (a) devices without peripheral dislocation loops, $\beta = 52$; (b) devices with dislocation loops, $\beta = 33$.

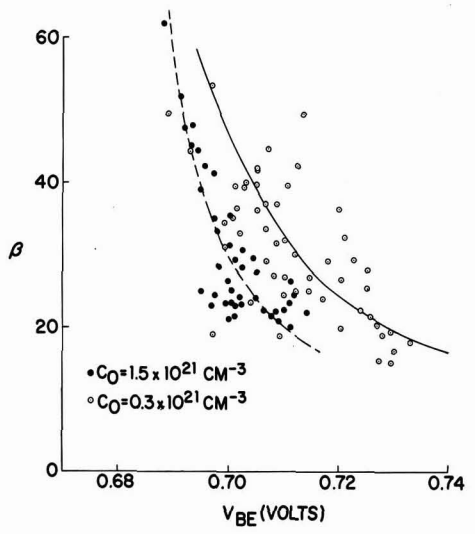

Fig. 6. Transistor gain, "β" vs. V_{be} taken at $I_e = 0.5$ ma for transistor made with high and low phosphorus emitter diffusions.

gion, 8000 ppm and 500 ppm, respectively. Those of higher concentration would have the peripheral dislocation loops but the others would not. It is obvious that the lower phosphorus concentration yields a higher gain for any given V_{be}.

Possible Mechanisms

At this time, it is not possible to establish a firm model to explain the retardation or ragged junction phenomenon; however, several possible contributory mechanisms may be discussed. As indicated above, the formation of dislocations and precipitates at high concentrations of phosphorus appears to correlate directly with the retardation of the phosphorus diffusion. This suggests a possible relation with relief of lattice strain through dislocations. The diffusing phosphorus concentration profile will introduce strains which are counterbalanced by tensile stresses of the silicon covalent bonds in the neighborhood of the profile itself (14). This strain may enhance the diffusion coefficients of the diffusing impurities. For example, Balluffi and Ruoff (15) proposed three possible mechanisms whereby diffusion is enhanced in strained lattices owing to an increased concentration of vacancies. (Phosphorus is generally believed to diffuse by vacancy exchange.) Two of their three mechanisms involve relationships of excess vacancies to moving dislocations, and the third involves merely an increase in vacancy formation rate in the bulk lattice. Now, the formation of high densities of dislocations (or precipitates) may either simply reduce the lattice strain and the strain enhanced diffusion, or it may "anchor" the dislocations at nodel points of the dislocation networks to prevent a dislocation movement. With respect to the latter possibility, Joshi and Wilhelm (9), show the existence of such nodal points in phosphorus diffusion induced dislocation networks and suggested their role in preventing dislocation movement. Thus, the diffusion induced dislocations may nullify a strain enhanced diffusion mechanism, which is operative just below the ragged junction region.

In addition, the diffusion induced dislocations and precipitates may reduce the effective mobility of the diffusing phosphorus atoms by providing precipitation sites for some phosphorus atoms. This possibility was suggested by Lawrence (16) to explain an apparent retarded phosphorus base diffusion of a PNP transistor when high concentrations of phosphorus were used as the base diffusant, and it was further discussed by Joshi and Dash. (17). However, it must be noted from Fig. 2b that the lower phosphorus concentration profile reflects a higher effective diffusion coefficient at depths well below the point at which precipitates cease.

Since high densities of dislocations correspond to the condition of retarded diffusion, any diffusion enhancement due to dislocations, or their formation, is secondary. This is reasonable since these dislocations normally lie perpendicular to the diffusion direction, see Fig. 3c, and are, thus, unlikely to provide preferential diffusion paths. Also, the formation of these dislocations need not produce a large excess of vacancies if their formation mechanism is by slip. Thus, Nicholas' model, whereby the mere formation of dislocations causes very high vacancy concentrations (3), is probably not important in our system.

Summary

A retardation effect of phosphorus diffusion at very high concentration is reported. This retardation is phenomenologically related to the formation of diffusion induced dislocations. It is suggested that this relation is through a reduction of strain enhanced diffusion through dislocation formation. However, precipitation at dislocations may also affect the system.

Also reported is the existence of large dislocation loops around planar structures diffused under conditions of retarded phosphorus diffusion. If these dis-

location loops occur around the emitters, they seriously reduce transistor gain.

Acknowledgments

The authors gratefully acknowledge the help of Dr. B. Masters, under whose direction the radiochemical profiles were obtained, and Mr. B. Medvecky for virtually all of the diffusion work.

Manuscript received June 26, 1967; revised manuscript received Sept. 11, 1967. This paper was presented at the Philadelphia Meeting, Oct. 9-14, 1966, as Abstract 193. Part of this work was supported under AFCRL Contract AF 19(628)-5059, Bedford, Massachusetts.

Any discussion of this paper will appear in a Discussion Section to be published in the December 1968 JOURNAL.

REFERENCES

1. E. Tannenbaum, *Solid State Electron.*, **2**, 123 (1961).
2. S. Maekawa, *J. Phys. Soc. Japan.*, **17**, 1592 (1962).
3. K. H. Nichols, *Solid State Electron*, **9**, 35 (1962).
4. U. K. Subashiev, A. P. Landsman, and A. A. Kukharskii, *Soviet Phys. Solid St.*, **2**, 2406 (1961).
5. P. A. Iles and B. Leibenhaut, *Solid State Electron.*, **5**, 331 (1962).
6. R. A. McDonald, G. G. Ehlenberger, and T. R. Huffman, *ibid.*, **9**, 807 (1966).
7. E. Kooi, *This Journal*, **111**, 1383 (1964).
8. G. H. Schwuttke, *J. Appl. Phys.*, **36**, 2712 (1965).
9. M. L. Joshi and F. Wilhelm, *This Journal*, **112**, 185 (1965).
10. E. Sirtl and A. Adler, *Z. Metallkde.*, **52**, 529 (1961).
11. G. H. Schwuttke and F. Wilhelm, *Bull. Am. Phys. Soc.*, **12**, 120 (1967).
12. H. K. Gummel, *Proc. I.R.E.*, **49**, 834 (1961).
13. G. H. Schwuttke and J. M. Fairfield, *J. Appl. Phys.*, **37**, (1966); and J. E. Lawrence, *This Journal*, **113**, 819 (1966).
14. S. Prussin, *J. Appl. Phys.*, **32**, 1876 (1961).
15. R. W. Balluffi and A. L. Ruoff, *ibid.*, **34**, 1634 (1963).
16. J. E. Lawrence, *ibid.*, **37**, 4106 (1966).
17. M. L. Joshi and S. Dash, *IBM J. Research and Dev.*, **10**, 446 (1966).

D-C Dielectric Breakdown of Amorphous Silicon Dioxide Films at Room Temperature

F. L. Worthing

Bell Telephone Laboratories, Incorporated, Murray Hill, New Jersey

ABSTRACT

The dielectric breakdown properties of atmospheric pressure steam-grown silicon dioxide films, grown on fresh epitaxial layers with degenerate silicon substrates, were studied at room temperature as a function of d-c voltage, time, polarity, thickness of the oxide, and rate of change of voltage. Contact was made to the oxide by 0.025 in. diameter evaporated gold dots. The observed phenomena were found to depend basically on the polarity of the applied potential. At positive silicon potentials (gold dots negative) dielectric breakdown occurred abruptly with no detectable conduction below breakdown. Positive breakdown is not time dependent and appears to be of the type generally referred to as intrinsic or disruptive breakdown. At negative silicon potentials (gold dots positive) these films exhibited conduction in the na range and a time dependence of dielectric breakdown. If t is the time it takes an oxide to breakdown at an applied voltage V, a linear relationship between V and $t^{-1/4}$ is observed over a range of approximately 150v. This is an empirical relationship known as Peek's law.

Several measurements have been found useful for the comparative evaluation of silicon dioxide films developed for device passivation. One of these is dielectric breakdown strength. However, there has frequently been confusion due to discrepancies between values obtained by different methods.

The dielectric breakdown properties of silicon dioxide films were studied at room temperature as a function of d-c voltage, time, polarity, thickness of the oxide, and rate of change of voltage. The films were grown on fresh epitaxial layers of approximately 25 ohm-cm, N-type with 0.01 ohm-cm, N-type silicon substrates. Surface cleaning of the substrates prior to epitaxial deposition consisted of a solvent degrease, a 2-min HF dip, a deionized water rinse, a 15-min soak in HNO_3 at 80°C, and a final deionized water rinse. Oxides were grown directly on the epitaxial layers, without additional cleaning, by heating the silicon substrates in 1050°C steam at atmospheric pressure. Oxide growth time was about 1 hr (depending on the desired oxide thickness) after which the samples were air quenched. Index of refraction for the oxide films was about 1.47.

For the tests about to be described, dielectric breakdown will be arbitrarily defined as occurring at that voltage which is sufficient to produce damage resulting in a sustained leakage current greater than 1 μa as long as the applied voltage is maintained. An order of magnitude change in either direction for this definition would not greatly alter the values of dielectric strength reported here. After-breakdown self-healing is excluded, and a contact dot generally exhibits current greater than 0.1 μa at any applied voltage in the same polarity.

Sample Preparation and Measuring System

The silicon wafers used were 0.250 × 0.420 × 0.015 in. Various samples having oxide thicknesses ranging from 3000 to 10,000Å were used, although the most commonly used oxide thickness was 6000Å. Fifty 0.025 in. diameter gold contact dots 5000Å thick were evaporated on the oxide. The underside of the silicon substrate was electroless nickel plated to make electrical contact with the test stage. Unless otherwise noted, all samples with their contact dots were baked at 400°C for aproximately 1 hr in air before breakdown tests were conducted. The gold dots were contacted by a 0.002 in. diameter gold probe.

Test equipment consisted of a Keithley Model 240 regulated high voltage power supply (accuracy ±1%) and a Hewlett-Packard 425A microammeter. Chart recordings were obtained from a Varian strip chart

recorder, Model G-11A, fed from the microammeter. Voltages were measured by a Keithley Model 610A electrometer. The experimental arrangement is shown in Fig. 1. In some cases voltage was applied at a constant rate by means of a motor driven potentiometer.

In defining polarities the convention will be to call the negative polarity that voltage which makes the silicon negative, or gold contact dot positive.

Results and Discussion

Incipient breakdown region.—Figure 2 shows the current-voltage characteristic of a contact dot for which the voltage was applied as a voltage ramp. The ramp was started from zero and increased at a constant rate of 10 v/min, in the negative direction, that is, with silicon negative. The start of a region which will be referred to as the "incipient breakdown region" is indicated by the increase in conduction at about 280v (4.7×10^6 v/cm). As application of the voltage ramp continued, conduction continued to increase more and more rapidly, until breakdown occurred at 395v (6.6×10^6 v/cm). Figure 3 shows the conduction pattern of a contact dot for which negative potential was again applied as a voltage ramp, increasing at the rate of 10 v/min. This time, however, the ramp was stopped at the very beginning of the "incipient breakdown region." With the resulting fixed voltage of 300v (5.0×10^6 v/cm) maintained on the sample conduction continued to increase, until breakdown occurred 46 min later. It was thus found convenient to define the "incipient breakdown region" as that region where the application of negative potential results in a leakage current sufficiently unstable that, with no further increase in the applied voltage, it will eventually rise continuously until breakdown occurs.

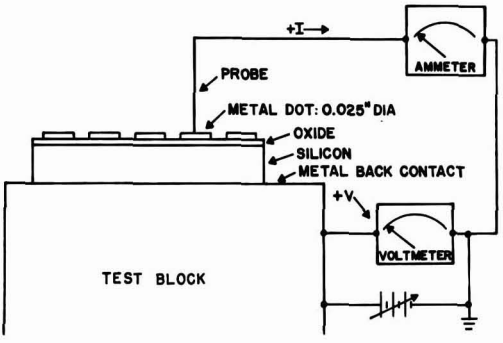

Fig. 1. Experimental arrangement for dielectric breakdown studies, shown for the case of positive silicon potential.

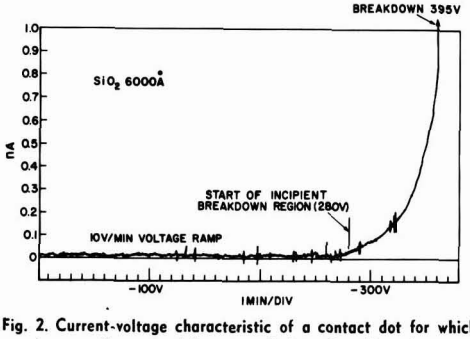

Fig. 2. Current-voltage characteristic of a contact dot for which increasing negative potential was applied to the silicon by means of a voltage ramp generator. Start of the incipient breakdown region is indicated by an increase in conduction at about 280v.

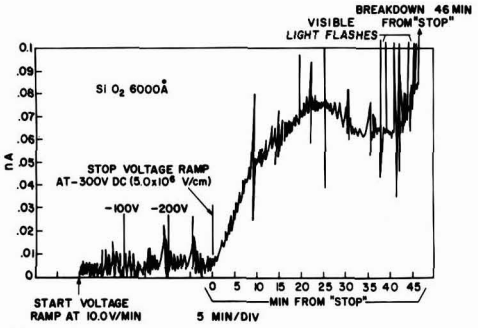

Fig. 3. Conduction pattern of a contact dot for which negative silicon potential was increased to 300v. Conduction continued to increase, with the voltage held constant, until dielectric breakdown occurred in 46 min. Note the appearance of transient current noise pulses, accompanied by visible light flashes, just prior to breakdown.

This is a characteristic feature of the conduction behavior for any fixed negative voltage in or close to the incipient breakdown region; over 100 dielectric breakdown tests were conducted in the manner described using various SiO_2 film samples. Thus the time required for breakdown to occur at the negative polarity is determined by the magnitude of the voltage and its rate of application prior to reaching that magnitude.

If the incipient breakdown region was approached repeatedly by the voltage ramp technique, the current instability started at a somewhat lower voltage each time and eventually breakdown occurred at about 250v (4.16×10^6 v/cm). This is about 150v lower than breakdowns obtained by a single continuous application of the voltage ramp. It thus appears that permanent damage was done each time the incipient breakdown region was approached, even though the current was never allowed to exceed 0.1 na. The phenomenon described here applies only to the case of silicon negative, since the incipient breakdown region is polarity dependent. The effect of lowering the breakdown strength by the previous application of stress has been noted previously by others (1). The foregoing observation would seem also to be in agreement with the theory of a constant volt-time life of insulation (2).

Time-voltage curves.—These experimental results show that, with negative voltages applied to the silicon, breakdown of SiO_2 usually is a gradual time dependent process. It is not therefore to be confused with intrinsic breakdown (to be discussed later) which would occur only as a very rapid process and for the most part at considerably higher field strengths.

In Fig. 4 each point represents time to breakdown, at negative silicon potential, for a different contact dot on the same sample. For example, the point indi-

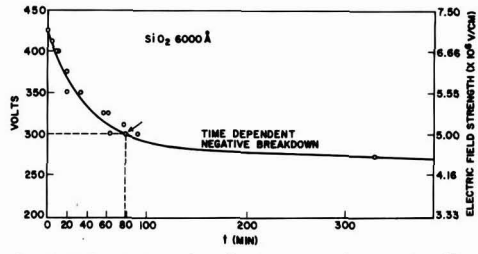

Fig. 4. Dielectric breakdown levels vs. time for negative silicon potential. Point indicated by the arrow was obtained by applying a negative potential of 300v until breakdown occurred in 78 min.

cated by the arrow was obtained by applying full stress at 300v until breakdown occurred in 78 min. ("Full stress" means that full voltage was reached in less than 1 min.) By choosing different test voltages for the various contact dots on a sample a time voltage curve is obtained. These test voltages are shown plotted against linear time. A replot of the same data is shown in Fig. 5 with the linear time scale replaced by a $t^{-1/4}$ scale, where t is time to breakdown. The $t^{-1/4}$ dependence is an empirical relationship known as Peek's law which may be stated as $V = V_o + at^{-1/4}$, where V is breakdown voltage at any time t, V_o is the infinite-time breakdown, and a is a constant (3). Materials for which curves obeying this law have been reported in the literature include synthetic plastics, various glasses, porcelain, and mica. (It should be noted, however, that in most of these cases there was no polarity effect, since the same electrodes were used on both sides of the insulator.) Peek's law appears to hold for d.c. only where there is some instability in conduction behavior which causes the current to tend to increase with the voltage held constant. This degradation of the dielectric with time has often been referred to in the literature as "thermal instability," although what actually happens may be gradual chemical or physical deterioration as suggested by Miller (4). The term thermal instability is used here with this qualification. Peek's law is applicable below some potential which is called the intrinsic breakdown level. In Fig. 5 the last two breakdown points, at the extreme right of the figure, fall short of the curve because they are in the intrinsic range which is not time dependent. The intrinsic level for this sample was about 410v. Time-voltage curves, similar to the one shown here, have been obtained for numerous samples with negative potentials applied over the range of 250-450v and at times ranging up to about 22 hr. These curves are reproducible on the same sample. Extrapolation of the curve of Fig. 5 to the intercept at $t^{-1/4} = 0$ yields an infinite-time breakdown voltage (V_o of Peek's law) of about 190v (3.16×10^6 v/cm).

Breakdown tests have been performed, using negative potentials, while a sample was held immersed in liquid nitrogen. Negative breakdown was found to be no longer time dependent. This result shows that heating of the stressed area must have some influence on the time dependent type of negative breakdown previously described. At a sufficiently high voltage breakdown occurred instantaneously in a manner similar to that to be described for positive potentials.

Transient current pulses.—Rather severe transient current noise pulses are frequently observed in the incipient breakdown region. Such pulses are shown in the chart recording of Fig. 3. A number of workers have reported the unsteady nature of currents just prior to breakdown. O'Dwyer has observed that one of the characteristics of avalanche breakdown in solids is that prebreakdown current will be very noisy, due to the buildup of avalanches which fail to reach the critical size (5). These pulses are randomly distributed although their magnitude increases with increasing voltage. They may appear with either fixed voltages or with voltage applied by the ramp technique.

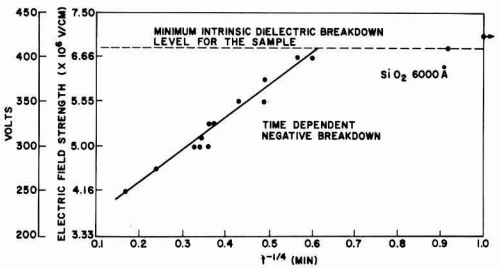

Fig. 5. Replot of the data of Fig. 4 with the linear time scale replaced by a $t^{-1/4}$ scale, where t is time to breakdown. The last two breakdown points, at the extreme right of the figure, are not in agreement with Peek's law because they are in the intrinsic range which is not time dependent.

Light emission and surface spots.—When the pulses described exceed approximately 10 na they are usually accompanied by visible light flashes which occur at various locations over the surface of the gold contact dot. The appearance is that of one or more pin point flashes of blue-white light, when the sample is viewed through a low power microscope in semidarkness. Where such flashes have occurred a change in the surface texture of the gold is usually observed. A portion of the surface of a gold contact dot is shown highly magnified in Fig. 6. The surface spots seen here are burned spots in the gold which indicate the location of previous flash sites. In some instances these spots are observed to have actual holes at their centers. There is evidence that these holes may extend through both the gold contact and the dielectric layer. In this respect they are apparently very similar to the self-healing breakdowns associated with weak spots in the dielectric, as recently reported by Klein and Gafni (6).

A sample on which the oxide under most of the gold contact dots had been broken down was subjected to a 20 to 1 mixture of nitrogen and chlorine gas at 800°C for 30 min (standard for all our chlorine etch studies) after the contact dots had been removed. Etch pits were found where contact dots had been located but not in the 0.024 in. margins between rows of dots.

To check the possibility that potential pinholes of the type discussed by Lopez (7) might be present within the film an ammonium fluoride-hydrofluoric acid etch was then used to reduce the oxide thickness from 6000 to 2500Å. The sample was again subjected to a hot chlorine etch for 30 min. No new etch pits developed in the margins.

As a further check for the possible presence of potential pinholes several samples were exposed to a water-amine-pyrocatechol etching system (8) at 110°C for 6 hr. This treatment removed approximately 1000Å of oxide, and the samples were found to have a negligible pinhole count. From these test results it was concluded that the oxide prior to dot evaporation was relatively free from pinholes or potential pinholes and that the reported light flashes are not caused by pinholes or potential pinholes which are detectable by chlorine or water-amine-pyrocatechol etching (9).

Discharges.—An obvious question concerning current pulses and flashes of the type described is whether they might be attributed to some type of discharge phenomena not occurring within the oxide itself. Possibilities include internal discharges (between the gold dot and the SiO_2 or in minute voids or cavities where the gold makes poor contact with the SiO_2), external or surface discharges (between the edges of

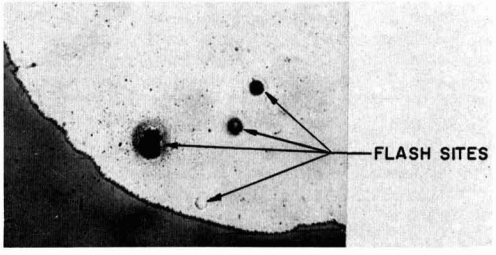

Fig. 6. A portion of the surface of a gold contact dot. Surface spots seen in this figure are burned spots in the gold which indicate the location of previous flash sites. Magnification *ca.* 100X.

the dot and the neighboring SiO_2), or corona type discharges. Mason has reported that surface discharges are often 10-50 times larger than internal discharges (10).

To determine whether these flashes were occurring in voids, cavities, or areas of poor contact between the gold and the SiO_2, the dots on one sample were subjected to rapid heating which caused the formation of many tiny bubbles under each dot. Electric field strengths sufficiently high to cause appearance of the usual flashes were then applied. It was observed that the flashes did not occur under or even near the edges of a bubble.

Next the possibility was investigated that some of these flashes might be the result of surface-type discharges occurring between the gold contact dot and the neighboring oxide. The gold probe was lowered to make contact with a gold contact dot, then paraffin wax was melted over the entire surface of the dot and around the gold probe. It was found that the flashes still occurred with about the same distribution and in the same field strength range. It was further found, however, that negative breakdown was no longer time dependent. Apparently in this case the heat produced when a flash occurred melted some of the adjacent wax which in turn cooled the flash site, thus preventing thermal instability. These results, along with those previously described concerning breakdowns obtained at liquid nitrogen temperature, reinforce speculation that the negative breakdowns observed were the result of thermal instability and were not influenced by external discharge effects.

Further evidence that external discharges need not occur in the range of field strengths observed is found in work done by Austen and Whitehead (11) in which they obtained even higher field strengths in air without encountering discharges. They measured the dielectric breakdown strength of thin sheets of mica at thicknesses of the same order as the SiO_2 films reported here. Their measurements were made using d-c voltage to obtain field strengths in the range of approximately 11 to 16 x 10^6 v/cm. They confirmed the absence of discharges by separate experiments. In later work Plessner has reported similar findings for silica films (12).

Dielectric breakdown at positive polarities.—Lack of positive conduction.—Dielectric breakdown at positive potentials (silicon positive) is not time dependent and appears to be of an intrinsic nature, which yields the true dielectric strength of the material itself (13). This lack of time dependence is attributed to the absence of thermal instability, which in turn results from the lack of conduction below breakdown at this polarity.[1] In other words, in the absence of conduction, thermal instability cannot occur. Oxide specimens appear to remain indefinitely stable at positive potentials below their intrinsic dielectric breakdown levels. A typical pattern illustrating the absence of conduction and the lack of time dependence of breakdown with positive silicon potential is shown in Fig. 7. Here the voltage ramp technique was used to apply positive potential at the rate of 10 v/min. Notice the capacitance charging current of about 3 pa which ceased when the ramp was stopped at the 400v level.

This sample was known to have an intrinsic dielectric breakdown of about 410v. However, a potential only 10v below this value could be maintained for over 10 hr with no sign of increased conduction or of breakdown. After this time the voltage ramp was restarted and breakdown occurred, as predicted, at the 410v level (~6.8 × 10^6 v/cm). Notice the contrast between this behavior and that of the sample shown in Fig. 3.

Conductivity and charge storage experiments, in which asymmetric conduction has been observed in

[1] The lowest current that could be accurately measured was around 2 pa.

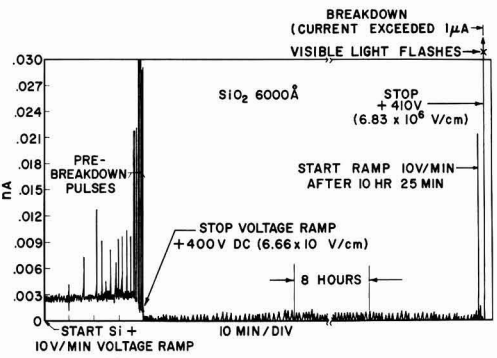

Fig. 7. Typical positive conduction pattern illustrating; (a) capacitive charging current of about 3 pa which ceased when the 10 v/min voltage ramp was stopped at the 400v level; (b) prebreakdown noise pulses; (c) absence of conduction and lack of time dependence with a positive potential of 400v applied to the silicon for over 10 hr; (d) a positive dielectric breakdown level of 410v (~6.8 × 10^6 v/cm) which was reached when the voltage ramp was restarted.

silica films at low voltage and high temperature, have been reported by (among others): Kerr, Logan, Burkhardt, and Pliskin; Ishikawa, Sasaki, Seki, and Inowaka; and by Yamin and Worthing (14). It was found that rectification occurred and that the conducting direction was with silicon negative, which is in agreement with observations reported here.

Voltage ramp technique and transient current pulses.—Some samples show current pulses in the prebreakdown region with changing positive potential. An example of this may be seen in Fig. 7. Samples which show this effect will often break down about 5-10% below what has been tentatively established (by the application of fixed stresses) as in intrinsic or disruptive breakdown level, if the voltage ramp is allowed to continue.

As previously described for pulses occurring at negative potentials, these current pulses are accompanied by visible light flashes at various locations on the surface of the gold contact dot when they exceed approximately 10 na. If at any time prior to breakdown the voltage ramp is stopped and the resulting fixed voltage maintained on the sample, charging current ceases and breakdown does not occur.

Other contact metals and films by other methods.—The polarity effects and the time dependence of dielectric breakdown reported have been observed for other contact metals such as aluminum and platinum.

The techniques described have been applied to the evaluation of films obtained by other methods on similar substrates. SiO_2 films obtained by plasma deposition, as reported by Ligenza and Povilonis (15), were tested by the methods described. Some differences in dielectric breakdown and prebreakdown conduction levels were observed, but in general the same basic phenomena as reported for steam-grown SiO_2 films were found.

Dielectric strength of atmospheric-pressure steam-grown SiO_2.—Approximately 50 positive dielectric breakdown tests were conducted using various SiO_2 film samples. Values of intrinsic dielectric strength, derived from the observed positive breakdown potentials, ranged from about 7 x 10^6 v/cm to about 1 x 10^7 v/cm. These values are in general agreement with those reported in the literature for quartz and vitreous silica (16). Positive breakdown values are, in general, highly reproducible for different contact dots on the same sample. A comparison of 12 positive breakdown values, obtained using several different SiO_2 film sam-

ples, showed an average dielectric strength value of 7.03×10^6 v/cm with a standard deviation of 0.30×10^6 v/cm. A comparison of dielectric strength values obtained using different area contact dots showed no significant area dependence. No variation in dielectric strength (volts/centimeter) with thickness of the oxide was found over the thickness range used (3000-10,000Å). Since the films were amorphous in structure, no variation of the dielectric strength with thickness was expected from Fröhlich's theory, because the mean-free paths for electrons would be too short (12).

Summary and Conclusions

Dielectric breakdown and prebreakdown phenomena, for SiO_2 films on silicon, are found to depend primarily on the polarity of the applied potential. This stems from a fundamental difference in the breakdown mechanism involved. At negative silicon polarities dielectric breakdown strength bears a linear relationship to $t^{-1/4}$, over a range of approximately 150v, where t is time for which voltage is applied. This is attributed to conduction and thermal instability. Time-voltage curves form a convenient means for displaying this time dependence at negative potentials.

Dielectric breakdown at fixed positive potentials is not time dependent. Breakdown appears to be of an intrinsic nature which yields the true electric strength of the dielectric independent of time. This is attributed to the lack of conduction below breakdown at positive potentials and the absence of thermal instability, whether due to electrical, thermal, chemical, or other effects. The polarity effects and time dependence of breakdown reported have been observed for other contact metals, such as aluminum and platinum.

In the breakdown experiments reported, which were performed at high voltages and room temperature, it was observed that the conducting direction is with silicon negative.

Conductivity and charge storage experiments have been performed on silica films at low voltage and high temperatures. These have been reported by, among others, Kerr *et al.*, Isikawa *et al.*, and by Yamin and Worthing (14). In these experiments it was also found that rectification occurred and that the conducting direction was with silicon negative.

Light flashes are usually observed at various locations over the surface of the contact dot when transient current noise pulses exceed approximately 10 na. Since both chlorine etch tests and the water-amine-pyrocatechol etching system indicate that the oxides used were initially free of pinholes or potential pinholes, it is concluded that the light flashes are not caused by pinholes which are detectable by these etches.

Values of intrinsic electric strength, derived from observed positive breakdown potentials, range from about 7 to 10×10^6 v/cm. These values are in general agreement with those reported in the literature for quartz and vitreous silica. Positive breakdown values are, in general, highly reproducible for different contact dots on the same sample. No variation in dielectric strength (volts/cm) with thickness of the oxide was found over the thickness range of 3000-10,000Å.

Manuscript received Aug. 23, 1966; revised manuscript received Sept. 29, 1967. This paper was presented at the San Francisco Meeting, May 9-13, 1965, as Abstract 97.

Any discussion of this paper will appear in a Discussion Section to be published in the December 1968 JOURNAL.

REFERENCES

1. S. Whitehead, "Dielectric Phenomena," Vol. III, "Breakdown of Solid Dielectrics," p. 248, Ernest Benn Limited, Bouverie House, London (1932).
2. D. F. Miner, "Insulation of Electrical Apparatus," p. 49, McGraw-Hill Book Co., New York (1941).
3. D. F. Miner, *ibid.*, p. 40 (1941).
4. H. N. Miller, "Nondestructive High Potential Testing," p. 17, Hyden Book Co., New York (1964).
5. J. J. O'Dwyer, "The Theory of Dielectric Breakdown of Solids," p. 12, Oxford at the Clarendon Press (1964). J. J. O'Dwyer, *Advances in Physics*, **7**, 349, (1958).
6. N. Klein and H. Gafni, *IEEE Trans. on Electron Devices*, Vol. ED-13, February 1966, pp. 281-289.
7. A. D. Lopez, *This Journal*, **113**, 89 (1966).
8. R. M. Finne and D. L. Klein, paper presented at the Toronto Meeting of the Society, May 3-7, 1964, Abstract 82.
9. J. V. Dalton, Private communication.
10. J. H. Mason, "Progress in Dielectrics," Vol. I, p. 33, John Wiley & Sons, Inc., New York (1959).
11. A. E. W. Austen and S. Whitehead, *Proc. Roy. Soc.*, **A176**, 33, (1940).
12. K. W. Plessner, *Proc. Phys. Soc.*, **60**, 243 (1948).
13. S. Whitehead, "Dielectric Breakdown of Solids," p. 5, Oxford at the Clarendon Press (1951). A. von Hippel, "Tables of Dielectric Materials," Lab for Insulation Research, MIT, Vol. II, p. 71, June 1945.
14. D. R. Kerr, J. G. Logan, P. J. Burkhardt, and W. A. Pliskin, *IBM J. Res. Developm.*, **8**, 376-384 (1964); Y. Ishikawa, Y. Sasaki, Y. Seki, and G. Inowaka, *J. of Apply. Phys.*, **34**, 867 (1963); M. Yamin and F. L. Worthing, Paper presented at the Toronto Meeting of the Society, May 3-7, 1964, Abstract 75; M. Yamin, *IEEE Trans. on Electron Devices*, Vol. ED-12, March 1965, pp. 88-96.
15. J. R. Ligenza and E. I. Povilonis, Paper presented at the Washington Meeting of the Society, Oct. 11-15, 1964, Abstract 138.
16. A. E. W. Austen and S. Whitehead, *Proc. Roy. Soc.* **A176**, 33 (1940); A von Hippel and R. G. Maurer, *Phys. Rev.*, **59**, 820 (1941); K. J. Keller, *Physics*, **14**, 15 (1948).

Mechanism of Branching and Kinking during VLS Crystal Growth

R. S. Wagner and C. J. Doherty

Bell Telephone Laboratories, Incorporated, Murray Hill, New Jersey

ABSTRACT

The morphology of the solid-liquid interface and the contact angle configuration of the liquid alloy droplet determine the direction of growth of crystals prepared by the vapor-liquid-solid (VLS) technique. There are four different processes by which both growth kinks and branches can be formed. A change in solid-liquid interface shape during VLS caused by a lateral temperature gradient results in the formation of growth kinks. Branches are formed if the alloy droplet ruptures during the kinking sequence. A sudden increase in temperature can cause an unstable contact angle configuration. The alloy droplet may run down the side faces of the growing crystal, leading to the formation of growth kinks or branches. A sudden decrease in temperature may cause "pinching off" of small droplets from the main droplet, giving rise to branches. Finally, the codeposition of liquid-forming impurities may also lead to branch and kink formation. The proposed models have been verified experimentally for VLS growth of silicon and germanium. Crystalline defects, such as dislocations, are not essential for the branching and kinking process. It is shown that "growth shaping" during the VLS process is possible.

Many whisker crystals grown from the vapor contain growth kinks and branches. The accidental attachment of two crystals during growth, which occurs rather frequently, will not be considered in this paper. The morphology of branched and kinked crystals has been studied for germanium (1) and silicon whiskers (2). It has been found that the various segments of these crystals constitute a single crystal. For a kinked germanium crystal, the direction of growth was found to change abruptly from [111] to [11$\bar{1}$]. Similarly, a branched silicon whisker with a [111] main direction was found to be a single crystal, the branch resulting from simultaneous growth in the [11$\bar{1}$] direction.

Many different theories (3-7) have been proposed to explain branching and kinking during vapor-phase growth of whisker crystals. All theories assume that the whisker crystals grow by the "screw dislocation" mechanism. Branching and kinking are explained by a variation of the dislocation model involving either a climb process of the dislocation at the whisker's tip or nucleation of a branch at a dislocation intersection. However, there is no reported experimental evidence to justify any of the proposed theories. It appears rather that the observation of growth kinking and branching has lead many investigators to believe that these changes in growth habit can be attributed to the operation of a screw dislocation mechanism in whisker growth.

It has been shown that the vapor-liquid-solid (VLS) (8-12) mechanism explains many features of the growth of whisker crystals. It is the purpose of this paper to show that branching, kinking, and the growth of curved crystals can also be accounted for by the VLS process. The present work is an outgrowth of an earier investigation on the controlled growth of silicon crystals in the form of intricate patterns on silicon substrates (10). The crystals shown in Fig. 8 in ref. (10) were grown under nearly isothermal conditions using a resistance heated furnace 10 in. long. Branched or kinked whiskers did not form under these experimental conditions. At this point of the investigation, it was considered worthwhile to take motion pictures during VLS growth. For this objective, the experimental conditions had to be changed drastically. The limited working distance of the microscope required an alteration of the heating system. The resistance furnace was replaced by a 2 in. long graphite tube which served as susceptor inside the reaction tube. A considerable lateral and axial temperature gradient in the growth zone could not be avoided. Motion pictures of VLS growth clearly showed that very frequently the crystal branched or kinked during growth. In some experiments all the crystals in an array kinked in the same direction, toward the higher temperature region. Because of the small thermal mass of the graphite susceptor, sudden changes in temperature in the growth zone could be obtained by changes in the r-f output of the generator. Such changes, whether intentional or accidental, quite often resulted in branched and kinked whiskers. Similar changes in growth morphology were obtained by sudden changes of the total gas flow through the reaction tube. These observations were studied in detail, and the results are discussed in the following sections.

The proposed models are both simple and unique, and the experimental verification is unequivocal. It will be shown that crystalline defects, such as dislocations, are not essential for the branching and kinking process. We discuss in the first part of the paper the factors which control the direction of growth of silicon crystals grown by VLS. In subsequent sections are described four different processes by which branches and growth kinks can be formed. It is shown that controlled "growth shaping" during whisker growth from the vapor phase is possible.

Experimental

The experimental procedure for controlled VLS growth of silicon crystals has been reported previously (10). The hydrogen reduction of $SiCl_4$ was used as the transport reaction and gold as the liquid-forming impurity. The following experimental parameters were used in this investigation. The mean temperature of crystal growth was 1000°C. Temperature changes which were introduced intentionally will be discussed in the appropriate sections. A temperature gradient smaller than 3°C/cm was used for the isothermal growth experiments. The gradient was increased to over 40°C/cm for nonisothermal growth. In some experiments, the gradient was further increased by focussing a high power heat source on the sides of the growing crystals. A total hydrogen flow of 300 cc/min was used with a $SiCl_4$-to-hydrogen mole ratio of 0.02. Preliminary experiments indicated that controlled doping during VLS growth can yield important information about the growth mechanism. It was found that the dopant, introduced in gaseous form, also preferentially enters the liquid alloy droplet at the tip of the growing crystal. Doping therefore results

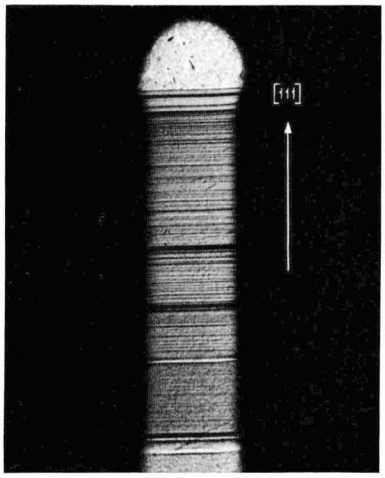

Fig. 1. Etched section of a [111] silicon crystal doped with phosphorus during isothermal growth. Magnification approximately 50X.

in clearly identifiable impurity striations which are parallel to the solid-liquid (SL) interface. These interface markers, introduced at given time intervals, permit a careful evaluation of interface transitions during branching and kinking. Ten cc/min hydrogen with a mole ratio of 0.0004 PCl_3 was used for the doping experiment. The duration of doping varied from 10 to 30 sec. Doped silicon crystals were sectioned parallel to the growth direction and etched with Sirtl (14) etch for about 1 to 4 min. The maximum diameter of all crystals shown in this paper is about 250-300μ. The measured rate of VLS growth was about 1 mm/hr. A high-temperature microscope[1] in conjunction with a movie camera was used to record the growth of individual crystals by time-lapse photography (13). X-ray topographs by the Lang (15) technique were taken on some samples using silver radiation.

Isothermal VLS growth.—The majority of silicon crystals prepared by the VLS technique, under isothermal conditions, grew in a [111] direction. It has been proposed (8) that this particular growth direction arises because the solid-liquid interface is a single (111) plane. It has been shown (12) that the interface can be very stable during VLS growth; the stabilizing factor is very likely the interface kinetics. To confirm this point, a number of silicon crystals were doped with phosphorus during isothermal growth. The crystals were subsequently sectioned on a plane parallel to the growth direction and etched as shown in Fig. 1. The pronounced bands indicate the introduction of dopant during growth, whereas the fine bands are produced by fluctuations in growth rate (12). The figure clearly shows that the solid-liquid interface remains stable, parallel to a (111) plane during isothermal VLS growth. It must be concluded that layer growth occurs on this interface; the alloy droplet advances therefore perpendicular to this face in a [111] direction.

It has been reported (12) that the shape of the solid-liquid interface of a [111] crystal is not circular but triangular with rounded corners. Microscopic observation shows that the solid-liquid contact angle along the meniscus of the droplet is nonuniform during growth, being slightly larger at the rounded corners. However, such a contact angle configuration, having threefold symmetry, stabilizes the liquid droplet on the growing crystal. The effect of gravity on the contact angle was found to be negligible. Crystals with diameters ranging from 50 to about 300μ were grown in the usual way, vertically upward. Subsequently, the whole growth apparatus was rotated 90°, and the VLS growth continued in a horizontal direction to about 1 cm length. The crystals were afterwards examined in an optical goniometer and found to be straight. Similarly, x-ray reflections obtained with a Weissenberg goniometer showed that the crystals were straight and grew in a [111] direction. It is evident, however, that any force which is strong enough to change the symmetry of the solid-liquid contact angle configuration can influence the direction of growth. Although layer growth still occurs on a (111) plane under isothermal conditions, the resultant growth direction will be controlled by the liquid contact angles.

A suitable combination of interface morphology and liquid contact angle can give rise to growth directions other than [111]. For example, silicon crystals can be grown in a [110] direction as shown in Fig. 2. The doping striations show that the interface consists of two {111} planes forming a ridge configuration. If the crystals are grown at about 1050°C, the prismatic side faces are four {111} planes which are parallel to the [110] growth direction. This configuration leads to a twofold symmetry of the contact angles, stabilizing the droplet on the growing crystals. VLS-grown germanium whiskers are frequently observed with the same [110] morphology. In addition, germanium crystals also grow in the [100] direction (16). In this case, the solid-liquid interface is formed by four {111} planes in the shape of a pyramid. Another morphology has been observed both for germanium and silicon, a twinned crystal growing in a [211] direction. The shape of the interface of these crystals is similar to that one of crystals with a [110] growth direction. However, the angle between the two {111} planes is 141.06° for twinned [211] crystals and 109.48° for [110] crystals, respectively. It can be said in conclusion that the solid-liquid interface is not necessarily perpendicular to the direction of growth. The interface morphology determines the direction of growth, and unidirectional growth is only possible for a stable contact angle configuration. It will be shown in the

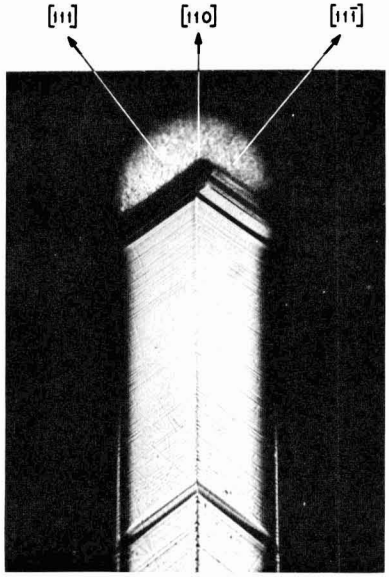

Fig. 2. Etched section of a [110] silicon crystal doped with phosphorus during isothermal growth. Magnification approximately 100X.

[1] American Optical long working distance microscope.

following section that a change in interface morphology during VLS growth invariably results in a change in growth direction.

Nonisothermal growth.—A model for branching and kinking during nonisothermal VLS growth has been proposed in a previous paper (11). The model is based on the assumption that a lateral temperature gradient can change the morphology of the SL-interface and thereby change the direction of crystal growth. The experimental verification of the proposed mechanism will be discussed in this section. The temperature conditions during VLS growth were changed from isothermal to nonisothermal. Time-lapse photography was used to obtain a permanent record of the growth sequence. The crystals were doped with phosphorus before, during, and after completion of the kinking process. Subsequently, the samples were sectioned, polished, and etched on a plane which is coplanar with the axial directions of the kinked crystal. A typical example of such an experiment is shown in Fig. 3 for a [111] to [$\bar{1}$11] kink. In this case the kinking was caused by exposing the right side of the growing crystal to a higher temperature than the left side.

The value of using controlled doping to study successive interface positions is evident. During isothermal conditions, the crystal grew perpendicular to the (111) plane, as discussed previously. However, the introduction of a lateral temperature gradient caused a change in interface morphology. The ($\bar{1}$11) plane was partly exposed in addition to the original interface. The growth rate perpendicular to the newly formed interface is slower than on the (111) plane because it is in a region of higher temperature. The new interface grew in area at the expense of the old one until finally the (111) interface has disappeared. The liquid droplet shifts during this process from the (111) to the ($\bar{1}$11) interface. Further VLS growth proceeds in the [$\bar{1}$11] direction. Figure 4 shows an enlargement of a (111) to ($\bar{1}$11) kink. Note that neither the (111) nor the ($\bar{1}$11) interface planes deviate from planarity during the kinking process. The macroscopic growth direction gradually changes from [111] to [$\bar{1}$11] resulting in the growth of a curved crystal. Figure 5

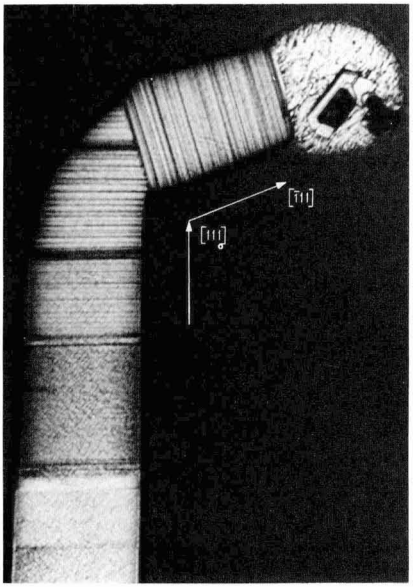

Fig. 3. Etched section of a [111] to [111] kinked silicon crystal doped with phosphorus. Magnification approximately 100X.

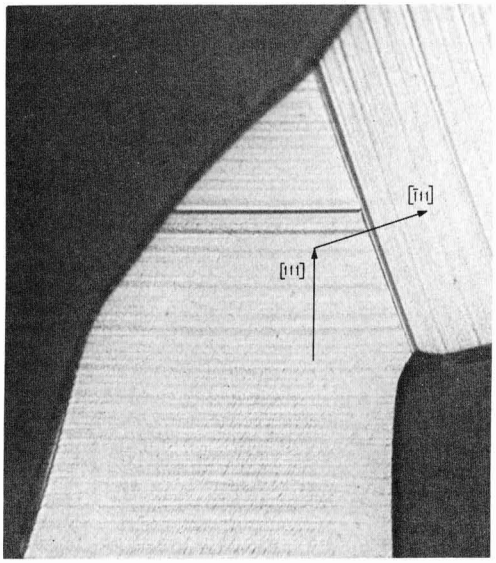

Fig. 4. Etched section of a [111] to [$\bar{1}$11] kink. Magnification approximately 275X.

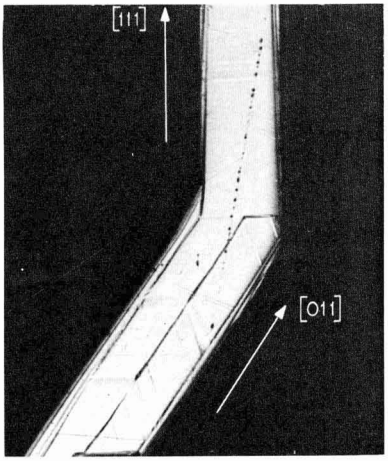

Fig. 5. Etched section of a [110] to [111] kink. Magnification approximately 50X.

shows a section of a crystal with a [011] to [111] kink. The [011] section of the crystal grew with an interface consisting of (111) and ($\bar{1}$11) planes. Again the SL interface changes in compliance with the proposed model. This sample was grown at a temperature of about 1050°C. The vapor-solid deposition rate becomes noticeable at this temperature (9, 12). This deposit surrounds the crystal grown by VLS. At even higher temperatures, the concave side of the kink becomes a preferred site for vapor-solid (VS) epitaxy. The true, original shape of the kink will be drastically altered by this deposit.

A small lateral temperature gradient may cause a gradual change in interface morphology. The growth direction will vary over a considerable length of the crystal, resulting in the growth of a curved whisker. Such events have been observed in a few cases. Figure 6 shows a photograph of a crystal curved during VLS growth. The liquid droplet is not supported by a single (111) interface, but rather extends downwards

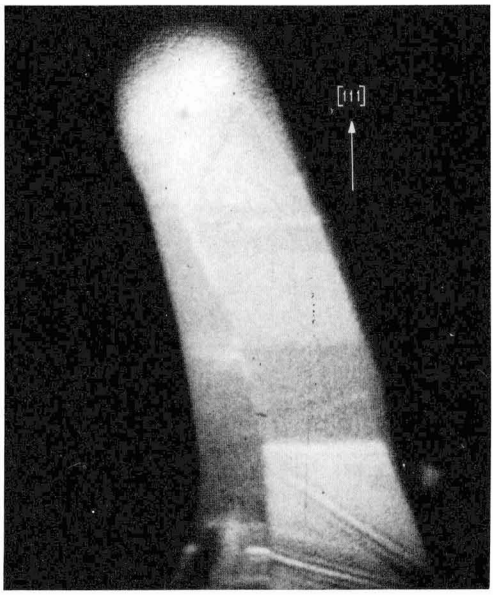

Fig. 6. Curved silicon crystal photographed during nonisothermal growth. Magnification approximately 50X.

at the left side of the growing crystal. Again, a VS deposit will obscure the shape of curved crystals. At high temperatures, the deposit ultimately will tend to "straighten" such curved sections, by increasing the diameter of the crystal.

Kinking under the influence of a temperature gradient was observed for over 100 crystals. About 20 crystals were examined for the presence of crystalline defects in the kink region. Lang topographs were taken and sectioned crystals were etched as shown in Fig. 3 and 5. The majority of the samples did not contain any observable defects in the kink region. A few specimens contained islands of Au-Si entrapments which are known to give rise to the generation of defects (12). It must be concluded that crystalline defects, such as dislocations, are not essential for the reported kinking process. Entrapment of liquid alloy may occur during kinking with subsequent formation of defects during cooling.

Figure 7 shows a Lang topograph of a [110] to [11$\bar{1}$] kink. The crystal was grown on an imperfect (111) substrate. Some dislocations continued to grow from the substrate into the crystal. All dislocations apparently grew out of the crystal at the lower section. The remainder of the sample, including the kink, is dislocation-free. Note the occurrence of "pendellösung" fringes both in the [110] and [11$\bar{1}$] sections of the crystal. The shapes of the fringes in the two sections are different because the cross section of the crystal is not the same in the two regions. The cross section is diamond-shaped in the [110] region and hexagonal in the [11$\bar{1}$] part. The occurrence of pendellösung fringes in the kink provides additional evidence that defects are not involved in the kinking mechanism.

It is evident from Fig. 4 that the area of the SL interface changes during the kinking process. The area first increases and finally returns to its original value after completion of kinking. The change in interfacial area imposes a constraint on the contact angle of the liquid alloy droplet. The constraint frequently causes rupture of the droplet, thereby giving rise to the formation of branch crystals as shown in Fig. 8. The time-lapse sequence, taken at constant magnification, illustrates four different stages during and after the kinking sequence. The crystal was grown on a (111) substrate at about 1050°C. The plane of the photograph is approximately (110). Figure 8a shows the trace of the SL interface and the droplet configuration during kinking at a time when the interfacial area is at a maximum. The kinking sequence is almost completed in Fig. 8b. The new {111} interface has increased considerably at the expense of the old interface. A small droplet, indicated by the arrow, has broken away from the main droplet during the transition. Figure 8c shows the interface and droplet configuration after completion of kinking. The small droplet gave rise to the growth of a branch crystal with a [111] growth direction. A later sequence of growth is shown in Fig. 8d. The effect of VS epitaxy in changing the

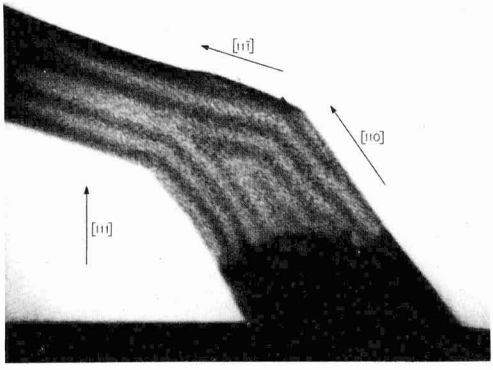

Fig. 7. (111) X-ray topograph of a [110] to [11$\bar{1}$] kinked silicon crystal. Magnification approximately 70X.

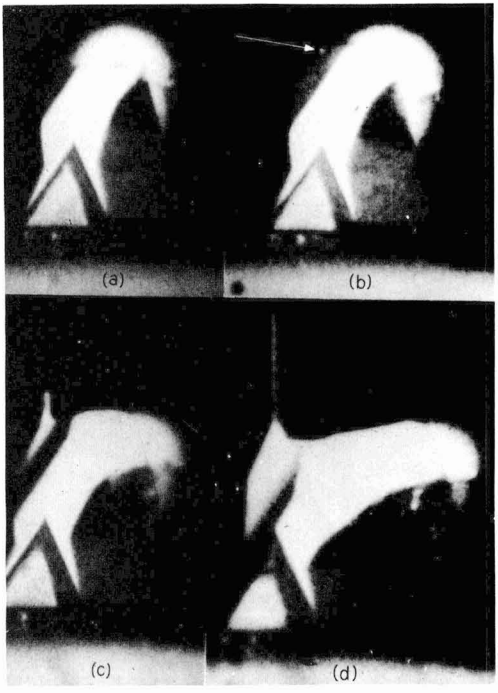

Fig. 8. Time-lapse sequence of branching and kinking caused by a lateral temperature gradient. Magnification approximately 120X.

external morphology can be seen at the base region of the small branch crystal by comparison of Fig. 8c and Fig. 8d. Some samples in which branching occurred during the kinking process were examined for perfection, both by x-ray topograph and etching. In most cases the branch and kink were found to be dislocation-free.

Generally, it is rather difficult to control the formation of a desired kink configuration under the influence of a lateral temperature gradient. Kinking can be initiated readily; however, there is little control over the shape of the liquid droplet during the transition process. The orientation of the growing crystal with respect to the isotherm is an important factor, as is evident from Fig. 3. The preferred orientation as indicated in the figure, is that in which only one plane, for example the $(\bar{1}11)$ plane, is parallel to the isotherm. If the interface transition occurs by exposing two or even three new {111} planes, the droplet invariably ruptures and multiple kinking ("antler" growth) will result. A slow VLS growth rate and a small temperature gradient help to prevent a rapid interface transition which also can cause a rupture of the liquid droplet.

Sudden increase in temperature.—It has been shown (10) that the volume of the liquid droplet during VLS growth depends on the deposition temperature. This dependency arises from the liquidus phase relationship of the particular alloy system. This feature has been used to change the diameter of silicon crystals during VLS growth by proper changes of the deposition temperature. It has been noted that such changes must be made gradually in order to avoid instability of the liquid droplet. A sudden increase in temperature, for example, from 1000° to 1100°C in 10 sec, will usually cause instability. The volume of the droplet will increase by about 13% for such a temperature change. The amount of silicon which is required to satisfy the new phase equilibrium cannot be supplied rapidly enough from the vapor-phase reaction. As a result, the necessary amount will be dissolved from the VLS crystal. The SL interfacial area, however, remains that for the 1000°C growth condition. As a consequence, the liquid will bulge over the side of the crystal. It will eventually wet the side faces in order to increase the interfacial area and to satisfy a stable contact angle configuration. The individual droplets will cause formation of branch crystals or kinks as VLS growth continues. A typical example of this process is shown in the time-lapse sequence in Fig. 9. Two crystals were initially grown at 1000°C, then the temperature was rapidly raised to about 1100°C. Figure 9a shows the droplet configuration during the rise in temperature. The solid-liquid contact angle which is slightly larger than 90° under equilibrium conditions has noticeably increased. In Fig. 9b, taken at maximum temperature, the droplet has increased its contact area by wetting the side faces of the crystal. Subsequently, the temperature was reduced to about 1000°C. The next two photographs show the resulting growth morphology at different times. The liquid broke up into smaller droplets giving rise to branch growth. Numerous experiments of the kind described in Fig. 9 were performed. It was found that the only important factor is a sufficiently large, rapid increase in temperature. The temperature does not have to be returned to its starting value. A large decrease in temperature after the instability has occurred must be avoided because this may lead to nucleation of silicon crystals in the droplets, resulting in uncontrolled growth (10). The droplet configuration during the rise in temperature was observed visually in some experiments. This provides some control over the resulting droplet configuration. Figure 10 is an etched $(0\bar{1}1)$ section of a crystal which was kinked by a controlled increase in temperature. Doping was used to mark the position of the SL interface during the growth experiment. Before raising the temperature, the droplet was on top of the [111] crystal which had grown under isothermal condition. The temperature was carefully increased until the droplet was clinging to the side of the crystal near its tip. The doping striations show that a new SL interface configuration was established. The crystal first grew in approximately a [011] direction and gradually changed to the stable

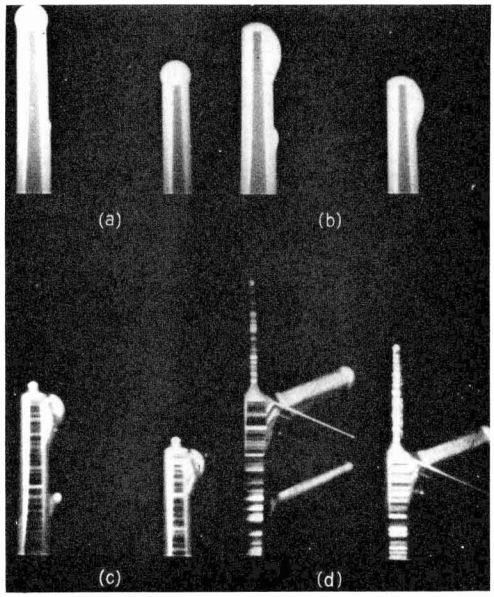

Fig. 9. Time-lapse sequence of kinking and branching caused by a sudden increase in temperature. Magnification approximately 13X.

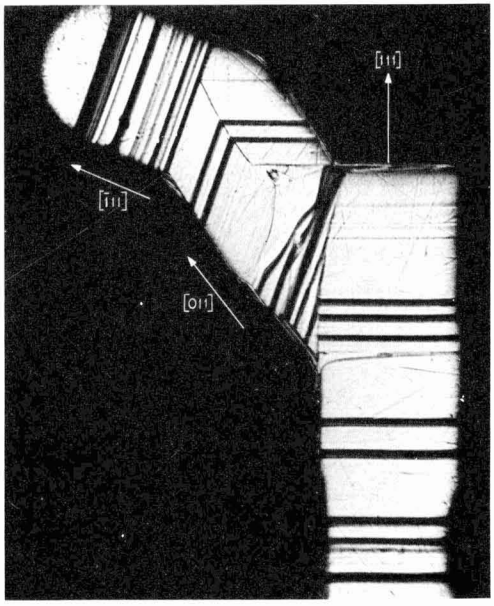

Fig. 10. Etched section of a silicon crystal kinked by a sudden increase in temperature, doped with phosphorus. Magnification approximately 100X.

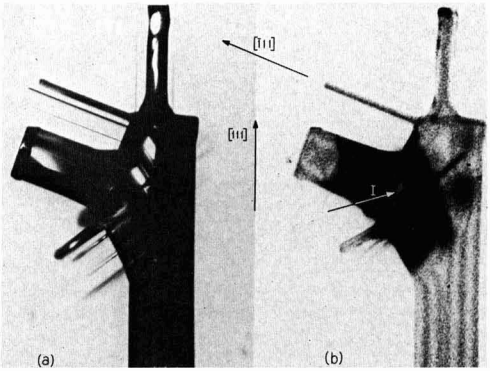

Fig. 11(a). Photograph of a branched crystal with alloy tips removed by etching. Fig. 11 (b). (111) X-ray topograph showing Au-Si entrapment. Magnification approximately 35X.

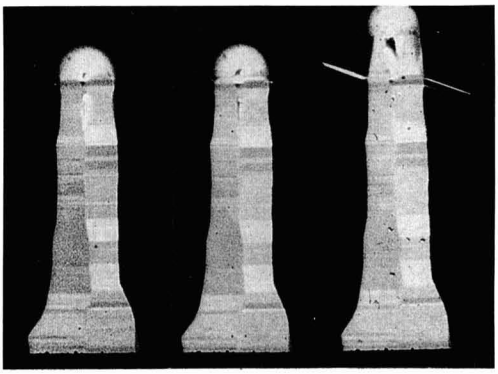

Fig. 12. Time-lapse sequence of branching caused by a sudden decrease in temperature. Magnification approximately 35X.

[$\bar{1}$11] direction. No dislocation etch pits could be found on this sample. Six crystals which branched or kinked by the discussed procedure were examined by x-ray topography. Entrapments of Au-Si alloy were found in four samples. Such a topograph and the actual sample are shown in Fig. 11. The hemispherical tips, composed of Au-Si alloy were removed from the crystals by etching. A significant aspect is that the crystallography of the branch and kink crystals is the same as that of the main crystal. Some of the fine crystals which can be seen on the actual sample could not be reproduced properly from the x-ray topograph. An island of Au-Si eutectic is indicated by an arrow. As usual, the inclusion gives rise to formation of defects (12).

Sudden decrease in temperature.—This mechanism is basically similar to the one discussed in the previous section. The volume of the liquid droplet decreases if the temperature is lowered during VLS growth. The excess of silicon freezes out of solution, by normal alloy regrowth, in order to establish the equilibrium composition. The solid-liquid contact angle, however, remains essentially constant during the change in temperature. This implies that a reduction in SL interfacial area is required to satisfy the same contact angle configuration. Therefore, a sudden decrease in temperature causes a sudden increase in growth rate because of alloy regrowth and a reduction of the diameter of the growing crystal. Small droplets frequently separate from the meniscus region of the droplet during the transition in volume. These droplets then give rise to formation of branches during subsequent VLS growth. The growth of branch crystals by this process is illustrated by the time-lapse sequence in Fig. 12. The crystal is shown in Fig. 12a during growth at about 1050°C. The temperature was subsequently decreased by 100°C in about 30 sec. Three small droplets were "pinched off" the main droplet during the transition, Fig. 12b. The last figure shows the crystal after continued VLS growth. The three branches grew in the same <111> direction, although inclined to the [111] direction of the main crystal.

It has been found in many experiments that this process of branch formation can be initiated easily by a sudden drop in deposition temperature. However, there is little control over the number of branches formed. The change in temperature must be rapid enough to cause separation of small droplets from the main body of the liquid alloy. A gradual decrease in temperature only causes a reduction in diameter of the growing crystal. The deposition temperature can be gradually raised after completion of branching. However, a sudden large reduction in temperature must be avoided because this may result in nucleation of silicon crystals in the liquid alloy. Such a large reduction may lead to uncontrolled VLS growth as shown in another paper (10).

The most common direction of the side branches is <111>. The <110> direction has been observed in a few cases. The diameters of the branches are usually small compared to the diameter of the main crystal. X-ray topography and etching studies indicate that the majority of the crystals are dislocation-free.

Codeposition of liquid-forming impurities.—The most likely process of branch and kink formation during vapor phase growth is due to codeposition of impurities. Impurities which satisfy the criteria for VLS growth may condense on an already grown whisker crystal. The transport can occur by a chemical reaction, for example, by disproportionation, or simply by an evaporation and condensation process. Such an impurity transport frequently has been observed during whisker growth of silicon or germanium using either a closed or a dynamic system. Each alloy droplet formed by this means may give rise to VLS growth of a branch crystal. The original crystal serves as substrate material. It should be emphasized that only extremely small amounts of impurities are required for this process. For example, a gold-silicon alloy droplet of about 100Å diameter can result in the growth of a silicon whisker a few millimeters long. The final morphology will be altered drastically in most cases because of VS deposition during and after VLS growth.

Many branched and kinked whisker crystals of silicon and of germanium were grown using codeposition of impurities. The experimental conditions for the growth of silicon whiskers have been described previously (2). Similar conditions were used for germanium (16). The formation of branch crystals is initiated by a sudden increase in supersaturation of liquid forming impurities in the growth zone, during or after completion of VLS growth. Numerous new alloy droplets will form and branch growth occurs. The resulting growth morphologies are similar to those in Fig. 3 and Fig. 8 in ref. (2). It is obvious that this process may not be used for controlled growth of branched and kinked crystals.

The mechanism discussed involving the codeposition of impurities probably is the most common cause of uncontrolled VLS growth. It should be noted that careful experimentation with codeposition of impurities originally lead to the discovery of the VLS mechanism (2).

Summary

The growth direction of silicon crystals prepared by the VLS technique is determined by both the shape

of the solid-liquid interface and the contact angle configuration of the alloy droplet. Unidirectional growth can occur only if these two parameters are kept constant during growth. A necessary condition for unidirectional growth is therefore an isothermal environment. Most crystals grown under this condition grow with a single {111} interface in a <111> direction. However, the macroscopic growth direction is not necessarily perpendicular to the growth interface. Specific interface configurations have been found where the interface consists of more than one {111} plane of equal area. These interfaces also form a stable contact angle configuration of the alloy droplet. The resulting growth direction is the vector sum of the individual interface growth directions.

A sufficiently large lateral temperature gradient changes the equilibrium interface, which invariably leads to a change in growth direction. A new stable interface will be formed during growth which is as parallel as possible to the isotherm. While a curved crystal is grown during the interface transition, subsequent growth is again unidirectional. Branches are formed if the alloy droplet ruptures during the kinking sequence. The likelihood of kinking for a given lateral gradient depends on the diameter of the growing crystal. It is the absolute temperature difference across the interface that causes interface transition.

Either a sudden increase or decrease in deposition temperature may introduce instability of the alloy droplet. A sudden rise in temperature causes an unstable contact angle configuration. The droplet may wet the side faces of the crystal to increase the interfacial area. The new droplet configuration results in formation of branches and or kinks. Similarly, a sudden decrease in temperature may cause pinching off of small droplets from the main droplet. These two processes of branching and kinking are more or less independent of the diameter of the growing crystal.

The most common cause of uncontrolled VLS growth of silicon or germanium was found to be the result of codeposition of liquid-forming impurities. The impurities can be transported to the reaction zone by a chemical reaction or by evaporation. Branches are formed when liquid-forming impurities condense on an already grown whisker crystal.

This investigation modifies the usual definition of a branch or kink. The terminology is unambiguous for a single kink, where the liquid droplet did not rupture during the interface transition. It is suggested that the growth direction which is associated with the main body of the liquid be used as the criterion. If this direction changes during growth, then the crystal is kinked. This is true even if small branch crystals continue to grow in the original growth direction. If the main growth direction remains constant, then any side crystal formed by small droplets is defined as a branch.

In conclusion it is emphasized that the proposed mechanism of unidirectional growth, branching, and kinking is strictly applicable only to whisker crystals grown by the VLS process.

Acknowledgments

The authors are grateful to W. G. Pfann, Professor N. Kato, and S. M. Arnold for many helpful contributions.

Manuscript received July 18, 1967; revised manuscript received Oct. 4, 1967.

Any discussion of this paper will appear in a Discussion Section to be published in the December 1968 JOURNAL.

REFERENCES

1. R. G. Treuting and S. M. Arnold, *Acta Met.*, **5**, 598 (1957).
2. R. S. Wagner, W. C. Ellis, K. A. Jackson, and S. M. Arnold, *J. Appl. Phys.*, **35**, 2993 (1964).
3. W. W. Webb, *ibid.*, **36**, 214 (1965).
4. J. P. Hirth and F. C. Frank, *Phil. Mag.*, **3**, 1110 (1958).
5. S. Amelinckx, *ibid.*, **3**, 425 (1958).
6. F. R. N. Nabarro and P. J. Jackson, "Growth and Perfection of Crystals," p. 81, John Wiley & Sons, Inc., New York (1958).
7. S. Amelinckx, *ibid.*, p. 144.
8. R. S. Wagner and W. C. Ellis, *Appl. Phys. Letters*, **4**, 89 (1964).
9. R. S. Wagner and W. C. Ellis, *Trans. Met. Soc. AIME*, **233**, 1053 (1965).
10. R. S. Wagner and C. J. Doherty, *This Journal*, **113**, 1300 (1966).
11. R. S. Wagner, "Crystal Growth," p. 347, Pergamon Press, Oxford and New York (1967).
12. R. S. Wagner, *J. Appl. Phys.*, **38**, 1554 (1967).
13. R. S. Wagner, C. J. Doherty, and S. M. Arnold, *J. Metals*, **17**, 1031 (1965).
14. E. Sirtl and A. Adler, *Z. Metallk.*, **52**, 529 (1961).
15. A. R. Lang, *J. Appl. Phys.*, **29**, 597 (1958); **30**, 1748 (1959).
16. R. S. Wagner, Unpublished work.

Diffusion Masking of Silicon Nitride and Silicon Oxynitride Films on Si

F. K. Heumann* and D. M. Brown

General Electric Research and Development Center, Schenectady, New York

and E. Mets*

General Electric Semiconductor Products Department, Auburn, New York

ABSTRACT

A qualitative study of the masking properties of thin (≤1500Å) silicon nitride and silicon oxynitride films on Si is presented. A range of diffusion conditions was studied for doping sources including B, P, Ga, and As. Silicon nitride was not found to be a diffusion mask for all conditions. Conditions under which it can be expected to mask are specified.

The work of Hu (1) and Doo (2) on the diffusion masking of silicon nitride films on Si showed that very thin layers (≤1200Å) of nitride would mask against B, P, As, and Ga, and might even be utilized as a universal diffusion mask, since no masking failures were encountered in their shallow junction diffusion studies. The studies reported here using B, P, As, and Ga diffusion sources were carried out over a wide range of conditions, and although the results do in-

* Electrochemical Society Active Member.

deed indicate that thin (≤1500Å) nitride and oxynitride films will mask for a certain set of diffusion conditions, it becomes clear that silicon nitride cannot be utilized as a universal diffusion mask. Various types of masking failures occur for temperatures and times required for deep junction diffusions.

Experimental Techniques

Chemically etched 1 ohm-cm Si wafers were coated with nitride or oxynitride films by the pyrolysis of silane and ammonia or silane, ammonia, and nitric oxide at 1000°C. The volumetric gas ratios used to form these films were: ammonia/silane = 40,000/1 for nitride films and ammonia/silane/nitric oxide = 40,000/1/500 for oxynitride films. No carrier gases were used in either case. Studies of these particular glassy amorphous oxynitride films indicate an equivalent SiO_2 composition of about 20% (3). The thickness of these films was varied between about 200 and 2000Å with a thickness variation over the inner 3/4 area of each 2.5 cm diameter wafer of only ± 3%. In some cases, the diffusion studies were carried out using two types of dopant sources: a semisealed quartz box diffusion using dry N_2 ambient and a glass source containing the dopant element to be studied (phosphosilicate glass or borosilicate glass) and a sealed tube or capsule containing the dopant material (As, P, Ga, B) which after loading, was degassed, evacuated, and back-filled with argon. The results were determined by the following procedure: the nitride film was removed using HF and a thermoelectric probe and surface resistivity measurements were used to indicate whether there was any detectable masking failure, and masked and unmasked portions of the wafer were angle lapped and stained to give junction penetration depths into the Si.

Results

A general summary of the results of the diffusion experiments using films of 2000Å or less are shown in Table I. In some cases, dry thermal oxides were used as control samples. In these instances no masking was evident. It must be pointed out, however, that the masking ability of oxides (and nitrides) are extremely dependent on the chemical nature of the diffusion conditions. For instance, Thomas *et al.* (4) have shown that very thin oxide films are excellent diffusion masks against B diffusion if the diffusions are carried out under nonglass-forming conditions.

Boron.—Amorphous silicon nitride films of thicknesses greater than 600Å are excellent masks for temperatures up to 1250°C for at least 10 hr if the sealed tube system is used. In these cases, the films after diffusion etched at the normal rate of 150Å/min in concentrated 48% HF; however, 1200°C diffusions for 30 hr resulted in films that would not dissolve in HF even though the films still masked against boron. X-ray diffraction indicated that the films were still amorphous so the original films had not yet converted to the more dense crystalline form. This phenomenon is not understood; perhaps an insoluble B-Si-N compound was formed. Silicon oxynitride films also appear to be suitable B diffusion masks; however, the thickness required for masking is somewhat greater than that for pure nitride. For instance, 500Å of oxynitride is not thick enough to mask boron for 4 hr at 1100°C; 1000Å suffices, however.

In the case of the borosilicate glass box system, it was found that at 1100°C nitride films of 500Å or more mask for at least 5 hr and dissolved at the normal etch rate. However, at 1200°C, the films failed as diffusion masks and dissolved at about 40 times the normal etch rate. This phenomenon is also not understood, but it suggests that borosilicate-nitride glass can be formed under certain diffusion conditions.

Phosphorus.—The results in Table I show that a 1500Å thick film of pyrolytic silicon nitride will mask against elemental phosphorus during a sealed tube diffusion at 1100°C for times up to 10 hr. For 4 hr at 1200°C, 1500Å is apparently not thick enough, however. Experiments with these particular silicon oxynitride films indicate that 1500Å will mask phosphorus for 4 hr at 1100°C; thinner films do not mask.

Silicon nitride films do not mask, however, when used in box diffusions where the source is vitrified phosphorous glass. In this case, the films become coated with phosphorus pentoxide or a phosphorous glass during the diffusion experiments and apparently rapidly convert to some kind of Si_3N_4-P_2O_5 glass as

Table I. $Si_xO_yN_z$ diffusion masking

Dopant	Diffusion system	Type of film	Thickness (Å)	Temp (°C)	Time (hr)	Masked	Masked junct. depth, μ*	Unmasked junct. depth, μ	Comments
B	Sealed Tube	SiO_2	2000	1100	4	No	6	6	Oxide control
B	Sealed Tube	Si_3N_4	≥300	1100	4	Yes	—	6	
B	Sealed Tube	Si_3N_4	≥400	1200	20	Yes	—	25	
B	Sealed Tube	Si_3N_4	≥500	1200	30	Yes	—	25	Film conversion
B	Sealed Tube	Si_3N_4	1000	1250	10	Yes	—	30	
B	Sealed Tube	Si_3N_4	≤600	1250	10	No	Spikes	30	Spiking failure
B	Sealed Tube	$Si_xO_yN_z$	500	1100	4	No	6	6	
B	Sealed Tube	$Si_xO_yN_z$	1000	1100	4	Yes	—	6	
B	Box	Si_3N_4	500-1500	1100	5	Yes	—	4	
B	Box	Si_3N_4	1500	1200	5	No	—		Film conversion
P	Sealed Tube	Si_3N_4	≥1500	1100	3	Yes	—	—	
P	Sealed Tube	Si_3N_4	≤1000	1100	3	No	—	—	
P	Sealed Tube	Si_3N_4	≥1500	1100	5	Yes	—	5	
P	Sealed Tube	Si_3N_4	≥1500	1100	10	Yes	—	9	
P	Sealed Tube	Si_3N_4	≤1100	1100	10	No	—	9	
P	Sealed Tube	Si_3N_4	1500	1200	4	No	3	12	
P	Sealed Tube	$Si_xO_yN_z$	≥1500	1100	4	Yes	—	5	
P	Box	Si_3N_4	1000	1100	1	No	—	6	Film conversion
Ga	Sealed Tube	SiO_2	2000	1100	4	No	6+	6	Oxide control
Ga	Sealed Tube	Si_3N_4	1000	1100	4	Yes	—	6	
Ga	Sealed Tube	$Si_xO_yN_z$	≤1000	1100	4	No	3.4	6	
Ga	Sealed Tube	$Si_xO_yN_z$	1500	1100	4	Yes	—	6	
Ga	Sealed Tube	Si_3N_4	300	1185	15	No	10	18	
Ga	Sealed Tube	Si_3N_4	1200	1185	15	Yes	Spikes	—	Localized spiking
Ga	Sealed Tube	Si_3N_4	1500	1200	4	Yes	Spikes	14	Localized spiking
As	Sealed Tube	Si_3N_4	1500	1100	4	Yes	—	0.6	
As	Sealed Tube	$Si_xO_yN_z$	1500	1100	4	Yes	—	0.6	
As	Sealed Tube	Si_3N_4	1000	1150	6	Yes	—	1.8	
As	Sealed Tube	Si_3N_4	1500	1150	6	Yes	Spikes	1.8	Films cracked
As	Sealed Tube	$Si_xO_yN_z$	≥1000	1150	6	Yes	Spikes	1.8	Films cracked
As	Sealed Tube	Si_3N_4	1500	1200	20	No	6	11	

* Where mask failure is noted but no masked junction depth is given, masking failure was determined by using a thermoelectric probe.

evidenced by the very rapid etch rate in concentrated HF. The results of a number of box diffusions indicate that P_2O_5 or P_2O_5 glass cannot be used as a diffusion source when thin Si_3N_4 films are used because of the formation of a glass which promotes mask failure. Similar results have been observed by Chu *et al.* (5) using a phosphorus oxytrichloride source.

Gallium.—2000Å of thermally grown SiO_2 does not mask Ga. However, 1000Å of Si_3N_4 completely masks Ga at 1100°C for 4 hr. This is also true of the silicon oxynitride film if it is 1500Å thick. The masking ability of the nitride is questionable above 1100°C. For instance, 300Å is not a satisfactory barrier at 1185°C for 15 hr; and as the thickness of the film is increased, cracking of the film occurs at these times and temperatures. Evidence for this problem are the diffusion spikes which occur at localized spots under the film. In one case, the film did not completely etch off in concentrated HF even after many hours. In this instance, a number of rod-shaped purple crystals were observed and identified as αSi_3N_4. Apparently the amorphous nitride was partially converted to the more dense crystalline form by the high temperature. This conversion may be catalyzed by gallium. Thus, we see that Si_3N_4 and silicon oxynitride can mask against Ga if the diffusion temperatures are not too high. However, at high temperatures, diffusion spikes appear which are probably caused by the cracking that occurs when the nitride films transform into the crystalline phase; thinner films do not crack, but do not mask either.

Arsenic.—As shown in Table I, 1500Å of silicon nitride and oxynitride mask at 1100°C for 4 hr; however, the diffusion depth into the unmasked Si is only 0.6μ. On the other hand, sealed tube diffusions at 1200°C for 20 hr showed that 1500Å of Si_3N_4 is not thick enough. Experiments at 1150°C showed that 1000Å masks for 6 hr; however, thicker films or oxynitride films cracked and allowed the As to penetrate these imperfections. When cracking occurred, it also crazed the Si surface.

Summary

A range of diffusion conditions using thin silicon nitride and silicon oxynitride films as a diffusion barrier against B, P, Ga, and As indicates that thin layers of nitrides are suitable diffusion masks for B if sealed tube diffusions are performed. For example, 1000Å of pure nitride will mask for at least 10 hr at 1250°C. In fact, no masking failure was ever found for these sealed tube diffusions if the film thickness was at least 1000Å. However, high temperatures and borosilicate glass sources can result in masking failure which may be caused by a film conversion to a borosilicate-nitride glass phase. This behavior is also generally true for phosphorus diffusions; however, in addition, masking failures at high temperatures in the elemental phosphorus sealed tube diffusions did occur. High temperature masking failure for thin films also occurs for sealed tube As diffusions. In the case of Ga, nitrides are much better diffusion masks than oxides, which do not deter this diffusant species at all. However, here again the nitride has a limited application. Although it masks at low diffusion temperatures, high temperature Ga diffusion experiments seem to indicate that the films of thicknesses required for complete masking crack as they change from an amorphous to crystalline phase.

Generally speaking, thin nitride and oxynitride films (thicknesses $\leq$1500Å) can be used as diffusion masks for the times and temperatures suitable for shallow ($\leq 9\mu$) junctions if the proper diffusant sources are used. In these instances, our results generally agree with those of Hu and Doo. Thin film nitride masking and much deeper Si junction depths (30μ) can be attained by using higher temperatures if boron is the diffusant and a sealed tube system is used. Masking of P, As, and Ga and deeper junctions might be obtained by using much thicker films and longer diffusion times, provided of course that the diffusion conditions are such that no catastrophic masking failure (film conversion, cracking) occurs.

Acknowledgments

We wish to thank Gerry Gidley for the many sample preparations required for this study.

Manuscript received July 21, 1967; revised manuscript received Sept. 8, 1967.

Any discussion of this paper will appear in a Discussion Section to be published in the December 1968 JOURNAL.

REFERENCES

1. S. M. Hu, *This Journal*, **113**, 693 (1966).
2. V. Y. Doo, *IEEE Trans. on Electron Devices*, **13**, 561 (1966).
3. D. M. Brown, P. V. Gray, F. K. Heumann, H. R. Philipp, and E. A. Taft, *This Journal*, To be published.
4. R. C. Thomas, J. W. Sprague, and E. L. Marcy, Paper presented at the Dallas Meeting of the Society, May 7-12, 1967, Abstract 93.
5. T. L. Chu, C. H. Lee, and G. A. Gruber, *This Journal*, **114**, 717 (1967).

Technical Notes

Silicon Oxide As An Etching Mask for Silicon Nitride

N. C. Tombs[1] and F. A. Sewell, Jr.

Sperry Rand Research Center, Sudbury, Massachusetts

The use of silicon nitride (1, 2) as a diffusion mask and passivation layer in semiconductor devices involves the etching of defined areas in the nitride. The relatively low etch rate of silicon nitride, compared with silicon oxide, can lead to problems in the securing of adequate definitions and steep etching angles when using conventional photoresist techniques with hydrofluoric acid etches. Van Gelder and Hauser (3, 4) have described the use of hot phosphoric acid (H_3PO_4) as an etch for silicon nitride, in conjunction with a pyrolitically deposited layer of silicon oxide as a mask against the phosphoric acid. Patterns were etched in

[1] Present address: NASA, Electronics Research Center, Cambridge, Massachusetts.

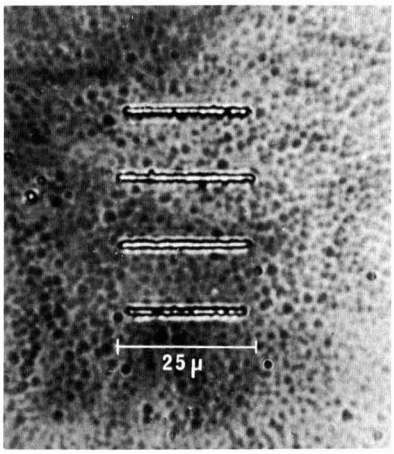

Fig. 1. Test pattern etched through 1500Å thick silicon nitride film using phosphoric acid with silicon oxide mask.

the silicon oxide overlayer using photoresist and hydrofluoric acid etch.

We have successfully utilized an analogous technique, in which the layer of silicon oxide was formed by thermal oxidation of the surface of the silicon nitride. The silicon nitride layer was pyrolytically deposited on a 10-mil silicon substrate to a thickness of 2500Å. The sample was then heated for 8 hr at 1200°C in oxygen. A surface layer of silicon oxide was thereby formed. Infrared absorption measurements revealed the presence of this oxide by an absorption maximum at 9.2μ. The height of the nitride absorption maximum at ~11μ was correspondingly decreased, although its wavelength remained unchanged. A test pattern was etched in the oxide layer using the photoresist-buffered HF method. The phosphoric acid etch was prepared by heating 85% H_3PO_4 to 190°C in an open beaker for 2 hr and cooling to 180°-185°C. The sample was immersed in the etch for 10-min periods. After each period it was removed, washed in water, and observed under the microscope. The interference colors given by the window (nitride) and mask (nitride plus oxide) regions at the different stages are shown below, together with the approximate thickness indicated by the colors. The nitride:oxide etch rate ratio was ~ 5:1.

Etch time	Nitride		(Nitride + Oxide)	
min	color	Å	color	Å
0	gold	2000	violet	2500
10	dark blue	1000	orange-red	2300
20	colorless	<400	orange	2100
30	colorless	0	blue	1500

A test pattern including lines of width 1μ was used to determine the possibility of etching windows of this width in the nitride. Figure 1 is a photomicrograph of the result obtained in a final nitride thickness of ~1500Å. Measurements of the width of the windows were made using a filar eyepiece with movable crosshair, calibrated against a stage micrometer. The results confirmed that the width was close to 1μ, although the resolution limits make it difficult to give a precise figure. The ultimate limitation in the technique would appear to be the photoresist stage for defining and etching the pattern in the oxide. Advantage can be taken of the fact that the oxide layer (~ 500Å) is much thinner than the layers normally required for diffusion masking and surface passivation. The photoresist layer likewise can be made thinner, and the pattern definition is thereby improved.

Practical advantages of the technique described include the excellent adherence between the oxide and nitride layers, and the avoidance of porosity or other imperfections in the oxide which might interfere with its effectiveness as an etching mask.

Manuscript received Sept. 25, 1967.

Any discussion of this paper will appear in a Discussion Section to be published in the December 1968 JOURNAL.

REFERENCES

1. V. Y. Doo, D. R. Nichols, and C. A. Silvey, *This Journal*, **113**, 1279 (1966).
2. J. J. Comer and N. C. Tombs, Paper presented at the Philadelphia Meeting of the Society, Oct. 9-14, 1966, as Abstract 153.
3. W. Van Gelder and V. E. Hauser, *This Journal*, **113**, 315C (1966).
4. W. Van Gelder and V. E. Hauser, *ibid.*, **114**, 869 (1967).

Defect Structure Model for Wustite

Per Kofstad and A. Zeev Hed

Metal Science Group, Columbus Laboratories, Battelle Memorial Institute, Columbus, Ohio

Wustite is a metal-deficient oxide ($Fe_{1-y}O$) (1-9). Its defect structure is commonly interpreted in terms of doubly charged iron ion vacancies (5-9). However, as discussed below such a defect structure model does not give a satisfactory interpretation of the observed behavior, and the purpose of this note is to propose a defect structure model which gives a more consistent interpretation of the experimental results.

The nonstoichiometry as a function of temperature and oxygen pressure has been studied by several investigators (1-4), and the results of the various studies are in good agreement. The results of Vallet and Raccah (3) at 800°-1200°C are shown in Fig. 1.

When assuming small defect concentrations, a defect structure model involving doubly charged iron ion vacancies predicts an oxygen pressure dependence of $y \propto p_{O_2}^{1/n}$ with $n = 6$. As seen in Fig. 1 such a relationship only accounts for the oxygen pressure dependence in the middle of the field, but does not explain the observed behavior over the whole homogeneity range. In view of the high defect concentrations in wustite, it would be highly surprising if such a model were applicable; one would rather expect that the activities of all atoms and sites involved in the defect reaction would have to be taken into account.

The assumption of divalent vacancies in wustite also seems doubtful in terms of charge carrier concentrations and their distribution on the iron lattice sites. A neutral iron vacancy consists of a vacant iron site associated with two nearest-neighbor atoms with trapped electron holes (trivalent iron atoms). The ionization of the vacancy essentially represents the transfer of the electron holes away from the neighborhood of the vacant site. When considering that each iron atom on a normal (octahedral) lattice site in $Fe_{1-y}O$ is surrounded by 12 nearest neighbor iron atoms, it follows that the structure can only contain about 4% of doubly ionized iron vacancies (8% Fe^{3+} ions on octahedral sites). At higher defect concentrations ($y > 0.04$), the divalent vacancies will have

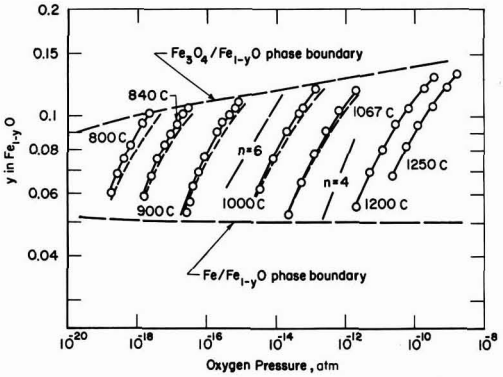

Fig. 1. Nonstoichiometry in wustite, y in $Fe_{1-y}O$, as a function of temperature and partial pressure of oxygen ($y \propto p_{O_2}^{1/n}$). Experimental results after Vallet and Raccah (3). Broken lines show calculated values for y if only singly charged complex defects are considered, while solid lines show calculated values when taking into account both singly charged and neutral defects.

Fe^{3+} ions on neighboring sites, and as such they really represent singly charged vacancies.

Neutron diffraction studies have suggested that for each vacancy which is formed in $Fe_{1-y}O$, an equal number of iron Frenkel defect pairs are formed in the metal lattice (9). Each defect may on this basis be considered as a complex defect consisting of two iron vacancies associated with an interstitial atom (9). Such a complex defect also results in the same local structure configuration as found in Fe_3O_4.

It is also noteworthy that the heat of formation of the defects in $Fe_{1-y}O$ is negative, *i.e.*, the deviation from stoichiometry at a given oxygen pressure increases with decreasing temperature. In oxides with single, unassociated vacancies the heat of formation is commonly positive (10), and the negative value found for $Fe_{1-y}O$ thus serves as a further indication that defects in this oxide are complex. In UO_{2+x}, which also contains complex oxygen defects, the heat of formation of the defects is also negative (11).

From these considerations we conclude that it is highly unlikely that the defects are doubly charged iron ion vacancies. From the available data it seems reasonable to assume that the predominating defects consist of the complex species, *i.e.*, two iron ion vacancies associated with an interstitial iron ion ($V_{Fe}Fe_iV_{Fe}$). Proceeding on this basis, we have considered several possible defect structure models, *e.g.*, simultaneous presence of simple vacancies and complex defects, ordering and association of defects, complex defects only, etc., in order to explain the data. In all these alternative models activities or concentrations of all atoms and sites were considered. The model which to us was the most consistent and simple in principle and which gave the best description of the observed behavior is given in the following.

It is assumed that the complex defects, ($V_{Fe}Fe_iV_{Fe}$) = Fe_c, may be neutral or singly charged. In writing the equations for the formation of these defects, one may write the equations for the formation of a single vacancy and a Frenkel defect pair followed by strong association between these defects. If the association is strong, as is assumed in this case, it is in terms of the law of mass action simpler to consider the complex defect as a unit, and the formation of these complex defects may then be written (13)

$$Fe_{Fe} + V_i + \tfrac{1}{2}O_2 = Fe_c^{\times} + O_O \qquad [1]$$

$$Fe_{Fe} + Fe_c^{\times} = Fe_c' + Fe_{Fe} \cdot e^+ \qquad [2]$$

$Fe_c^{\times}$ and Fe_c' are neutral and singly ionized complex defects, respectively; V_i represents an interstitial (tetrahedral) site available for occupancy by the complex defect, Fe_{Fe} is a divalent Fe atom on a normal (octahedral) site, $Fe_{Fe} \cdot e^+$ atom is a Fe atom on an octahedral site with one trapped electron hole (a trivalent iron ion), and O_O is an oxygen atom on an oxygen lattice site.

In terms of the law of mass action Eq. [1] and [2] may be written

$$[Fe_c^{\times}][O_O] = K_1[V_i][Fe_{Fe}]p_{O_2}^{1/2} \qquad [3]$$

$$[Fe_c'][Fe_{Fe} \cdot e^+] = K_i[Fe_c^{\times}][Fe_{Fe}] = K_iK_1[V_i][Fe_{Fe}]^2[O_O]^{-1}p_{O_2}^{1/2} \qquad [4]$$

where K_1 is the equilibrium constant for the formation of neutral complex species, and K_i is the equilibrium constant for the first ionization. In terms of single defects, K_1 is a combined value for the formation of the single defects and their association. The electroneutrality conditions require that

$$[Fe_{Fe} \cdot e^+] = [Fe_c'] \qquad [5]$$

Expressing the concentrations of the defects in molar fractions, y is given by

$$y = [Fe_c^{\times}] + Fe_c'] \qquad [6]$$

As oxygen defects are considered to be negligible, $[O_O] = 1$. However, at the high defect concentrations in $Fe_{1-y}O$ activities (or corrections for nonstoichiometry and interactions of defects) for $[Fe_{Fe}]$ and $[V_i]$ have to be considered. In this respect, $[Fe_{Fe}]$ is not equal to unity, but part of Fe_{Fe} sites are occupied by electron holes (Fe^{+3}-ions on octahedral sites) and part of the Fe_{Fe}-sites are unoccupied due to the formation of the complex defects. When making these corrections, the concentration or activity of Fe_{Fe}-atoms available for the defect formation is given by

$$[Fe_{Fe}] = 1 - [Fe_{Fe} \cdot e^+] - 2([Fe_c^{\times}] + [Fe_c']) \qquad [7]$$

In considering the activity of $[V_i]$ a correction must be made for the fact that part of the sites are occupied by the complex defects. In addition, we also propose a correction for defect interaction and suggest that once a tetrahedral site is occupied by a defect, some neighboring sites are blocked for occupancy by additional defects (9). Specifically we propose that each occupied tetrahedral site blocks the six nearest-neighbor tetrahedral sites. The number of tetrahedral interstitial sites is twice that of the octahedral (normal Fe_{Fe}) sites, and on this basis $[V_i]$ is given by

$$[V_i] = 2 - ([Fe_c^{\times}] + [Fe_c']) - 6([Fe_c^{\times}] + [Fe_c']) = 2 - 7y \qquad [8]$$

This proposed blocking mechanism accounts for the marked decrease in the oxygen pressure dependence of y as the FeO/Fe_3O_4 phase boundary is approached.

By combining Eq. [3]-[8], the value of y may be expressed as a function of p_{O_2} but for the sake of brevity the complicated relationship is not given. The internal consistency of the model is illustrated in Fig. 1, where the solid lines represent calculated values of y by simultaneous solution of Eq. [3]-[8] for values of the equilibrium constants

$$K_iK_1 = 1.45 \times 10^{-6} \exp(+64{,}000/RT) \qquad [9]$$

$$K_1 = 1.9 \times 10^{-10} \exp(+81{,}500/RT) \qquad [10]$$

$$K_i = 7.65 \times 10^{-4} \exp(-17{,}500/RT) \qquad [11]$$

The stippled lines represent values when only singly charged defects are considered, and the model thus suggests that the neutral defects become increasingly important the lower the temperature. The model suggests an ionization energy of 17.5 kcal/mole or 0.75 ev for the neutral complex defect.

Additional ordering or association of the complex defects is not considered in the model. This may take place, particularly as one approaches the temperature (570°C) at which $Fe_{1-y}O$ becomes unstable or in specimens which are quenched below the decomposi-

tion temperature. However, in terms of the model such additional association is suggested to be of secondary importance in considerations of over-all defect concentrations above 800°C. Only two different states (neutral and singly charged) of the defect are considered, and this does not seem unlikely in view of the fact that the defect concentration only changes by a factor of 3 (from 5 to 15%) when going from the Fe/FeO to the FeO/Fe_3O_4 phase boundaries.

The electrical conductivity of $Fe_{1-y}O$ exhibits the same general oxygen pressure dependence as that for y at high temperatures (7, 8). This is also to be expected in terms of the proposed model at temperatures where the singly charged defects predominate. However, under conditions where the neutral vacancies affect the values of y, the oxygen pressure dependence of the electrical conductivity ($\sigma \propto p_{O_2}^{1/n}$), should yield somewhat larger values of n than that for the deviation from stoichiometry. At the high defect concentrations in $Fe_{1-y}O$ the mobility of the charge carriers may also be a function of the defect concentration. In addition, there is evidence that grain boundaries affect the semiconducting properties, as polycrystalline $Fe_{1-y}O$ exhibits n-conductivity at the highest defect concentrations, while single crystal oxide remains p-conducting under the same conditions (8).

Kleman (14) has interpreted the results of Vallet and Raccah (Fig. 1) in terms of three separate "phases" within the $Fe_{1-y}O$ domain, but no interpretation is given in terms of the defect structure. Carel *et al.*, have later briefly described dilatometric (15) and x-ray diffraction (16) studies on $Fe_{1-y}O$, the results of which are interpreted as a confirmation of the existence of these three phases. The transformations from one phase to another are proposed to reflect second order transitions (15), but no attempt is made to give physical interpretations of the transitions. The possible existence of these three phases reflecting minor changes in the properties is not necessarily at variance with the proposed model. If the transitions are of the second order, this implies that there is no latent heat involved and this, in turn, means that the transitions do not significantly affect thermodynamic properties such as the partial molar heat of dissociation of oxygen (7) or the heat of formation of the defects. As such the proposed phases are of but minor importance in consideration of the over-all equilibrium defect concentrations and have not at this stage been considered in the above model.

Acknowledgment

One of the authors (P. Kofstad) is indebted to the Battelle Memorial Institute for a Battelle Institute Fellowship in the Metal Science Group, Columbus Laboratories, where this work was carried out.

Manuscript received May 17, 1967; revised manuscript received Oct. 8, 1967.

Any discussion of this paper will appear in a Discussion Section to be published in the December 1968 JOURNAL.

REFERENCES

1. L. S. Darken and R. W. Gurry, *J. Am. Chem. Soc.*, **68**, 798 (1946).
2. L. Himmel, R. F. Mehl, and C. E. Birchenall, *Trans. AIME*, **197**, 822 (1953).
3. P. Vallet and P. Raccah, *Mem. Sci. Rev. Met.*, **62**, 1 (1965).
4. N. A. Hovgard and P. N. Jensfelt, *Jernkontorets Ann.*, **140**, 467 (1956).
5. K. Hauffe and H. Pfeiffer, *Z. Metallk.*, **44**, 27 (1953).
6. D. M. Smyth, *J. Phys. Chem. Solids*, **19**, 167 (1961).
7. G. H. Geiger, R. L. Levin, and J. B. Wagner, Jr., *J. Phys. Chem. Solids*, **27**, 947 (1966).
8. I. Bransky and D. S. Tannhauser, *Trans. AIME*, **239**, 75 (1967).
9. W. L. Roth, *Acta Cryst.*, **13**, 140 (1960).
10. P. Kofstad, *J. Phys. Chem. Solids*, **28**, 1842 (1967).
11. For a review of studies on UO_{2+x}, see F. A. Kröger, *Z. Physik, Chem.*, **49**, 178 (1966).
12. B. T. M. Willis, *Nature* (London), **167**, 755 (1963); *J. Phys.*, **25**, 431 (1964).
13. F. A. Kröger, "The Chemistry of Imperfect Crystals," North Holland, Amsterdam, John Wiley and Sons, Inc., New York (1964).
14. M. Kleman, *Mem. Scient. Rev. Met.*, **62**, 457 (1965).
15. C. Carel and P. Vallet, *Compt. rend.*, **258** 3281 (1964).
16. C. Carel, D. Weigel, and P. Vallet, *ibid.*, **260**, 4325 (1965).

Luminescence of Dy^{3+}-Activated β-Ga_2O_3

William C. Herbert,[1] Henry B. Minnier, and Jesse J. Brown[2]

Chemical and Metallurgical Division, Sylvania Electric Products, Inc., Towanda, Pennsylvania

Although trivalent dysprosium is a known coactivator or sensitizer in luminescent systems (1), few phosphors of significance are known in which Dy^{3+} is the sole activator ion. Jenkins, McKeag, and Ranby (2) have activated various alkaline earth phosphate compounds, most notably $Ca_2P_2O_7$, with Dy^{3+} and made special note of their x-ray and cathode-ray-excited luminescent decay characteristics.

In the present note we describe the photoluminescence of Dy^{3+}-activated β-Ga_2O_3. Although this material is not as efficient as the general class of commercial phosphors, it is one of the brightest Dy^{3+}-activated oxide phosphors thus far reported. In addition, the emission of β-Ga_2O_3 : Dy is remarkably similar to that of the standard commercial warm white phosphor, $Ca_5F(PO_4)_3$: Sb : Mn.

Dy^{3+}-activated β-Ga_2O_3 is prepared by intimately blending the constituent oxides and heat-treating the mixture in air at 1400°C, for several hours. Dy_2O_3 additions from 0.5 to 20.0 m/o (mole per cent) were investigated. Maximum photoluminescent brightness was observed in the range 5-10 m/o activator concentration.

Luminescence spectral measurements were obtained using a Perkin-Elmer Model 236 Spectrophotofluorimeter. Emission spectra were recorded in terms of relative energy. Identification of the intense line emissions is accurate to ± 3Å. C.I.E. chromatricity coordinates were obtained using a Librascope integrator.

The excitation and emission spectra of β-Ga_2O_3 : Dy are shown in Fig. 1. Since no direct adsorptions by dysprosium are observed in the excitation spectrum, it must be assumed that the major portion of the energy involved in luminescence arises from the broad host lattice absorptions. These peak at 250 nm and below.

The emission spectrum is dominated by two main groups of lines in the ranges 460-505 and 570-600 nm. A third group of weak lines, not shown in Fig. 1, was

[1] Present address: Drexel Institute of Technology, Philadelphia, Pennsylvania.

[2] Present address: Department of Metals and Ceramic Engineering, Virginia Polytechnic Institute, Blacksburg, Virginia. Electrochemical Society Active Member.

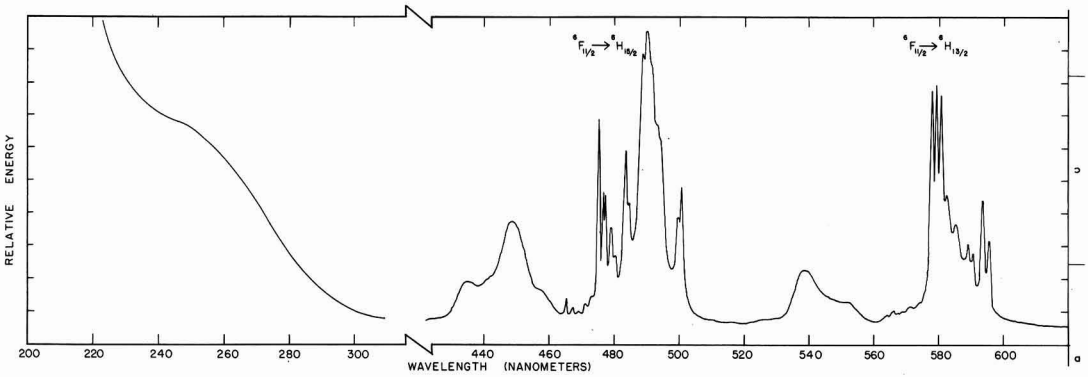

Fig. 1. Excitation and emission spectra of β-Ga_2O_3:Dy

observed between 660 and 690 nm. Several diffuse bands occurring near 435, 450, 540, and 550 nm are believed to be caused by either impurities or host lattice emissions and are not characteristic of Dy^{3+} fluorescence.

Table I lists the observed emission lines, their intensities, and most probable ground state for the β-Ga_2O_3 : Dy fluorescence. In Table II the fluorescence of this new phosphor is compared with that of a standard "warm white" halophosphate phosphor, Sylvania Type 4356.

Table I. Visible fluorescence spectrum of β-$(Ga_{0.95}, Dy_{0.05})_2O_3$

λ, Å	I/I_0	Lowest state
4650*	9	$^6H_{15/2}$
4675*	7	
4690*	5	
4710*	8	
4730*	10	
4752	72	
4765	49	
4772	47	
4790	35	
4802	25	
4835	61	
4845	42	
4887	95	
4900	100	
4915	91	
4930	69	
4940	65	
4995	38	
5005	48	
5780	82	$^6H_{13/2}$
5795	83	
5805	80	
5825	46	
5850	35	
5890	28	
5905	25	
5935	43	
5955	25	
6678	4	$^6H_{11/2}$
6775	8	
6840	11	
6865	7	

* These lines may be due to impurities.

Table II. Comparison of fluorescence of β-$(Ga_{0.95}, Dy_{0.05})_2O_3$ with a standard warm white halophosphate phosphor

Phosphor		Relative peak height	Chromaticity coordinates x	y	% Total light output
$Ca_5F(PO_4)_3$:Sb:Mn (Sylvania No. 4356)		100	0.445	0.420	100
β—$(Ga_{0.95}, Dy_{0.05})_2O_3$	495 nm emission	173	0.036	0.422	51
	588 nm emission	167	0.585	0.415	
	Sum of both	—	0.439	0.416	

Hund's rule for a $4f^9$ electronic configuration predicts that the ground state of Dy^{3+} is an inverted ^6H state. The lowest-lying level in this multiplet would be the $^6H_{15/2}$ with 8 doubly degenerate Stark components, the next $^6H_{13/2}$ with 7 components, etc. Dicke and Singh (3) have successfully identified the experimental absorption and fluorescence transitions of $DyCl_3 \cdot 6H_2O$ in this framework.

An equally successfully term assignment of the Dy^{3+} transitions in β-Ga_2O_3 (Table I) is not immediately possible. The three observed groups of emission lines at 460-505, 570-600, and 660-690 nm apparently arise from $^6F_{11/2} \rightarrow {}^6H_{15/2}$, $^6H_{13/2}$, and $^6H_{11/2}$ transitions, respectively. However, in the first group at least 14 lines are observed when one would not expect more than 8 Stark components for a $^6H_{15/2}$ transition; likewise 9 lines are observed for the $^6H_{13/2}$ transition when not more than 7 are predicted. (The lines corresponding to the $^6F_{11/2} \rightarrow {}^6H_{11/2}$ transition are too weak and diffuse to be accurately resolved.)

Assuming that all observed fluorescence lines in β-Ga_2O_3 : Dy arise from the $^6F_{11/2}$ level and not higher-lying excited levels, and that Hund's rules are valid for this case, one possible explanation of the extra emission lines is that Dy^{3+} occupies two nonequivalent sites in the β-Ga_2O_3 lattice. This would effectively double the number of fluorescence transitions expected experimentally and be much more in line with the observed spectrum. In fact, Geller (4) has established the existence of two different cation sites in the β-Ga_2O_3 crystal structure, one tetrahedrally and one octahedrally coordinated by oxygen.

Acknowledgment

The authors are indebted to Mr. D. T. Palumbo for several helpful discussions and for assisting with the fluorescence measurements.

Manuscript received Sept. 28, 1967.

Any discussion of this paper will appear in a Discussion Section to be published in the December 1968 JOURNAL.

REFERENCES

1. M. J. Taylor, *Proc. Phys. Soc.*, **87**, 281 (1966).
2. H. G. Jenkins, A. H. McKeag, and P. W. Ranby, U.S. Pat. 2427728, Sept. 23, 1947.
3. G. H. Dieke and S. Singh, *J. Opt. Soc. Am.*, **46**, 495 (1956).
4. S. Geller, *J. Chem. Phys.*, **33**, 676 (1960).

Optical Properties by Far Infrared Ellipsometry

Charlie E. Jones and A. Ray Hilton

Texas Instruments Incorporated, Dallas, Texas

The authors recently described (1), an infrared ellipsometer used to measure the thickness of thin silicon and germanium epitaxial layers. The measurement of thin film thickness by ellipsometry requires an accurate knowledge of the optical constants, n and k, of the film and substrate at the wavelength of measurement (54.6μ in this case). The optical constants n and k (real and imaginary parts of the refractive index, respectively) were calculated from an expression given by Lyden (2) for free carrier and lattice absorption in semiconductors. The method was used by the authors in earlier studies (3). The experimental data required for the calculations was supplied from electrical measurements of the semiconductor films and substrates (1). Optical constants can also be calculated directly from ellipsometric measurement of the substrate surface and is the technique commonly used in the visible spectrum range (4). This note presents a comparison of the optical constants obtained on highly doped silicon using ellipsometric measurements to those obtained using the above mentioned techniques. The ellipsometric curves generated for epitaxial layers of undoped silicon on substrates having the different optical constants are presented and compared. Comments are made regarding the fit of experimental data to the various curves.

Four methods have been used to determine n and k:

A. Measure the resistivity (probe), determine the number of carriers from a literature curve relating resistivity to carriers (5), and the mobility from a literature curve relating resistivity to mobility (6). Calculate n and k from Lyden's expression.

B. Same as A except mobility is calculated from:

$$\text{Mobility} = \frac{6.25 \times 10^{18}}{(\text{number of carriers})\,(\text{resistivity})}$$

C. Measure the number of carriers and mobility by Hall techniques then proceed with Lyden's expression.

D. Measure, with the infrared ellipsometer, the Δ and ψ value for the substrate and calculate the optical constants from the exact equation given by Winterbottom (7).

Methods A and B depend on resistivity values obtained by the simple probe technique and are therefore not expected to yield as accurate values for optical constants as will method C which utilizes the reliable Hall technique.

The optical constants obtained from each method for a substrate of 0.016 ohm-cm n-type silicon were:

Method	n	k
A	2.18	2.44
B	2.48	2.18
C	2.21	1.49
D	2.59	1.38

Four curves relating to the ellipsometer parameters Δ and ψ were plotted assuming each of the above optical constants for the substrate and undoped silicon (optical constants 3.38 — 0.i), as the epitaxial layer. The other parameters of interest are $\lambda = 54.6\mu$; angle of incidence = 50°. These curves are shown in Fig. 1. The arrows on each curve indicate the thickness of the epitaxial layer in microns. The data points (solid dots) are Δ and ψ measurements made on 16 samples of undoped silicon layers deposited on 0.016 ohm-cm n-type silicon. The data points fit best the curve plotted using the ellipsometrically measured substrate optical constants. The measuring accuracy of the ellipsometer in present form is about $\pm$ 3° for ψ and Δ. Since in method C the electrical properties were measured to a high degree of reliability, curve C represents the best of the calculated optical constants. Curves A and B can be considered deviations from curve C due to a lack of accuracy in the electrical values obtained by methods A and B. The difference between the optical constants obtained by methods C and D are not due to inaccuracies in the equations relating resistivity and mobility to the optical constants. We have previously shown (1) good agreement between measured and calculated absorption coefficients of 0.01 to 1.0 ohm-cm n-type silicon using these same relationships. The difference probably results from the fact that in method C the resistivity and mobility, used to calculate the optical constants, are values of bulk material while the ellipsometer measures the optical constants of the materials surface.

If ellipsometry is used in the far infrared to measure layer thicknesses ellipsometry should be used for determining the optical constants of the materials in question. It should be noted that by using the n and k calculated from the ellipsometric readings and back calculation some insight may be gained as to the accurate electrical characteristics of the surface of the material. This will of course depend on the exactness of the theory relating the electrical and optical properties.

Manuscript received Aug. 17, 1967; revised manuscript received Oct. 15, 1967.

Any discussion of this paper will appear in a Discussion Section to be published in the December 1968 JOURNAL.

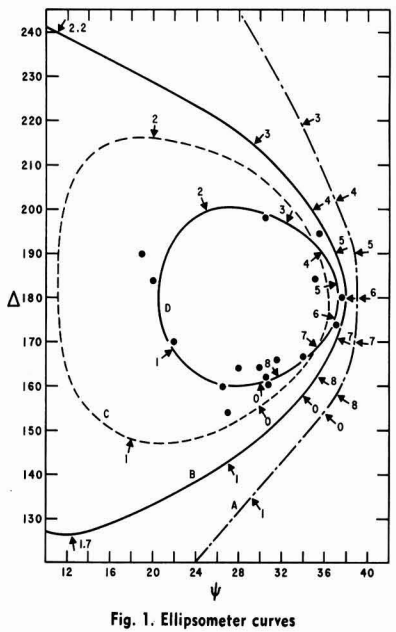

Fig. 1. Ellipsometer curves

REFERENCES

1. A. Ray Hilton and Charlie E. Jones, *This Journal*, **113**, 472 (1966).
2. Henry A. Lyden, *Phys. Rev.*, **134**, A1106 (1964).
3. Charlie E. Jones and A. Ray Hilton, *This Journal*, **112**, 908 (1965).
4. R. J. Archer, *Phys. Rev.*, **110**, 354 (1958).
5. R. C. Wackwitz, TI Memo ICRL-M 103 63621-02.
6. M. Bullis, Private communication.
7. A. B. Winterbottom, "Optical Studies of Metal Surfaces," Publisher F. Burns, Trondheim Norway.

The Preparation and Examination of PbTe by Transmission Electron Microscopy

E. Levine

Department of Mechanics, Rutgers—The State University, New Brunswick, New Jersey

and R. N. Tauber

Department of Metallurgy and Materials Science and The Materials Research Center, Lehigh University, Bethlehem, Pennsylvania

The preparation of thin foils of the compound semiconductor PbTe for transmission electron microscopy has not been reported previously. Electron microscopy can be employed in this compound for the study of defects and precipitation effects. The following note describes the preparation technique and some preliminary observations made on thin foils of PbTe.

It has been suggested by various investigators (1-3) that the change of carrier concentration of PbTe on annealing is due to precipitation of Pb or Te from the supersaturated crystal. This is further evidenced by the fact that both the Pb and Te concentration are retrograde in nature (1,2). In this investigation a single crystal of PbTe grown by the Bridgman technique was heat-treated so as to produce precipitation of Pb from the lattice. The procedure was as follows: (a) diffusing the specimens in a Pb-rich atmosphere at 775°C for 28 hr and brine quenching; this produces a maximum Pb-rich PbTe (1, 2). (b) Aging the specimen at 504°C for 25 hr and brine quenching; this should produce precipitates of Pb in the lattice, particularly on dislocation sites (3).

Thin foils of the specimen were prepared for electron microscopy using a combination of mechanical and electropolishing. The specimen was mechanically polished to approximately 200μ on various grades of paper with a final polishing on both sides using Linde Gamma AB alumina powder. It was then electropolished using a solution described by Norr (4) which consisted of 20g KOH in 45 ml H_2O, 35 ml glycerol, 20 ml of ethyl alcohol. The polishing was performed at 4-6v and 0.2 amp/cm^2. The sample was suspended without any edge masking in the electropolishing solution. Small black dots of apezion wax were placed on opposite sides in the center of the specimen. Accelerated attack occurred in the vicinity of these dots and also around the periphery of the specimen. Polishing was continued until the hole formed under the dots joined up with the peripheral region. Extremely rapid stirring was necessary in order to prevent the build up of a contamination layer.

The PbTe was found to be very brittle before polishing, and considerable care was necessary to avoid shattering. The electropolished thin specimen, however, was found to be very ductile in certain thin regions and could be bent plastically at the edges by 180° and then straightened out again without fracture occurring. This behavior is similar to that found with alkali halide crystals when deformed in a solvent environment (5), *i.e.*, the specimens are notch brittle. The removal of notches or cracks renders the crystal somewhat ductile although even in the thinned specimen cutting with a knife results in brittle fracture along the cleavage planes.

The thinned specimen was examined in a Hitachi Electron Microscope operated at 100 kv. The density of dislocations was found to be quite high and accurate estimates were not possible due to their inhomogeneity. A typical area is shown in Fig. 1. Precipitation was not observed at dislocations as has been previously suggested (3). Arrays of dislocations on their inclined slip planes were observed throughout the foil. Some of these dislocations appeared to be either dipoles or dissociated dislocations (Fig. 2). Stacking fault contrast was not observed between these dislocation pairs. Further contrast experiments on their exact nature are planned for the future. The presence of dissociated dislocations in PbTe has been proposed previously be Rachinger (6).

In the background of Fig. 2 in the neighborhood of the extinction contour many elongated images may be seen which are not visible in the area on the right side of the figure. These images were only visible in the vicinity of an extinction contour and may correspond to an early stage in a precipitation process. The associated diffraction pattern did not show any evidence of such precipitates indicating their volume fraction is small or we are observing a preprecipitation stage of clustering similar to that found in Al-4% Cu alloys (7). Figure 3 is a diffraction pattern of a {100} orientation from a bent portion of the specimen. (The major portion of the thinned specimen was of {112} orientation.) Weak streaking in the <100> directions may be observed which usually

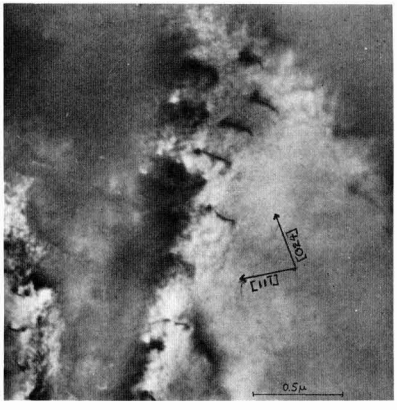

Fig. 1. Dislocation arrays in PbTe

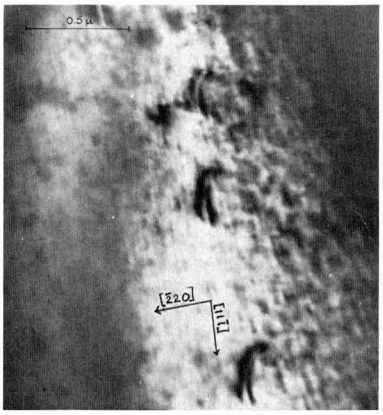

Fig. 2. Possible dipole or dissociated dislocations in PbTe. In the background anomalous images, possibly precipitates, are observed.

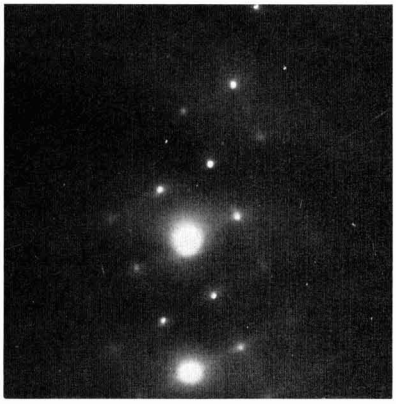

Fig. 3. {100} Diffraction pattern of PbTe. Streaks are observed in <100> directions indicating either anisotropic expansion coefficient or a strain displacement in this direction.

characterizes the preprecipitation stage in metal systems (7). However, one cannot unambiguously assign these "streamers" to precipitation. Similar streaking has been observed in Ge crystals in the <110> directions and their origin is speculative. They may arise from thermal vibrations or anisotropic strain displacements (8). The latter may be created by clustering of atoms. Further work on aging experiments is now in progress to clarify this point.

The dislocations were observed to be quite mobile during observation in the electron microscope. Dislocations in thin foils may move as a result of the stresses set up by the electron beam. That such movement readily occurred is another indication of the possible room temperature ductility of suitably prepared specimens. The movement of dislocations produced a variety of slip trace contrasts as may be seen in Fig. 4 at A and B. The slip trace contrast in some cases rapidly disappeared after a few seconds while other slip traces were of indefinite duration.

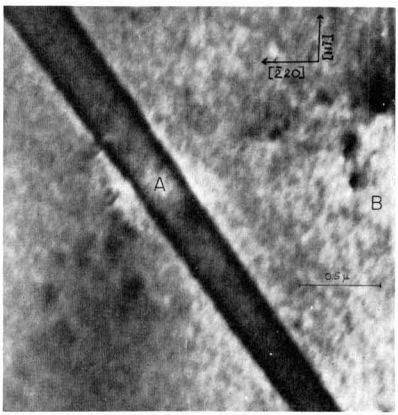

Fig. 4. Persistent slip traces due to movement of dislocations while under observation in electron microscope. Slip trace at A clearly visible while that at B is weakly visible.

Slip trace contrast is thought to be due to a surface layer of oxide or other contamination layer on the foil which prevents the slip from penetrating the surface. The observation of the variability of duration and contrasts produced in the same area of the foil suggests that the phenomenon is strongly dependent on the slip vector of the dislocations involved.

Slip trace analysis assuming either {110} or {100} glide planes indicated that dislocations on both planes were capable of movement. Rachinger (6) using trace analysis in bulk specimens observed both glide planes to be operative in PbTe although Buerger (9) had found only evidence of {100} glide plane activity. Evidence of both {110} and {100} glide plane activity had been observed by Seltzer (10) and Matthews *et al.* (11) in PbS. Our observation suggests that PbTe behaves similarly to PbS in that slip (at least in thin films) occurs on both glide planes.

Acknowledgment

This work was supported in part by the National Science Foundation under Grant No. GK-1607.

Manuscript received July 17, 1967; revised manuscript received Sept. 19, 1967.

Any discussion of this paper will appear in a Discussion Section to be published in the December 1968 JOURNAL.

REFERENCES

1. R. F. Brebrick and R. S. Allgaier, *J. Chem. Phys.*, **32**, 1826 (1960).
2. R. F. Brebrick and E. Gubner, *ibid.*, **36**, 1283 (1962).
3. W. W. Scanlon, *Phys. Rev.*, **126**, 509 (1962).
4. M. K. Norr, DDC Document AD 423 367, Naval Ordnance Laboratory, White Oak, Maryland (1963).
5. A. R. C. Westwood, *Ind. Eng. Chem.*, **56**, 15 (1964).
6. W. A. Rachinger, *Acta Met.*, **4**, 647 (1956).
7. R. B. Nicholson and J. Nutting, *Phil. Mag.*, **3**, 531 (1958).
8. R. D. Heidenreich, "Fundamentals of Transmission Electron Microscopy," p. 260, Interscience Publishers, (Wiley), New York (1964).
9. M. J. Buerger, *Am. Mineralogist*, **13**, 1 (1928).
10. M. S. Seltzer, *J. Appl. Phys.* **37**, 4780 (1966).
11. J. W. Matthews and K. Isebeck, *Phil. Mag.*, **8**, 469 (1963).

Formation of Crystalline Films by Laser Evaporation

P. D. Zavitsanos and W. E. Sauer

Space Sciences Laboratory, Missile and Space Division, General Electric Company, King of Prussia, Pennsylvania

Vacuum evaporation techniques have been used for the preparation of films of elements and some compounds. When these techniques are applied to compounds or alloys which contain elements of widely different vapor pressures, vapor fractionation takes place to produce films containing an excess of the most volatile component.

A definite improvement was brought about by the "flash" evaporation technique as outlined first by Siegel and Harris (1) and applied in the preparation of compound semiconductor films (2). The "co-evaporation" technique (3-5) also served as an improvement.

Both techniques, however, sometimes suffer from contamination effects due to impurity vapors present in high-temperature furnaces and vacuum atmospheres. Another disadvantage present in the above techniques, as well as in the "sputtering" technique, is the fact that for many materials of interest, amorphous films are produced unless the substrate is independently heated (6, 7).

The evaporation of solids with a pulsed laser beam for the purpose of producing good optical films has been investigated by Smith and Turner (8), and Schwartz (9) with some degree of success. In the present work, the use of a laser beam appears to produce (*a*) congruent vaporization and films of the same composition as the parent material, and (*b*) crystalline films without heating the substrate (independently).

Experimental

The laser used in this investigation was a Lear-Siegler Model H-140Q. It had a maximum output of 10 joules, and a pulse duration of 5-6 x 10^{-4} sec, and was operated in the burst mode.

The vapor generated by laser evaporation formed a jet, the center of which was always normal to the surface of the source material, independent of the incident angle of the laser beam. For this work, the laser beam entered a glass vacuum system through a glass window and was focused by a 75 mm focal length lens on the surface of the source material at a 45° angle. The source material was mounted (inside the vacuum system) on a holder which could be moved up and down or rotated for focusing or exposure of a new segment of the surface to the beam. Films of Ge and GaAs were prepared by condensing the vapor on various substrates, at room temperature, placed parallel to the specimen 2.5 cm away. Prior to vaporization, the substrates were washed first with acetone and then with ethyl alcohol and air dried at 120°C. Satisfactory films were produced at chamber pressures as high as 1μ.

For lasers operating in the burst mode, it can be assumed that there is sufficient power density in the beam to raise the surface temperature of the target to its boiling point at a relatively short time compared to the length of the pulse, and the rate of surface recession reaches a steady state rapidly (10). (Time resolved microwave attenuation measurements (11) indicate that this assumption is correct.) If energy losses due to reflection, radiation, conduction through the solid, superheating of solid and gas are negligible, the mass of the generated vapor, m is given by

$$m = E/[(C\Delta T_1)_{\text{solid}} + \Delta H_f + (C\Delta T_2)_{\text{liquid}} + \Delta H_v]$$

where E = energy output of laser, C = specific heat capacity, $(C\Delta T_1)_{\text{solid}}$ = energy required to heat the solid to its melting point, ΔH_f = heat of fusion and or heat of decomposition, $(C\Delta T_2)_{\text{liquid}}$ = energy required to heat the liquid to its boiling point, and ΔH_v = heat of vaporization of liquid at the boiling point. The energy output, E, used in these experiments was 3 joules per pulse. In the case of Ge and GaAs, the amounts of vapor generated (per pulse) are calculated to be 0.48 and 0.9 mg, respectively.[1]

The deposited area was usually about 3-4 cm^2, and if the condensation coefficient was unity, the resulting films would have a thickness in the order of 1600-3500Å. Our present estimates, however, (based on optical opacity) indicate that the film thickness (per pulse) was considerably less and of the order of 500-1000Å. In view of the high reflectance of the Ge and GaAs source materials, it is felt that reflection was not negligible and probably was the dominant mechanism of energy loss. The extent of laser energy absorption by the vapor is usually considered to be small at this power level (10) although not proven for our experimental conditions. The resulting deposition rate is extremely high compared to conventional techniques and in the range of 10^6 Å/sec. As far as the source temperature is concerned, although it was not measured, by analogy to graphite (13) targets it is felt that it did not exceed the boiling point of the less volatile component by a significant amount. The temperature of the substrates could not have been significantly raised by the laser energy in view of the fact that the substrates were transparent and rather massive (10-15g); even if all the available energy went into heating the substrate, its temperature could not be raised by more than 2°-3°.

Results

The results which follow were typical of those obtained from measurements on several films (2-3 of each case). Films prepared by laser evaporation were studied by reflection and transmission optical microscopy. Figure 1 shows optical photomicrographs of Ge and GaAs films deposited on glass and sodium chloride substrates. It can be seen that the films are smooth, continuous, and free of "chunks" of materials.

The films were removed from their substrates, and high resolution transmission electron diffraction patterns were obtained using an Hitachi HU-11 electron microscope. Figure 2A is an electron diffraction pattern from a germanium film which had been laser deposited on a glass substrate. Figure 2B is from another germanium film which had been produced by evaporation of the same source material from a resistance heated molybdenum boat. In neither case was the substrate heated by external means. The conventionally

[1] For germanium, the following steps were assumed to lead to vaporization

$$\text{Ge(s)} \rightarrow \text{Ge(l)} \rightarrow \text{Ge(g)}$$

with T_{melting} = 1210°K, T_{boiling} = 3100°K, C = 6 cal · deg^{-1} mole^{-1}, ΔH_f = 8.83 kcal mole^{-1}, and ΔH_v = 79.1 kcal · mole^{-1}. For gallium arsenide, the corresponding gasification processes (12) are

$$\text{GaAs(s)} \rightarrow 1/2\text{As}_2\text{(g)} + \text{Ga(l)}$$

$$\text{Ga(l)} \rightarrow 2\ \text{Ga(g)}$$

with $T_{\text{decomposition}}$ = 1000°K, T_{boiling}(Ga) = 2520°K, $\Delta H_{\text{decomposition}}$ = 45 kcal/mole (GaAs), and ΔH_v = 61.5 kcal/mole (Ga).

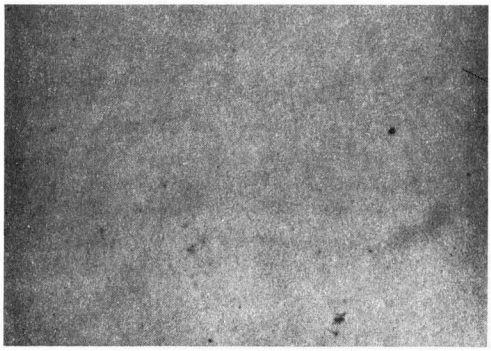

Fig. 1A. Reflection optical photomicrograph of laser evaporated film: germanium film on glass substrate. Magnification 350X.

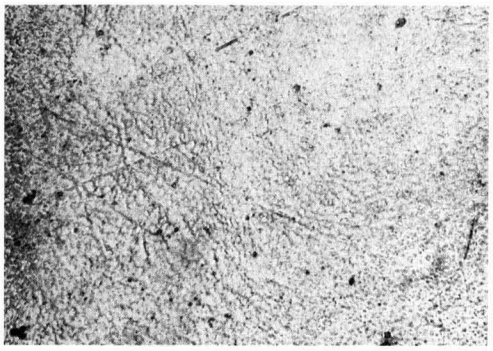

Fig. 1B. Reflection optical photomicrograph of laser evaporated film: gallium arsenide film on sodium chloride substrate. Magnification 350X.

Fig. 2. Transmission electron diffraction patterns produced by evaporated germanium films. A(left), laser evaporation; B(right), conventional evaporation.

evaporated film exhibits an amorphous structure which is typical of germanium films condensed on unheated substrates. However, the laser evaporated film exhibits a degree of crystallinity which is typical of films deposited by conventional evaporation onto substrates heated to 300°C or more (7).

In addition to the elemental films, films of GaAs were prepared. The laser evaporation of GaAs was found to proceed congruently. Figure 3A is an electron diffraction pattern produced from a film which had been prepared on a calcium fluoride substrate by

Fig. 3. Transmission electron diffraction patterns produced by evaporated gallium arsenide films. A(left), calcium fluoride substrate; B(right), sodium choride substrate.

the laser evaporation of gallium arsenide. Figure 3B is from a gallium arsenide film similarly deposited on sodium chloride. The diffraction lines in these two patterns are listed in Table I. Both sets of data are in good agreement with the literature interplanar spacing values for gallium arsenide (14). If the constituents of the deposited film had condensed noncongruently, a second phase would have been present, because of the very limited solubility of gallium and arsenic in gallium arsenide (15). Thus, since all of the diffraction lines could be assigned to gallium arsenide, it was concluded that laser evaporation did produce congruent deposition and crystalline films of gallium arsenide on calcium fluoride and sodium chloride substrates. In the case of laser evaporation (16), coevaporation (4, 16) and sputtering (17) techniques, substrate temperatures of the order of 220°-400°C were required to produce crystalline films of GaAs.

Discussion

The two most evident features of films prepared by the laser evaporation technique are the congruent deposition of compounds and the degree of film crystallinity achieved on unheated substrates. The reason for congruent evaporation is that conduction of heat away from the focal point and through the solid (target) is a slow process compared to local heating and evaporation. A small volume of material (at the focal point) is raised to a high temperature which is apparently sufficient to produce vapor having the stoichiometry of the target. In a way, this heating process is similar to flash evaporation but more efficient.

Table I. Analysis of electron diffraction patterns from gallium arsenide films

GaAs* on CaF		GaAs* on NaCl		ASTM value for GaAs[14]		
I	d(A)	I	d(A)	d(A)	I/I_o	hkl
S	3.25	S	3.25	3.26	100	111
				2.83	1	200
S	2.00	S	2.00	2.00	35	220
S	1.71	S	1.70	1.70	35	311
W	1.38	W	1.39	1.41	6	400
MS	1.29	MS	1.29	1.30	8	331
MS	1.51	MS	1.16	1.15	6	422
M	1.08	M	1.08	1.09	4	333
W	1.00	W	0.99	0.999	2	440
M	0.953	M	0.953	0.956	2	531
VVW	0.910	VVW	0.890	0.894	4	620
WW	0.870	VVW	0.857	0.862	2	533
VVW	0.817	VVW	0.811	0.816	4	444
VW	0.794	VW	0.788	0.792	2	711
W	0.753	W	0.753	0.755		642**
W	0.728	W	0.733	0.736		731**

* S = Strong; M = Medium; W = Weak; V = Very.
** Calculated from ASTM value for a_o.

The crystallization of the films is probably affected by several factors. The high deposition rates and temperatures would tend to increase the mobility of atoms in the depositing films by providing a high energy environment. Heating of the films (during formation) by reflected laser light (which is preferentially absorbed in the film as compared to the substrate) could also take place and, thus, increase the mobility of the condensing vapor.

Acknowledgments

The authors are grateful to Dr. J. R. Richardson and Dr. C. A. Neugebauer (of the R&D Center, General Electric Company) and to Dr. E. Feingold (of the Space Sciences Laboratory, General Electric Company) for helpful discussions and comments. The technical assistance of B. Migliorino is also gratefully acknowledged.

Manuscript received June 9, 1967; revised manuscript received Sept. 14, 1967.

Any discussion of this paper will appear in a Discussion Section to be published in the December 1968 JOURNAL.

REFERENCES

1. L. Harris and B. M. Siegel, *J. Appl. Phys.*, **19**, 739 (1948).
2. J. L. Richards, P. B. Hart, and L. M. Gallone, *ibid.*, **34**, 3418 (1963).
3. K. G. Gunther, *Z. Naturforsch*, **13**, 1081 (1958).
4. J. E. Davey and T. Pankey, *J. Appl. Phys.*, **35**, 2203 (1964).
5. R. F. Bis, A. S. Rodolakis, and J. N. Zemel, *Rev. Sci. Instr.*, **36**, 1626 (1965).
6. E. Krikorian, "Single Crystal Films," M. H. Francombe and H. Sato, Editors, Macmillan Co., New York (1964).
7. R. E. Thun, "Physics of Thin Films," Vol. 1, G. Hass, Editor, Academic Press, New York (1963).
8. H. M. Smith and A. F. Turner, *Appl. Optics*, **4**, 147 (1965).
9. H. Schwartz, 1966 Natl. Vac. Symp. Abstracts, p. 87.
10. J. F. Ready, *J. Appl. Phys.*, **36**, 462 (1964).
11. P. D. Zavitsanos and L. E. Brewer, *J. Chem. Phys.*, **35**, 3093 (1967).
12. H. B. Guthier, *Z. Naturforsch.*, **16a**, 268 (1961).
13a. Hugo Weichel and P. V. Avizonis, *Appl. Phys. Let.* **9**, 334 (1966); b. J. Berkowitz and W. A. Chupka, *J. Chem. Phys.*, **40**, 2735 (1964); c. P. Zavitsanos, *J. Carbon*, to be published.
14. ASTM, Card #14-450.
15. Max Hansen, "Constitution of Binary Alloys," p. 165, McGraw-Hill Book Co., New York (1958).
16. J. Richardson, Private communication.
17. B. Molnar, J. J. Flood, and M. H. Francombe, *J. Appl. Phys.*, **35**, 3554 (1964).

Brief Communications

Reply to Comments on the Paper "Transport Processes in the Thermal Oxidation of Silicon"

Douglas O. Raleigh

Science Center, North American Rockwell Corporation, Thousand Oaks, California

A recent communication (1) has raised a number of questions concerning my paper "Transport Processes in the Thermal Oxidation of Silicon" (2). Since it is felt that the comments made represent a misunderstanding of the assertions in this paper, a reply was felt necessary.

In a paper in 1962, Jorgenson (3) reported experiments on the effect of an electric field on the thermal oxidation of silicon at elevated temperatures. From the results, he asserted that the normal thermal oxidation process occurred by the diffusion of oxygen ions through the SiO_2 reaction layer. My own paper was an attempt to clarify the matter of what can be meant by the "effect of an electric field" on a thermal oxidation process. I asserted that an electric field *per se* cannot provide a steady-state driving force for diffusion-controlled thermal oxidation, since the net process involved in normal oxidation is the transport of an electroneutral species (elemental oxygen in the case of SiO_2) through the reaction layer. Accordingly, in examining electric field effects, one must consider the role of the experimental arrangement in altering the nature of the oxidizing system. Specifically, the application of an electric field via ohmic leads provides an external path for electron flow and results in an electrolysis experiment rather than an electric field experiment. Since thermal oxidation by an ionic mechanism involves the transport of both ions and electrons through the oxide layer and electrolysis involves only ion transport, it is not possible to say *a priori* that an electrolysis experiment proves normal oxidation occurs by an ionic mechanism. It may well be that the electronic conductivity in the oxide is too low to permit more than a minor contribution by an ionic mechanism.

In the recent communication (1), it was said that I asserted the so-called halt voltage is, as a general matter, unrelated to the free energy of formation of the oxide. Reference to an unpublished memo by Wagner was made to show that this is not the case in cells of the type $Me|MeO|O_2$ with an externally applied voltage. In fact, while I might have made myself clearer, I did not assert this as a general matter, but merely for the cell arrangement Jorgenson (3) employed. In the latter case, a constant current was passed through two conjoined cells $O_2,Pt|SiO_2|Si$ and the voltage monitored across each oxide layer. The SiO_2 in these cells was a growing oxide layer on the surface of an initially clean silicon sample with sputtered platinum electrodes on the two ends. An oxygen atmosphere served for both the normal oxidation and the oxygen electrodes. If the voltage leads across the cells were properly contacted, the cell voltages should have been given by $V = E \pm iR$, where E is the galvanic emf and the sign of the iR drop depends on the direction of the current. E is ideally given by $t_{ions}\Delta F^\circ_f(SiO_2)/4F$, equal to t_{ions} (1.69v) at 850°, where t_{ions} is the effective ionic transport number in the ox-

ide film. Since the iR drop would be proportional to the SiO_2 film thickness, extrapolation of V *vs.* t back to $t = 0$ should give E. Instead, all V *vs.* t plots extrapolated back to zero volts, indicating no galvanic emf contribution. As explained in my paper, this would have been the case if the voltage lead to the Si were unprotected from oxidation, since one would then have had an O_2,SiO_2 electrode at this site, identical to the main oxide electrode. In this case, one would have been measuring purely iR drop in the oxide film, which would be unrelated to the free energy of formation of SiO_2.[1]

Jorgenson's report of recent galvanic emf data on the cell

$$O_2(p''_{O_2}),Pt|SiO_2(\text{membrane})|Pt,O_2(p'_{O_2})$$

is very interesting and may, indeed, indicate both sufficient ionic and electronic conduction in SiO_2 to support an ionic oxidation mechanism. Caution, however, is required in interpreting the experimental results. It was said that p''_{O_2} was 323 Torr and that p'_{O_2} was maintained at an ambient value of 10^{-7} Torr by vacuum pumping on the right-hand side of the cell. Ionic transport numbers of 0.40-0.53 were obtained, which were presumably calculated from the galvanic emf via the expression

$$E = t_{\text{ions}} \frac{RT}{4\mathbf{F}} \ln \frac{p''_{O_2}}{p'_{O_2}}$$

In this, of course, it is important that the ambient value of 10^{-7} Torr for p'_{O_2} be also the pressure value inside the sputtered Pt film at the Pt|oxide interface, since it is the latter pressure that determines E. This is a matter of concern, since oxygen was continually permeating the silica membrane and, indeed, the permeation rate was measured in the same experiment. Jorgenson implied that there was no pressure differential across the Pt, since his measured permeation rates agreed to 10% with those of Norton (4). This, however, is not very convincing, since the permeation rate only depends on Δp and would be essentially the same for any p'_{O_2} value small compared that of p''_{O_2}. Thus, any of a wide range of p'_{O_2} values $> 10^{-7}$ Torr could have been present at the $Pt|SiO_2$ interface and would have the effect of lowering the calculated values of the ionic transport number. Experiments with silica membranes thick enough to retard permeation greatly would be very helpful. Likewise helpful would be the use of a "buffered" oxygen atmosphere, such as a $CO\text{-}CO_2$ gas mixture, which establishes a low oxygen pressure chemically instead of by evacuation.

Regarding the many small points in my paper which were allegedly incorrect, I can only comment on the two that were actually brought up. Regarding Jorgenson's experiments on the effect of an electric field on the oxidation of zinc (5), I stand corrected in that the author did not assert the results showed diffusion control by oxygen ions, but merely by ions. I must still maintain, however, that the results did not prove diffusion control by ions, but merely showed the presence of some ionic conductivity in the oxide, for the reasons mentioned above and in my original paper. Regarding my model for the stopping voltage, its calculation did not require an assumed value for the ionic transport number, but a value for the ionic conductivity. The latter was obtained from Jorgenson's own data and a value in good agreement with it was obtained from oxygen diffusion data in SiO_2. Thus, the original prediction for the stopping voltage remains.

In conclusion, it is felt that the distinction between experiments on the effect of an electric field on thermal oxidation and electrolysis experiments is still an important one. Wagner, in fact, has independently employed the concept of superposed electrolysis to explain oxidation effects in the presence of an external electric field in what I believe is the same unpublished memo to which Jorgenson referred (6). It is felt that this concept provides a rational electrochemical basis for such field effects and clearly indicates their limited relevance in deducing the predominant oxidation mechanism.

Manuscript received Sept. 11, 1967.

Any discussion of this paper will appear in a Discussion Section to be published in the December 1968 JOURNAL.

REFERENCES

1. P. J. Jorgenson, *This Journal*, **114**, 820 (1967).
2. D. O. Raleigh, *ibid.*, **113**, 782 (1966).
3. P. J. Jorgenson, *J. Chem. Phys.*, **37**, 874 (1962).
4. F. J. Norton, *Nature*, **191**, 701 (1961); "Transactions of the 8th Vacuum Symposium and 2nd International Congress," pp. 8-16, Pergamon Press, New York (1962).
5. P. J. Jorgenson, *This Journal*, **110**, 461 (1963).
6. C. Wagner, Unpublished memo, "Considerations on the Effect of an External Electrical Field Applied to an Oxide Layer Growing on a Metal in Oxygen," Feb. 13, 1966.

[1] Note added in proof: Dr. Jorgenson has communicated to the author that he has re-examined his original voltage-time data and finds that it is best fitted to a zero-time intercept not of zero volts, but of 0.61v. If so, this would indicate that there was a galvanic contribution, which should be added to my estimate of the iR drop. This would yield 1.86v for the predicted halt voltage, in somewhat better agreement with the observed value than my previous estimate.

Application of the Peltier Effect for the Determination of Crystal Growth Rates

Ranjit Singh, August F. Witt,* and Harry C. Gatos*

Department of Metallurgy and Center for Materials Science and Engineering, Massachusetts Institute of Technology, Cambridge, Massachusetts

A method for the determination of microscopic rates of solidification during crystal growth has been reported recently (1). The method is based on the introduction of relatively high-frequency impurity striations in the growing crystal. Such striations referred to from here on as "rate striations" were induced by establishing controlled low amplitude vibrations of known frequency in the melt during crystal growth. While the exact mechanism responsible for the formation of these striations is as yet not unambiguously determined, it is most likely that they are caused by instantaneous growth rate fluctuations associated with thermal and fluid-dynamic perturbations. It was found that they do not interfere to any detectable extent with the over-all solidification process (2).

The present communication reports on the successful formation of rate striations by employing the Peltier effect. Current pulses of short duration and of the appropriate frequency applied across the crystal-

* Electrochemical Society Active Member.

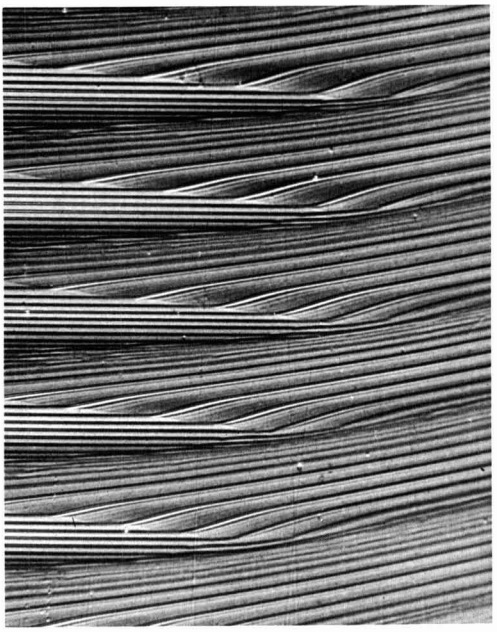

Fig. 1. Off-core on-core transition region in a Czochralski grown single crystal of InSb. Rate striations (introduced by employing the Peltier effect) reveal major variations of the microscopic crystal growth rate. Magnification 380X.

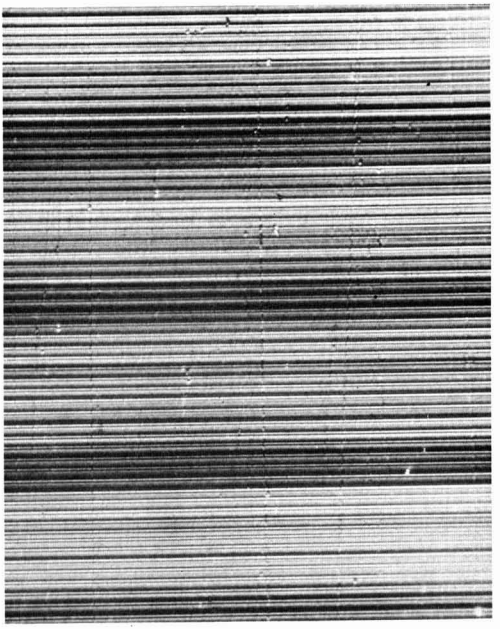

Fig. 2. Core region (facet growth) in an InSb single crystal. The microscopic rate of growth as revealed by the rate striations is constant. The alternating light and dark areas indicate impurity concentration changes which are unrelated to the microscopic rate of growth. Magnification 410X.

melt interface during crystal growth cause corresponding fluctuations in the instantaneous growth rate due to Peltier heating (or cooling). These fluctuations are incorporated in the growing crystal as impurity striations [revealed by polishing and etching (1)] which exhibit the same characteristics as the previously discussed rate striations introduced by vibrations. Like the vibrational striations, the presently reported striations do not effect the over-all crystal growth process and can thus be utilized for the investigation of localized microscopic growth rates and interface morphologies. Instantaneous growth rate changes resulting from Peltier heating (or cooling) have been previously studied extensively in connection with the formation of p-n junctions (3, 4).

In the present study a standard Czochralski pulling system was modified to permit the passage of current pulses across the crystal-melt interface during rotational and nonrotational pulling. A pulse generator in conjunction with a low-frequency current amplifier provided pulses of the desired frequency (5 to 40 cps). With this arrangement it was possible to control the current density and the duration of the current pulses which in turn determine the intensity and width of the induced striations respectively.

Some typical results obtained with Te-doped InSb single crystals are shown in Fig. 1 and 2. Local variations in growth rate within a given single crystal are readily seen in Fig. 1. It is apparent that these variations can be quantitatively evaluated. The constancy of the microscopic growth rate in the "core" of the crystal (2) is seen in Fig. 2. This figure shows also impurity concentration changes (dark and light areas) which obviously do not result from microscopic growth rate changes.

The Peltier effect permits excellent control of the intensity and the width of the induced rate striations. Possible side effects associated with the current transport across the growth interface (mass transport) may limit its usefulness particularly in multicomponent systems.

The detailed nature of the rate striations and their application to the study of solidification processes is being studied in our laboratory.

Acknowledgment

This work was supported by the National Science Foundation under contract GK-1653.

Manuscript received Oct. 17, 1967.

Any discussion of this paper will appear in a Discussion Section to be published in the December 1968 JOURNAL.

REFERENCES

1. A. F. Witt and H. C. Gatos, *This Journal*, **114**, 413 (1967).
2. A. F. Witt and H. C. Gatos, *ibid.*, **115**, 70 (1968).
3. W. G. Pfann, K. E. Benson, and J. H. Wernick, *J. Electronics*, **2**, 597 (1957).
4. C. A. Domenicali, *J. Appl. Phys.*, **28**, 749 (1957).

Electrochemical Books in Print

John Wiley Publications In-Print

The following are books developed and sponsored by The Electrochemical Society and published by John Wiley & Sons Inc., 605 Third Ave., New York, N. Y., 10016. Members of the Society can receive a 33 1/3% discount by ordering from Society Headquarters. Book and invoice mailed by the publisher. Nonmembers (including subscribers) must order direct from the publisher.

Corrosion Handbook. Edited by Herbert H. Uhlig. Published 1948, 1188 pages, **$21.00.**

Modern Electroplating, Second Edition. Edited by Frederick A. Lowenheim. Published 1963, 769 pages, **$16.00.**

Electrochemistry in Biology and Medicine. Edited by Theodore Shedlovsky. Published 1955, 369 pages, **$12.50.**

Arcs in Inert Atmospheres and Vacuum. Edited by W. E. Kuhn. Published 1956, 188 pages, **$7.50.** A 1956 Spring Symposium.

The Structure of Electrolytic Solutions. Edited by Walter J. Hamer. Published 1959, 441 pages, **$19.50.** A 1957 Spring Symposium.

Ultrafine Particles, Editor-in-Chief—William E. Kuhn. Published 1963, 561 pages, **$15.00.**

First International Conference on Electron and Ion Beam Science and Technology. Edited by R. Bakish. Published 1965, 945 pages, **$24.50.** (Sponsored by the Electrothermics and Metallurgy Division of The Electrochemical Society and the Metallurgy Society of AIME.)

The Electron Microprobe. Edited by T. D. McKinley, K. F. J. Heinrich, and D. B. Wittry. Published 1966, 1035 pages, **$27.50.** A 1964 Fall Symposium.

Chemical Physics of Ionic Solutions. Edited by B. E. Conway and R. G. Barradas. Published 1966, 622 pages. **$25.00.** A 1964 Spring Symposium.

Vapor Deposition. Edited by C. F. Powell, J. H. Oxley, and J. M. Blocher, Jr. Published 1966, 725 pages, **$19.95.**

The Stress Corrosion of Metals by Hugh I. Logan. Published 1966, 306 pages; **$13.95.**

High Temperature Oxidation of Metals by Per Kofstad. Published 1966, 340 pages; **$13.50.**

The Corrosion of Light Metals, by H. P. Godard, W. B. Jepson, M. R. Bothwell, and R. L. Kane. Published 1967, 360 pages; **$13.95.**

High-Temperature Materials and Technology. Edited by I. E. Campbell and E. M. Sherwood. Published 1967, 1022 pages, $27.50.

Other ECS Publications

The following books are available through The Electrochemical Society and various other publishers. Consult each listing for ordering instructions.

Vacuum Metallurgy, third printing, 1958, Edited by J. M. Blocher, Jr.; 216 pages; **$5.00,** less a 20% discount to ECS members only. Available from Electrochemical Society Headquarters, 30 East 42 St., New York, N. Y. 10017. A 1954 Fall Symposium.

Rhenium. Edited by B. W. Gonser. Published by Elsevier Publishing Co., 1962; 225 pages; **$12.50.** A 1960 Spring Symposium. ECS Members can obtain a 30% discount by sending their orders directly to Society Headquarters, 30 East 42 St., New York, N. Y. 10017. Remittance, made payable to American Elsevier Publishing Co., 52 Vanderbilt Ave., New York, N. Y. 10017 should accompany the order. Nonmembers must order direct from the publisher.

Iron Ore Reduction. Edited by R. R. Rogers. Published by Pergamon Press Ltd., New York and London, 1962; 359 pages; **$12.50** A 1960 Spring Symposium. Send all orders to The Macmillan Co., 60 Fifth Ave., New York, N. Y.

Stress Corrosion Cracking and Embrittlement. Edited by W. D. Robertson. Published 1956 by John Wiley & Sons Inc., New York. 202 pages **$2.50** (Hard cover book originally priced at $7.50.) Distributed by Dover Publications, Inc., 180 Varick St., New York. Send all orders to Dover Publications, Inc.

Electrode Processes. Published by The Electrochemical Society, 1966. c. 160 pages; **$5.00.** Edited from invited papers and full discussion presented by the Theoretical Electrochemistry Division, and supported by the United States Air Force Office of Scientific Research, at the Spring Meeting held May 1-5, 1966 in Cleveland, Ohio. Order direct from Society Headquarters.

Measurement Techniques for Thin Films. Published by The Electrochemical Society, 1967. Edited by B. Schwartz and N. Schwartz. c. 380 pages; **$9.00.** Edited from selected papers presented by the Dielectrics and Insulation Division and by the Electronics Division at the 128th and 130th National Meeting, held October 1965 and October 1966. Order direct from Society Headquarters.

Electrolytic Rectification and Conduction Mechanisms in Anodic Oxide Films. Published by The Electrochemical Society, 1967. Edited by P. F. Schmidt and D. M. Smyth. c. 230 pages; **$7.00.** Papers presented at the Dielectrics and Insulation Division. Symposium on Anodic Oxides at the 131st Spring Meeting held in Dallas, Texas. Order direct from Society Headquarters.

ELECTROCHEMICAL SOCIETY

NEWS AND REVIEWS — JANUARY 1968

Report from Ad Hoc Committee on Publication Plans

Because of the widespread interest of the members of the Society in publication activities, we are presenting a slightly abbreviated version of the report from the Committee to the Board of Directors.

At the meeting of the Board of Directors on January 6, 1967, extensive discussion of a recommendation by the Publication Committee that The Electrochemical Society undertake the publication of a three-part JOURNAL OF THE ELECTROCHEMICAL SOCIETY indicated that more information was needed as to the wishes and interests of our members and of our nonmember subscribers. This ad hoc committee was instructed to prepare questionnaires, analyze the returns, and prepare recommendations to the Board of Directors.

Of the 2855 questionnaires sent to nonmember subscribers, 711 (25%) were returned, and of 3961 sent to members, 2064 (52.1%) were returned. In each case, the percentage of returns is more than ample to represent a significant sample on the basis of polling experience.

The returns were analyzed by appropriate computer techniques. This permitted the writing of a program that revealed something about the nature of the respondents. For nonmember subscribers, the responses were broken down into three categories: all answers, United States answers, and foreign answers. For the member questionnaire the main categories were based on years of membership.

Member Questionnaire

In the following listing (A), (B), (C), and (D) stand respectively for all answers, less than 10 years, 10-20 years, and more than 20 years of membership.

QUESTION 1.
Do you favor the present format (starting with January 1967 issue) rather than dividing the JOURNAL into separate publications?

	(A)	(B)	(C)	(D)
Yes	54%	51%	58%	63%
No	46%	49%	42%	37%

QUESTION 2.
If your answer is YES to 1., and if you had a choice with your membership between the present two journals, ELECTROCHEMICAL TECHNOLOGY and JOURNAL OF THE ELECTROCHEMICAL SOCIETY, which one would you choose?

	(A)	(B)	(C)	(D)
Journal of The Electrochemical Society	79%	83%	77%	66%
Electrochemical Technology	21%	17%	23%	34%

QUESTION 3.
If you prefer separate publications, which one of the three, along with a monthly news bulletin, would you elect to receive as part of your membership?

	(A)	(B)	(C)	(D)
Electrochemical Science	42.7%	39.7%	44.7%	53.5%
Solid State Science	33.8%	41.6%	27.3%	3.2%
Electrochemical Technology	23.5%	18.7%	28.0%	43.3%

	All Returns	No to Question 1	Yes to Question 1
Electrochemical Science	42.7%	40.6%	46.5%
Solid State Science	33.8%	36.9%	28.4%
Electrochemical Technology	23.5%	22.5%	25.1%

QUESTION 4.
Would your choice of which publication to receive as part of your membership be influenced by whether it is issued monthly or bimonthly?

	(A)	(B)	(C)	(D)
Yes	14%	16%	13%	11%
No	86%	84%	87%	89%

QUESTION 5.
If you prefer separate publications, to which ones would you subscribe in addition to the one you elect to receive as part of your membership?

	(A)	(B)	(C)	(D)
Electrochemical Science	20.0%	19%	22%	22%
Solid State Science	9.5%	8%	11.2%	14.2%
Electrochemical Technology	41.6%	43%	38.3%	36.8%
No additional journal	38.6%	37.4%	40%	42.5%

QUESTION 6.
Would your selection of paid subscriptions be influenced by whether publication is monthly or bimonthly?

	(A)	(B)	(C)	(D)
Yes	15%	16%	13%	12%
No	85%	84%	87%	88%

QUESTION 7.
Do you now subscribe to ELECTROCHEMICAL TECHNOLOGY?

	(A)	(B)	(C)	(D)
Yes	30%	24%	39%	43%
No	70%	76%	61%	57%

QUESTION 8(a).
Would the subscription price affect your decision on Question 6. in the price range of $17 to $22?

	(A)	(B)	(C)	(D)
Yes	53%	54%	53%	44%
No	47%	46%	47%	56%

QUESTION 8(b).
Would the subscription price affect your decision on Question 6. in the price range of $12 to $17?

	(A)	(B)	(C)	(D)
Yes	30%	30%	30%	28%
No	70%	70%	70%	73%

QUESTION 9.
How long have you been a member of the Society?

Less than 10 years	61%
10-20 years	27%
Over 20 years	12%

QUESTION 10.

What is your current professional activity?

	(A)	(B)	(C)	(D)
1. Teaching	12%	13%	10%	10%
2. Consultant	4%	1%	5%	12%
3. Management Administration	2%	2%	3%	3%
4. Management Technical	9%	6%	14%	13%
5. Research and Development	9%	8%	10%	10%
6. Basic Research	4%	5%	3%	2%
7. Other	12%	11%	11%	19%
8. Battery	8%	9%	7%	5%
9. Solid State & Dielectrics	24%	31%	18%	4%
10. Industrial Electrolytic and E & M	4%	4%	5%	6%
11. Corrosion and Electrodeposition	5%	4%	7%	9%
12. No Response	7%	6%	7%	7%

Questionnaire to Nonmember Subscribers Journal of The Electrochemical Society

The findings were reported three ways: (A) all answers; (B) United States answers; and (C) foreign answers.

QUESTION 1.

Which or both of the present publications do you subscribe to?

	(A)	(B)	(C)
Journal of The Electrochemical Society	49%	47%	51.5%
Electrochemical Technology	51%	53%	48.5%
Both	51%	53%	48.5%

QUESTION 2.

Has frequency of publication influenced your choice of subscriptions?

	(A)	(B)	(C)
Yes	8.5%	5%	13%
No	91.5%	95%	87%

QUESTION 3.

Would you prefer that the Society continue publishing the JOURNAL in the format established with the January 1967 issue?

	(A)	(B)	(C)
Yes	90%	91%	89%
No	10%	9%	11%

QUESTION 4.

If the three components become available as separate publications, which ones would you subscribe to?

	(A)	(B)	(C)
Journal of The Electrochemical Society —Electrochemical Science	82%	84%	80%
Journal of The Electrochemical Society —Solid State Science	64%	63%	65%
Journal of The Electrochemical Society —Electrochemical Technology	63.5%	67.6%	59%

Analysis of Replies

On the question of dividing the JOURNAL according to three major areas a majority of the members responding favor the retention of the present format, as did a large majority of the nonmember subscribers. The comments relative to this point were much more numerous in opposition than in support, but even more significantly, the opposing comments were predominantly specific and objective whereas the supporting comments were often vague and subjective. Outstanding amongst the comments in opposition were those whose theme was the value of the interdisciplinary aspects of covering all areas in one journal, particularly the cross fertilization that arises from learning of what is going on in other areas. Furthermore, among the cogent reasons for not changing to the proposed scheme was the distaste for proliferation and splintering of publications, thereby adding to the burden of technical reading and to the cost of subscriptions.

Although no question in either questionnaire dealt with the possibility of returning to the single journal, numerous comments recommended this either explicitly or implicitly.

When many of the returns expressing approval of the 3-unit publication were examined in the light of accompanying comments, distaste for another title and even greater distaste for any increase in cost that might develop were revealed.

It is amply evident both from answers to questions and from comments that a majority of both members and nonmember subscribers like the present format of the JOURNAL.

A clear-cut response showed that frequency of publication is not significant in determining paid subscriptions.

There is not much objection to a modest increase in subscription prices. A substantial increase in costs to members owing to proliferation of titles is widely opposed.

Comments that obviously spring from readers show that the appearance in a single publication of papers in both electrochemical science as well as those that are either basic or applied is a matter of concern to only a relatively small number of respondents. It is evident that members desire the interdisciplinary flavor that follows from this situation. Those who would avoid it are not responsive to members' wishes.

A gratifying number of comments indicated explicitly or by implication that the respondents are well satisfied with the present publication policies. Unhappily, some commented in the adverse sense. So far as the specific questions are concerned, the opposition to change is an implicit endorsement of present publication policies. The questionnaires will be held in the Society's offices at 30 East 42nd Street, New York City until January 1, 1969, and any member is welcome to study them at whatever length he may desire.

The number (591 or 28.6% of those answering) and the serious tenor of the comments together with the remarkably large percentage return of the questionnaires (52.1%) constitute clear evidence that the members are not only deeply concerned with publication matters, but that they are ready to help with advice. We must conclude, therefore, that the poll was successful in providing the information and the guidance that were needed.

Recommendations

1. Don't separate publications according to individual narrow subjects.

2. Retain the basic features of the present mode of publication, which are:

(a) Keep electrochemical science and solid state science in one journal because of interdisciplinary value to reading membership.

(b) Although these items should appear in the same journal, they should be separated as in the present format.

3. Because of the unsolicited expression of interest in returning to a single publication, the Publication and Finance Committees should study the implications of this suggestion, which obviously was not made lightly by many members and nonmember subscribers, and jointly report their findings to the Board of Directors in time for consideration at the January 1968 meeting of the Board.

Charles Faust
Ralph A. Schaefer
Harold J. Read, Chairman

(Note: The findings and recommendations have been referred by President Gatos to the Publication Committee and the Finance Committee for study and possible implementation.)

Extended Abstracts Program for Boston

The January 1968 issue of the Journal carries for the first time a special insert including an extended abstract order card. You will find this perforated order form inside the first cover. To most Society members it is the first notice of important changes to the extended abstract publication program.

Before each National Meeting since 1963 the Society in collaboration with various Divisions has offered extended abstract volumes. These books have provided a record of significant experimental data contained in papers delivered at such meetings. Often they have been the only record. Individual volumes have been issued for each participating Division.

At each meeting during the past two years a combined volume containing each of the single volumes has also been available. Acceptance of this mode of publication has been most favorable. For example, at the Chicago Meeting the number of combined volumes sold exceeded the sales of most single volumes.

The Board of Directors has decided, based on studies of several Standing Committees, that our authors, members, and nonmember subscribers will benefit through improved service by discontinuing individual volumes and by issuing only a combined volume of all available meeting paper abstracts.

This change will mean both a shorter lead time for authors and a longer opportunity to purchase the abstracts and still receive the volume before the meeting. With all extended abstracts in one volume, for premeeting study and post-meeting reference, interdisciplinary exposure is encouraged. Quite important will be the cost. A set of individual volumes for a meeting has cost as much as $14.00. The price for the combined volume has been set for $10.00 for the Boston Meeting.

Please read carefully the special insert found inside the front cover. It contains instructions and tear-out order form for purchasing the extended abstract volume for the Spring 1968 Meeting in Boston. This insertion replaces the previously mailed notice and order forms. It is anticipated that this change will improve and strengthen our extended abstract program and that you will endorse the change.

SECTION NEWS

Boston Section

Dr. John A. Copeland was the speaker at the sixty first meeting of the Boston Section held on September 20, 1967 at the Ledgemont Laboratory of Kennecott Copper Corp., Lexington, Mass.

The subject of Dr. Copeland's talk was "Bulk Negative Resistance Semiconductor Devices." He explained how the properties of bulk negative resistivity in certain semiconductors such as GaAs has led to new devices for millimeter-wave power generation, amplification, and logic function generation.

In reviewing the physical principles of present bulk effect devices such as Gunn diodes, he showed how application of a voltage greater than a certain threshold value across a block of GaAs triggered the formation of high field domains which travelled through the device. The initiation and motion of these domains was illustrated by a computer generated motion picture and it was shown how domain motion could be used to perform logic functions.

A new mode of operation bulk effect devices, the LSA (Limited Space Charge Accumulation) mode was described which makes possible oscillators which will deliver useful power at much higher frequencies than with transit time devices such as transistors. Future applications of bulk effect devices may include functional blocks very different from today's integrated circuits.

R. G. Donald,
Secretary

Chicago Section

The Chicago Section of the Society met on November 16, 1967 at the Chicago Engineers Club. The speaker for the evening was Dr. Donald E. Smith, Associate Professor of Chemistry, Northwestern University, Evanston, Ill., who spoke on "Modern Approaches to the Study of Kinetics and Mechanisms of Electrode Reactions: Techniques and Instrumentation." Dr. Smith described a decade of advances which have a profound influence on approaches to the study of the chronology of electrode reactions. Developments in techniques and electronic hardware have reduced substantially the tedium and uncertainty associated with such investigations. The nature, scope, and implications of these advances were discussed at length. Specific examples of investigations which took advantage of these advances were covered.

The section has proposed the following tentative program for the 1968 season.

January 11, 1968—"On the Kinetics of Iron Dissolution in Acid Chloride Solutions," Z. Andrew Foroulis, Esso Research and Development, Florham Park, N. J.

February 15, 1968—"Artificial Renal Dialysis," James Greenwald, M.D., Internist, St. Catherine Hospital Heart Station, East Chicago, Ind.

March 14, 1968—"Modern Techniques in Battery Research and Development," N. Corey Cahoon, Union Carbide Corp., Cleveland, Ohio.

April 17, 1968—"Electrochemical Machining; Some Unanswered Questions for Electrochemists" Garret K. Vandenburgh, Anocut Engineering Co., Elk Grove Village, Ill.

"Ladies Night" Program and date to be announced.

I. H. Pronger, Jr.,
Secretary

Detroit Section

The Detroit Section held its first dinner-meeting of the 1967-1968 season at Wayne State University on October 26, 1967. The speaker for the evening was Dr. Seymour Senderoff of the Union Carbide Corp. Dr. Senderoff presented a talk on "The Mechanisms of Electrode Reactions in the Electrodeposition of Metals from Molten Salts," reviewing the chronopotentiometric studies of the electrode reactions in the electrodeposition of niobium, tantalum, zirconium, chromium, molybdenum, and tungsten from molten fluoride solutions, showed irreversible phenomena in the metal production step. The nature of this irreversibility and its significance in the electrodeposition of coherent coatings was discussed.

E. A. Romanowski,
Second Vice-Chairman

Metropolitan-New York Section

The Metropolitan-New York Section met on November 1, 1967 at the Stone Hall Inn, New York City.

Dr. Henry Brown, Director of Research, Udylite Corp., spoke on "The Role of Organic Addition Agents in the Electrodeposition of Metals," describing the role of various classes of organic compounds used as addition agents in aqueous electroplating baths for the purpose of altering the appearance, structure, and properties of the metal deposit. Special attention was given to molecular structure of the addition agents used in bright nickel and cobalt electroplating. Also the corrosion resistance of the deposits was discussed.

Eric Rau,
Secretary-Treasurer

Three $800 Electrochemical Society Summer Fellowships to be Awarded

The Board of Directors of The Electrochemical Society recently appropriated funds to support three 1968 Summer Fellowships for qualified graduate students. Each fellowship has a stipend of $800 and the purpose of the fellowship is to assist a student to continue his graduate work during the summer months in a "field of interest to The Electrochemical Society." These fellowships are to be known as the Edward Weston Fellowship, the Colin Garfield Fink Fellowship, and the ECS Fellowship Award.

Candidates' Qualifications: "The award shall be made without regard to sex, citizenship or race, or financial need. It shall be made to a graduate student pursuing work between the degree of B.S. and Ph.D. who has received a nine months' grant preceding the summer period and who will continue his studies after the summer period. A previous holder of the award is eligible for reappointment."

Qualified graduate students are invited to apply for these summer fellowships and should submit the following items:

1. a brief statement of educational objectives.
2. a brief statement of thesis research problems including objectives, work already accomplished, and work planned for the summer of 1968.
3. a transcript of undergraduate and graduate academic work.
4. two letters of recommendation.

The applicant should request his research advisor and one additional faculty member familiar with his work to write letters of recommendation. Application material and letters of recommendation should be sent to: Dr. Douglas N. Bennion, School of Engineering, University of California, Los Angeles, Calif.

Applications must be received by March 1, 1968 and award winners will be announced on May 1, 1968.

Midland Section

On November 15, 1967 the Midland Section held a meeting in the Sales Training Conference Room of The Dow Chemical Co., Midland.

Prior to the technical meeting a dinner in honor of the speaker was held at the Country Squire Inn in Midland. The speaker for this meeting was Mr. Gilbert S. Keeley, a Nuclear Engineer for Consumer's Power Co., who spoke on "Nuclear Energy Plants in Operation by Consumer's Power." Mr. Keeley described engineering details and economic considerations for the two nuclear facilities of Consumer's Power, showed slides of actual facilities, and answered many specific questions as to future plans in nuclear generation both for Consumer's and the industry in general.

John A. Van Westenburg,
Secretary-Treasurer

National Capital Area Section

The National Capital Area Section held its first meeting of the 1967-1968 season on October 5, 1967, at the American University, Washington, D.C. Dr. Kurt Stern, Chairman of the Section, presented a Past-President pin to the retiring Chairman, Frederic M. Bower, Naval Ordnance Laboratory, in recognition of his excellent service to the Section.

Dr. Ralph J. Brodd, Union Carbide Corp., spoke on "Faradaic Rectification." He discussed the method and the results of applying an alternating current through a range of frequencies on an electrode reaction. Systems such as a cadmium electrode in a cadmium chloride solution and zinc electrodes in zinc chloride and zinc bromide solutions were described.

The tentative schedule for the 1968 season is as follows:

February 1—"Forecast for Space Fuel Cells, Ernst M. Cohn, NASA.

March 7—"Society Activity and New Developments in Batteries," N. Corey Cahoon, Vice-President of The Electrochemical Society and Senior Scientist, Union Carbide Corp.

April 4—"Corrosion Research," H. H. Uhlig, Massachusetts Institute of Technology.

May 2—Tour of Goddard Space Flight Center, Maryland, and High School Science Fair Awards.

Frank X. McCawley,
Secretary

Pittsburgh Section

On October 27, 1967 the Pittsburgh Section held its fall meeting at the Westinghouse Research and Development Center, Pittsburgh. The technical program consisted of the following papers:

"Stress Corrosion Cracking," Fred Pement, Westinghouse Research Laboratories.

"Initiation of Stress Corrosion Cracks in Aluminum," M. S. Hunter, Alcoa Research Laboratories.

"Some Modern Techniques in Battery Research and Development," N. Corey Cahoon, Union Carbide Corp.

"Role of Defect Structure in Alloy Oxidation," Sven Jansson, Westinghouse Research Laboratories.

"Chemical Properties of PbO_2 Electrodeposited from Organic Solvents," C. W. Lewis and P. C. Edge, Pittsburgh Plate Glass.

"Use of Polarization Resistance as a Guide in Making Inhibitor Additions to Pickling Solutions," C. J. Warning, U.S. Steel Applied Research Laboratories.

As it has done in previous years, the Section voted to contribute a $25 award to the Buhl Planetarium for their forthcoming School Science Fair. The award will go to the student submitting the best exhibit in the field of electrochemistry.

R. L. Horst, Jr.,
Secretary-Treasurer

San Francisco Section

The San Francisco Section will hold its 1st Western Regional Technical Session on "Electrochemical Aspects of Thin Films and Semiconductors," on March 7, 1968 at the San Francisco Airport Hilton Inn.

For additional information write: E. F. Duffek, Chairman, Fairchild Semiconductors Corp., 4001 Junipero Serra Blvd., Palo Alto, Calif. 94304.

Southern California-Nevada Section

The Third Advances in Battery Technology Symposium sponsored by the Southern California-Nevada Section was held on December 1, 1967 at the Union Oil Auditorium, Los Angeles. The purpose of this symposium is to bring into focus the technical progress that is being made by electrochemists and engineers in these various industries on the development of advanced batteries and fuel cells.

The program consisted of the following papers:

"Fuel Cells for Electric Automobiles: A Prognosis" N. A. Cook, Allis-Chalmers.

"Silver-Zinc Batteries," G. A. Dalin, Yardney Electric Corp.

"Sodium-Air Secondary Battery," L. A. Heredy, M. L. Iverson, L. R. McCoy, and R. D. Oldenkamp (A.I.)

"Sohio Secondary Molten Salt Battery," E S. Buzzelli, Standard Oil of Ohio.

"Electrochemical Aspects of the General Atomic Zinc-Air Battery System," G. Caprioglio and J. T. Porter, General Atomics.

"Electric-Microwave Hybrid Cars and Smog," M. L. Brubacher and I. Ettinger, California Motor Vehicle Pollution Control Board.

"Lithium Organic Electrolyte Batteries," R. C. Shair, A. E. Lyall, and H. N. Seiger, Gulton Industries.

"Metal-Air Batteries," N. Palmer, Leesona-Moos Laboratories.

"Sodium-Sulfur Batteries," N. Weber, Ford Motor Co.

As in the case of the first two symposia, the proceedings of the meeting will be published and distributed. The proceedings of the first two symposia are available at $5.00 each; softcover copies are 5½ x 8½, with 130 pages for 1965 and 137 pages for 1966. All orders are to be sent to Carl Berger, 13401 Koutenay Dr., Santa Ana, Calif. 92705

South Texas Section

A meeting of the South Texas Section was held on October 27 at the Geo Club

in Houston. Mr. John J. Newport was presented with a Past-Chairman pin in appreciation of his service in that office. Dr. H. A. Liebhafsky was welcomed as a new member of the Section. Dr. Liebhafsky is recently retired from the General Electric Co. and presently holds the position of Professor of Chemistry at Texas A&M University.

Dr. Thomas C. Franklin, Professor of Chemistry at Baylor University, presented a talk on "Processes Occurring at Metal Solution Interfaces." Dr. Franklin summarized the results of several research areas with which he and his students have been concerned for several years. These included studies of hydrogen sorption and adsorption on various electrode surfaces by coulometric methods with applications to the determination of surface areas and degree of coverage, activity of adsorption sites and catalytic activity, hydrogen permeation and embrittlement, and the elucidation of oxidation and reduction mechanisms. A comparison of surface areas determined by oxygen adsorption with those from hydrogen adsorption showed good agreement.

Ron Darby,
Secretary-Treasurer

DIVISION NEWS

Electrodeposition Division

The annual business meeting of the Electrodeposition Division was held on October 18, 1967, in the Kingston Room of the Sheraton-Chicago Hotel in Chicago, Ill.

Chairman E. J. Smith extended his thanks to Professors H. A. Pohl of Oklahoma State University and W. F. Pickard of Washington University for organizing and running the very interesting and challenging symposium on "Dielectro- and Electrophoretic Deposition." In his response, Professor Pohl pointed out that he had detected an increasing interest in the bioelectrochemical field, and that the whole area of the electrochemistry of life processes might become a new venture for The Electrochemical Society.

Dr. E. J. Seyb announced that the 1968 symposium, to be held in Montreal, will be on the subject of "Corrosion in Multilayered Deposits." The symposium will be held jointly with the Corrosion Division, the cochairman being Karl Willson. Dr. Seyb appealed for papers and enumerated a number of subject areas which might be the basis for papers.

Dr. S. E. Beacom discussed selection of a topic for the 1969 symposium. He distributed sheets which listed the subjects of previous symposia held by the Division and by the American Electroplaters' Society, and proposed that "Plating on Plastics" might be a suitable topic for 1969. Dr. F. A. Lowenheim commented that the scope might be broadened to include plating on all nonconductors, and that electroforming should be considered. Dr. E. J. Seyb suggested that electroless metal plating aspects might be included. A variety of other topics was also proposed for consideration.

The following officers were elected for a two year term:

Chairman—J. V. Petrocelli, Research and Engineering Center, Ford Motor Corp., P.O. Box 2053. Dearborn, Mich. 48121

Vice-Chairman—S. E. Beacom, Research Laboratories, General Motors Corp., 12 Mile and Mound Roads, Warren, Mich. 48090

Secretary-Treasurer—E. B. Saubestre, 24 West Slopeln, Hamden, Conn. 06517

Members-at-Large—I. W. Wolf, 1285 Hamilton, Palo Alto, Calif. 94301 and R. Weil, Department of Metallurgy, Stevens Institute of Technology, Hoboken, N. J. 07030

Chairman E. J. Smith expressed his pleasure at having been permitted to serve as Chairman for three years and mentioned that many interesting problems had required solutions. He gave special thanks to Dr. McGraw for his assistance, and mentioned that action should be started on the 3rd edition of

Acheson Medal Award

The Acheson Medal Award can be made no oftener than every two years. The next opportunity for the Society so to honor someone is at the Montreal, Canada Meeting in the Fall of 1968.

The Honors and Awards Committee is charged by the Bylaws to recommend a selection to the Board. The Rules adopted by the Society, amended as of April 30, 1961, require that the Award shall be made without distinction on account of sex, citizenship, race, or residence.

In addition to the above, with regard to the selection, the Rules have the following provisos:

1. Nominations shall be accepted, also, from the membership at large. Announcement to this effect shall be made by the Secretary through the Journal of The Electrochemical Society as promptly as possible after the appointment of the Committee.

2. All nominations, whether made by a member of the Nominating Committee or by another member of the Society, must be accompanied by a full record of qualifications of the nominee for the Award. Such supporting documents from friends of the candidate or from his organization shall be in order.

3. The nominator must assume the responsibility for providing the Chairman of the Honors and Awards Committee with nine copies of the supporting documents, one for each member.

It is desired that such suggestions be in the hands of the Committee not later than February 1, 1968.

Following is a list of Acheson Medalists since the Award was founded:

Edward G. Acheson*—1929
Edwin F. Northrup*—1931
Colin Garfield Fink*—1933
Frank J. Tone*—1935
Frederick M. Becket*—1937
Francis C. Frary—1939
Charles F. Burgess*—1942
William Blum—1944
H. Jermain Creighton—1946
Duncan A. MacInnes*—1948
George W. Vinal—1951
J. W. Marden—1953
George W. Heise—1954
Robert M. Burns—1956
William J. Kroll—1958
Henry B. Linford—1960
C. L. Faust—1962
Earl A. Gulbransen—1964
Warren C. Vosburgh—1966

Please address all nominations to the Chairman of the Honors and Awards Committee, Dr. Walter J. Hamer, Electrochemistry Section, National Bureau of Standards, Washington, D. C. 20234.

* Deceased

"Modern Electroplating." Dr. J. V. Petrocelli, in accepting the office of Chairman, thanked Mr. Smith for his leadership over the past three years

Dr. Lowenheim, in commenting about the revision of "Modern Electroplating," pointed out that the 2nd edition was now in its fifth year, and that work on the 3rd edition needs to be started now by the appointment of an Editor and an Editorial Board, and by the solicitation of potential authors.

Seward E. Beacom,
Past Secretary-Treasurer

NEWS ITEMS

1967 Annual Index for the Journal

The Annual Index for Volume 114 (1967) will appear in the February 1968 issue of the JOURNAL. The February issue will be in two parts: Part I, the regular issue of the JOURNAL; Part II, the Index for Volume 114 (1967). Part II will be inserted in front of cover three of the JOURNAL.

Gordon Research Conferences

The Winter Gordon Research Conferences will be held from January 22 to February 2, 1968 in Santa Barbara, Calif., at the Miramar Hotel and at the Santa Barbara Biltmore Hotel. The purpose of the Gordon Research Conferences is to stimulate research in universities, research foundations, and industrial laboratories.

Meetings are held in the morning and in the evening, Monday through Friday, with the exception of Friday evening.

Requests for application forms for attendance at the Conferences, or for additional information, should be addressed to Dr. W. George Parks, Director, Gordon Research Conferences, University of Rhode Island, Kingston, R. I. 02881.

The following portions of the Conference on electrochemistry are of particular interest to ECS members.

Electrochemistry

January 22-26, 1968
Miramar Hotel
Paul Delahay, Chairman;
Isaac Trachtenberg, Vice-Chairman

January 22

"Some Charge-Transfer Processes in Non-Aqueous Solvents," **M. E. Peover, National** Physical Laboratory, England
"Structure of Water," **H. S. Frank, University of Pittsburgh**

January 23

"The Ellipsometric Techniques and the Mechanism of Certain Film Forming Reactions," **J. O'M. Bockris, University of Pennsylvania**
"Critical Factors Affecting Sensitivity and Accuracy of Ellipsometer Measurements," **R. H. Muller, University of California, Berkeley**
"Study of Concentration Gradients by Optical Methods," **R. N. O'Brien, University of Victoria**
"Double Beam Interference Techniques for Mass Transfer and Electrode Surface Studies," **R. H. Muller, University of California, Berkeley**

January 24

"Spectoreflectance Studies of Electrode Surfaces," **J. D. E. McIntyre,** Bell Telephone Laboratories

"Time-Domain Reflectometry for the Study of Electrode Processes in the Picosecond Range," **H. R. Fellner,** Hewlett-Packard Laboratories

January 25

"Mechanism Studies Using Optically Transparent Electrodes," **T. Kuwana,** Case Western Reserve University

"Potentialities and Limitations of Optical Methods in the Study of Electrode Processes," **J. Kruger,** National Bureau of Standards

"Experimental Studies in Convective Mass Transport in Channel Type Electrolysis Cells," **C. W. Tobias,** University of California, Berkeley

"The Combined Processes of Diffusion and Migration," J. Newman, University of California, Berkeley

January 26

"Electrode Processes in Solid-Electrolyte Cells," D. O. Raleigh, North American Aviation, Inc.

"High Conductivity Solid Electrolytes MAg_4I_5," **B. B. Owens,** Atomics International

(Boldface indicates active member of The Electrochemical Society.)

Appalachian Underground Course

The Thirteenth Annual Appalachian Underground Corrosion Short Course at the West Virginia University, School of Mines, Morgantown, W. Va., will be held on May 21-23, 1968, and covers basic, intermediate, and advanced education in corrosion control practices as related to underground pipe, cables, and water systems, as well as many special topics.

Additional information regarding the course can be obtained by contacting R. L. Clay, Publicity Chairman, U.S. Steel Corp., Pittsburgh, Pa. 15230.

University of Missouri Names Laboratory

The electrochemistry laboratory in the new materials research building at the University of Missouri at Rolla has been named for Dr. Martin E. Straumanis. Dr. Straumanis at present is professor of metallurgical engineering and research professor of materials at the university.

The plaque designating the honor was presented to Dr. Straumanis at the recent dedication ceremonies of the building.

Notice to Members

The National Headquarters has mailed, on the first of October, dues bills for 1968. These are a special IBM card which must be returned in the special envelope provided with the bill.

In addition to the dues bill you have the opportunity to subscribe to ELECTROCHEMICAL TECHNOLOGY and purchase bound volumes of the JOURNAL and ELECTROCHEMICAL TECHNOLOGY. At the same time you will have the opportunity to purchase the new 1968 DIRECTORY OF MEMBERS.

Ph.D. Program Established

The Department of Materials Science, State University of New York at Stony Brook, Stony Brook, L. I., N. Y., has announced the initiation of a Ph.D. program in Materials Science as an expansion of the existing M.S. program in Materials Science. Any student with a bachelor degree in physical sciences or engineering from an accredited school is eligible for admission.

Additional information can be obtained by writing: Professor Leslie L. Seigle, Acting Chairman, Department of Materials Science, State University of New York at Stony Brook, Stony Brook, L. I., N. Y. 11790

PEOPLE

Norman Hackerman has been named president of The University of Texas at Austin. Dr. Hackerman joined the faculty in 1945 and since that time has distinguished himself in research, teaching, and administration.

He was chairman of the Chemistry Department from 1952 to 1961 and also served as director of the Corrosion Research Laboratory. He was dean of the

Norman Hackerman

University's research and sponsored programs during 1960-1961, vice-president and provost of the University in 1961 and 1962, and vice-chancellor for academic affairs of the UT system from 1963-1967.

He received the Whitney Award of

the National Association of Corrosion Engineers in 1956 for outstanding work toward the advancement of corrosion science. In 1964 he was selected to give the 16th Joseph L. Mattiello Memorial Lecture in Chemistry in Chicago. He was recipient of The Electrochemical Society's Palladium Medal Award in 1965 and also received the 1965 Southwest Regional Award of the American Chemical Society.

Dr. Hackerman, a member of the Society since 1943, served as Chairman of the Corrosion Division in 1951, as Vice-President 1954-1957, and President in 1957-1958. He has been Technical Editor of the JOURNAL OF THE ELECTROCHEMICAL SOCIETY since 1950, and Interim Editor of ELECTROCHEMICAL TECHNOLOGY since 1965.

Dr. Hackerman's studies of corrosion in natural gas and sulfur production processes have proved valuable to Texas' petroleum industry. In 1956, during a chronic newsprint shortage, he and a student obtained a patent for a de-inking process whereby waste paper is treated with chemicals, heat and electricity to restore the qualities of original pulp.

He is coauthor of a textbook, "Pre-Medical Physical Chemistry," and has written numerous articles for scientific journals. His present research is concerned principally with chemistry and physics of surfaces, especially metal-solution interfaces.

Martin E. Kagan, executive officer and director, Yardney Electric Corp., New York, N. Y., has been elected president, it was announced. Mr. Kagan fills the

Martin E. Kagan

position formerly held by Michel N. Yardney, who has been elevated to chairman of the board of directors and chief executive office.

Mr. Kagan joined Yardney in 1949 following graduation from City College of New York. He was elected a senior vice-president of the organization in 1953 and a director in 1961. He resigned his position in 1964 to enter the publishing field but continued as a director and consultant of the company.

POSITIONS AVAILABLE

Research Chemist, B.S.—laboratory studies on electrode reactions in non-aqueous electrolytes, electrochemical syntheses, electroanalytical devices, etc. The successful applicant will have "ground floor" opportunity with this young, dynamic electrochemical R&D organization located just minutes from Times Square. Please send resume to: Dr. Ralf H. Koslow, Electrochemical Research Associates, 70 Hudson St., Hoboken, N. J. 07030.

Please address replies to the box number shown c/o The Electrochemical Society, Inc., 30 East 42 St., New York, N. Y. 10017.

Executive Position—reporting to director of research, is available to one who possesses a high-level of technical competence in the chemistry of metallurgy of coatings, corrosion, and surfaces. Reply Box B-25.

Electrochemist—wanted by small, but well financed private company to supervise and work in new processes of electrochemical orientation. Work hard, exciting. Applicants who like challenges should write to Box B-26.

Fuel Cell and Battery Engineers—career positions open for chemical engineers with B.S. and M.S. in Ch.E. with solid background of proven engineering experience in fuel cell and/or battery systems. Reply Box B-27.

Chemical Engineers and Physical Engineers—with Ph.D. degree. Opportunities for independent and imaginative experimentation in the study and scale-up of new high-temperature fused salt processes involving heat generation and transfer, corrosion, mass transport and separation, and instrumentation. Reply Box B-28.

S/C Development Engineers—duties include design and fabrication of new, bulk gallium arsenide (Gunn) devices, and silicon planar devices for microwave applications. Basic materials fabrication "know how" and/or gallium arsenide technology necessary. Reply Box B-29.

Plating Engineers—openings in Advanced Structures group in fuel cell program for engineers with at least 2 years experience in electroplating, electroforming or chemical machining methods. Familiarity with electroforming nickel and nickel alloys and electroplating noble metals on substances of all kinds is necessary. Reply Box B-30.

NEW MEMBERS

It is a pleasure to announce the following new members of The Electrochemical Society as recommended by the Admissions Committee and approved by the Board of Directors in December 1967.

Active Members

Andreassen, Knut, Foregrunn, Norway
Bower, V. E., Washington, D. C.
Brose, R. U., Oakland, Calif.
Chiang, P.-W., Ann Arbor, Mich.
Christopher, H. A., Scotia, N. Y.
Dobbs, P. J. M., Bridgeton, Mo.
Gothelf, Morton, Somerset, N. J.
Guidotti, R. A., Pasadena, Calif.
Karlan, J. H., Riverdale, N. Y.
Kasbarian, H. S., Richardson, Texas
Lawson, James C., West Acton, Mass.
Mamantov, Gleb, Knoxville, Tenn.
McCandless, J. T., Bradford, Pa.
McKenna, T. S., Succasunna, N. J.
Nancollas, G. H., Williamsville, Buffalo, N. Y.
Nisbet, A. R., Arkadelphia, Ark.
Novick, D. T., New York City, N. Y.
Oroshnik, Jesse, Raleigh, N. C.
Ross, S. E., Warrensville Heights, Ohio
Salama, C. A. T., Toronto, Ont., Canada
Sohm, Jean-Claude, La Tronche, France
Van Nynatten, Fred, Philadelphia, Pa.
Wagner, P. R., Lake Katrine, N. Y.
Warrock, R. V., San Diego, Calif.

Associate Member

Wilcock, R. E., Havertown, Pa.

Student Members

Atkins, J. K., Jr., University, Ala.
Condit, D. O., Columbus, Ohio
Cowan, R. L., II, Columbus, Ohio
Flinn, D. R., Denton, Texas
Kramer, L. D., University Park, Pa.

Reinstatements to Active Membership

Bernstein, Leonard, Cupertino, Calif.
Monteith, L. K., Durham, N. C.

ADVERTISER'S INDEX

This issue contains, on the inside of Cover I, an order form for ordering the Bound Volume of Extended Abstracts for the Boston Meeting.

Notice to ECT Subscribers

Nonmember subscriptions to ELECTROCHEMICAL TECHNOLOGY expired on December 31, 1967. Avoid missing any issue. A subscription renewal card invoice and return envelope has been mailed to all subscribers. To insure proper handling, mail your check for $15.00 with the completed card invoice in the enclosed envelope. [Subscribers located outside the Continental United States must add $1.00 to the subscription price for postage ($16.00), and payment must be made by money order or check in U.S. Funds.]

The 1968 bound volume of ELECTROCHEMICAL TECHNOLOGY can be obtained at the price of $6.00 by adding this amount to your remittance. The bound volume is not offered independently of your ECT subscription.

Notice to JOURNAL Subscribers

Your subscription to the JOURNAL OF THE ELECTROCHEMICAL SOCIETY has expired on December 31, 1967. Avoid missing any issue. A subscription renewal card invoice and return envelope have been mailed to all subscribers. To insure proper handling, mail your check for $24.00 with the completed card invoice in the enclosed envelope. [Subscribers located outside the Continental United States must add $1.50 to the subscription price for postage ($25.50), and payment must be made by money order or check in U.S. Funds.]

Because of the increasing number of pages published each year, the bound volume of the 1968 JOURNAL will be in two parts: Part I, January-June; Part II, July-December. The two parts of the volume will not be sold separately. The bound volume can be obtained for $15.00 by checking the appropriate box on the card invoice and adding this amount to your remittance. The bound volume is not offered independently of your JOURNAL subscription.

Call for Papers
134th National Meeting
Montreal, October 6-11, 1968

Divisions which have scheduled sessions are listed overleaf, along with symposium topics.

1. Symposium Papers.

Authors desiring to contribute papers to a symposium listed overleaf should check first with the symposium chairman to ascertain appropriateness of the topic.

2. General Session Papers.

Each of the several Society Divisions which meets in Montreal can plan a general session. If your paper does not fit readily into a planned symposium, you should specify "General Session."

3. To Submit a Meeting Paper.

Each author who submits a paper for presentation at a Society National Meeting should do three things:

A—Determine whether the meeting paper is to be submitted to a Society journal for publication. If so, see below for details.

B—No later than May 15, 1968, submit three copies, on the form printed overleaf, of a 75-word abstract of the paper to be delivered. You may use a facsimile of the form if necessary. These abstracts are required for publication in the printed program of the meeting.

C—No later than July 1, 1968, submit three copies of an extended abstract of your paper. See below for details. No deadline extension is possible.

Send all material to The Electrochemical Society, Inc., 30 East 42 St., New York, N. Y. 10017.

4. Meeting Paper Acceptance.

Notification of acceptance for meeting presentation, along with scheduled time, will be mailed to authors with general instructions no earlier than two months before the meeting. Those authors who require more prompt notification are requested to submit with their abstracts a self-addressed postal card with full author-title listing on the reverse.

5. Extended Abstract Book Publication.

Division programs will be the subject of an extended abstract volume in a manner prescribed by the Society Board of Directors. The volume is published by photo offset directly from typewritten copy submitted by the author. Therefore, special care should be given to the following typing instructions to insure legibility.

A—Abstracts are to be from 500-1000 words in length (two pages single-spaced) and are to contain to whatever extent practical all significant experimental data to be presented during oral delivery.

B—Please send original and two copies of the abstract typed single-spaced. Use white bond paper, size 8½ x 11 inches, with 1¼ margins on all sides. Typing guide forms are available from Symposium Session Chairman and from National Headquarters.

C—Title of paper should be in capital letters. Author(s) name and affiliation should be typed immediately below. It is not necessary in the heading or body to designate paper as "Extended Abstract" or to quote the divisional symposium involved.

D—Submit all copy, including figures, symbols and corrections, in black ink. No handwritten corrections, please. Submit graphs on onion skin without grids, or on graph paper specifically designed for offset reproduction; strip-on tape is acceptable.

E—Paste figures within typing dimensions indicated, with lettering no smaller than ⅛ inch. Submit only the important illustrations. Avoid use of half-tones except where absolutely necessary. Type captions no wider than figure dimensions and paste in proper place in the abstract. Place figure caption at bottom of figure. Place table title at top of table.

F—Mail to The Electrochemical Society. Inc., unfolded.

G—Please note that the extraordinarily low price of the extended abstract volume is made possible only through your strict adherence to these instructions. Any deviation threatens this low cost.

6. Manuscript Publication in a Society Journal.

Presentation of a paper at a Society National Meeting incurs no obligation to publish. However, all meeting papers upon presentation become the property of The Electrochemical Society, Inc., and should be submitted as promptly as possible in full manuscript form in order to be considered for publication in a Society publication. The Society "Instructions to Authors," are available from National Headquarters, set forth manuscript style and format.

Montreal Meeting Symposia Plans—Fall 1968

Battery Division Symposia Plans

The program for the Fall Meeting in Montreal, October 6-11, 1968 in addition to a general session will include the regular biennial symposium on Fuel Cells and a special symposium on Silver-Zinc Batteries.

Fuel Cells

Papers are solicited from those active in research and development on fuel cells of all types. Contributions ranging from fundamental aspects of electrode behavior and electrocatalytic phenomena to performance of fuel cells and fuel cell batteries in relation to design are desired. Questions and suggestions concerning the program should be addressed to the Program Chairman, R. R. Witherspoon, General Motors Research Laboratories, Warren, Mich. 48090.

Silver-Zinc Batteries

A symposium consisting completely of invited papers and reviews thereof will be held as a separate session lasting approximately four and one-half days. The symposium, cosponsored by the Air Force Aero Propulsion Laboratory, will feature papers on the history, electrode chemistry and electrochemistry, thermodynamics, mass transport, materials and manufacturing techniques, separators, and specifications, applications and performance of silver-zinc batteries. After editing, the contents of the symposium will be published as a hard-bound book which will bring together for the first time under one cover the science and technology of this high-energy electrochemical battery. This is not a closed meeting; attendance by all will be welcome.

Chairman for this symposium is J. J. Lander, Delco-Remy, Division of General Motors, Anderson, Ind. 46011.

Corrosion Division Symposia Plans

Three symposia in addition to general sessions are planned for the Fall 1968 Meeting of the Corrosion Division in Montreal.

Corrosion of Multilayer Deposits

Corrosion of Multilayer Deposits will be held jointly with the Electrodeposition Division. Chairmen for this symposium are: Karl Willson, Harshaw Chemical Co., 1945 E. 97 St., Cleveland, Ohio 44106 and E. J. Seyb, Jr., M&T Chemicals Inc., 1700 East Nine Mile Rd., Detroit, Mich. 48220.

Corrosion in Desalination

Corrosion in Desalination will be chaired by M. J. Pryor, Olin Matheson Chemical Corp., Metals Research Division, 275 Winchester Ave., New Haven, Conn. 06511.

Corrosion of Architectural Materials

Corrosion of Architectural Materials will be chaired by Henry Leidheiser, Jr., Virginia Institute for Scientific Research, P.O. Box 8315, Richmond, Va. 23226.

Those desiring to present papers at these symposia are requested to communicate directly with the symposium chairman. Several sessions of general papers will also be included.

The Corrosion Division will also institute on a trial basis a short session devoted to research results of newsworthy interest. Presentation time will be limited to 5 minutes and an abstract must be available at the meeting for posting. Permission to appear on the program must be obtained from the Chairman of the Division at the meeting. No advance permission is required.

No later than May 15, 1968, submit three copies, on the form overleaf, of a 75-word abstract of the paper to be delivered. No later than July 1, 1968, submit three copies of an extended abstract, 500-1000 words. Send all material to The Electrochemical Society, Inc., 30 E. 42 St., New York, N. Y. 10017

Corrosion and Electrodeposition Divisions Symposia Plans

Corrosion of Multilayer Deposits

The Corrosion and Electrodeposition Divisions have scheduled a joint symposium on Corrosion of Multilayer Deposits for the Fall 1968 Meeting in Montreal.

This symposium will include reports on systems including at least one applied metallic deposit (vapor, electroless or electrolytic). Subsequent or concurrent layers may be metallic or nonmetallic. Papers are particularly solicited on chromium-chromium oxide on steel, conversion and organic coatings over metal layers as well as multilayer metal coatings over metallic or plastic substrates.

Inquiries and suggestions should be addressed to either of the Symposium Chairmen: E. J. Seyb, M&T Chemicals Inc., 1700 East Nine Mile Rd., Detroit, Mich. 48220 or K. S. Willson, Harshaw Chemical Co., 1945 East 97 St., Cleveland, Ohio 44106.

Dielectrics and Insulation Division Symposia Plans

Deposited Thin Film Dielectric Materials

A symposium on Deposited Thin Film Dielectric Materials is scheduled for the Fall 1968 Meeting in Montreal.

F. Vratny, Bell Telephone Laboratories, Inc., Murray Hill, N. J., is Chairman.

There will be a number of invited papers; contributed papers are also being solicited.

Categories of subject matter being actively considered for the symposium include: (a) studies on the electrical and mechanical properties of deposited thin film dielectrics; (b) new techniques for the deposition of thin film dielectrics; (c) properties and applications of thin film dielectrics.

This symposium is particularly directed to the new sputtering technology, new means of evaporative deposition, and recent advances in vapor deposition techniques for preparation of dielectric thin films.

Suggestions and questions are welcome, and should be directed to the Chairman of the Symposium, F. Vratny.

Ferroelectrics

A symposium on Ferroelectric Materials is scheduled. The following topic areas are being actively considered for the sessions: (a) growth and characterization of ferroelectric crystals, (b) phenomenological and theoretical treatments of ferroelectricity, (c) dielectric properties of single crystals, polycrystal and composite materials, (d) domain structure and polarization reversal, (e) optical and electro-optic properties, and (f) device applications of ferroelectric materials.

There will be a number of invited speakers; contributed papers are also being solicited. Suggestions and questions concerning this symposium are welcome, and should be directed to the Chairman, Leslie E. Cross, Materials Research Laboratory, The Pennsylvania State University, University Park, Pa. 16802.

Electronics Division Symposia Plans

Electrical Contacts to Semiconductors

The Electronics Division is sponsoring a special symposium on Electrical Contacts to Semiconductors to be held at the Fall 1968 Meeting in Montreal. The fundamentals of the physics, chemistry, and metallurgy of ohmic contacts will be explored, and advances of technological importance will be discussed. The program is to include both con-

tributed papers and invited speakers. Papers are being solicited on such topics as: theory of ohmic contacts, techniques of ohmic contact fabrication, evaluation of contact properties, modes of contact failure, composite contacts, special property contacts (e.g. optical transparency, thermal conductivity).

Any questions or suggestions should be addressed to the Symposium Chairman, Bertram Schwartz, Bell Telephone Laboratories, Inc., Murray Hill, N. J. 07974.

Photosensitive Materials for Electronic Applications

This symposium will cover the properties and uses of photosensitive materials in the electronics industry. Topics which will be considered for the program include xerography, photochromism, novel photographic techniques, photochemistry (e.g. photoresists), vidicons, storage phosphors etc. Papers on the above or closely related topics are solicited.

Questions concerning this symposium should be addressed to the Symposium Chairman, Erik M. Pell, Manager, Physics Research Laboratory, Xerox Corp., 800 Phillips Rd. Webster, N. Y. 14580.

Electrothermics and Metallurgy Division Symposium Plans

Preparation and Purification of Ultra-Pure Metals

A symposium on Preparation and Purification of Ultra-Pure Metals in addition to general sessions will be held at the Fall 1968 Meeting in Montreal. This symposium forms the first of a series planned by the Division to deal with materials of particular interest to Society members.

Papers are solicited from those active in research and development of these metals. Invited key-note speakers will survey theory and methods for preparation, purification, and determination of residual elements in ultra-pure metals.

Sessions will encompass contributions on preparation by electrochemical deposition, electron beam melting and volatilization; purification by zone refining, electrochemical and vaporization methods, determination of residual elements by micro-chemical techniques, and influence of residual elements on chemical and physical properties.

Inquiries and suggestions should be directed to either of the cochairmen: W. C. Cooper, Noranda Research Centre, 240 Hymus Blvd., Pointe Claire, Quebec, Canada or W. W. Smeltzer, Department of Metallurgy and Materials Science, McMaster University, Hamilton, Ont., Canada.

75-Word Abstract Form—Montreal Meeting October 6-11, 1968

Mail no later than May 15, 1968 to The Electrochemical Society, Inc., 30 East 42 St., New York, N. Y. 10017

Abstract No. .....
(do not write in this space)

.....
(Title of paper)

.....

.....
(Author) (Underline name of author presenting paper)

.....
(Business Affiliation)

.....
(Address)

(Type your abstract in this space—double space with two carbon copies on plain white paper.)

Division and Symposium .....

Do you require any audiovisual equipment? ☐ 35 mm (2x2 in.) slide projector; ☐ 3¼ x 4 in. slide projector; ☐ other (specify) _____.

Is a full length paper on this work to be submitted for Society publication? ☐ Yes ☐ No

Papers presented before a national technical meeting become the property of the Society and may not be published elsewhere without written permission of the Society.

For Office Use

Extended Abstract rec'd: ..... requested: .....

Sent to: .....

75-word Abstract sent to: ..... date: .....

SUSTAINING MEMBERS (CONTINUED)

Fairchild Semiconductor Corp.,
Palo Alto, Calif.

FMC Corp.,
Inorganic Chemicals Div.,
Buffalo, N. Y.
Inorganic Chemicals Div.,
South Charleston, W. Va.

Foote Mineral Co.,
Exton, Pa.

Ford Motor Co.,
Dearborn, Mich.

General Motors Corp.,
Allison Div., Indianapolis, Ind.
Delco-Remy Div., Anderson, Ind.
Research Laboratories Div., Warren, Mich.

General Telephone & Electronics Laboratories, Inc., Bayside, N. Y.

Globe-Union, Inc.,
Milwaukee, Wis.

B. F. Goodrich Chemical Co.,
Cleveland, Ohio

Gould-National Batteries, Inc.,
Minneapolis, Minn.

Great Lakes Carbon Corp.,
New York, N. Y.

Harshaw Chemical Co.,
Cleveland, Ohio (2 memberships)

Hercules Inc.,
Hercules Research Center,
Technical Information Div.,
Wilmington, Del.

Hill Cross Co., Inc.,
West New York, N. J.

Hoffman Electronics Corp.,
Semiconductor Div.,
El Monte, Calif.

Honam Electric Industrial Co.,
Kwangju City, Korea

Honeywell, Inc.,
Minneapolis, Minn.

Hooker Chemical Corp.,
Niagara Falls, N. Y. (2 memberships)

HP Associates,
Palo Alto, Calif.

Hughes Research Laboratories, Div. of Hughes Aircraft Co., Malibu, Calif.

International Business Machines Corp.,
New York, N. Y.

International Minerals & Chemical Corp.,
Skokie, Ill.

International Resistance Co.,
Philadelphia, Pa.

ITT Federal Laboratories, Div. of International Telephone & Telegraph Corp.,
Nutley, N. J.

Jones & Laughlin Steel Corp.,
Pittsburgh, Pa.

K. W. Battery Co.,
Skokie, Ill.

Kaiser Aluminum & Chemical Corp.,
Metals Div. Research,
Permanente, Calif.
Div. of Metallurgical Research,
Spokane, Wash.

Kawecki Chemical Co.,
Boyertown, Pa.

Kennecott Copper Corp.,
New York, N. Y.

Leesona Moos Laboratories, Div. of Leesona Corp., Great Neck, N. Y.

Arthur D. Little, Inc.,
Cambridge, Mass.

Lockheed Aircraft Corp.,
Missiles & Space Div.,
Sunnyvale, Calif.

Mallinckrodt Chemical Works,
St. Louis, Mo.

P. R. Mallory & Co.,
Indianapolis, Ind.

Melpar, Inc.,
Falls Church, Va.

Miles Chemical Co., Div. of Miles Laboratories, Inc., Elkhart, Ind.

Mobil Oil Corp.,
Dallas, Texas

Monsanto Chemical Co.,
St. Louis, Mo.

M&T Chemicals Inc.,
Detroit, Mich.

Nalco Chemical Co.,
Chicago, Ill.

National Cash Register Co.,
Dayton, Ohio

National Lead Co.,
New York, N. Y.

National Steel Corp.,
Weirton, W. Va.

North American Aviation, Inc.,
El Segundo, Calif.

Northern Electric Co.,
Montreal, Que., Canada

Norton Co.,
Worcester, Mass.

Owens-Illinois Glass Co.,
Toledo, Ohio

Pennsalt Chemicals Corp.,
Philadelphia, Pa.

Phelps Dodge Refining Corp.,
Maspeth, N. Y.

Philips Laboratories, Inc.,
Briarcliff Manor, N. Y.

Pittsburgh Plate Glass Co.,
Chemical Div.,
Pittsburgh, Pa.

Potash Co. of America,
Carlsbad, N. Mex.

Radio Corp. of America
Electronic Components and Devices,
Lancaster, Pa.
RCA Victor Record Div.
Indianapolis, Ind.

Republic Foil Inc.,
Danbury, Conn.

Reynolds Metals Co.,
Richmond, Va.

Shawinigan Chemicals Ltd.,
Montreal, Que., Canada

Sonotone Corp.,
Elmsford, N. Y.

Speer Carbon Co.,
International Graphite & Electrode
Div., St. Marys, Pa.

Sprague Electric Co.,
North Adams, Mass.

Stackpole Carbon Co.,
St. Marys, Pa.

The Standard Oil Company of Ohio,
Cleveland, Ohio

Stauffer Chemical Co.,
Dobbs Ferry, N. Y.

Texas Instruments, Inc.,
Dallas, Texas
Metals and Controls Corp.,
Attleboro, Mass.

3M Company,
St. Paul, Minn.

Titanium Metals Corp. of America,
Henderson, Nev.

Tyco Laboratories, Inc.,
Waltham, Mass.

Udylite Corp.,
Detroit, Mich. (4 memberships)

United States Steel Corp.,
Pittsburgh, Pa.

Univac, Div. of Sperry Rand Corp.,
New York, N. Y.

Upjohn Co.,
Kalamazoo, Mich.

Varian Associates,
Palo Alto, Calif.

Western Electric Co., Inc.,
Chicago, Ill.

Wyandotte Chemicals Corp.,
Wyandotte, Mich.

Yardney Electric Corp.,
New York, N. Y.

THE ELECTROCHEMICAL SOCIETY PATRON MEMBERS

Aluminum Co. of Canada, Ltd., Montreal, Que., Canada

Dow Chemical Co.
Chemicals Dept., Midland, Mich.
Metals Dept., Midland, Mich.

General Electric Co.
Capacitor Dept., Hudson Falls, N. Y.
Chemical Laboratory, Knolls Atomic Power Laboratory, Schenectady, N. Y.
Chemical Systems and Processes Laboratory, Research and Development Center, Schenectady, N. Y. (3 memberships)
Direct Energy Conversion Operation, West Lynn, Mass.
Lamp Div., Cleveland, Ohio
Materials & Processes Laboratory, Large Steam Turbine-Generator Dept., Schenectady, N. Y.

The International Nickel Co., Inc., New Yok, N. Y.

Olin Mathieson Chemical Corp.
Chemicals Div., Research Dept., New Haven, Conn.

Union Carbide Corp.
Divisions:
Carbon Products Div., New York, N. Y.
Consumer Products Div., New York, N. Y.

Westinghouse Electric Corp.
Electronic Tube Div., Elmira, N. Y.
Lamp Div., Bloomfield, N. J.
Molecular Electronics Div., Elkridge, Md.
Semiconductor Div., Youngwood, Pa.
Research Laboratories, Pittsburgh, Pa.

THE ELECTROCHEMICAL SOCIETY SUSTAINING MEMBERS

Air Reduction Co., Inc., New York, N. Y.

Allen-Bradley Co., Milwaukee, Wis.

Allied Chemical Corp., General Chemical Div., Morristown, N. J.

Aluminum Co. of America, New Kensington, Pa.

American Metal Climax, Inc., New York, N. Y.

American Potash & Chemical Corp., Los Angeles, Calif.

American Smelting and Refining Co., South Plainfield, N. J.

American Zinc Co., St. Louis, Mo.

American Zinc Co. of Illinois, East St. Louis, Ill.

The M. Ames Chemical Works, Inc., Glens Falls, N. Y.

Ampex Corp., Redwood City, Calif.

Armco Steel Corp., Middletown, Ohio

Basic Inc., Bettsville, Ohio

Bell Telephone Laboratories, Inc., New York, N. Y. (2 memberships)

Bethlehem Steel Corp., Bethlehem, Pa. (2 memberships)

Boeing Co., Seattle, Wash.

Burgess Battery Co., Freeport, Ill. (2 memberships)

Burndy Corp., Norwalk, Conn.

Canadian Industries Ltd., Montreal, Que., Canada

Carborundum Co., Niagara Falls, N. Y.

Chrysler Corp., Detroit, Mich.

Cominco Ltd., Trail, B. C., Canada (2 memberships)

Corning Glass Works, Corning, N. Y.

Cyclops Corp., Universal-Cyclops Specialty Steel Div., Bridgeville, Pa.

Diamond Alkali Co., Painesville, Ohio

Wilbur B. Driver Co., Newark, N. J.

E. I. du Pont de Nemours & Co., Inc., Wilmington, Del.

Eagle-Picher Industries, Inc., Electronics Div., Joplin, Mo.

Eastman Kodak Co., Rochester, N. Y.

Eltra Corp.
Prestolite Div., Toledo, Ohio
C&D Batteries, Conshohocken, Pa.

Engelhard Industries, Inc., Newark, N. J.

The Eppley Laboratory, Inc., Newport, R. I.

ESB Inc., Philadelphia, Pa. (2 memberships)

Esso Research and Engineering Co., Engineering Technology Div., Florham Park, N. J.

Exmet Corp., Bridgeport, Conn.